OUKA
The University of Osaka
Institutional Knowledge Archive

Title	Control of Photodriven Electron-Transfer Processes within the Columnar Perylenediimide Nanostructures via Weak Interactions for Efficient Light-Energy Conversion
Author(s)	Supur, Mustafa
Citation	大阪大学, 2013, 博士論文
Version Type	VoR
URL	https://doi.org/10.18910/26209
rights	
Note	

The University of Osaka Institutional Knowledge Archive : OUKA

https://ir.library.osaka-u.ac.jp/

The University of Osaka

Doctoral Dissertation

Control of Photodriven Electron-Transfer Processes within the Columnar Perylenediimide Nanostructures via Weak Interactions for Efficient Light-Energy Conversion

Mustafa SUPUR

July 2013

Department of Material and Life Science
Graduate School of Engineering
Osaka University

Contents

General Introduction		1
Chapter 1	Efficient Electron Transfer Processes of the Covalently Linked Perylenediimide–Ferrocene Systems: Femtosecond and Nanosecond Transient Absorption Studies	7
Chapter 2	Electron Delocalization in One-Dimensional Perylenediimide Nanobelts via Photoinduced Electron Transfer	31
Chapter 3	Excitation Energy Transfer from Non-Aggregated Molecules to Perylenediimide Nanoribbons via Ionic Interactions in Water	48
Chapter 4	Enhancement of Photodriven Charge Separation by Conformational and Intermolecular Adaptations of an Anthracene–Perylenediimide–Anthracene Triad to an Aqueous Environment	61
Chapter 5	Photodriven Electron Transport within the Columnar Perylenediimide Nanostructures Self-Assembled with Sulfonated Porphyrins in Water	79
Chapter 6	Tuning the Photodriven Electron Transport within the Columnar Perylenediimide Stacks by Changing the π-extent of the electron donors	97
Concluding Remarks		115
List of Publications		117
Acknowledgment		119

General Introduction

Photoinduced electron transfer is a crucial way for the conversion of solar energy into a usable form of chemical potential in organic photovoltaic devices[1-4] and in natural photosynthesis.[5-8] In organic solar cells, charge generation (i.e., formation of electron and hole) is achieved by initial charge separation as a result of exciton dissociation at the interface of electron-donor and electron-acceptor domains and this process is followed by charge migration from the bulk of the active layer towards the corresponding electrodes of the device to obtain a current flow. Charge separation at the interface competes with charge recombination, which impedes the charge collection at the electrodes and substantially decreases the device efficiency.[1-4] Morphological arrangements at nanometer scale in the active layer of the photovoltaic devices are suggested to restrain the fast recombination, thereby improving the efficiency values.[9-12] Ideally, electron and hole generated at the interface should be properly directed to the interspaced one-dimensional conduits of the donor and the acceptor tailored in accordance with the efficient light harvesting and exciton diffusion length before they wasted by fast charge recombination in the bulk (Figure 1).[12]

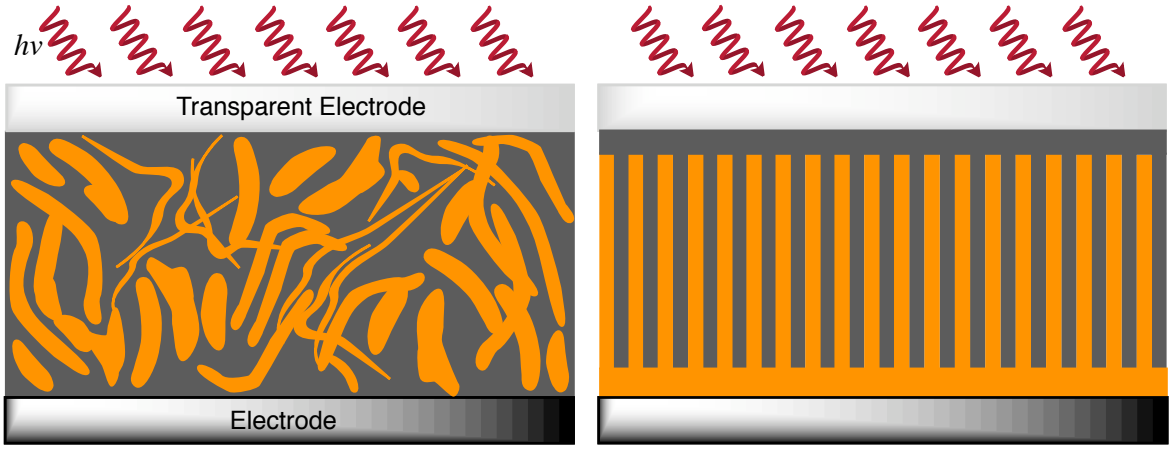


Figure 1. Realistic (left) and ideal (right) active layer morphology of a bulk heterojunction solar cell at nanometer scale.

Involving the long-lived charge separated states,[5,13] photoconversion reactions of photosynthesis take place in the photosynthetic reaction centers.[14] These reaction centers are protein-cofactor complexes embedded in the thylakoid membrane by non-covalent interactions and involved in the electron transport chain during the light-dependent reactions of the photosynthesis (Figure 2).[14-18] The transmembrane helical sections of the protein subunits surrounding the reaction centers are mainly composed of amino acids bearing hydrophobic residues. This provides an orientation control by which the protein is tightly positioned in the membrane in a unique position.[19-21] Besides the oriented protein structure to conduct the

products of electron transfer event (i.e., radical ion pair), the reaction center cofactors are spatially ordered to prevent the fast charge recombination.[13,22-24] The electron is rapidly transferred towards the stromal surface to the electron acceptor, plastoquinone Q_A, through a chlorophyll (Chl_{D1}) and a pheophytin ($Pheo_{D1}$) to create a $P680^{\bullet+}$-$Q_A^{\bullet-}$ charge-separated pair, distant from each other around 3.4 nm (Figure 2).[25]

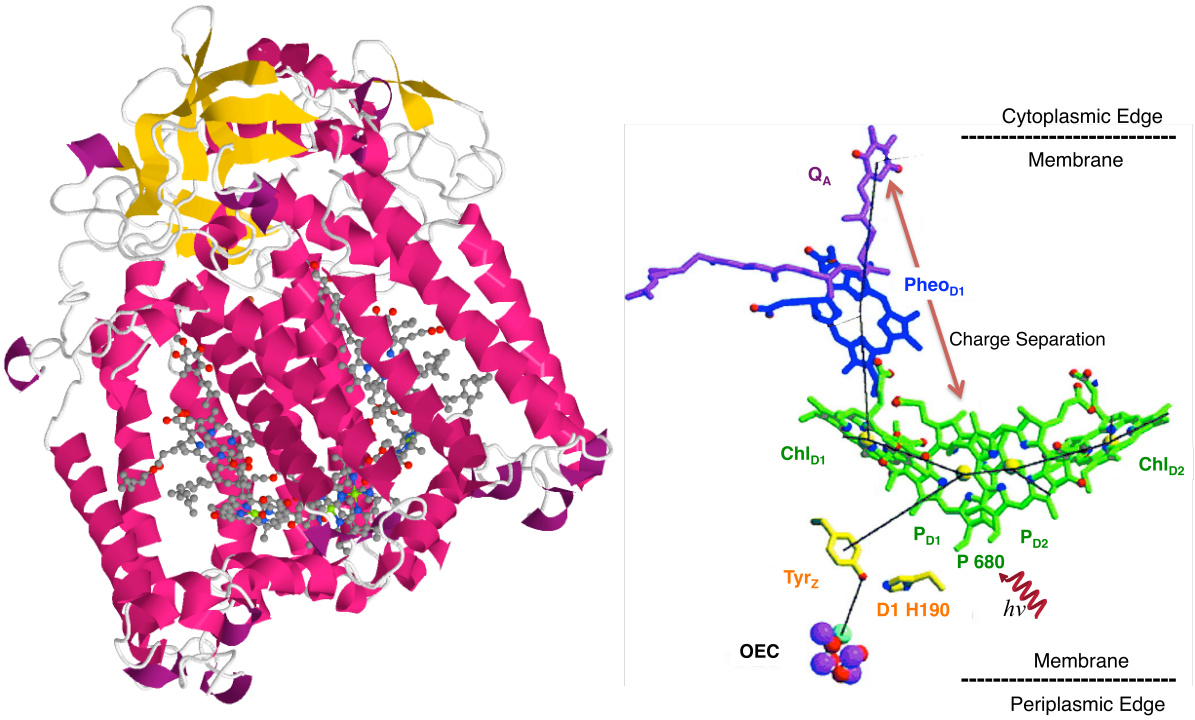


Figure 2. Entire structure of photosynthetic reaction center complex of *Rhodobacter sphaeroides*, including protein subunits and cofactors (left) and photoinduced charge separation among the cofactors of reaction center of *Thermosynechococcus elongates* (right). Structures were obtained from Protein Data Bank (structure ID: 1AIJ) and ref. 16 and modified for clarity.

As in the protein-cofactor arrangements existing in the photosynthetic reaction centers, well-ordered orientation at the nanoscale can be controlled by the intermolecular weak interactions among the molecules of the materials designed for photonics and electronics wherein the efficient electron transfer is critically of importance.[26-35] In this context, perylenediimide dyes (PDIs)[36] emerge as quintessential building blocks of one-dimensional self-assemblies at nanoscale (Figure 3).[37-39] Known for high persistency against harsh physical and chemical conditions (i.e., high temperature, concentrated sulfuric acid, molten potassium hydroxide, and concentrated bleach),[40,41] PDIs are quite invaluable for optoelectronic applications because they possess high absorption features in the visible region, strong fluorescence emission with quantum yields close to unity, and proper redox activity.[42] Its intrinsic low solubility has been overcome by introducing substituents from imides or bay region (Figure 3).[41] Large aromatic plane of PDI causing the low solubility actually promotes strong π-π interactions, which

eventually result in the formation of nanostructures aligned in one dimension.[38,43] PDIs are good electron acceptors due to four electron-withdrawing oxygen atoms. Therefore, the nanostructures of PDIs have high electron transport potential along their long axes [44] to effectively channel the electrons obtained by photodriven charge separation to the electrodes to prevent the fast charge recombination in the organic photovoltaic devices.

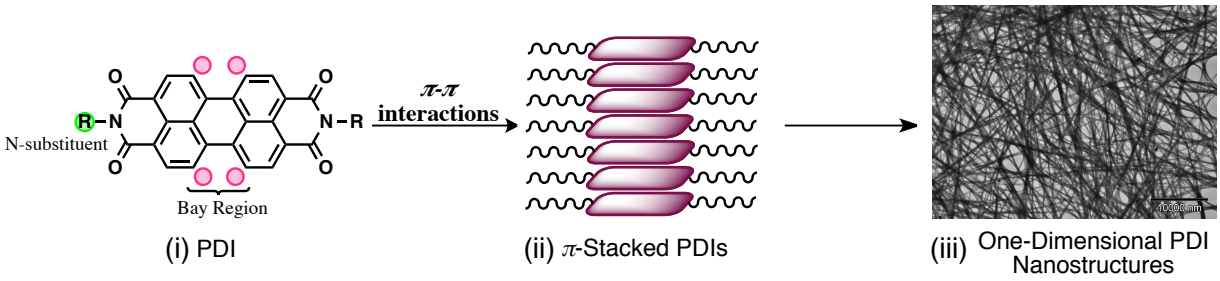


Figure 3. (i) Molecular structure of PDI showing the substitution from N-atoms and bay region (ii) Illustration of π-stacked PDIs via π-π interactions, and (iii) Transmission electron microscopy image of one-dimensional nanostructures of PDI obtained by solution-based self-assembly.

Due to above-mentioned spectral and electrochemical properties, PDI dyes have been employed in many donor-acceptor systems mimicking the photosynthetic reaction center. Photoinduced electron-transfer processes within molecular polyad systems,[45-48] hybrid systems with carbon nanostructures[49,50] and the supramolecular self-assembly models[51-57] of PDIs have been reported in various studies. However, the light induced electron transfer from donor moieties to columnar PDI nanostructures and the spectroscopic characterization of the electron transport along these structures have yet to be clarified.

The Contents of This Doctoral Thesis

This thesis describes herein the photodriven electron-transfer processes of the columnar PDI nanostructures for efficient light-energy conversion by employing the self-assembly models in the corresponding chapters. The charge separation and the directional charge transport in the following chapters have been clarified by using time-resolved transient absorption techniques.

In chapter 1, photoinduced electron transfer taking place in the newly synthesized covalently linked PDI-donor dyad and triad has been studied. PDI derivatives employed in this study bear electron-withdrawing cyano or electron-donating pyrrolidone groups at the bay region. Electron-transfer dynamics of monomer PDI have been obtained for understanding and comparison with those of the PDI π-stacks.

In chapter 2, the nature of the electron migration within the one-dimensional nanobelts of PDI has been explained spectroscopically during the photoinduced electron transfer from a strong electron donor.

In chapter 3, supramolecular self-assembly systems have been constructed by using various weak interactions to understand the effect of the distance between the PDI nanoribbons and the donor moieties on the dynamics of the electron and energy transfer events.

In chapter 4, the effect of π-stacking and conformational changes on the photoinduced charge separation process of PDI, which is covalently attached to electron-donor substituents has been studied in organic and aqueous media.

In chapter 5, electron-accepting columnar PDI nanostructures have been doped with π-electron donors by utilizing strong π-π and ionic interactions in aqueous environment. Charge separation and recombination processes have been studied to observe the effect of electron transport on the elongation of the lifetime of the charge-separated states.

In the last chapter, the control of photodriven electron transport within the columnar π-stacks of PDIs by changing the π-extent of the electron donors has been discussed. The lifetimes of the charge-separated states has been drastically altered by electron donors with varying π-extent due to enhanced charge migration within the columnar arrays of PDIs.

References

(1) Bredas, J.-L.; Beljonne, D.; Coropceanu, V.; Cornil, J. *Chem. Rev.* **2004**, *104*, 4971.

(2) Hoppe, H.; Sariciftci, N. S. *J. Mater. Res.* **2004**, *19*, 1924.

(3) Thompson, B. C.; Frechet, J. M. J. *Angew. Chem., Int. Ed.* **2008**, *47*, 58.

(4) Clarke, T. M.; Durrant, J. R. *Chem. Rev.* **2010**, *110*, 6736.

(5) Farid, R. S.; Moser, C. C.; Dutton, P. L. *Curr. Opin. Struct. Biol.* **1993**, *3*, 225.

(6) Gray, H. B.; Winkler, J. R. *Ann. Rev. Biochem.* **1996**, *65*, 537.

(7) Stowell, M. H. B.; McPhillips, T. M.; Rees, D. C.; Soltis, S. M.; Abresch, E.; Feher, G. *Science* **1997**, *276*, 812.

(8) Heathcote, P.; Fyfe, P. K.; Jones, M. R. *Trends Biochim. Sci.* **2002**, *27*, 79.

(9) Österbacka, R.; An, C. P.; Jiang, X. M.; Vardeny, Z. V. *Science*, **2000**, *287*, 839.

(10) Hoppe, H.; Niggemann, M.; Winder, C.; Kraut, J.; Hiesgen, R.; Hinsch, A.; Meissner, D.; Sariciftci, N. S. *Adv. Funct. Mater.* **2004**, *14*, 1005.

(11) Grimsdale, A. C.; Müllen, K. *Angew. Chem., Int. Ed.* **2005**, *44*, 5592.

(12) Günes, S.; Neugebauer, H.; Sariciftci, N. S. *Chem. Rev.* **2007**, *107*, 1324.

(13) Marcus, R. A. *Angew. Chem., Int. Ed.* **1993**, *32*, 1111.

(14) Blankenship, R. E. *Molecular Mechanisms of Photosynthesis*; Blackwell Science: Oxford, U.K., 2002.

(15) Ferreira, K. N.; Iverson, T. M.; Maghlaoui, K.; Barber, J.; Iwata, S. *Science* **2004**, *303*, 1831.

(16) Huynh, M. H. V.; Meyer, T. J. *Chem. Rev.* **2007**, *107*, 5004.

(17) Barber, J. *Chem. Soc. Rev.* **2009**, *38*, 185.

(18) Umena, Y.; Kawakami, K.; Shen, J.-R.; Kamiya, N. *Nature* **2011**, *473*, 55.

(19) Barber, J.; Nield, N.; Morris, E. P.; Hankamer, B. *Trends Biochim. Sci.* **1999**, *24*, 43.
(20) Balabin, I. A.; Onuchic, J. *Science* **2000**, *290*, 114.
(21) Roose, J. L.; Wegener, K. M.; Pakrasi, H. B. *Photosynth. Res.* **2007**, *92*, 369.
(22) Boxer, S. G. *Annu. Rev. Biophys. Bioeng.* **1990**, *19*, 267.
(23) Moser, C. C.; Dutton, P. L. *Biochim. Biophys. Acta* **1992**, *1101*, 171.
(24) Brettel, K. *Biochim. Biophys. Acta* **1997**, *1318*, 322.
(25) Loll, B.; Kern, J.; Saenger, W.; Zouni, A.; Biesidka, J. *Nature* **2005**, *438*, 1040.
(26) Meijer, E. W.; Schenning, A. P. H. J. *Nature* **2002**, *419*, 353.
(27) Lehn, J.-M. *Science* **2002**, *295*, 2400.
(28) Reinhoudt, D. N.; Crego-Calama, M. *Science* **2002**, *295*, 2403.
(29) Ikkala, O.; ten Brinke, G. *Science* **2002**, *295*, 2407.
(30) Whitesides, G. M.; Grzybowski, B. *Science* **2002**, *295*, 2418.
(31) Jonkheijm, P.; van der Schoot, P.; Schenning, A. P. H. J.; Meijer, E. W. *Science* **2006**, *313*, 80.
(32) Green, J. E.; Choi, J. W.; Boukai, A.; Bunimowich, Y.; Johnston-Halperin, E.; Delonno, E.; Luo, Y.; Sheriff, B. A.; Xu, K.; Shin, Y. S.; Tseng, H.-R.; Stoddart, J. F.; Health, J. R. *Nature* **2007**, *445*, 414.
(33) Hochbaum, A. I.; Yang, P. *Chem. Rev.* **2010**, *110*, 527.
(34) Hains, A. W.; Liang, Z.; Woodhouse, M. A.; Gregg, B. A. *Chem. Rev.* **2010**, *110*, 6689.
(35) Hasegawa, M.; Iyoda, M. *Chem. Soc. Rev.* **2010**, *39*, 2420.
(36) Alternatively, perylene-3,4:9,10-tetracarboxylic diimide (PTCDI) or perylene bisimide (PBI).
(37) Schmidt-Mende, L.; Fechtenkötter, A.; Müllen, K.; Moons, E.; Friend, R. H.; MacKenzie, J. D. *Science* **2001**, *293*, 1119.
(38) Zang, L.; Che, Y.; Moore, J. S. *Acc. Chem. Res.* **2008**, *41*, 1596.
(39) Briseno, A. L.; Mannsfeld, S. C. B.; Reese, C.; Hancock, J. M.; Xiong, Y.; Jenekhe, S. A.; Bao, Z.; Xia, Y. *Nano Lett.* **2007**, *7*, 2847.
(40) Langhals, H. *Heterocycles* **1995**, *40*, 477.
(41) Langhals, H. *Helv. Chim. Acta* **2005**, *88*, 1309.
(42) Würthner, F. *Chem. Commun.* **2004**, 1564.
(43) Balakrishnan, K.; Datar, A.; Naddo, T.; Huang, J.; Oitker, R.; Yen, M.; Zhao, J.; Zang, L. *J. Am. Chem. Soc.* **2006**, *128*, 7390.
(44) Che, Y.; Datar, A.; Yang, X.; Naddo, T.; Zhao, J.; Zang, L. *J. Am. Chem. Soc.* **2007**, *129*, 6354.
(45) Cespedes-Guirao, F. J.; Ohkubo, K.; Fukuzumi, S.; Sastre-Santos, A.; Fernandez-Lazaro, F. *J. Org. Chem.* **2009**, *74*, 5871.

(46) Cespedes-Guirao, F. J.; Martin-Gomis, L.; Ohkubo, K.; Fukuzumi, S.; Fernandez-Lazaro, F.; Sastre-Santos, A. *Chem.–Eur. J.* **2011**, *17*, 9153.

(47) Berberich, M.; Natali, M.; Spenst, P.; Chiorboli, C.; Scandola, F.; Würthner, F. *Chem.–Eur. J.* **2012**, *18*, 13651.

(48) Blas-Ferrando, V. M.; Ortiz, J.; Bouissane, L.; Ohkubo, K.; Fukuzumi, S.; Fernandez-Lazaro, F.; Sastre-Santos, A. *Chem. Commun.* **2012**, *48*, 6241.

(49) Hahn, U.; Engmann, S.; Oelsner, C.; Ehli, C.; Guldi, D. M.; Torres, T. *J. Am. Chem. Soc.* **2010**, *132*, 6392.

(50) Oelsner, C.; Schmidt, C.; Hauke, F.; Prato, M.; Hirsch, A.; Guldi, D. M. *J. Am. Chem. Soc.* **2011**, *133*, 4580.

(51) Würthner, F.; Chen, Z.; Hoeben, F. J. M.; Osswald, P.; You, C.-C.; Jonkheijm, P.; Herrikhuyzen, J. v.; Schenning, A. P. H. J.; van der Schoot, P. P. A. M.; Meijer, E. W.; Beckers, E. H. A.; Meskers, S. C. J.; Janssen, R. A. *J. Am. Chem. Soc.* **2004**, *126*, 10611.

(52) Bullock, J. E.; Carmieli, R.; Mickley, S. M.; Vura-Weis, J.; Wasielewski, M. R. *J. Am. Chem. Soc.* **2009**, *131*, 11919.

(53) Wasielewski, M. R. *Acc. Chem. Res.* **2009**, *42*, 1910.

(54) Grimm, B.; Schornbaum, J.; Jasch, H.; Trukhina, O.; Wessendorf, F.; Hirsch, A.; Torres, T.; Guldi, D. M. *Proc. Nat. Acad. Sci. USA* **2012**, *109*, 15565.

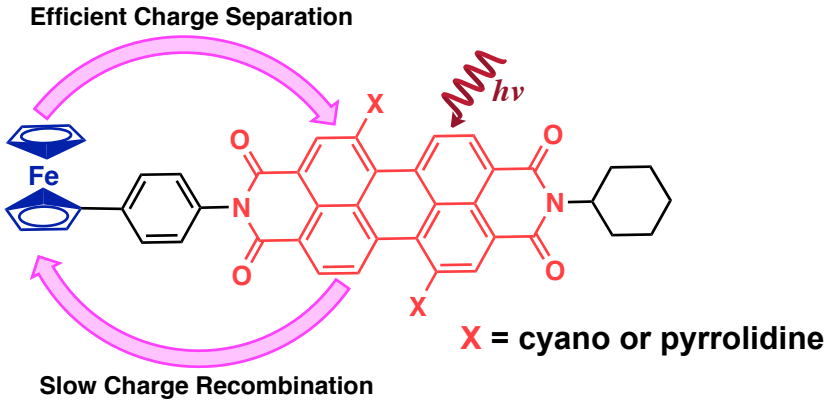
(55) Lefler, K. M.; Co, D. T.; Wasielewski, M. R. *J. Phys. Chem. Lett.* **2012**, *3*, 3798.

(56) Mickley Conron, S. M.; Shoer, L. E.; Smeigh, A. L.; Ricks, A. B.; Wasielewski, M. R. *J. Phys. Chem. B* **2013**, *117*, 2195.

(57) Jimenez, A. J.; Calderon, R. M. K.; Rodriguez-Morgade, M. S.; Guldi, D. M.; Torres, T. *Chem. Sci.* **2013**, *4*, 1064.

Chapter 1

Efficient Electron Transfer Processes of the Covalently Linked Perylenediimides–Ferrocene Systems: Femtosecond and Nanosecond Transient Absorption Studies



Abstract: Photoinduced electron-transfer processes of the newly synthesized rodlike covalent donor-acceptor molecules consisting of electron-donating ferrocenes (Fc) with electron-accepting perylenediimides (PDIs) with core-substituted cyano and pyrrolidine groups, forming Fc-PDI$(CN)_2$ dyad, Fc_2-PDI$(CN)_2$ triad, and Fc-PDI$(Py)_2$ dyad, have been investigated in benzonitrile. The geometric and electronic structures of the dyads and triad were probed by ab initio B3LYP/6-311G methods. The distribution of the highest occupied molecular orbitals (HOMOs) was on the ferrocene entities, while the distribution of lowest unoccupied molecular orbitals (LUMOs) was on the PDI entities. Free-energy calculations verify that the light-induced processes from excited states of PDIs are exothermic. The excited state photochemical events are monitored by femtosecond and nanosecond transient absorption techniques. In benzonitrile, the quenching pathway involves fast and efficient charge-separation from the ferrocenes to the excited PDIs. The finding that the lifetime of Fc_2^{+}-$[PDI(CN)_2]^{\bullet-}$ triad (59 ps) was found to be longer than that of Fc^{+}-$[PDI(CN)_2]^{\bullet-}$ dyad (25 ps) in benzonitrile reflects the effect of the second ferrocene entity in stabilizing the radical ion-pairs in the triad. In addition, photoinduced electron transfer in Fc-PDI$(Py)_2$ dyad occurs via the drastic quenching of singlet state of PDI$(Py)_2$, resulting in the enhancement of triplet state of PDI$(Py)_2$ due to charge recombination of the radical-ion pairs.

Introduction

Perylene dyes continue to emerge as archetypal components in a variety of photofunctional materials. Due to their unique light-harvesting[1] and redox properties[2] as well as high chemical persistency, thermal durability, and photostability,[3] perylene dyes have been regarded as potential candidates for numerous applications, spanning from optoelectronics to biological fields, such as organic light-emitting diodes (OLED),[4] optical switches,[5] organic field-effect transistors (OFET),[6] xerographic materials,[7] organic solar cells,[8] laser dyes,[9] and biosensors,[10] and so forth.

Among the derivatives of perylene dyes, the perylenediimide (PDI) dyes seem to be ideal for light-based applications due to their excellent photophysical properties. The PDI dyes have strong absorption with high molar absorption coefficients (ε = 58000 $M^{-1}cm^{-1}$ at 490 nm in $CHCl_3$), a long fluorescence lifetime, near unity fluorescence quantum yields.[3a] PDIs with their low reduction potentials are very convenient electron acceptors.[2a] A more practical aspect of PDIs concerns the optical absorption spectra of their radical anions, which show strong and characteristic absorption bands (ε = 10^4–10^5 M^{-1} cm^{-1}) in the Vis-NIR region of the spectra, serving as diagnostic probes for their identification.[11] Furthermore, these isolated absorptions of the radical anions, especially in the NIR region, allow an accurate analysis of inter- and intramolecular electron-transfer dynamics of PDI-based compounds.

PDIs present a chemical versatility to introduce new substituents from imide groups and bay region (positions 1, 6, 7, and 12) in order to overcome their inherent low solubility[12] and adjust spectral and electrochemical properties.[2a,3a,13] For example, appendage of electron-withdrawing cyano groups to 1-and 7-positions of perylenediimides, $PDI(CN)_2$, leads into a significant positive shift of reduction potentials of PDI without changing its parental steady-state spectral characteristics.[14] Attachment of pyrrolidine groups to 1-and 7-positions of perylenediimides, $PDI(Py)_2$, on the other hand, results in different consequences such as appearance of intense absorption at NIR region canceling the absorption bands around 530 nm and electron-donating character by reason of amine groups.[14]

To date, many redox active chromophores were involved in various donor-acceptor systems based on the PDI derivatives.[2b,15] To the best of our knowledge, the combinations of PDIs as electron acceptors with the ferrocenes, as electron donors, are rare. Recently, such combinations have been used as an electrochemical indicator for human telomeric DNA tetraplex,[16] supramolecular[2d] and multistate[2e] redox-active structures, unimolecular electrical rectifier,[17] and molecular fluorescent switch,[2f] exposing their wide-range applicability. The details of intramolecular photoinduced electron-transfer (PET) mechanisms of perylenediimides-ferrocene systems have yet to be explored.

In this work, we described in details the photochemical properties of the newly synthesized dyad and triad molecules composed of $PDI(CN)_2$ with one and two ferrocenes attached (Figure 1). The photophysical properties of $PDI(Py)_2$ with one ferrocene have also been investigated

because of its NIR light absorbing characteristics which is of importance for optical data processing[18a] as well as energy conversion and strorage.[19] In the literature, contrary to usual cases of PDI dyes, where they are conventionally used as electron acceptors,[2b,15] $PDI(Py)_2$ has been insistently assessed as electron-donor moiety due to amine groups in various donor-acceptor models.[18] Both femtosecond and nanosecond transient absorption spectral studies were performed in order to characterize the electron-transfer species in polar benzonitrile and to explore the mechanistic details of the light-induced electron-transfer reactions from the ferrocene to the singlet-excited $PDI(CN)_2$ and $PDI(Py)_2$.

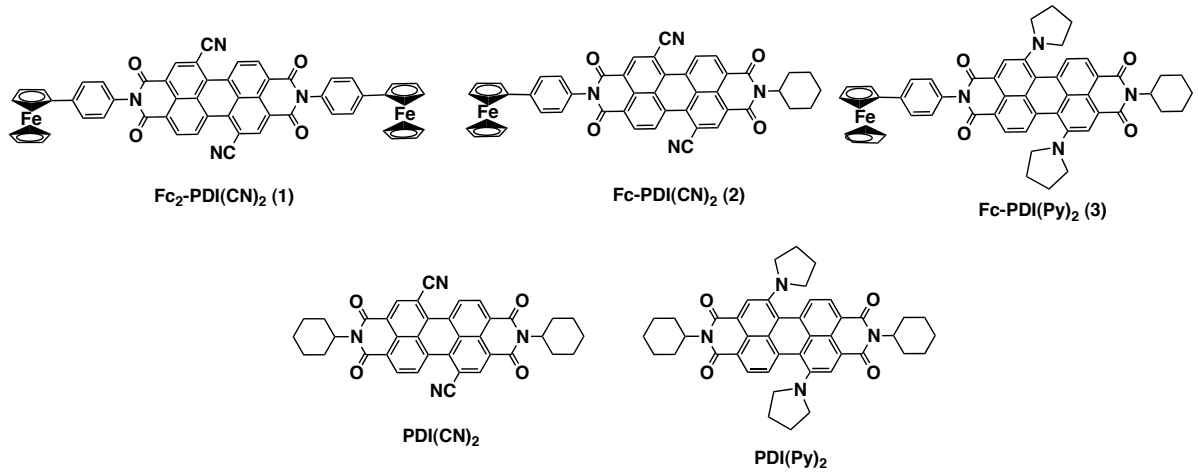


Figure 1. Molecular structures of the investigated compounds **1**-**3** and their references.

Experimental Section

Materials and Instruments. Steady-state absorption measurements were recorded on a Shimadzu UV-3100PC spectrometer or a Hewlett Packard 8453 diode array spectrophotometer at room temperature. IR spectra were recorded by using a ThermoNicolet NEXUS 670 FTIR spectrometer in the range of ν = 500 to 4000 cm^{-1} at room temperature. Samples were prepared as KBr pellets at different concentrations. MALDI-TOF MS spectra were recorded with an Applied Biosystems Voyager-DE-STR using dithranol as a matrix.

Fluorescence measurements were carried out on a Shimadzu spectrofluorophotometer (RF-5300PC). Phosphorescence spectra were obtained by a SPEX fluorolog τ3 spectrophotometer. Emission spectra in the NIR region were detected by using a Hamamatsu Photonics R5509-72 photomultiplier. An Ar-saturated 2-MeTHF solution containing $PDI(CN)_2$ and $PDI(Py)_2$ at 77 K was excited at indicated wavelengths.

Electrochemical measurements were performed on an ALS630B electrochemical analyzer in deaerated benzonitrile (PhCN) containing tetra-*n*-butylammonium hexafluorophosphate ($TBAPF_6$ 0.10 M) as supporting electrolyte at 298 K. A conventional three-electrode cell was used with a platinum working electrode (surface area of 0.3 mm^2) and a platinum wire as the counter electrode. The Pt working electrode was routinely polished with BAS polishing

alumina suspension and rinsed with acetone before use. The measured potentials were recorded with respect to SCE reference electrode. All electrochemical measurements were carried out under an atmospheric pressure of argon. Femtosecond transient absorption spectroscopy experiments were conducted using an ultrafast source: Integra-C (Quantronix Corp.), an optical parametric amplifier: TOPAS (Light Conversion Ltd.) and a commercially available optical detection system: Helios provided by Ultrafast Systems LLC. The source for the pump and probe pulses were derived from the fundamental output of Integra-C (780 nm, 2 mJ/pulse and fwhm = 130 fs) at a repetition rate of 1 kHz. 75% of the fundamental output of the laser was introduced into TOPAS which has optical frequency mixers resulting in tunable range from 285 nm to 1660 nm, while the rest of the output was used for white light generation. Typically, 2500 excitation pulses were averaged for 5 seconds to obtain the transient spectrum at a set delay time. Kinetic traces at appropriate wavelengths were assembled from the time-resolved spectral data. All measurements were conducted at 298 K. The transient spectra were recorded using fresh solutions in each laser excitation. For nanosecond transient absorption measurements, deaerated solutions of the compounds were excited by a Panther OPO equipped with a Nd:YAG laser (Continuum, SLII-10, 4-6 ns fwhm) with a power of 10-15 mJ per pulse. The photochemical reactions were monitored by continuous exposure to a Xe lamp (150 W) as a probe light and a photomultiplier tube (Hamamatsu 2949) as a detector. Solutions were deoxygenated by argon purging for 15 min prior to the measurements.

Density-functional theory (DFT) calculations were performed on a COMPAQ DS20E computer. Geometry optimizations were carried out using the Becke3LYP functional and 3-61G basis set with the unrestricted Hartree-Fock (UHF) formalism and as implemented in the *Gaussian 03* program *Rev. C.02*. Graphical outputs of the computational results were generated with the *Gauss View* software program (ver. 3.09) developed by Semichem, Inc.

Synthesis of 1,7-dibromoperylene-3,4;9,10-tetracarboxydianhydride (6). Compound **6** was synthesized according to the literature procedures.[22] To a solution of compound **5** (10.0 g, 25 mmol) were added conc. sulfuric acid (300 mL) and then stirred for 24 hours at room temperature. The mixture was warmed to 55~60^{o}C and iodine (0.23 g, 2.5 mmol) was added. After 5 hours, the mixture was added bromine (7.6 mL, 62.5 mmol) slowly and then warmed to 80^{o}C and stirred for 8 hours. The mixture was quenched with ice water and filtered under reduced pressure to give compound **6** (12.5 g, 89%).

Synthesis of *N,N*-bis(ferrocenylphenyl)-1,7-dibromoperylene-3,4;9,10-bis(dicarboximide) (7). To a solution of compound **6** (1.0 g, 1.81 mmol) in DMF (60mL) were added zinc acetate (2.4 g, 6.6 mmol) and 4-ferrocenylaniline (1.6 g, 5.77 mmol). The mixture was warmed to 80^{o}C and stirred for 8 hours. The solvent was stripped under reduced pressure, and the residue was purified by column chromatography over silica gel with dichloromethane/acetone (10/1 v/v) to give compound **7** (0.8 g, 41%). ^{1}H NMR (400 MHz,

$CDCl_3$): δ 9.46 (d, 4H), 8.95(s, 2H), 8.91(d, 2H), 7.68(d, 2H), 7.24(d, 2H), 4.68(s, 2H), 4.36(s, 2H), 4.12(s, 10H); Anal. Calcd for $C_{56}H_{32}Br_2N_2O_4Fe_2$: C, 62.95%; H, 3.02%; N, 2.62%. Found: C, 62.71%; H, 2.87%; N, 2.46%.

Synthesis of *N,N*-bis(ferrocenylphenyl)-1,7-dicyanoperylene-3,4;9,10-bis(dicarboximide) (1). To a solution of compound **7** (0.05 g, 0.046 mmol) in 4-dioxane (50mL) were added CuCN (0.03 g, 0.33 mmol), $Pd_2(dba)_3$ (0.01 g, 0.01mmol) and dppf (0.01g, o.o1 mmol). The mixture was heated to reflux under N_2 and kept at reflux for 3 days. The solvent was stripped under reduced pressure and the residue was purified by column chromatography over silica gel with dichloromethane and then followed with dichloromethane/acetone (150/1 v/v). The last trace of impurities was eliminated by column chromatography over silica gel with dichloromethane/acetone (98/2 v/v) to give compound **1** (0.02 g, 45%). ^{1}H NMR (400 MHz, $CDCl_3$): δ 9.59 (d, 2H), 9.00(s, 2H), 8.81(d, 2H), 7.65(d, 2H), 7.24(d, 2H), 4.71(s, 2H), 4.39(s, 2H), 4.14(s, 10H); UV/vis (toluene): max λ (log ε) = 428 (4.03), 493 (4.45), 530 (4.64) nm; IR (KBr): ν 2963, 2923, 2363, 2322, 1713, 1675, 1652, 1602, 1406, 1352, 1260, 1092, 1026, 831, 802, 771, 740, 705, 668 cm^{-1}; MS (MALDI-TOF) (dithranol matrix): *m/z* for $C_{58}H_{32}N_4O_4Fe_2$ Calcd 960.56. Found 959.77 (M^+); Anal. Calcd for $C_{58}H_{32}N_4O_4Fe_2$: C, 72.52%; H, 3.36%; N, 5.83%. Found: C, 72.29%; H, 3.44%; N, 5.61%.

Synthesis of *N*-cyclohexyl-1,7-dibromoperylene-3,4-dicarboxyanhydride-9,10-dicarboximide (8) and *N,N*-bis(cyclohexyl)-1,7-dibromoperylene-3,4:9,10-tetracarboxydiimide (9). To a solution of compound 6 (3.0 g, 5.45 mmol) in pyridine (120mL) were added cyclohexylamine (3.12 g, 31.5mmol). The mixture was warmed to 75^{o}C and then stirred for 10 hours. The solvent was stripped under reduced pressure and the residue was tried to purify by column chromatography over silica gel several times. However, the compound 8 and 9 were adsorbed together to silica gel as a mixture and could not be separated. Therefore, the mixture was used for the next step without further separation. ^{1}H NMR (400 MHz, $CDCl_3$): δ 9.45 (d, 2H), 8.85(s, 2H), 8.63(d, 2H), 5.02 (t, 1H), 2.54 (q, 4H), 1.93 (q, 4H), 1.48 (q, 2H).

Synthesis of *N,N*-(cyclohexyl)-(4-ferrocenylphenyl)-1,7-dibromoperylene-3,4;9,10-bis(dicarboximide) (10). To a solution of the mixture of compounds **8** and **9** (0.1 g, 0.14 mmol on the assumption that the mixture is **8**) in toluene (50mL) were added zinc acetate (0.12 g, 0.66 mmol) and 4-ferrocenylaniline (0.1g, 0.56 mmol). The mixture was heated to reflux under N_2 and kept at reflux for 4 days. The solvent was stripped under reduced pressure. The residue was purified by column chromatography over silica gel with dichloromethane/acetone (120/1 v/v) to give 0.06g of red compound **10 (**0.06 g, 50% based on **8**). ^{1}H NMR (400 MHz, $CDCl_3$): δ 9.46 (d, 4H), 8.76(s, 2H), 8.65(d, 2H), 7.63 (d, 2H), 7.24 (d, 2H), 5.03 (t, 1H), 4.69 (s, 1H), 4.36 (s, 1H), 4.12 (s, 5H), 2.55 (q, 4H), 1.93 (q, 4H), 1.48 (q, 2H); Anal. Calcd for $C_{46}H_{30}Br_2N_2O_4Fe$: C, 62.05%; H, 3.40%; N, 3.15%. Found: C, 61.88%; H, 3.19%; N, 3.07%.

Synthesis of *N,N*-(cyclohexyl)-(4-ferrocenylphenyl)-1,7-dicyanoperylene-3,4;9,10-bis(dicarboximide) (2). To a solution of compound **10** (0.03 g, 0.033 mmol) in 4-dioxane (40mL) were added CuCN (0.1 g, 1.12 mmol), $Pd(dba)_3$ (0.02 g, 0.022mmol) and dppf (0.01 g, 0.018 mmol). The mixture was heated to reflux under N_2 and kept at reflux for 3 days. The solvent was stripped under reduced pressure and the residue was purified by column chromatography over silica gel with dichloromethane and then with dichloromethane/acetone (50/1 v/v) to give compound **2** (0.018g, 69%). ^{1}H NMR (400 MHz, $CDCl_3$): δ 9.46 (d, 2H), 8.92 (s, 2H), 8.65 (d, 2H), 7.63 (d, 2H), 7.24 (d, 2H), 5.03 (t, 1H), 4.69 (s, 1H), 4.36 (s, 1H), 4.12 (s, 5H), 2.55 (q, 4H), 1.93 (q, 4H), 1.48 (q, 2H); UV/vis (toluene): max λ (log ε) = 428 (4.03), 494 (4.45), 530 (4.64) nm; IR (KBr): ν 2927, 2854, 2359, 2322, 1701, 1663, 1594, 1406, 1338, 1259, 1106, 1030, 8311, 746, 693, 652 cm^{-1}; MS (MALDI-TOF) (dithranol matrix): *m/z* for $C_{48}H_{30}N_4O_4Fe$ Calcd: 782.60. Found: 782.03 (M^+); Anal. Calcd for $C_{48}H_{30}N_4O_4Fe$: C, 73.66%; H, 3.86%; N, 7.16%. Found: C, 73.74%; H, 3.99%; N, 7.07%.

Synthesis of *N,N*-bis(cyclohexyl)-1,7-bis(*N*-pyrrolidinyl) perylene-3,4;9,10-bis(dicarboximide) (11). To a solution of compounds **8** and **9** (0.5 g, 0.70 mmol on the assumption that the mixture is **9** were added pyrrolidine (30mL). The mixture was warmed to 55^{o}C and then stirred for 10 hours. The solvent was stripped under reduced pressure and the residue was purified by column chromatography over silica gel with dichloromethane to give compound **11** (0.12 g, 24% based on **9**). ^{1}H NMR (400 MHz, $CDCl_3$): δ 8.48 (s, 2H), 8.40 (d, 2H), 7.71 (d, 2H), 5.02 (t, 2H), 3.79 (s, 4H), 2.89 (s, 4H), 2.54 (q, 8H), 1.93 (q, 8H), 1.48 (q, 4H); Anal. Calcd for $C_{44}H_{44}N_4O_4$: C, 76.27%; H, 6.40%; N, 8.09%. Found: C, 76.10%; H, 6.53%; N, 7.88%.

Synthesis of *N*-cyclohexyl-1,7-bis(*N*-pyrrolidinyl) perylene-3,4-dicarboxydianhydride-9,10-dicarboximide (12). To a solution of compound **11** (0.24 g, 0.34 mmol) were added 2-propanol (100mL) and potassium hydroxide (0.3 g, 4.9 mmol). The mixture was stirred for 5 minutes at ambient temperature and heated to reflux under N_2 and kept at reflux for 30 minutes. The reaction mixture were added to 400ml of acetic acid solution (20mL of acetic acid in 400mL solution) and stirred for 10 minutes. The product was extracted with dichloromethane (400mL), and the organic extracts were washed 3 times with distilled water and dried. The dichloromethane was stripped under reduced pressure and the residue was purified by column chromatography over silica gel with dichloromethane/methanol (17/1 v/v) and then followed with dichloromethane/acetone (150/1 v/v) to give compound 12 (0.07 g, 38%). Compound 12: ^{1}H NMR (400 MHz, $CDCl_3$): δ 8.42 (s, 2H), 7.68 (d, 2H), 7.50 (d, 2H), 5.02 (t, 1H), 3.79 (s, 4H), 2.89 (s, 4H); Anal. Calcd for $C_{38}H_{33}N_3O_5$: C, 74.61%; H, 5.44%; N, 6.87%. Found: C, 74.39%, H, 5.63%, N, 6.96%.

Synthesis of *N,N*-(cyclohexyl)-(4-ferrocenylphenyl)-1,7-bis(*N*-pyrrolidinyl) perylene-3,4;9,10-bis(dicarboximide) (3). To a solution of compound **12** (0.05 g, 0.081 mmol) in pyridine (60mL) were added zinc acetate (0.15g, 0.83 mmol) and 4-

ferrocenylaniline (0.08 g, 0.29 mmol). The mixture was heated to reflux under N_2 and kept at reflux for 4 days. The solvent was stripped under reduced pressure and the residue was purified by column chromatography over silica gel with dichloromethane and then followed with dichloromethane/acetone (150/1 v/v) to give compound **3** (0.016 g, 23%). ^{1}H NMR (400 MHz, $CDCl_3$): δ 8.53 (s, 2H), 8.48 (d, 2H), 7.78 (d, 2H), 7.72(d, 2H), 7.64 (d, 2H), 5.11 (t, 1H), 4.71 (s, 1H), 4.38 (s, 1H), 4.14 (s, 5H), 3.80 (s, 8H), 2.87 (s, 8H), 2.61 (q, 4H), 1.79 (q, 4H); UV/vis (toluene): max λ (log ε) = 430 (4.21), 688 (4.64) nm; IR (KBr): ν 2928, 2853, 1690, 1655, 1592, 1579, 1560, 1417, 1339, 1257, 1243, 1123, 806 cm^{-1} MS (MALDI-TOF) (dithranol matrix): *m/z* for $C_{54}H_{46}N_4O_4Fe$ Calcd: 870.79. Found: 870.18 (M^+); Anal. Calcd for $C_{54}H_{46}N_4O_4Fe$: C, 74.48%; H, 5.33%; N, 6.43%. Found: C, 74.21%; H, 5.48%; N, 6.24%.

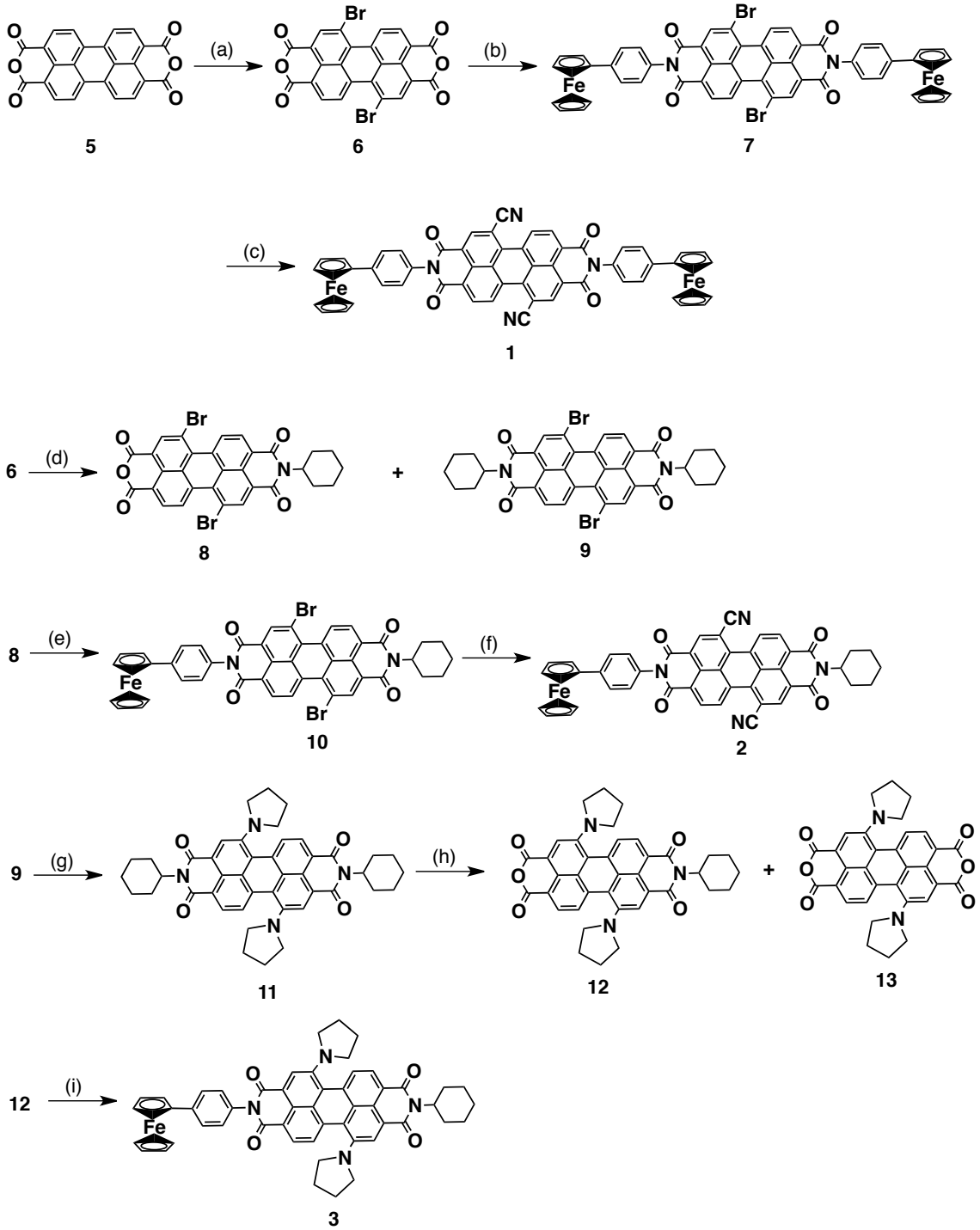
Results and Discussion

Synthesis and Characterization. Preparation of ferrocene–perylenediimide compounds **1-3** was performed by following the steps as depicted in Scheme 1. Every step of the reaction sequence proceeded smoothly and efficiently to give a good or moderate yield of the product. Commercially available perylene dianhydride (PDA, **5**) was brominated at 1 and 7 positions of the molecule according to the literature procedures[20] to give **6** in 89%. Subsequent reaction of **6** with 4-ferrocenylaniline was performed in the presence of $Zn(OAc)_2$ according to the literature procedures[21] to afford the corresponding diimide **7** in 41%. The bromine groups in **7** were substituted with CuCN by using tris(dibenzylideneacetone)-dipalladium(0), $[Pd_2(dba_3)_2]$ as a catalyst[11] to produce triad **1** in a yield of 45%. On the other hand, the reaction of PDA **6** with cyclohexyl amine gave a mixture of the corresponding perylene monoimide (PMI) **8** and PDI **9.** However, **8** and **9** could not be separated by chromatography as well as recrystallization methods. Therefore, the reaction mixture was used for the subsequent reactions without further purification. Reaction with 4-ferrocenylaniline gave **10** in 50%, and two bromine groups in **10** were substituted by CuCN to provide dyad **2** in 69%. Pyrrolidine groups were introduced to the 1 and 7 positions of **9** by substitution reaction according to the literature procedures[14] to give **11** in 24% and the following conversion to the corresponding compound **12** was carried out in basic condition by using KOH to afford **12** in 38%. Dyad **3** was finally obtained by the reaction of **12** with 4-ferrocenylaniline in the presence of $Zn(OAc)_2$ according to the literature procedures[21] in a yield of 23%.

Compounds **1-3** and their precursor compounds **5–13** are soluble in common organic solvents. ^{1}H NMR and elemental analysis mainly confirmed the structure and purity of the new compounds. ^{1}H NMR spectra of **1–3** are consistent with the proposed structures, showing the expected features with the correct integration ratios. The MALDI-TOF mass spectra provided a direct evidence for the structures of **1–3** showing a singly charged molecular ion peak, respectively, that matches the calculated value for the molecular weight of each compound.

Further confirmation of the compounds **1–3** was obtained from the steady-state absorption measurements as shown in the forthcoming sections.

Scheme 1. Synthesis of compounds **1**–**3**[a]



[a] (a) I_2, Br_2, H_2SO_4, 89%. (b) 4-Ferrocenylaniline, pyridine, $Zn(OAc)_2$, 80˚C, 8 hrs, 41%. (c) and (f) CuCN, $Pd_2(dba)_3$, dppf, 4-dioxane, reflux, 72 hrs, 45% for compound **1**, 69% for compound **2**. (d) Cyclohexylamine, pyridine, 75˚C, 10 hrs. (e) 4-Ferrocenylaniline, pyridine, $Zn(OAc)_2$, rt. 1 hr, 50%. (g) Pyrrolidine, 55˚C, 24%. (h) KOH, 2-propanol, rt, 30 min, 38%. (i) 4-Ferrocenylaniline, pyridine, $Zn(OAc)_2$, reflux, 96 hrs, 23%.

Steady-State Absorption and Fluorescence Measurements. As shown in Figure 2, the cyano-substituted and unsubstituted PDI exhibit quite the same absorption spectral patterns with the maxima at 532 nm, whereas due to the amino substitution from 1-and 7-positions, dyad **3** displays dramatic red shift of maximum from 530 nm to 707 nm in PhCN which is explained by charge transfer (CT) transition from electron-donating amino groups towards the PDI core.[18a] Remarkable shift of maxima of $PDI(Py)_2$ due to solvatochromism (684 nm in toluene and 700 nm in PhCN) peculiar to CT bands supports this idea. In cases of **1**–**3**, appendage of ferrocene(s) leads to slightly different maxima than those of $PDI(CN)_2$ and $PDI(Py)_2$ references probably owing to the replacement of cyclohexane with benzene link attached to ferrocene.[18a] It is worth to mention that the presence of planar node lying between two nitrogen atoms of imide groups of PDI precludes extensive electronic communication with the imide substituents.[22]

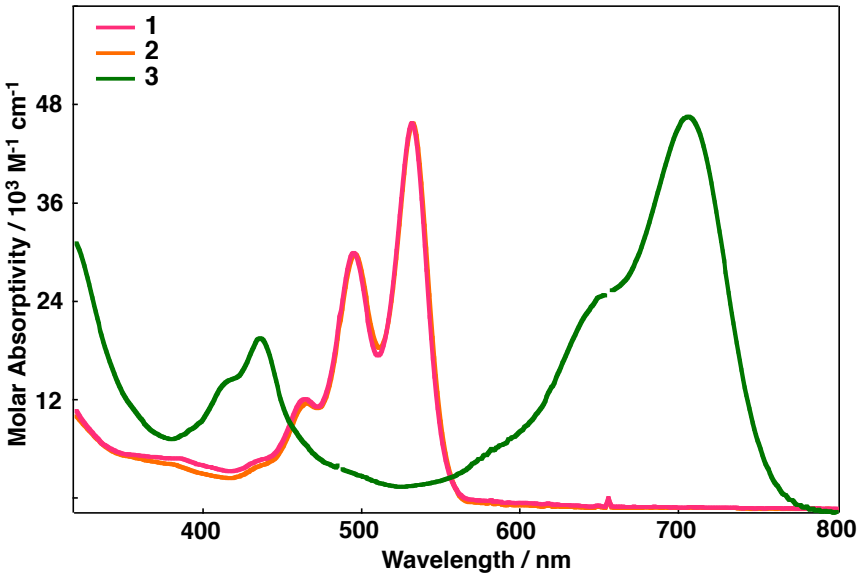


Figure 2. Steady-state absorption spectra of **1**–**3** in PhCN.

Photoinduced intramolecular events of **1**–**3** were investigated, firstly, by using steady-state fluorescence spectroscopy on exciting the PDI entities in PhCN. The emission spectra of $PDI(CN)_2$ and $PDI(Py)_2$ exhibited emission bands at 543 and 732 nm, respectively (Figure 3). Singlet excited state energies (ΔE_{0-0}) are calculated as 2.30 eV for $PDI(CN)_2$ and as 1.70 eV for $PDI(Py)_2$ with respect to the emission data in PhCN. In addition, energy levels of the triplet states of $PDI(Py)_2$ and $PDI(CN)_2$ are figured as 1.20 eV and 1.16 eV, respectively, according to phosphorescence measurements in which the former shows a peak at 1035 nm and the latter has a triplet emission at 1070 nm (Figure 4). The efficient quenching of the singlet excited state of the $PDI(CN)_2$ by the appended ferrocene entities is clearly seen in case of **1** and **2** in polar benzonitrile (Figure 3). The quenching process may involve the electron transfer from the ferrocene to the singlet excited state of $PDI(CN)_2$ and/or the energy transfer from the $PDI(CN)_2$ to ferrocene. The singlet excited state of the ferrocene (2.46 eV)[23] is above that of PDI

chromophores, ruling out the quenching due to the energy transfer. When turning to **3**, one could also observe a chiefly quenched fluorescence (82%) of the $PDI(Py)_2$ by the attached ferrocene in PhCN. It is likely that the fluorescence quenching is due to the electron-transfer process from the Fc to the $PDI(Py)_2$.

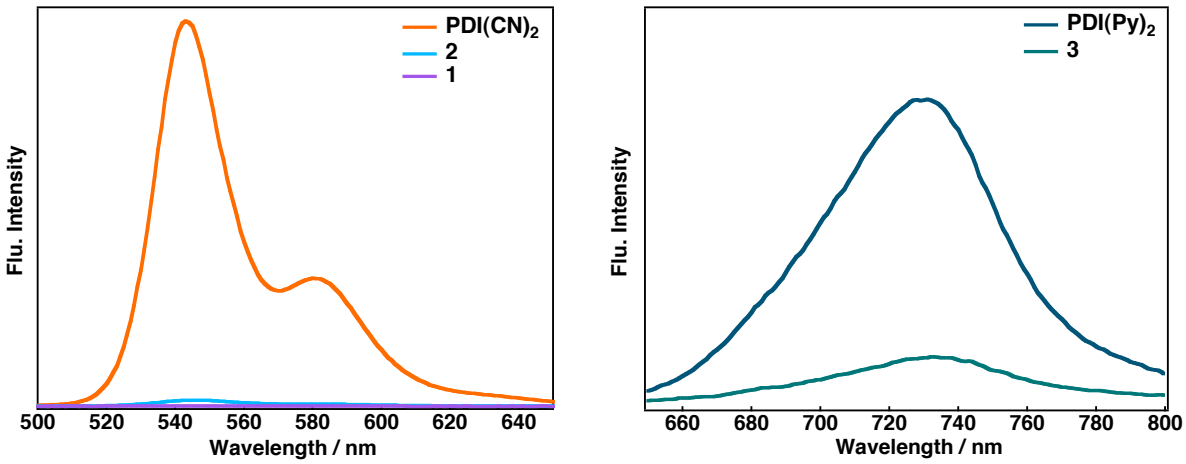


Figure 3. Steady-state emission of **1**–**3** and the reference compounds in PhCN (λ_{exc} = 490 and 430 nm, respectively).

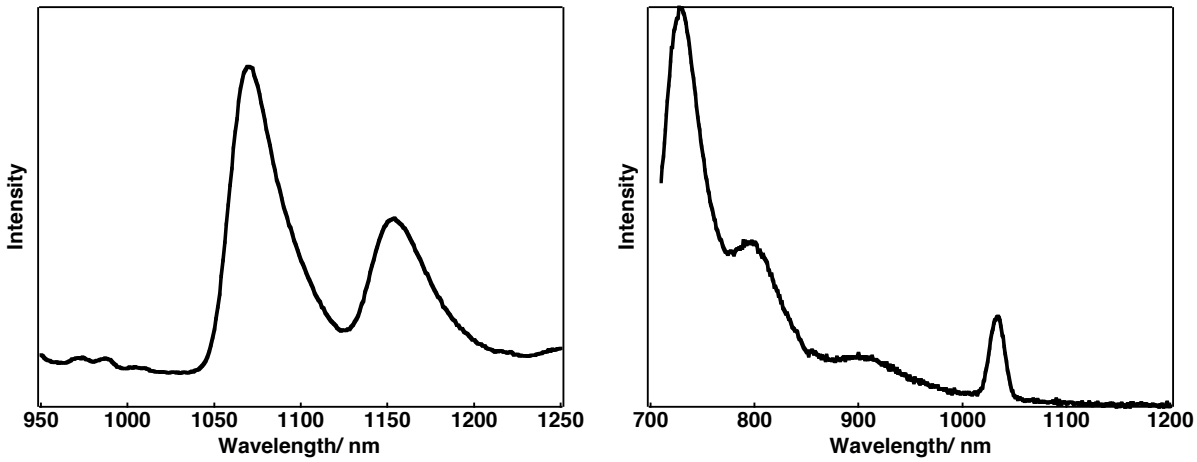


Figure 4. Phosphorescence spectra of $PDI(CN)_2$ (left) and $PDI(Py)_2$ (right) in frozen 2-MeTHF at 77 K (λ_{exc} = 460 and 650 nm, respectively) .

Computational Studies. To gain insight into the molecular and electronic structures of the investigated systems, computational studies were performed by using density functional methods (DFT) at the B3LYP/6-311G level.[24] The structures were optimized to a stationary point on the Born–Oppenheimer potential energy surface. DFT optimized structures of reference $PDI(CN)_2$ and $PDI(Py)_2$ with the highest occupied frontier molecular orbital (HOMO) and the lowest unoccupied molecular orbital (LUMO) calculated have shown in Figure 5. Planar node disappears in HOMO level of the $PDI(Py)_2$ reference.

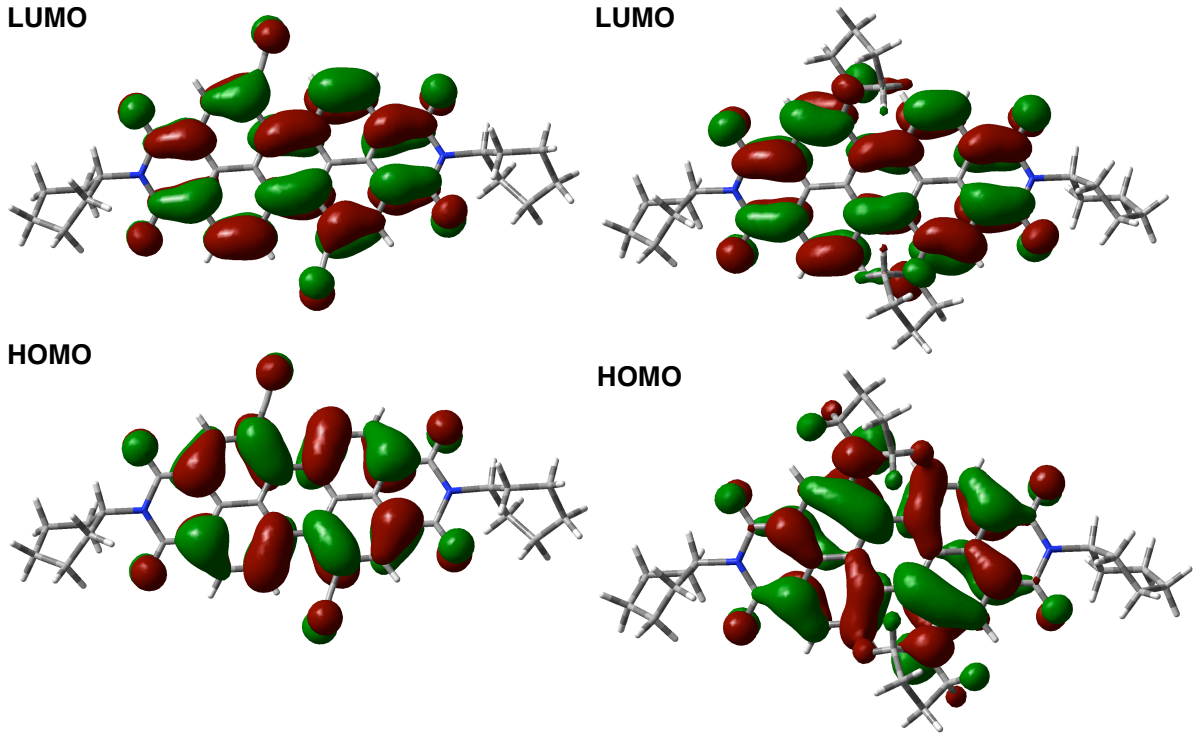


Figure 5. DFT optimized molecular structures of reference $PDI(CN)_2$ (left) and $PDI(Py)_2$ (right) with frontier HOMOs and LUMOs.

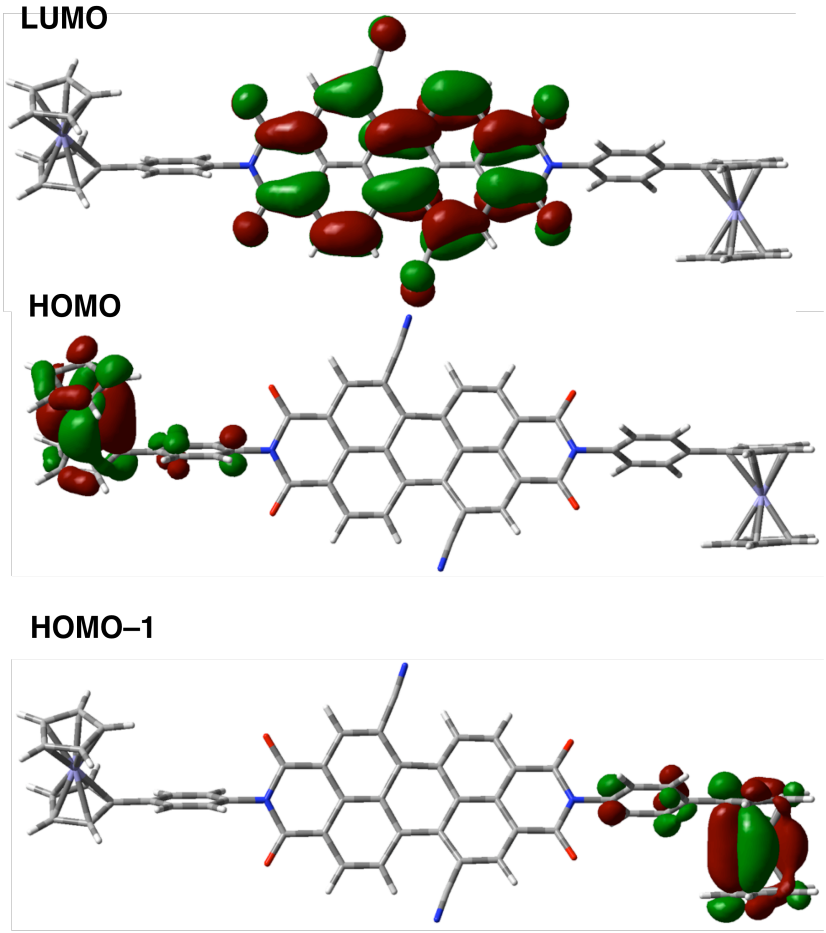


Figure 6. DFT optimized molecular structure of **1** with frontier HOMOs and LUMO.

In case of triad **1** and dyad **2 (**Figures 6 and 7), the majority of the orbital distributions of the HOMO were located mutually over the ferrocene entities. The orbital energies of the HOMO and HOMO–1 for the triad **1** are calculated as –5.337 and –5.343 eV, respectively. These two levels have energetically quite close values. On the other hand, the majority of the orbital distributions of the LUMO was located over the PDI body and substituted cyano groups (in cases of **1** and **2**). The absence of HOMOs on $PDI(CN)_2$ and LUMOs on the ferrocene suggests weak or no charge transfer interactions between the $PDI(CN)_2$ unit and ferrocene entities in the ground state. These results propose the formation of charge-separated states in electron-transfer reactions of the triad **1** and dyad **2**.

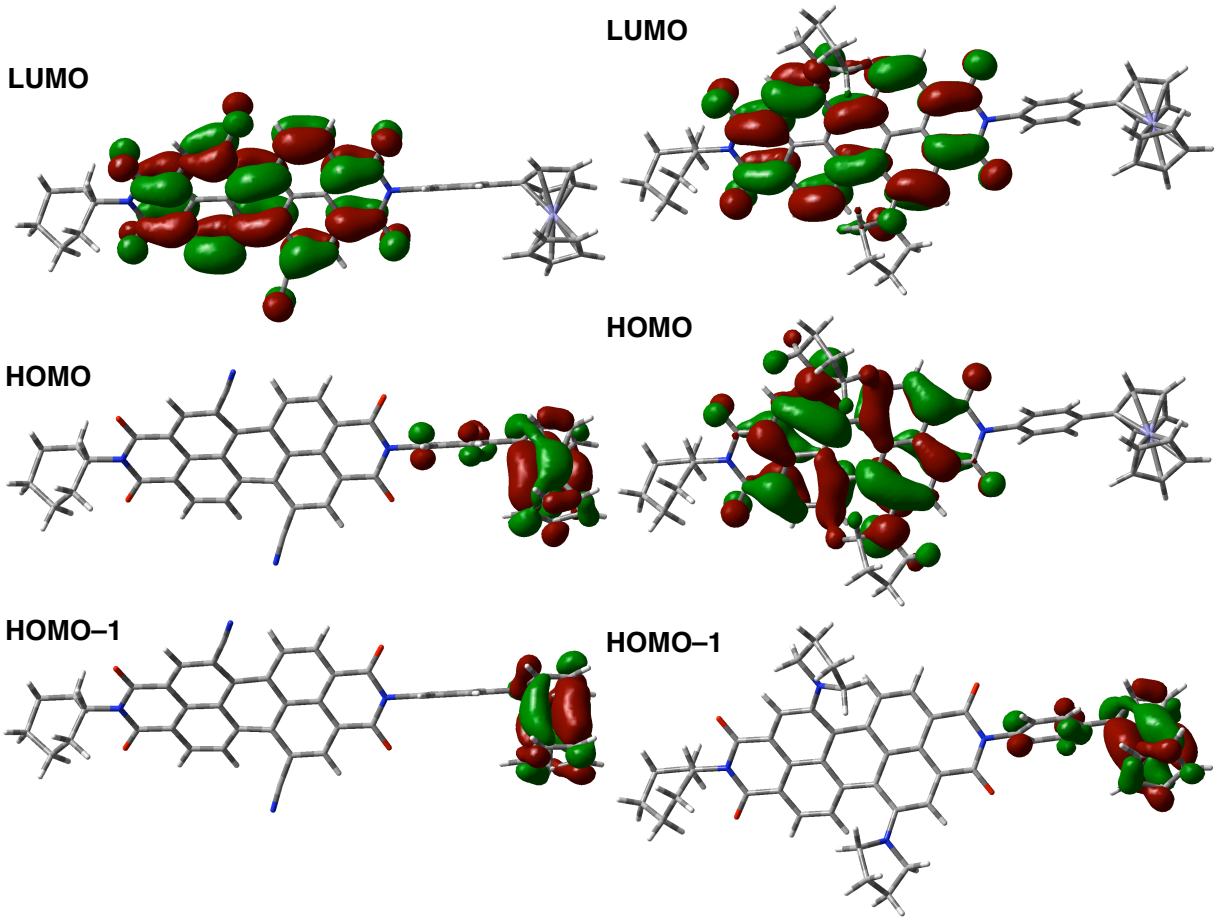


Figure 7. DFT optimized molecular structures of reference **2** (left) and **3** (right) with frontier HOMOs and LUMOs.

In the case of dyad **3**, the majority of the orbital distributions of the LUMO and HOMO were found to be located on the PDI core with small orbital coefficients on the substituted pyrrolidine groups (Figure 7). On the other hand, the majority of the orbital distributions of the HOMO–1 was located over the ferrocene. These results also suggest that the charge-separated state in electron-transfer reactions of **3** is Fc^{+}-$[PDI(Py)_2)]^{\bullet-}$ over HOMO–1. The center-to-

center distance (R_{DA}), that is, the distance between the PDI cores and the ferrocene, was computed to be 12.9 Å.

Electrochemical Studies and Electron-Transfer Driving Force. Cyclic voltammetry (CV) measurements have been performed as a means to clarify electrochemical properties of **1**–**3** and the reference compounds in PhCN containing 0.10 M $TBAPF_6$ as supporting electrolyte (Table 1). The first reduction potential (E_{red}) of unsubstituted PDI reference was recorded at -600 mV vs. SCE, whereas the Fc reference undergoes one-electron oxidation (E_{ox}) at 470 mV.[25] As expected, attaching the electron-withdrawing cyano groups to PDI aromatic core leads to large cathodic shift of nearly 380 mV for the first reduction potential (E_{red} = –220 mV) while $PDI(Py)_2$ displays anodic shift very close to 280 mV for the first reduction potential (E_{red} = –880 mV) (Figure 8). In addition, the $PDI(Py)_2$ dye undergoes one-electron oxidation at

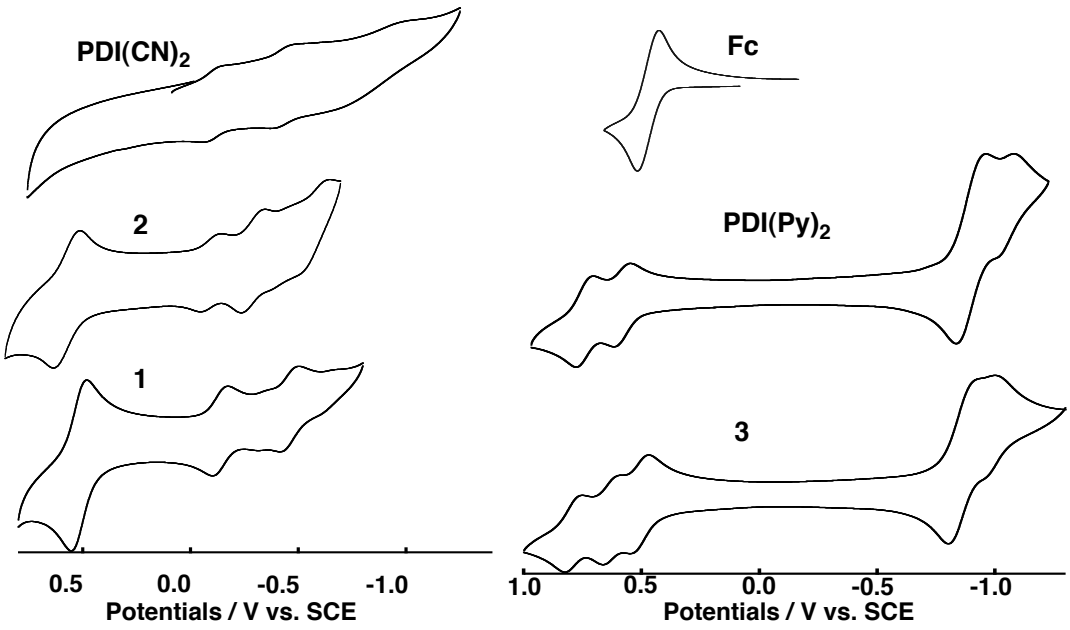


Figure 8. Cyclic voltammograms of **1**–**3** and the reference compounds in deaerated PhCN containing 0.1 M $TBAPF_6$ (Sweep rate: 0.1 mV/s).

590 and 760 mV as anticipated from the bay-substitution of electron-donating amino groups.[14] From these redox values, one could see that $PDI(CN)_2$ acts as a strong electron acceptor, whereas $PDI(Py)_2$ can be utilized as a convenient electron acceptor, as well as an electron donor. Further reductions at –160 and –190 mV were observed corresponding to the reduction of $PDI(CN)_2$ in triad **1** and dyad **2**, respectively (Figure 8). The slight positive shift of the E_{red} of $PDI(CN)_2$ in **1** and **2** compared with $PDI(CN)_2$ reference may be explained by the inductive stabilization of the radical anion by the replacement of cyclohexanes with the benzene rings. On the other hand, the first oxidation corresponding to ferrocene in **1** and **2** was located at 490 mV.

When turning to **3**, the redox measurements portray similar characteristics to those of reference $PDI(Py)_2$, where it differently exhibits its first oxidation potential at 480 mV, clearly

originating from fused ferrocene, which brings about a slight positive shift of reduction and oxidation potentials of dyad molecule relative to those of $PDI(Py)_2$ (Figure 8).

Table 1. Redox potentials of compounds **1**, **2**, and **3** (mV vs. SCE) and free energy changes of the charge-recombination ($-\Delta G_{CR}$) and charge-separation ($-\Delta G_{CS}$) processes in PhCN.

compound	E_{red1}	E_{ox1}	$-\Delta G_{CR}$ / eV	$-\Delta G_{CS}$ / eV
Fc		470		
PDI	–600			
1	–190	490	0.61	1.69
2	–160	490	0.64	1.66
3	–870	480	1.31	0.39

The free-energy change for electron transfer (ΔG_{CS} in eV) was calculated using the following expression:[26]

$$\Delta G_{CS} = e(E_{ox} - E_{red}) - \Delta E_{0\text{-}0} + \Delta G_s \quad (1)$$

where E_{ox} is the first one-electron oxidation potential of ferrocene, E_{red} is the first one-electron reduction potential of PDIs, $\Delta E_{0\text{-}0}$ is the energy of the 0–0 transition energy gap between the lowest excited state and the ground state of PDIs, and ΔG_s refers to the static Coulomb energy in benzonitrile, calculated by using the "dielectric continuum model"[26] according to the following equation:

$$\Delta G_s = e^2/4\pi\varepsilon_0\varepsilon_S R_{CC} \quad (2)$$

The center-to-center distance, R_{CC}, was calculated for the optimized structures to be 12.90 Å. The symbols ε_0 and ε_S represent vacuum permittivity and dielectric constant of solvent used for photochemical and electrochemical studies, respectively. Based on the first oxidation potential of ferrocene and the reduction potential of PDIs in **1–3**, the driving forces for charge-recombination processes ($-\Delta G_{CR}$) are calculated as 0.61, 0.64, and 1.31 eV for **1**, **2**, and **3**, respectively. Based on the $-\Delta G_{CR}$ values and the energy of singlet excited state of PDIs, the driving forces for charge-separation processes ($-\Delta G_{CS}$) are calculated as 1.69, 1.66, and 0.39 eV for **1**, **2**, and **3**, respectively, indicating exothermic photoinduced electron transfer from ferrocene to the singlet excited states of PDIs.

Femtosecond and Nanosecond Transient Absorption Measurements. The transient absorption spectra of $PDI(CN)_2$ in toluene at selected time delays were obtained by a given excitation at 460 nm (Figure 9). The symmetric negative signal shows mirror-imaged spectra, corresponding to ground state absorption and stimulated emission.[27] The peak formed at around 775 nm is assigned to excited-state absorption of the singlet state. The decay of

singlet-excited state is not completed within the time course of measurement as the singlet excited state lifetime as determined from fluorescence lifetime is 4.5 ns.[2a]

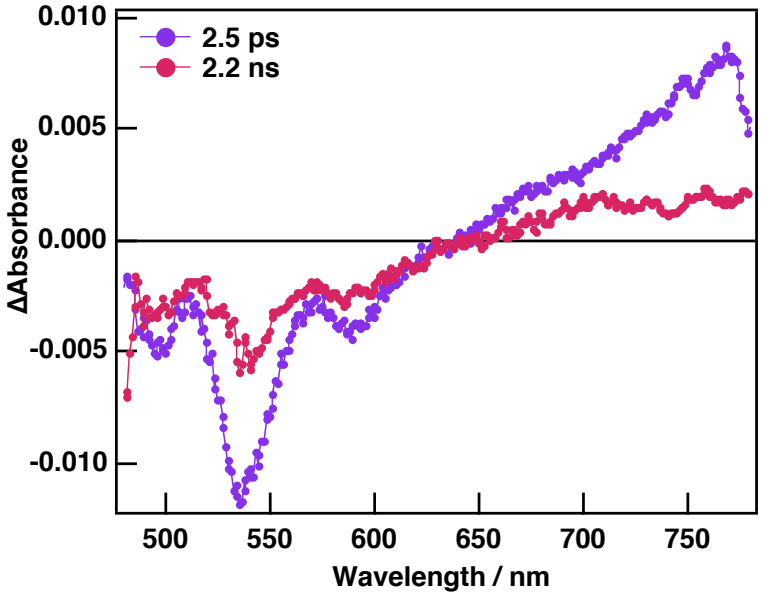


Figure 9. Femtosecond transient absorption spectra of the reference $PDI(CN)_2$ in deaerated toluene (λ_{exc} = 460 nm).

The femtosecond transient absorption spectra of Fc-$PDI(CN)_2$ in PhCN recorded after an excitation at 460 nm (Figure 10) display a quenching of the singlet state of $PDI(CN)_2$ at 775 nm (8.2 ps) followed by the formation of positive absorption instead of bleaching arising from stimulated emission at 570 nm and the formation of peaks positioned at 695 and 940 nm. These peaks are attributed to radical anion of $PDI(CN)_2$, $[PDI(CN)_2)]^{\bullet-}$, since they match with the radical anion peaks of $PDI(CN)_2$ obtained by addition of tetrakis(dimethylamino)ethylene (TDAE)[28] in steady-state absorption spectroscopy (Figure 11). Positions of $[PDI(CN)_2)]^{\bullet-}$ peaks are also confirmed by literature data.[11] We could not observe the absorption band of Fc^+ because it has an almost insignificant extinction coefficient (ε = 450 $M^{-1}cm^{-1}$ at 617 nm).[29] From the rise of $[PDI(CN)_2)]^{\bullet-}$ at 695 nm, the rate of electron transfer from the ferrocene to the excited-singlet state of $PDI(CN)_2$ is estimated to be extremely fast and efficient. The decay-rate of $[PDI(CN)_2]^{\bullet-}$ at 695 nm was fitted with clean first-order plot where the rate of charge-recombination process (k_{CR}) was found to be 4.1 x 10^{10} s^{-1}. Based on the k_{CR}, the lifetime of the charge-separated state (τ_{CS}) is calculated as 25 ps in PhCN.

When turning to Fc_2-$PDI(CN)_2$ triad, the femtosecond transient absorption spectra reveal similar spectral features to those of Fc-$PDI(CN)_2$ dyad after an excitation given at 460 nm (Figure 10). The lifetime of the charge-separated state of **1** is found to be 59 ps, which is two times longer as that of Fc-$PDI(CN)_2$ dyad in PhCN. Elongated τ_{CS} value of Fc_2-$PDI(CN)_2$ triad may be reasoned from the hole stabilization between the two ferrocenes, with the assistance of polar solvent molecules. The rigid phenyl linkers shortening the distance between two

ferrocene may improve such a stabilization effect. Also, computational studies of **1**, where the distributions of HOMO and HOMO–1 realize on disparate ferrocenes reinforce this conception (vide supra).

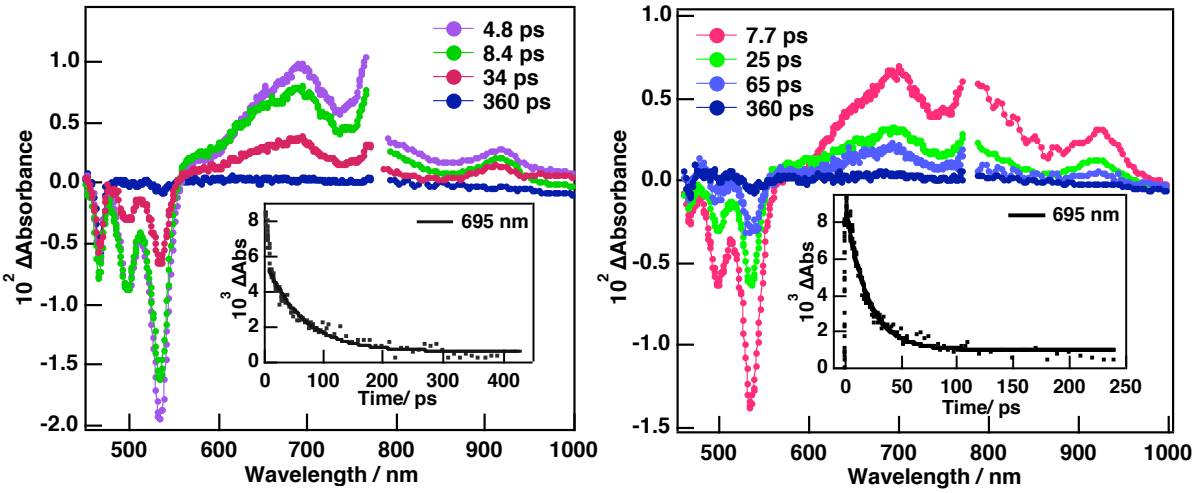


Figure 10. Femtosecond transient absorption spectra of the triad **1** and dyad **2** in deaerated PhCN (λ_{exc} = 460 nm). Insets: Time profiles at 695 nm.

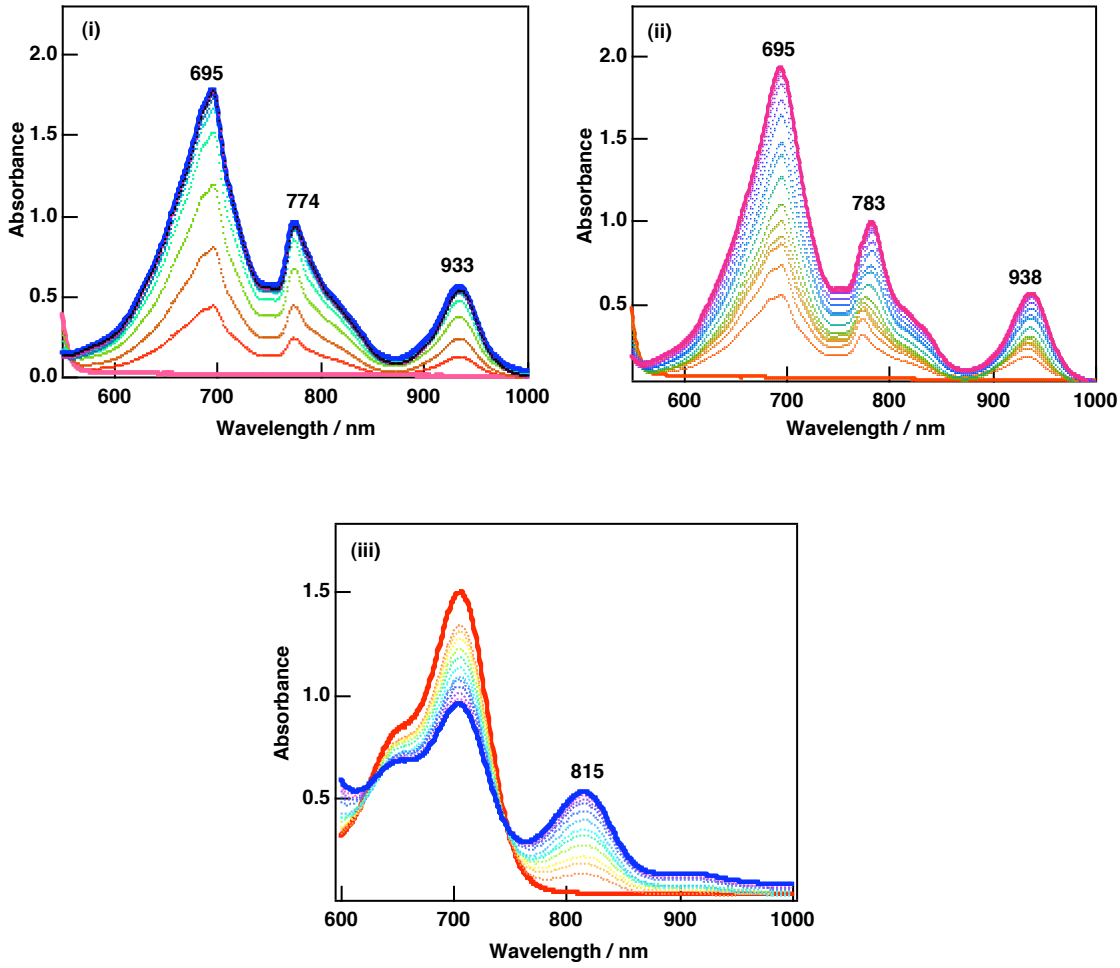


Figure 11. Absorption spectra of (i) **1**, (ii) **2**, and (iii) **3** in benzonitrile treated with TDAE. Peaks at indicated wavelengths are assigned to radical anions of studied compounds.

In the complementary nanosecond laser measurements, the transient spectra show no signal for the formation of triplet states of **1** and **2**, which can be explained by the efficient electron transfer via the singlet-excited state of $PDI(CN)_2$. This is in a good agreement with the lower energy of the singlet radical ion pair compared with that of the triplet $PDI(CN)_2$.

The femtosecond transient spectra of the $PDI(Py)_2$ reference exhibited broad absorption band in the NIR region (800-1000 nm) in PhCN that is assigned to the formation of the singlet excited state of $PDI(Py)_2$ (Figure 12).[18b] Small positive absorption arises between 460 nm and 590 nm, while a bleaching centered around 700 nm appears due to ground-state absorption and stimulated emission.[18a] The lifetime of singlet $PDI(Py)_2$ determined from the decay at 940 nm is 2.6 ns in PhCN and 4.2 ns in toluene.[18b] Excitation of Fc-$PDI(Py)_2$ in PhCN with 460 nm laser pulses showed almost identical spectral features of $PDI(Py)_2$ reference, except for the shorter lifetime of singlet state at 940 nm which is 525 ps (Figure 7). The lifetime of the bleaching around 730 nm is reduced to 400 ps. In spite of the fact that we could not detect the formation the radical anion of $PDI(Py)_2$ directly, taking into account that the radical anion of $PDI(Py)_2$ is hidden under the huge absorption of the singlet excited state of $PDI(Py)_2$ in the NIR region (Figure 11), it is most likely that the quenching of the singlet state of **3** is due to the electron transfer from the attached ferrocene to the $PDI(Py)_2$ core. It should be noted herein that intersystem crossing from singlet state to triplet state is hardly preferred by PDIs[30] and there is no energy transfer process from $PDI(Py)_2$ to ferrocene due to energetic considerations.[23]

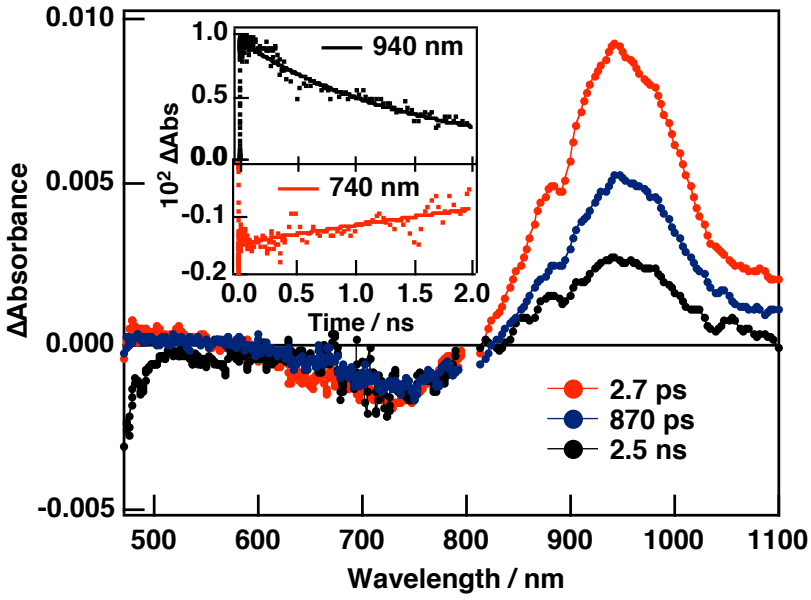


Figure 12. Femtosecond transient absorption spectra of $PDI(Py)_2$ reference in PhCN (λ_{exc} = 460 nm). Inset: Time profiles at 740 nm and 940 nm.

In contrast with the nanosecond transient absorption data of triad **1** and dyad **2**, the triplet state of Fc-$PDI(Py)_2$ is clearly seen during the nanosecond transient absorption measurements

by utilizing 430 nm laser excitation (Figure 14). The formation of the triplet $PDI(Py)_2$ was not efficient in the case of the reference $PDI(Py)_2$.[30] Hence, it can be concluded that the population of Fc-^{3}[$PDI(Py)_2$]* occurs via the charge-recombination[31] of the Fc^+-[$PDI(Py)_2$]$^{\bullet-}$ by taking into account that the energy level of the triplet Fc-$^3PDI(Py)_2$* (1.20 eV) is lower than that of Fc^+-[$PDI(Py)_2$]$^{\bullet-}$ (1.35 eV). The decay-rate constant of Fc-^{3}[$PDI(Py)_2$]* to the ground state was found to be 2.9 x 10^4 s^{-1}.

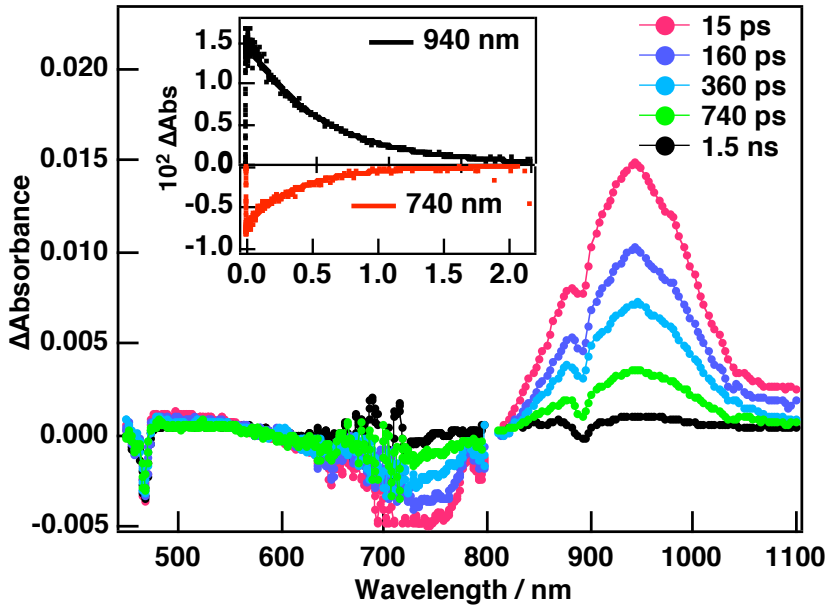


Figure 13. Femtosecond transient absorption spectra of **3** in deaerated PhCN (λ_{exc} = 460 nm). Insets: Time profiles at 740 nm and 940 nm.

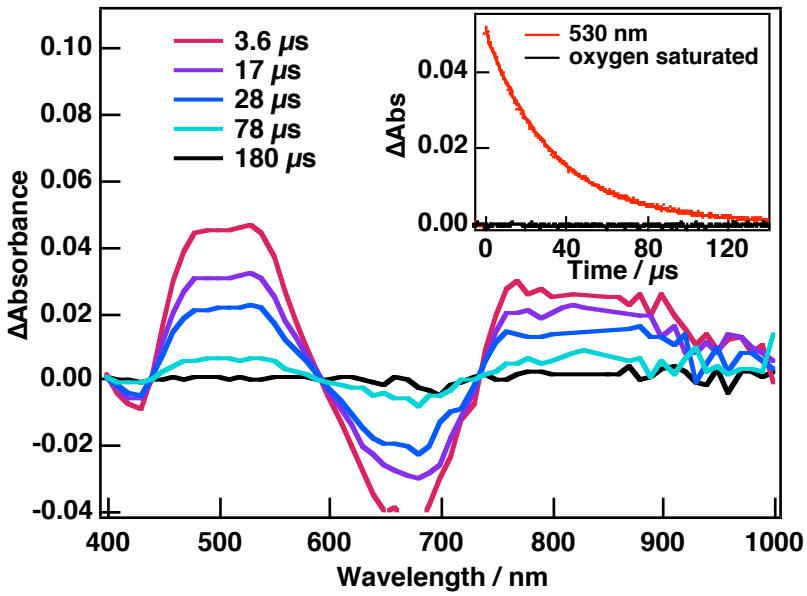


Figure 14. Nanosecond transient absorption spectra of **3** in deaerated PhCN (λ_{exc} = 430 nm). Inset: Time profiles at 530 nm in deaerated and oxygen saturated solutions.

The intramolecular photoinduced processes of Fc-PDI(CN)$_2$ and Fc$_2$-PDI(CN)$_2$ are compiled in the energy level diagram (Figure 15). Excitation of the PDI chromophores at 460 nm leads to very fast formation of the charge-separated states with high efficiency as confirmed by femtosecond transient absorption measurements. The charge-separated state decays to the ground state with lifetimes of 25 ps for **2** and 59 ps for **1** without utilizing triplet state manifold. Photoinduced electron-transfer process in Fc-PDI(Py)$_2$ is a rational pathway in order to explain the quenching of singlet excited state and the population of triplet state. It most probably follows intersystem crossing to generate triplet state, which is observed by nanosecond laser measurements, after the charge separation. It is also possible that the charge-separated state undergoes to ground state as in the cases of **1** and **2**. The quantum yields of charge-separation processes (Φ_{CS}) for dyad **3** (0.79) is found to be smaller than that of triad **1** and dyad **2** (~1.0).[32,33]

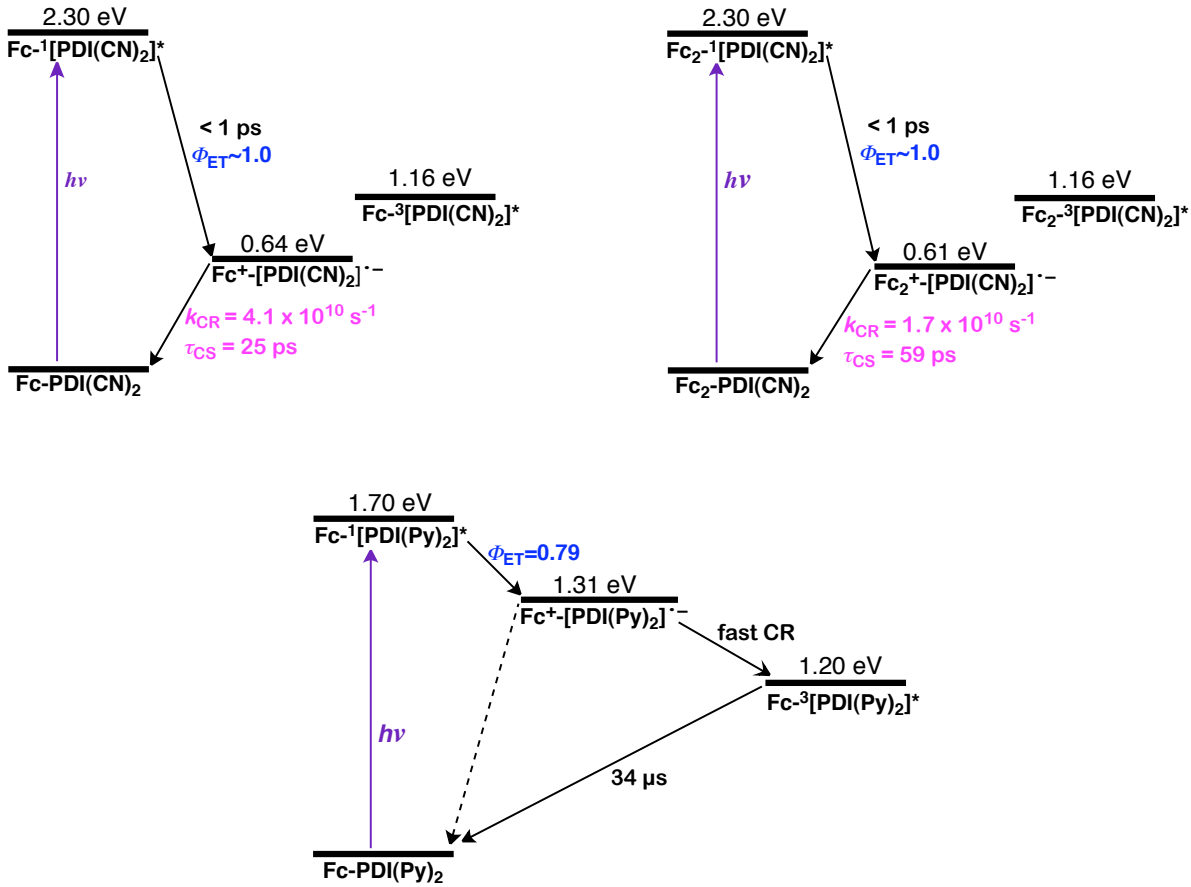


Figure 15. Energy level diagrams showing intramolecular events of **1**, **2**, and **3** induced by excitation of PDIs in PhCN.

Conclusion

Photophysical events taking place in Fc$_2$-PDI(CN)$_2$ and Fc-PDI(CN)$_2$ as well as in Fc-PDI(Py)$_2$ have been investigated by time-resolved and steady-state spectral, electrochemical, and

computational studies. Efficient charge separation of dyad **1** and triad **2** takes place in a few picoseconds after laser excitation. The charge-separated states formed by electron-transfer reaction recombine to the ground state with lifetimes of 25 ps and 59 ps in polar media. The finding that the lifetime of the charge-separated state of triad **1** is longer than that of dyad **2** suggests the effect of second ferrocene on stabilizing the charge-separated state. Electron-accepting features of $PDI(Py)_2$ have also been investigated through an electron donor (ferrocene) and quenching of singlet excited state of $PDI(Py)_2$ is interpreted for charge separation in PhCN. NIR characteristics and high solubility of $PDI(Py)_2$ can prompt it to be a promising component for further applications as an electron acceptor.

References and Notes

(1) (a) De Schryver, F. C.; Vosch, T.; Cotlet, M.; Van der Auweraer, M.; Muellen, K.; Hofkens, J. *Acc. Chem. Res.* **2005**, *38*, 514. (b) Baffreau, J.; Ordronneau, L.; Leroy-Lhez, S.; Hudhomme, P. *J. Org. Chem.* **2008**, *73*, 6142. (c) Gomez, R.; Segura, J. L.; Martin, N. *Org. Lett.* **2005**, *7*, 717. (d) Qu, J.; Zhang, J.; Grimsdale, A. C.; Müllen, K. M.; Jaiser, F.; Yang, X.; Neher, D. *Macromolecules* **2004**, *37*, 8297. (e) Li, C.; Schoeneboom, J.; Liu, Z.; Pschirer, N. G.; Erk, P.; Herrmann, A.; Müllen, K. *Chem. Eur. J.* **2009**, *15*, 878. (f) Rlehm, T.; Wadepohl, H.; Gade, L. H. *Inorg. Chem.* **2008**, *47*, 11467.

(2) (a) Würthner, F. *Chem. Commun.* **2004**, 1564. (b) Ohkubo, K.; Ortiz, J.; Gutiérrez, A. M.; Fernández-Lázaro, F.; Sastre-Santos, A. *Chem. Commun*. **2005**, 3814. (c) Fukuzumi, S.; Ohkubo, K.; Ortiz, J.; Gutierrez, A. M.; Fernandez-Lazaro, F.; Sastre-Santos, A. *J. Phys. Chem. A* **2008**, *112*, 10744. (d) You, C.-C.; Würthner, F. *J. Am. Chem. Soc.* **2003**, *125*, 9716. (e) Goretzki, G.; Davies, E. S.; Argent, S. P.; Warren, J. E.; Blake, A. J.; Champness, N. R. *Inorg. Chem.* **2009**, *48*, 10264. (f) Zhang, R.; Wang, Z.; Wu, Y.; Fu, H.; Yao, J. *Org. Lett.* **2008**, *10*, 3065.

(3) (a) Langhals, H. *Helv. Chim. Acta* **2005**, *88*, 1309. (b) Hua, J.; Meng, F.; Ding, F.; Tian, H. *Chem. Lett.* **2004**, *33*, 432. (c) Tian, Z.; Shaller, A. D.; Li, A. D. Q. *Chem. Commun.* **2009**, 180.

(4) (a) Schols, S.; Verlaak, S.; Rolin, C.; Cheyns, D.; Genoe, J.; Heremans, P. *Adv. Funct. Mater.* **2008**, *18*, 136. (b) Chiu, T.-L.; Xu, W.-F.; Lee, J.-H.; Chao, C.-C.; Leung, M.-K. *Appl. Phys. Lett.* **2009**, *94*, 013307. (c) Pu, Y.-J.; Higashidate, M.; Nakayama, K.; Kido, J. *J. Mater. Chem.* **2008**, *18*, 418. (d) Kraft, A. *ChemPhysChem* **2001**, *2*, 163. (e) Ding, B.; Zhu, W.; Jiang, X.; Zhang, Z. *Solid State Commun.* **2008**, *148*, 226. (f) Jeong, C. H.; Lim, J. T.; Kim, M. S.; Lee, J. H.; Bae, J. W.; Yeom, G. Y. *Org. Electron.* **2007**, *8*, 683.

(5) (a) O'Neil, M. P.; Niemczyk, M. P.; Svec, W. A.; Gosztola, D.; Gaines III, G. L.; Wasielewski, M. R. *Science* **1992**, *257*, 63. (b) Szacilowski, K. *Chem. Rev.* **2008**, *108*, 3481.

(6) (a) Jones, B. A.; Ahrens, M. J.; Yoon, M.-H.; Facchetti, F.; Marks, T. J.; Wasielewski, M. R. *Angew. Chem., Int. Ed.* **2004**, *43*, 6363. (b) Kuo, M.-Y.; Chen, H.-Y.; Chao, I. *Chem. Eur. J.* **2007**, *13*, 4750. (c) Li, Y.; Wang, Z.; Qian, H.; Shi, Y.; Hu, W.; *Org. Lett.* **2008**, *10*, 529. (d) Schmidt, R.; Oh, J. H.; Sun, Y.-S.; Deppisch, M.; Krause, A.-M.; Radacki, K.; Braunschweig, H.; Koenemann, M.; Erk, P.; Bao, Z.; Würthner, F. *J. Am. Chem. Soc.* **2009**, *131*, 6215.

(7) (a) Law, K.-Y. *Chem. Rev.* **1993**, *93*, 449. (b) Vajiravelu, S.; Ramunas, L.; Vidas, G. J.; Valentas, G.; Vygintas, J.; Valiyaveettil, S. *J. Mater. Chem.* **2009**, *19*, 4268. (c) Kim, Y. D.; Kim, J. P.; Kwon, O. S.; Cho, I. H. *Dyes Pigments* **2009**, *81*, 45.

(8) (a) Wang, M.; Wang, X. *Sol. Energ. Mat. Sol. C.* **2007**, *91*, 1782. (b) Liscio, A.; De Luca, G.; Nolde, F.; Palermo, V.; Müllen, K.; Samori, P. *J. Am. Chem. Soc.* **2008**, *130*, 780. (c) Mikroyannidis, J. A.; Stylianakis, M. M.; Sharma, G. D.; Balraju, P.; Roy, M. S. *J. Phys. Chem. C* **2009**, *113*, 7904. (d) Imahori, H.; Umeyama, T.; Ito, S. *Acc. Chem. Res.* **2009**, *42*, 1809. (e) Koyuncu, S.; Zafer, C.; Baycan Koyuncu, F.; Aydin, B.; Can, M.; Sefer, E.; Ozdemir, E.; Icli, S. *J. Polym. Sci. A: Polym. Chem.* **2009**, *47*, 6280. (f) Cappel, U. B.; Karlsson, M. H.; Pschirer, N. G.; Eickemeyer, F.; Schoeneboom, J.; Erk, P.; Boschloo, G.; Hagfeldt, A. *J. Phys. Chem. C* **2009**, *113*, 14595. (g) Bartelt, A. F.; Schuetz, R.; Neubauer, A.; Hannapel, T.; Eichberger, R. *J. Phys. Chem. C* **2009**, *113*, 21233. (h) Planells, M.; Cespedes-Guirao, F. J.; Forneli, A.; Sastre-Santos, A.; Fernandez-Lazaro, F.; Palomares, E. *J. Mater. Chem.* **2008**, *18*, 5802. (i) Planells, M.; Cespedes-Guirao, F. J.; Goncalves, L.; Sastre-Santos, A.; Fernandez-Lazaro, F.; Palomares, E. *J. Mater. Chem.* **2009**, *19*, 5818.

(9) (a) Tanaka, N.; Barashkov, N.; Heath, J.; Sisk, W. N. *Appl. Optics* **2006**, *45*, 3846. (b) Calzado, E. M.; Villalvilla, J. M.; Boj, P. G.; Quintana, J. A.; Gomez, R.; Segura, J. L.; Diaz-Garcia, M. A. *J. Phys. Chem. C* **2007**, *111*, 13595. (c) Garcia-Moreno, I.; Costela, A.; Martin, V.; Pintado-Sierra, M.; Sastre, R. *Adv. Funct. Mater.* **2009**, *19*, 2547. (d) Diaz-Garcia, M. A.; Calzado, E. M.; Villalvilla, J. M.; Boj, P. G.; Quintana, J. A.; Cespedes-Guirao, F. J.; Fernandez-Lazaro, F.; Sastre-Santos, A. *Synth. Met.* **2009**, *159*, 2293.

(10) (a) Dincalp, H.; Avcibasi, N.; Icli, S. *J. Photochem. Photobiol. A* **2007**, *185*, 1. (b) Zhu, L.; Wu, W.; Zhu, M.-Q.; Han, J. J.; Hurst, J. K.; Li, A. D. Q.; *J. Am. Chem. Soc.* **2007**, *129*, 3524. (c) Peneva, K.; Mihov, G.; Herrmann, A.; Zarrabi, N.; Boersch, M.; Duncan, T. M.; Müllen, K. *J. Am. Chem. Soc.* **2008**, 130, 5398. (d) Bittermann, H.; Siegemund, D.; Malinovskii, V. L.; Haener, R. *J. Am. Chem. Soc.* **2008**, *130*, 15285. (e) Wang, B.; Yu, C. *Angew. Chem., Int. Ed.* **2010**, *49*, 1485.

(11) Ahrens, M. J.; Fuller, M. J.; Wasielewski, M. R. *Chem. Mater.* **2003**, *15*, 2684.

(12) (a) Zhao, Y.; Wasielewski, M. R. Tetrahedron Lett. 1999, 40, 7047. (b) Yukruk, F.; Dogan, A. L.; Canpinar, H.; Guc, D.; Akkaya, E. U. *Org. Lett.* **2005**, *7*, 2885.

(13) (a) Langhals, H.; Kirner, S. *Eur. J. Org. Chem.* **2000**, 365. (b) Uzun, D.; Ozser, M. E.; Icil, H.; Demuth, M. *J. Photochem. Photobiol. A* **2003**, *156*, 45. (c) An, Z.; Odom, S. A.; Kelley, R. F.; Huang, C.; Zhang, X.; Barlow, S.; Padilha, L. A.; Fu, J.; Webster, S.; Hagan, D. J.; Van Stryland, E. W.; Wasielewski, M. R.; Marder, S. R. *J. Phys. Chem. A* **2009**, *113*, 5585.

(14) Shin, W. S.; Jeong, H.-H.; Kim, M.-K.; Jin, S.-H.; Kim, M.-R.; Lee, J.-K.; Lee, J. W.; Gal, Y.-S. *J. Mater. Chem.* **2006**, *16*, 384.

(15) (a) Miura, A.; Chen, Z.; Ujii, H.; De Feyter, S.; Zdanowska, M.; Jonkheijm, P.; Schenning, A. P. H. J.; Meijer, E. W.; Wuerthner, F.; De Schryver, F. D. *J. Am. Chem. Soc.* **2003**, *125*, 14968. (b) Jimenez, A. J.; Spaenig, F.; Rodriguez-Morgade, M. S.; Ohkubo, K.; Fukuzumi, S.; Guldi, D. M.; Torres, T. *Org. Lett.* **2007**, *9*, 2481. (c) Chen, Y.; Lin, Y.; El-Khouly, M. E.; Zhuang, X.; Araki, Y.; Ito, O.; Zhang, W. *J. Phys. Chem. C* **2007**, *111*, 16096. (d) Xu, W.; Chen, H.; Wang, Y.; Zhao, C.; Li, X.; Wang, S.; Weng, Y. *ChemPhysChem* **2008**, *9*, 1409. (e) Odom, S.; Kelley, R. F.; Ohira, S.; Ensley, T. R.; Huang, C.; Padilha, L. A.; Webster, S.; Coropceanu, V.; Barlow, S.; Hagan, D. J.; Van Stryland, E.W.; Bredas, J.-L.; Anderson, H. L.; Wasielewski, M. R.; Marder, S. R. *J. Phys. Chem. A* **2009**, *113*, 10826. (f) Huang, J.; Wu, Y.; Fu, H.; Zhan, X.; Yao, J.; Barlow, S.; Marder, S. R.; *J. Phys. Chem. A* **2009**, *113*, 5039. (g) Zhang, Q.; Cirpan, A.; Russell, T. P.; Emrick, T. *Macromolecules* **2009**, *42*, 1079. (h) Wolffs, M.; Delsuc, N.; Veldman, D.; Ahn, N. V.; Williams, R. M.; Meskers, S. C. J.; Janssen, R. A. J.; Huc, I.; Schenning, A. P. H. J. *J. Am. Chem. Soc.* **2009**, *131*, 4819. (i) Wicklein, A.; Ghosh, S.; Sommer, M.; Wuerthner, F.; Thelakkat, M. *ACS Nano* **2009**, *3*, 1107. (j) Jaggi, M.; Blum, C.; Dupont, N.; Grilj, J.; Liu, S.-X.; Hauser, J.; Hauser, A.; Decurtins, S. *Org. Lett.* **2009**, *11*, 3096. (k) Seitz, W.; Jimenez, A. J.; Carbonell, E.; Grimm, B.; Rodriguez-Morgade, M. S.; Guldi, D. M.; Torres, T. *Chem. Commun.* **2010**, *46*, 127.

(16) Fujikawa, R.; Watanabe, S.; Ohtsuka, K.; Sato, S.; Takenaka, S. Nucleic Acid Symposium Series 52, 2008, Oxford University Press, pp 241-242.

(17) Shumate, W. J.; Mattern, D. L.; Jaiswal, A.; Dixon, D. A.; White, T. R.; Burgess, J.; Honciuc, A.; Metzger, R. M.; *J. Phys. Chem. B* **2006**, *110*, 11146.

(18) (a) Lukas, A. S.; Zhao, Y.; Miller, S. E.; Wasielewski, M. R. *J. Phys. Chem. B* **2002**, *106*, 1299. (b) Shibano, Y.; Umeyama, T.; Matano, Y.; Tkachenko, N. V.; Lemmetyinen, H.; Araki, Y.; Ito, O.; Imahori, H. *J. Phys, Chem. C* **2007**, *111*, 6133. (c) Berberich, M.; Krause, A.; Orlandi, M.; Scandola, F.; Wuerthner, F. *Angew. Chem., Int. Ed.* **2008**, *47*, 6616.

(19) Shibano, Y.; Umeyama T.; Matano, Y.; Imahori, H. *Org. Lett.* **2007**, *9*, 1971.

(20) Bohm, A.; Arms, H.; Henning, G.; Blaschka, P. (BASF), German Patent, No. DE 19547209AI

(21) Langhals, H. *Heterocycles* **1995**, *40*, 477.

(22) Correa, D. S.; Oliveira, S. L.; Misoguti, L.; Zilio, S. C.; Aroca, R. F.; Constantino, C. J. L.; Mendonça, C. R. *J. Phys. Chem. A* **2006**, *110*, 6433.

(23) Giasson, R.; Lee, E. J.; Zhao, X.; Wrighton, M. S. *J. Phys. Chem.* **1993**, *97*, 2596.

(24) (a) Hehre, W. J.; Radom, L.; Schleyer, P. V. R.; Pople, J. A. *Ab Initio Molecular Orbital Theory*; Wiley: New York, 1986. (b) Frisch, M. J.; Trucks, G. W.; Schlegel, H. B.; Scuseria, G. E.; Robb, M. A.; Cheeseman, J. R.; Montgomery, J. A.; Vreven, J., T.; Kudin, K. N.; Burant, J. C.; Millam, J. M.; Iyengar, S. S.; Tomasi, J.; Barone, V.; Mennucci, B.; Cossi, M.; Scalmani, G.; Rega, N.; Petersson, G. A.; Nakatsuji, H.; Hada, M.; Ehara, M.; Toyota, K.; Fukuda, R.; Hasegawa, J.; Ishida, M.; Nakajima, T.; Honda, Y.; Kitao, O.; Nakai, H.; Klene, M.; Li, X.; Knox, J. E.; Hratchian, H. P.; Cross, J. B.; Adamo, C.; Jaramillo, J.; Gomperts, R.; Stratmann, R. E.; Yazyev, O.; Austin, A. J.; Cammi, R.; Pomelli, C.; Ochterski, J. W.; Ayala, P. Y.; Morokuma, K.; Voth, G. A.; Salvador, P.; Dannenberg, J. J.; Zakrzewski, V. G.; Dapprich, S.; Daniels, A. D.; Strain, M. C.; Farkas, O.; Malick, D. K.; Rabuck, A. D.; Raghavachari, K.; Foresman, J. B.; Ortiz, J. V.; Cui, Q.; Baboul, A. G.; Clifford, S.; Cioslowski, J.; Stefanov, B. B.; Liu, G.; Liashenko, A.; Piskorz, P.; Komaromi, I.; Martin, R. L.; Fox, D. J.; Keith, T.; Al-Laham, M. A.; Peng, C. Y.; Nanayakkara, A.; Challacombe, M.; Gill, P. M. W.; Johnson, B.; Chen, W.; Wong, M. W.; Gonzalez, C.; Pople, J. A. *Gaussian 03, Revision C.02*, Gaussian, Inc.: Wallingford CT, 2004.

(25) Wang, H. J. H.; Jaquinod, L.; Olmsted, M. M.; Vicente, G. H.; Kadish, K. M.; Ou, Z.; Smith, K. M. *Inorg. Chem.* **2007**, *46*, 2898.

(26) (a) Mataga, N.; Miyasaka, H. In *Electron Transfer*; Jortner, J.; Bixon, M.; Eds.; John Wiley & Sons: New York, 1999; Part 2, pp 431. (b) Ziessel. R.; Allen, B. D.; Rewinska, D. B.; Harriman, A. *Chem.–Eur. J.* **2009**, *15*, 7382. (c) Flamigni, L.; Wyrostek, D.; Voloshchuk, R.; Gryko, D. T. *Phys. Chem. Chem. Phys.* **2010**, *12*, 474.

(27) Danilov, E. O.; Rachford, A. A.; Goeb, S.; Castellano, F. N. *J. Phys. Chem. A* **2009**, *113*, 5763.

(28) Xiao, S.; El-Khouly, M. E.; Li. Y.; Gan, Z.; Liu, H.; Jiang, L.; Araki, Y.; Ito, O.; Zhu, D. *J. Phys. Chem. B* **2005**, *109*, 3658.

(29) (a) Fery-Forgues, S.; Delavaux-Nicot, B. *J. Photochem. Photobiol. A* **2000**, *132*, 137. (b) Fukuzumi, S.; Okamoto, K.; Gros, C. P.; Guilard, R. *J. Am. Chem. Soc*. **2004**, *126*, 10441.

(30) (a) Rachford, A. A.; Goeb, S.; Castellano, F. N. *J. Am. Chem. Soc.* **2008**, *130*, 2766. (b) Weissman, H.; Shirman, E.; Ben-Moshe, T.; Cohen, R.; Leitus, G.; Shimon Linda, J. W.; Rybtchinski, B. *Inorg. Chem.* **2007**, *46*, 4790.

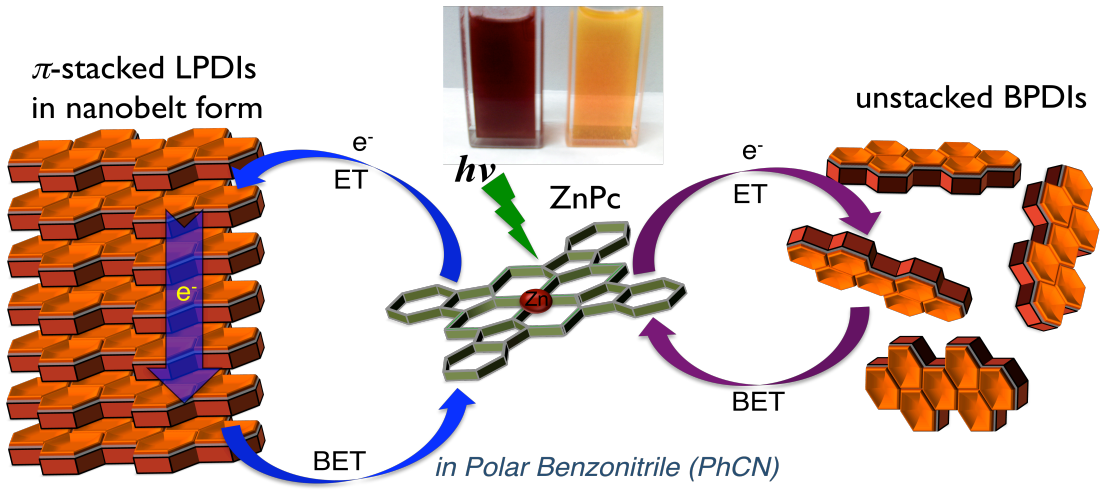
(31) Veldman, D.; Chopin, S. M. A; Meskers, S. C. J.; Janssen, R. A. J. *J. Phys. Chem. A* **2008**, *112*, 8617.

(32) Quantum yields of photoinduced electron transfer (Φ_{ET}) for dyads and triad are calculated according to equations: $k_{ET} = 1/\tau - k_D$, $\Phi_{ET} = k_{ET}\ \tau$, where k_{ET} is rate constant of electron transfer, τ denotes experimentally observed decay time of singlet excited state and, k_D stands for rate constant of decay of singlet excited state other than electron transfer. For this case, the triplet state as an alternative for decay pathway is not involved since it hardly follows intersystem crossing.

(33) (a) Straight, S. D.; Kodis, G.; Terazono, Y.; Hambourger, M.; Moore, T. A.; Moore, A. L.; Gust, D. *Nat. Nanotechnol.* **2008**, *3*, 280. (b) Williams, R. M. *Turk. J. Chem.* **2009**, *33*, 727.

Chapter 2

Electron Delocalization in One-Dimensional Perylenediimide Nanobelts through Photoinduced Electron Transfer



Absract: Photoinduced electron transfer (PET) of a hybrid system comprising *N*,*N*'-ditridecylperylenediimide (LPDI), which forms nanobelt structure $(LPDI)_n$, and soluble zinc (tetra-*tert*-butyl)phthalocyanine (ZnTBPc) has been investigated in polar benzonitrile. PET of a mixture system comprising *N*,*N*'-diheptadecan-9-ylperylenediimide (BPDI) dissolved thoroughly in benzonitrile and ZnTBPc has also been examined for comparison. LPDI nanobelt structures have been identified by using steady-state absorption and emission spectroscopies as well as dynamic light scattering (DLS) technique in the suspension and detected by transmission electron microscopy (TEM) at the solid state. The electron paramagnetic resonance (EPR) spectrum of radical anion of LPDI nanobelts [$(LPDI)_n^{\bullet-}$] was quite different from that of BPDI ($BPDI^{\bullet-}$) due to enhanced electron delocalization within the one-dimensional LPDI aggregates. Polar benzonitrile enables intermolecular light-induced electron transfer from low-lying triplet state of ZnTBPc to LPDI nanobelt due to its stabilization effect on the electron-transfer species, as indicated by the free energy calculations. Nanosecond transient absorption spectra displayed remarkable broadening of the radical anion peak of LPDI nanobelt in the near-infrared (NIR) region upon excitation, proving the delocalization of the transferred electron within the nanostructure. While both hybrid and mixture systems have nearly the same rate constants (k_{et}) of PET from PDIs to ZnTBPc, the rate of back electron transfer (k_{bet}) of $(LPDI)_n^{\bullet-}/ZnTBPc^{\bullet+}$ is slower than that of $BPDI^{\bullet-}/ZnTBPc^{\bullet+}$, which can result from the effect of electron delocalization within the nanobelt structure.

Introduction

Well-ordered assemblies via weak interactions at nanoscale are indispensable components of advanced materials for photonics and electronics in which the electron transfer and/or transport is of critical importance.[1] Perylenediimide (PDI) and its derivatives are common building blocks of many self-assembly models designed for various applications due to their large planar π-systems as well as their high photoemission and electron deficiency.[2] Large π-plane of PDIs is responsible for their intrinsic insolubility, however this aromatic core facilitates intermolecular π-π interactions. Substitution from nitrogen atoms of PDI brings about remarkable solubility variations and shapes the aggregation pattern[3] although they have negligible effect on spectroscopic and electrochemical properties of PDIs due to the lack of electronic communication with the aromatic core.[4] Linear side-chains generally introduce one-dimensional (1D) morphologies in aggregation, whereas branched substituents lead to zero-dimensional (0D) aggregates at nanoscale or enhanced solubility due to steric hinderance in many solvents.[3,5] 1D-semiconducting nanostructures formed by π-π stacking of PDIs (nanobelts) promise a potential for high charge carrier mobility along the long-axis through π-electron delocalization,[6] which is an essential parameter to increase the performance of optoelectronic devices. Despite the fact that many photoinduced applications of PDI nanobelts are present, a fundamental study on π-electron delocalization within the nanobelt via photo-initiated electron-transfer process is still in demand for understanding its insight mechanism.

In this study, we scrutinized the photoinduced electron-transfer (PET) mechanism of a hybrid system consisting of suspended electron-accepting PDI nanobelt structures and a soluble electron-donor molecule, for the first time. For this purpose, the polar environment has been selected which provides a pivotal assistance to the stabilization of electron-transfer species by way of lowering the energy level of the charge-separated state so that even low-energy-level triplet-excited states can supply an exothermic driving force for PET reactions.[7] In order to appreciate the contribution of 1D self-assembly to the charge stabilization by delocalization, we examined and compared the intermolecular PET processes existing between (i) zinc (tetra-*tert*-butyl)phthalocyanine (ZnTBPc) and *N*,*N*'-ditridecylperylenediimide (LPDI), having linear alkyl chains and forming 1D nanobelt structure in polar benzonitrile (PhCN) and (ii) ZnTBPc and *N*,*N*'-diheptadecan-9-ylperylenediimide (BPDI), possessing branched alkyl chains, which are dissolved thoroughly in PhCN at room temperature (Figure 1). In these systems, LPDI nanobelts and BPDI act as electron acceptors and ZnTBPc is used as a photosensitizer as well as an electron-donor component in both cases.[8] In most cases, where PDIs are covalently linked to the phthalocyanines, intramolecular PET takes place via the singlet-excited states to yield charge separation decayed to low-lying ^{3}PDI* or ^{3}ZnTBPc* states and the lifetimes of charge-separated state were found to be in the range of picoseconds and nanoseconds.[9] However, intermolecular photoinduced events of PDIs and phthalocyanines has been examined in only one study in the literature, in which electron transfer has achieved

via triplet-excited state of phthalocyanine moieties in PhCN.[10] In this study, the bimolecular electron-transfer processes of LPDI/ZnTBPc and BPDI/ZnTBPc systems were studied by employing the nanosecond laser photolysis with the visible/near-IR detectors.

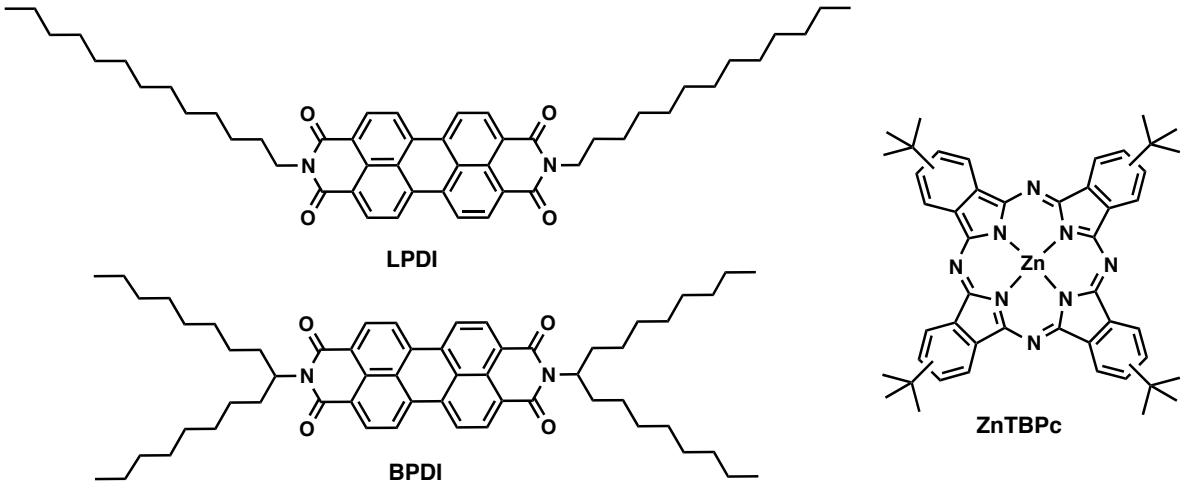


Figure 1. Molecular structures of investigated compounds.

Experimental Section

Materials. Zinc(tetra-*tert*-butyl)phthalocyanine (ZnTBPc)[11] and *N*,*N*'-diheptadecan-9-ylperylenediimide (BPDI)[12] were synthesized according to a reported procedure. *N*,*N*′-ditridecylperylenediimide (LPDI) was purchased from commercial sources and used as received. Fabrication of LPDI nanobelts was achieved through solution-based self-assembling.[3] The 1D growth of the molecular assembly was processed by slow crystallization at the interface between chloroform in which PDI is dissolved appreciably and acetonitrile or methanol, in which PDI has very limited solubility. Polarity difference in the solvents provides separate phases for an extended period. Larger amount of polar solvent, i.e., acetonitrile or methanol, is transferred atop a concentrated chloroform solution. Red crystals formed at the interface within minutes, followed by slow diffusion into upper phase of polar solvent. The nanobelts, transferred by pipetting, were cast onto a glass surface to dry.

Instruments. Steady-state absorption measurements were recorded on a Shimadzu UV-3100PC spectrometer or a Hewlett Packard 8453 diode array spectrophotometer. Fluorescence measurements were carried out on a Shimadzu spectrofluorophotometer (RF-5300PC). Dynamic light scattering (DLS) measurements were carried out using a Zetasizer Nano S (Malvern Instruments ltd., USA). The DLS instrument used in this work has a range between 0.6 nm and 6000 nm, and thereby any structures over this limit cannot be detected. Electron paramagnetic resonance (EPR) spectra were taken on a JEOL X-band spectrometer (JES-RE1XE) at room temperature and 77 K. EPR spectra of radical anions of BPDI and LPDI nanobelt in benzonitrile were measured right after the addition of hydrazine under inert atmosphere. The *g* value was calibrated by using an Mn^{2+} marker. Transmission electron

microscopy (TEM) images were collected on a HITACHI Model H-800 transmission emission microscope operating at an accelerating voltage of 200 kV. TEM samples were prepared by depositing a drop of dispersion on carbon-coated copper grids (250 mesh). X-ray diffraction (XRD) patterns were recorded by a Rigaku Ultima IV. Incident X-ray radiation was produced by Cu X-ray tube, operating at 40 kV and 40 mA with Cu K_α radiation of 1.54 Å. A scanning rate was 4°/min from 10 to 70° in 2θ. Density-functional theory (DFT) calculations were performed on a COMPAQ DS20E computer. Geometry optimizations were carried out using the Becke3LYP functional and 3-61G basis set,[13] with the unrestricted Hartree-Fock (UHF) formalism as implemented in the *Gaussian 03* program *Rev. C.02*. Graphical outputs of the computational results were generated with the *Gauss View* software program (ver. 3.09) developed by Semichem, Inc. Electrochemical measurements were performed on an ALS630B electrochemical analyzer in deaerated PhCN containing 0.10 M $TBAPF_6$ as a supporting electrolyte at 298 K. A conventional three-electrode cell was used with a platinum working electrode (surface area of 0.3 mm^2) and a platinum wire as the counter electrode. The Pt working electrode was routinely polished with BAS polishing alumina suspension and rinsed with acetone before use. The measured potentials were recorded with respect to an $Ag/AgNO_3$ (0.01 M) reference electrode. All potentials (vs Ag/Ag^+) were converted to values versus saturated calomel electrode (SCE) by adding 0.29 V. All electrochemical measurements were carried out under an atmospheric pressure of argon. For nanosecond transient absorption measurements, deaerated solutions of the compounds were excited by a Panther OPO equipped with a Nd:YAG laser (Continuum, SLII-10, 4-6 ns fwhm) with a power of 10-15 mJ per pulse. The PET reactions were monitored by continuous exposure to a Xe lamp (150 W) as a probe light and a photomultiplier tube (Hamamatsu 2949) as a detector. Solutions were deoxygenated by argon purging for 15 min prior to measurements.

Results and Discussion

Spectral Characterization of LPDI Nanobelts in Solution. As shown in Figure 2, LPDI molecules undergo suspension as a result of low solubility at room temperature in PhCN, while BPDI, thoroughly dissolved in PhCN, conserves its pronounced peaks with the maximum at 530 nm corresponding to the 0–0 transition. Aggregation of LPDI molecules can be recognized from enhanced 0–1, 0–2, and 0–3 transitions compared to 0–0 transition. Aggregation also affords a bathochromic shift from 530 nm to 537 nm. In addition, the absorption spectrum of LPDI suspension displays the formation of new band at around 590 nm, resulted from the co-facial stacking via π-π interactions of PDI planes.[4a,14] Such stacking of PDI planes generally leads to relatively long 1D organizations with the help of long linear alkyl chains attached to the nitrogen atoms of PDI.[3,5] On the contrary, BPDI molecules do not show such aggregation behavior in PhCN due to the steric hindrance of branched alkyl chains.[3,5] Absorption spectra of LPDI and BPDI in chloroform exhibit the same characteristics

with the maximum at 526 nm, showing no evidence for aggregation. LPDI molecules also yield aggregation in acetonitrile (ACN) with remarkable red shift to 544 nm and appearance of a new absorption band at around 585 nm (Figure 2).

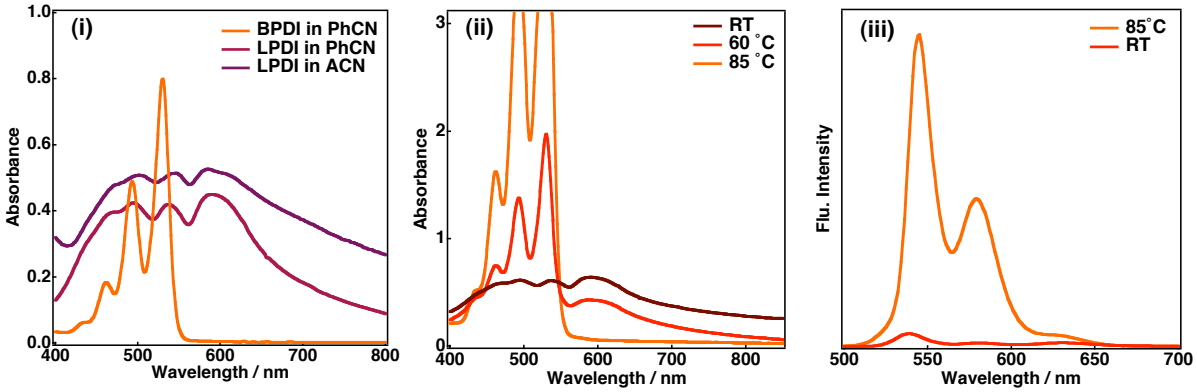


Figure 2. (i) Steady-state absorption spectra of 0.01 mM BPDI and 0.19 mM LPDI in PhCN at room temperature. (ii) Steady-state absorption and (iii) emission spectra of LPDI in PhCN at indicated temperatures (λ_{exc} = 490 nm).

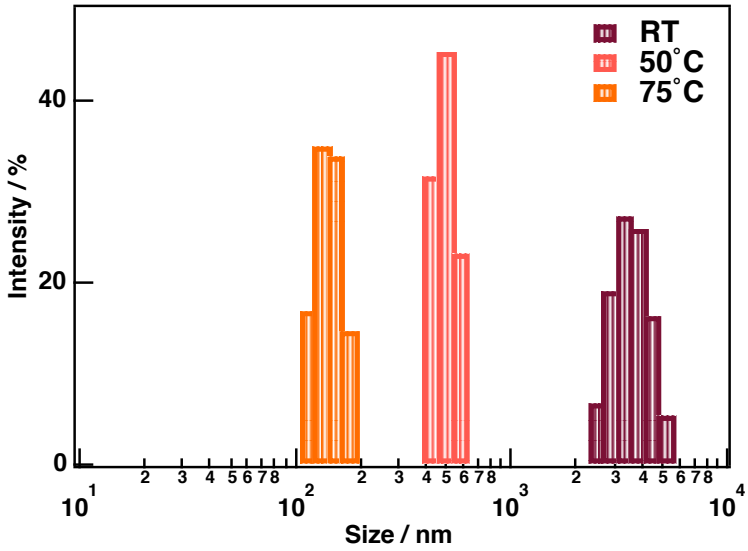


Figure 3. Size distribution diagram of LPDI nanobelts (2.5 mM) in PhCN at indicated temperatures.

LPDI molecules tend to dissolve in PhCN at high temperatures as indicated by the absorption and emission spectra. The 0–0 transition at 530 nm is restored and compared to this recovery, electronic transitions at shorter wavelengths start to decrease gradually along with disappearance of the long-wavelength band at 590 nm by heating the suspension up to 85˚C (Figure 2). The full conversion of LPDI aggregates into free molecules as a result of decomposition of the molecular organization at nanoscale can be recognized through a clear isobestic point at 550 nm. As expected, the quenched fluorescence of LPDI molecules in aggregate due to symmetry-forbidden transition involving the lower-energy π-stacking state[5] is

recovered at high temperatures because of enhanced solubility (Figure 2). Hence, the aggregation yield[3] of LPDI molecules in PhCN is estimated to be 96% at room temperature by comparison of the emission intensities at room temperature and at 85˚C, where LPDI molecules are assumed to dissolve completely and to have a quantum yield of the fluorescence close to unity.[15]

The size distribution of LPDI aggregates in PhCN is examined by dynamic light scattering (DLS) measurements. The DLS diagram of LPDI aggregates reveals a size distribution ranging from 2300 nm to 4800 nm, with a mean size of 3312 nm (Figure 3). Dimensions at micrometer scale are most likely to result from long length size of 1D nanobelts as observed in solid state. The decomposition of LPDI aggregates can also be followed by DLS measurements at high temperatures.

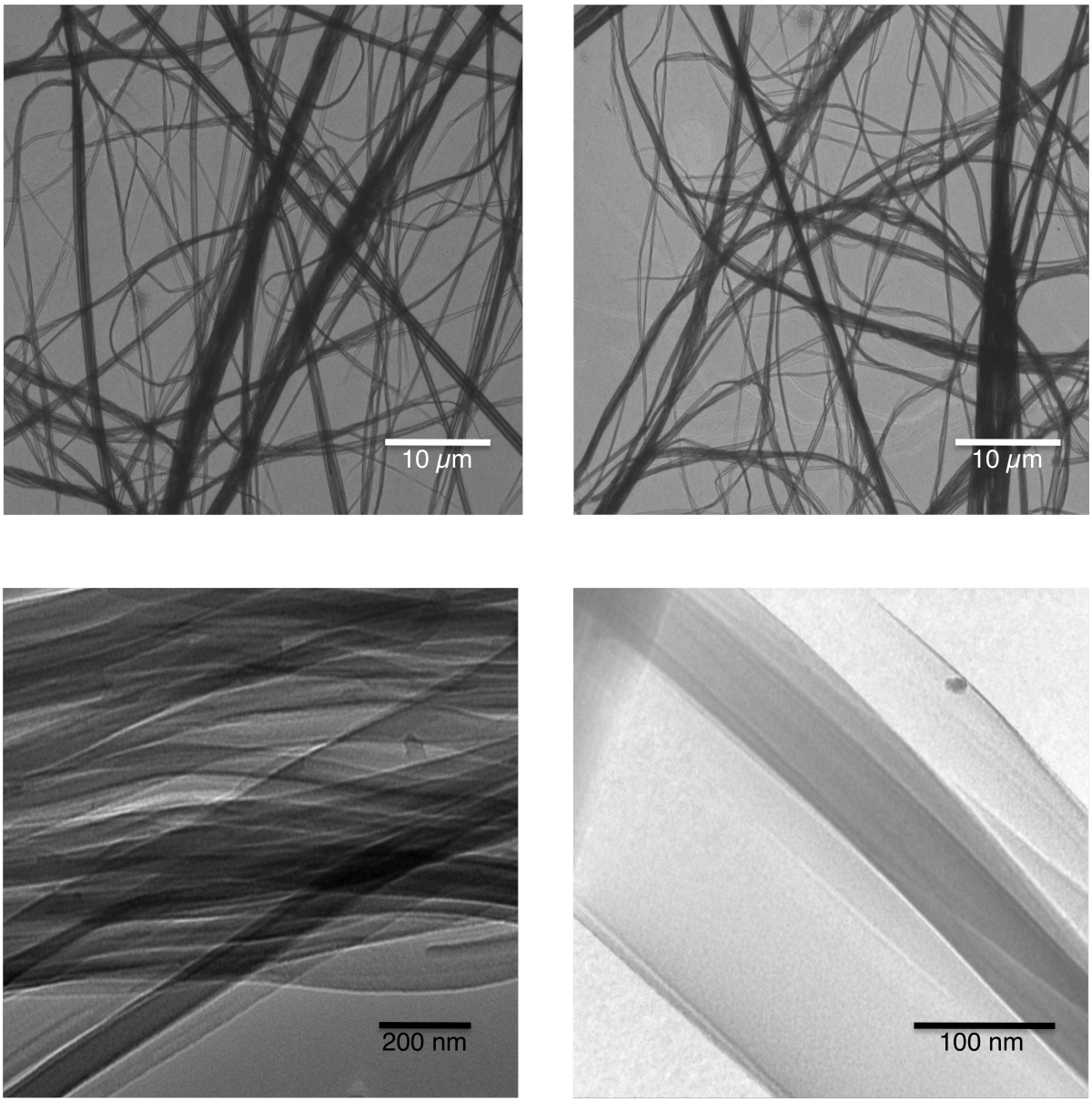


Figure 4. TEM images of LPDI nanobelts at different scales, fabricated by the phase-transfer crystallization.

Characterization of LPDI Nanobelts in Solid State. The aggregation behavior of LPDIs in the solid state was investigated by transmission electron microscopy (TEM). The π-stacked LPDI molecules are prompted to form 1D nanobelt morphology as shown in TEM images (Figure 4). LPDI nanobelts were fabricated by the phase-transfer self-assembly[3] between excess acetonitrile or methanol and a concentrated chloroform solution. As shown in the TEM images, the average width is a few hundreds of nanometers and the length is in the range of a few tens of micrometers. This gives an average aspect ratio (length/width) much more than 100.

X-ray diffraction measurements of powder LPDI nanobelts display the long axis of a unit cell to be 26.1 Å which is about 28% shorter than the full length of an LPDI molecule, which is calculated as 36.2 Å by using density functional calculations at the B3LYP/6-31G level (Figure 5). From the average width of nanobelts, it can be estimated that ca. 100 LPDI molecules with side-chain interdigitation fit in a nanobelt laterally. PDIs substituted by linear chains like LPDI, as in many examples,[2,3,5] produce 1D molecular organizations when phase transfer techniques are applied, in contrast to the ones having branched appendages similar to BPDI.[3,5] Hence, the electron transferred from a donor moiety is allowed to move along the one-dimensionally stacked LPDI molecules via the overlapping π-orbitals.

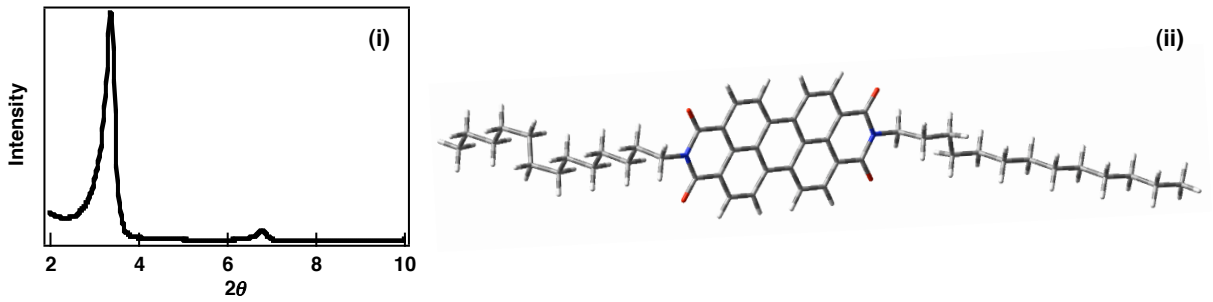


Figure 5. (i) X-ray diffraction pattern of LPDI nanobelts. The sample was deposited on glass cover slips suited for the X-ray measurements and (ii) Optimized molecular structure of LPDI by DFT (B3LYP/6-31G).

Spectral Characterization of Radical Anions of LPDI Nanobelts in Solution. Characterization of radical anions of LPDI aggregate [$(LPDI)_n^{\bullet-}$] and BPDI ($BPDI^{\bullet-}$) in PhCN was made by using electron paramagnetic resonance (EPR). $BPDI^{\bullet-}$ and $(LPDI)_n^{\bullet-}$ are generated chemically by electron-donating hydrazine[6d] in PhCN.[16] The hyperfine coupling structure of $BPDI^{\bullet-}$, showing a non-aggregated molecule behavior (g = 2.0042), is quite matching with the literature data (Figure 6).[6d,9d,17] In the frozen solvent, EPR spectrum of BPDI with similar g value shows no hyperfine splitting. Spin distribution of unpaired electron of $(LPDI)_n^{\bullet-}$, on the other hand, apparently has a different EPR spectrum as shown in Figure 6. Firstly, the hyperfine splitting disappeared because the unpaired electron is averaging many hyperfine environments by a fast hoping mechanism throughout the large LPDI aggregate on

the microsecond time scale of the EPR experiment.[6d,17] Secondly, the EPR spectrum of $(LPDI)_n^{\bullet-}$ shows asymmetric trait around the line center due to anisotropic *g*-tensor, which is *x*-*y* rotationally symmetric ($g_{//}$ = 2.0038). Anisotropy of the spectrum, which depends on the sample orientation in the magnetic field, implies that LPDI aggregates possess a one-dimensional organization at room temperature rather than a zero-dimensional aggregation because they have a very large radius of gyration compared to spherical species of the same molecular weight.[17] In the frozen PhCN, the EPR spectrum of $(LPDI)_n^{\bullet-}$ displays the same powder pattern with the disappearance of hyperfine splitting and anisotropy due to the *g*-tensor ($g_{//} \sim$ 2.0037). Thus, we can conclude that the electron chemically transferred from hydrazine delocalizes within the electron-accepting LPDI aggregate, which is ordered one-dimensionally by cofacial π-π stacking.

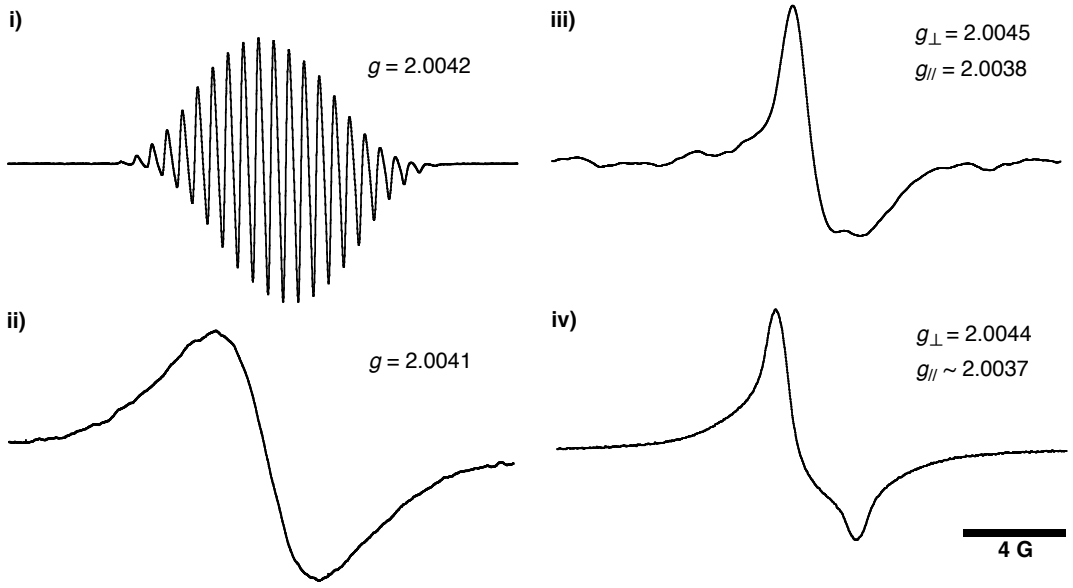


Figure 6. EPR spectra of (i) the radical anion of 0.02 mM BPDI at room temperature and (ii) at 77 K and (iii) the radical anion of ca. 2.8 mM LPDI nanobelts at room temperature and (iv) at 77 K in the presence of hydrazine (260 mM) in deaerated PhCN.

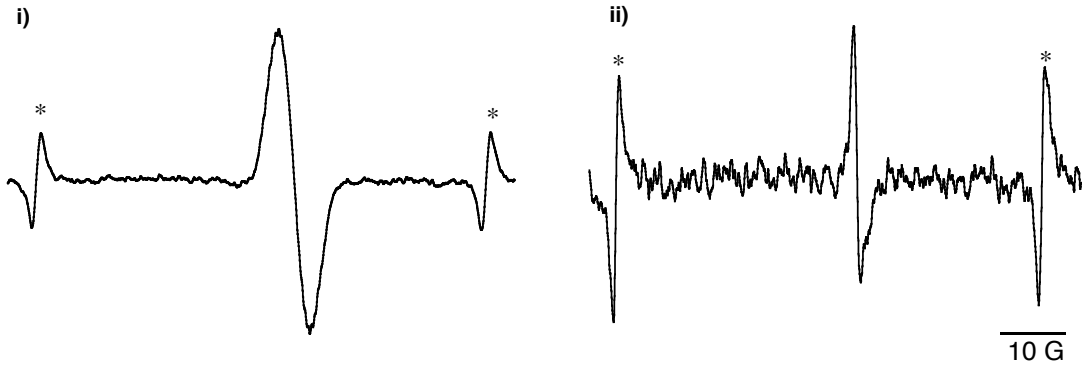


Figure 7. EPR spectra of radical anions of (i) 0.01 mM BPDI in PhCN and (ii) 1.0 mM LPDI nanobelts in ACN in the presence of hydrazine (160 mM) at room temperature. Asterisks denote Mn^{2+} markers.

The EPR spectrum of LPDI radical anion in ACN is consistent with that of LPDI in PhCN, also resulting in electron delocalization along the nanobelt structure (Figure 7).

Intermolecular Photoinduced Electron-Transfer Dynamics. PET of the LDI nanobelts with ZnTBPc has been scrutinized in comparison with the mixture system comprising ZnTBPc and BPDI. Both systems in PhCN energetically possess the necessary conditions for intermolecular PET from electron-donating ZnTBPc to electron-accepting LPDI nanobelts and BPDI molecules. As in similar intermolecular PET processes,[18] the lifetime of the triplet-excited state of ZnTBPc is long enough to allow the PET reactions.[18a,b] PDIs are not convenient photosensitizers for these systems because the intersystem crossing pathway is extremely inefficient.[19] Besides, the aggregation of LPDI molecules in PhCN already leads to fluorescence quenching, deactivating an efficient photosensitization.

The driving force for electron transfer (ΔG_{et}^{T}) is determined according to the following equation:[7,20]

$$\Delta G_{et}^{T}\ (\text{kcal mol}^{-1}) = 23.06\ (E_{ox} - E_{red}) - E_{T} - E_{c} \qquad (1)$$

where E_{ox} is the first one-electron oxidation potential of the electron donor, E_{red} is the first one-electron reduction potential of the electron acceptor, E_T is the triplet state energy of ZnTBPc (27.2 kcal mol^{-1}),[21] and E_c is the Coulomb energy term (1.40 kcal mol^{-1} in polar PhCN[22]). The E_{ox} and E_{red} values of ZnTBPc and BPDI in PhCN are determined to be 0.58 and –0.53 V, respectively, by using a differential pulse voltammetry (DPV) technique (Figure 8). BPDI is used for these measurements because of low solubility of LPDI in PhCN. The side-chain substituents have almost no effect on electrochemical properties of PDIs (vide supra).

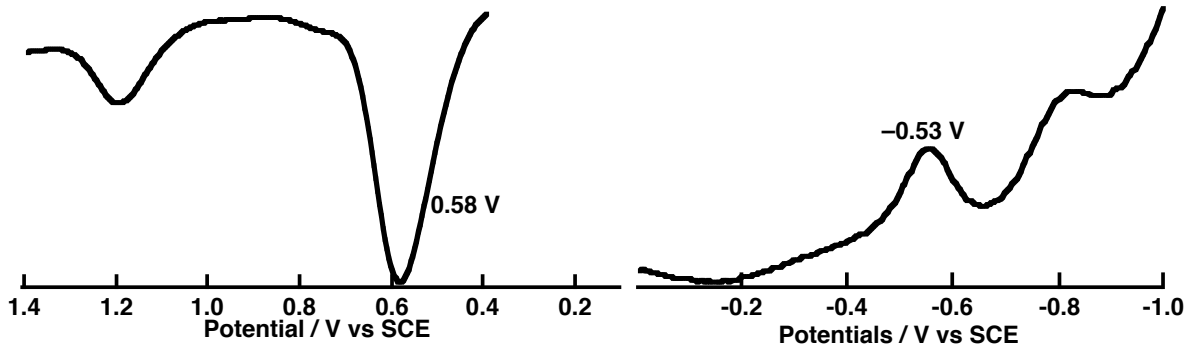


Figure 8. Diffrential Pulse Voltammograms of ZnTBPc (left) and PDI (right) in deaerated PhCN containing 0.1 M $TBAPF_6$ (sweep rate: 0.1 mV/s).

Based on these values, the free energy change of electron transfer (ΔG_{et}^{T}) via the triplet excited state of ZnTBPc was determined to be –3.0 kcal mol^{-1} in PhCN.[20,22,23] The negative ΔG_{et}^{T} value via the triplet excited state of ZnTBPc suggests that the quenching rate should be close to the diffusion-controlled limit (k_{diff}).[24,25] Polar PhCN, stabilizing the radical ion pair of

the radical cation ($ZnTBPc^{\bullet+}$) and the radical anion ($LPDI^{\bullet-}$), has an important role to obtain such an exothermic driving force.[7] In addition, the BDPI/ZnTBPc mixture system has the same thermodynamic properties, because BPDI and LPDI have the same first one-electron reduction potentials. Estimated intermolecular PET processes are compiled in the qualitative energy level diagram (Figure 9).

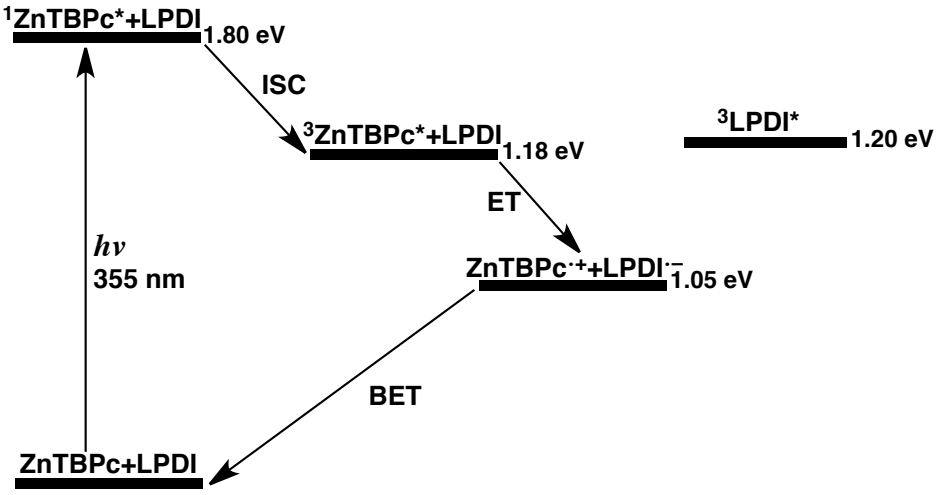


Figure 9. Energy level diagram (in eV) for intermolecular ET process of LPDI/ZnTBPc system via triplet state of ZnTBPc.

Nanosecond transient spectral measurements were performed to identify the products of the photoinduced electron transfer and the kinetics of the electron-transfer and back electron-transfer reactions. The transient absorption spectra of ZnTBPc and LPDI nanobelt in PhCN at selected time delays were obtained by an excitation given at 355 nm. Upon excitation, the maximum at 490 nm and the bleaching signal centered around 680 nm are assigned to the triplet-excited state of ZnTBPc in PhCN (Figure 10). In the presence of the LPDI aggregates, formation of the new peaks in the near-infrared (NIR) region following the quenching of ^{3}ZnTBPc* was observed as shown in Figure 11. The peaks with the maxima at 720, 800 and 980 nm can be assigned to the radical anion of LPDI nanobelts by comparing with the steady-state absorption spectra of PDI radical anion obtained by the chemical reduction of PDI (Figure 12).[26,27] The relatively sharp peak at 960 nm due to PDI radical anion in Figure 12 is red shifted to 980 nm with a remarkable broadening up to 1070 nm for the radical anion of LPDI nanobelts in Figure 11. Such a broadening of the absorption band can result from an electron migration as reported for a similar oligomer system of PDI in solution.[28] In addition, 1D aggregates of PDI containing reduced dopant molecules[17] are reported to show the absorption in the NIR region similar to transient spectra in Figure 11. This also indicates an electron delocalization in the LPDI nanobelts following PET from ZnTBPc. The intense transient absorption peak at 840 nm in Figure 11 is attributed to radical cation of ZnTBPc as recognized from the steady-state absorption spectra of ZnTBPc radical cation (Figure 12).[18a,b,29,30]

Normally, BPDI has a molar extinction coefficient (ε) of 13500 M^{-1} cm^{-1} at 840 nm (Figure 12), which is about twice larger than that of $ZnTBPc^{\bullet+}$ at the same wavelength in PhCN.[31] Because we can clearly observe the formation of $ZnTBPc^{\bullet+}$ at 840 nm without any shielding, it can be concluded that the ε value of $(LPDI)_n^{\bullet-}$ is lower than that of the non-aggregated PDI molecule. Thus, the concentration of $ZnTBPc^{\bullet+}$ can be determined from the absorbance at 840 nm with the known ε value to analyze the kinetics of the back electron-transfer reactions (vide infra). It should be noted that there is no transient signal due to the formation of triplet-excited state of LPDI[19] via a triplet-triplet energy transfer from ^{3}ZnTBPc* although their energy levels are very close (Figure 9).

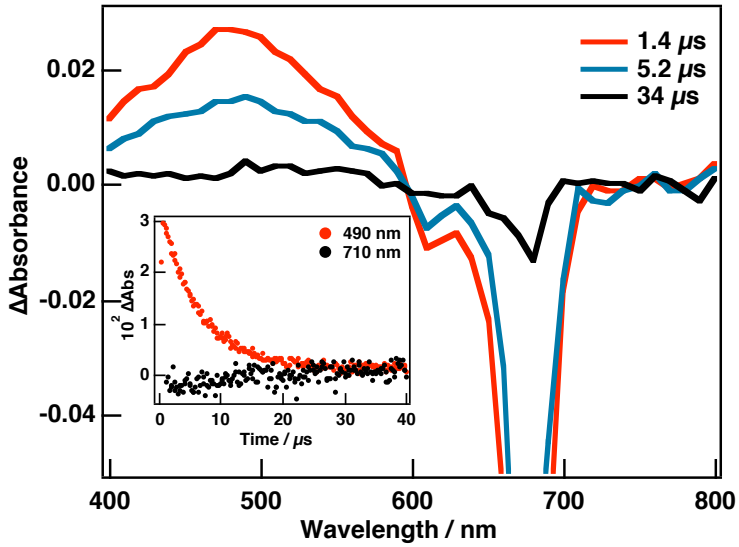


Figure 10. Nanosecond transient absorption spectra of ZnTBPc in deaerated PhCN at indicated time delays (λ_{exc} = 355 nm).

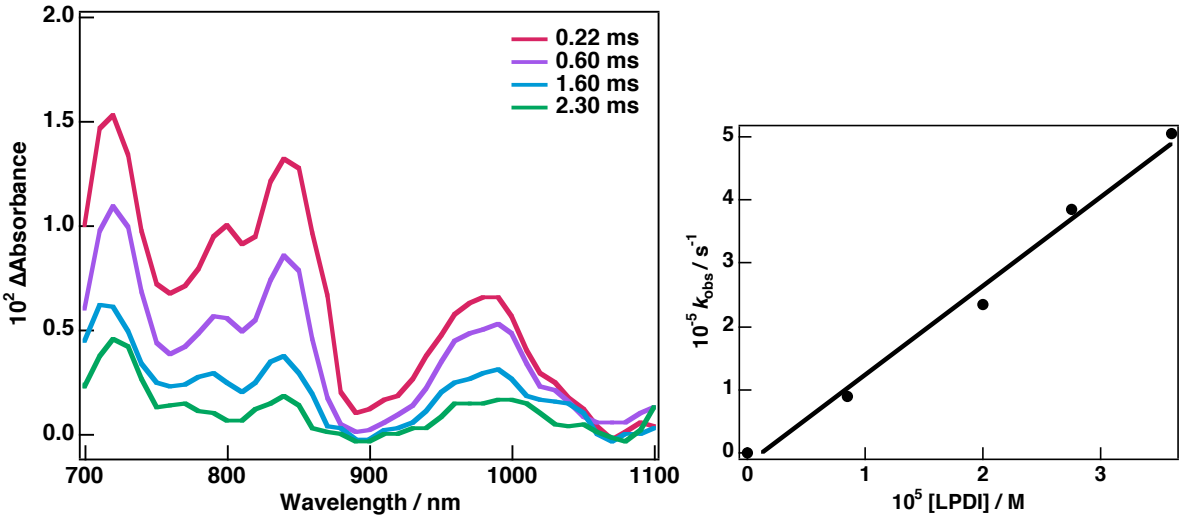


Figure 11. Nanosecond transient absorption spectra of 0.06 mM ZnTBPc and ca. 0.5 mM LPDI aggregates in deaerated PhCN at indicated time delays, λ_{exc} = 355 nm (left) and plot of the pseudo-first order rate constant (k_{obs}) as a function of the concentration of LPDI determined from absorbance change at 720 nm due to $LPDI^{\bullet-}$ (right).

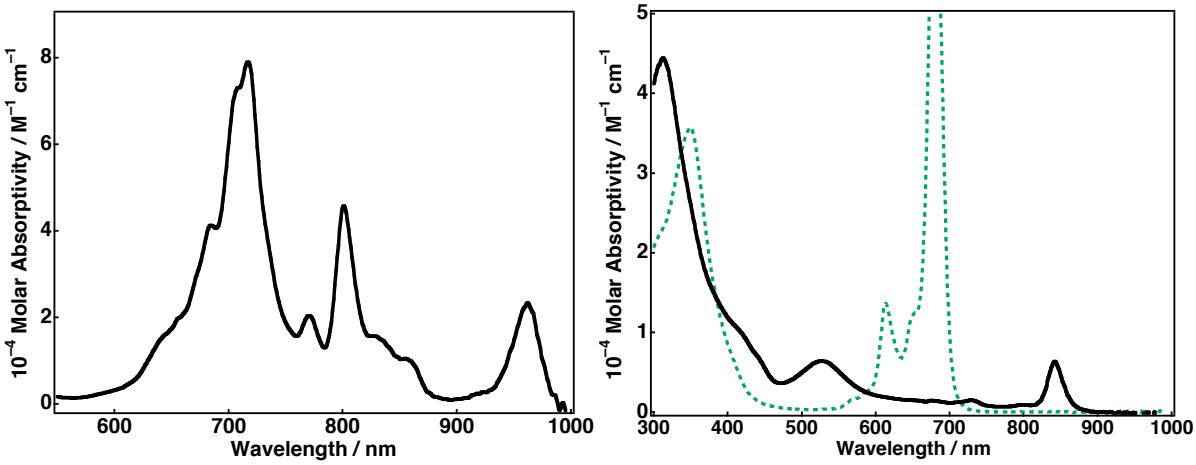


Figure 12. Steady-state absorption spectra of radical anion of BPDI (left) and radical cation of ZnTBPc in deaerated PhCN.

The rate of electron transfer obeys pseudo-first-order kinetics. The pseudo-first-order rate constant increases linearly with increasing concentration of LPDI. From the slope of the linear plot in Figure 11 (right), the rate constant of electron transfer (k_{et}) from ^{3}ZnTBPc* to LPDI is determined to be 1.7×10^9 M^{-1} s^{-1}.

As for the back electron transfer (BET) from $(LPDI)_n^{\bullet-}$ to $ZnTBPc^{\bullet+}$, the rate constant of BET (k_{bet}) follows second-order kinetics. As shown in Figure 13, the decay profile of absorbance at 840 nm due to $ZnTBPc^{\bullet+}$ is converted to a linear second-order plot. The k_{bet} value is determined from the slope in Figure 13 (inset), where the concentration of $ZnTBPc^{\bullet+}$ is estimated through the transient absorbance and the molar absorptivity (ε) of $ZnTBPc^{\bullet+}$ at 840 nm.[31] The slope affords the k_{bet} value of 6.9×10^8 M^{-1} s^{-1}. Second-order kinetics also confirms that ZnTBPc and LPDI nanobelts has no non-covalent interactions, as was concluded from the steady-state absorption spectrum of the hybrid system.

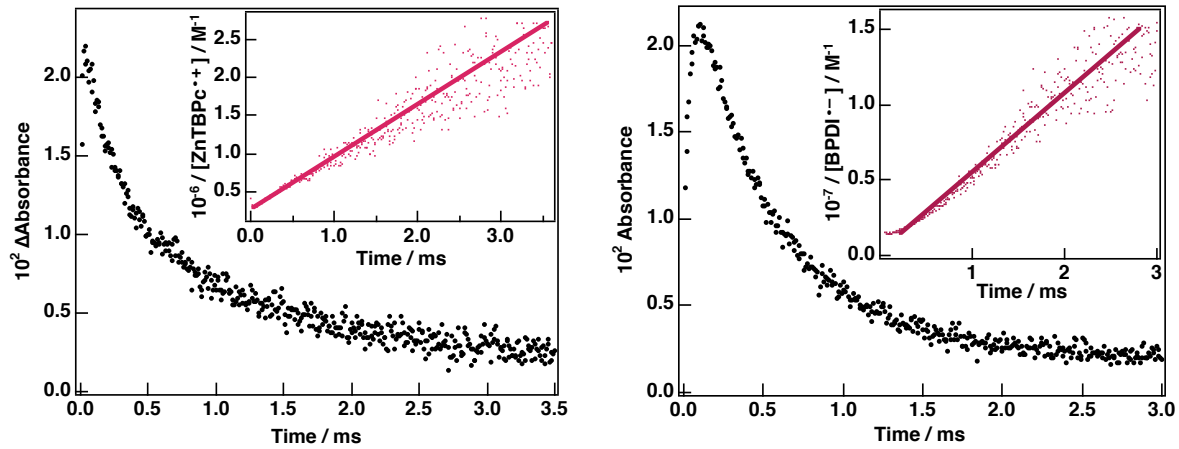


Figure 13. Decay time profiles of absorbance at 840 nm due to $ZnTBPc^{\bullet+}$ (left) and at 720 nm due to $BPDI^{\bullet-}$ (right) in deaerated PhCN (λ_{exc} = 355 nm). Insets: Second-order plots.

The photodynamics of a mixture system comprising ZnTBPc and BPDI was also investigated by utilizing the nanosecond transient absorption spectroscopy techniques for comparison. Following excitation at 355 nm, nanosecond differential spectra in Figure 14 display the same spectral features of that obtained chemically (Figure 12), which can be interpreted for PET from ^{3}ZnTBPc* to BPDI in PhCN bereft of π-electron delocalization. Electron transfer rate from ^{3}ZnTBPc* to BPDI also obeys pseudo-first-order kinetics, which was monitored by absorbance change at 720 nm as displayed in Figure 14. The pseudo-first-order rate constant of formation of BPDI$^{\bullet-}$ increases linearly with the increasing concentration of ZnTBPc. From the slope of linear plot in Figure 14 (right), the k_{et} value is calculated as 2.2 $\times$ 10^9 M^{-1} s^{-1}, which is very close to that of the ZnTBPc/LPDI nanobelt mixture system.

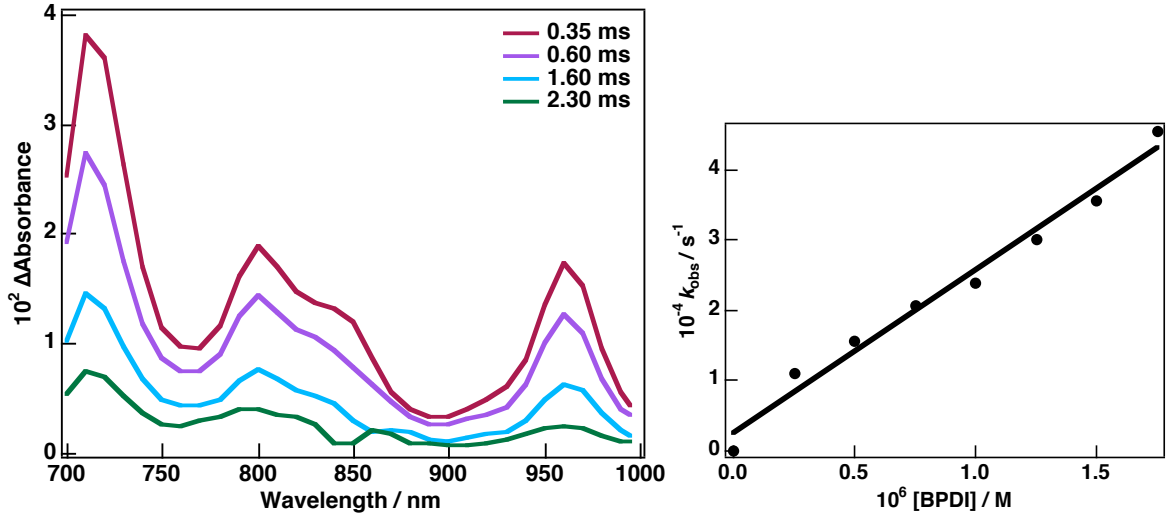


Figure 14. Nanosecond transient absorption spectra of 0.06 mM ZnTBPc and 0.1 mM BPDI in deaerated PhCN at indicated time delays, λ_{exc} = 355 nm (left) and plot of the pseudo-first order rate constant (k_{obs}) versus the concentration of BPDI determined from absorbance change at 720 nm due to BPDI$^{\bullet-}$ (right).

In the BPDI-ZnTBPc mixture system, transient trait of ZnTBPc$^{\bullet+}$ at 840 nm overlaps with the shoulder of transient absorption of BPDI$^{\bullet-}$ at 800 nm due to its low ε compared to that of BPDI$^{\bullet-}$. Therefore, the back electron-transfer kinetics can be assessed according to the absorbance of BPDI$^{\bullet-}$ at 720 nm.[32] The BET process from BPDI$^{\bullet-}$ to ZnTBPc$^{\bullet+}$ trails second-order kinetics (Figure 13). The k_{bet} value is determined from the slope of the linear plot in the inset of Figure 13 to be 4.8 $\times$ 10^9 M^{-1} s^{-1}, which is significantly larger than that of the ZnTBPc-LPDI nanobelt system (6.9 $\times$ 10^8 M^{-1}s^{-1}). The smaller k_{bet} value of ZnTBPc-LPDI nanobelt system can be reasoned from the electron delocalization within the π-system of the LPDI nanobelt. Even though diffusion behaviors of suspended LPDI aggregates and dissolved BPDI molecules may be different in the solvent, close k_{et} values of both systems show that the effect of this difference on k_{bet} values may be neglected. Very fast delocalization inside the nanobelts may be compensating for a bigger difference between the k_{bet} values. In any case, distinctive

transient absorption spectral characteristics of the radical anion of LPDI monitored in the NIR region declare the presence of delocalized electron on nanobelt after photoinduced electron transfer occurs.

Conclusion

The LPDI nanobelt structure and its radical anion have been characterized spectroscopically. Photodynamics of electron-transfer events taking place between (i) LPDI nanobelt and ZnTBPc and (ii) BPDI and ZnTBPc have been investigated by time-resolved transient absorption studies. Because of stabilization effect of polar benzonitrile, the low-energy ^{3}ZnTBPc* was used as driving force for photoinduced electron transfer. An explicit broadening of the radical anion peak of LPDI nanobelt at 980 nm has been monitored by nanosecond transient absorption spectroscopy, confirming the delocalization of the transferred electron inside the LPDI nanobelt. The significantly slower rate of back electron transfer from $(LPDI)_n^{\bullet-}$ to $ZnTBPc^{\bullet+}$ than that from $BPDI^{\bullet-}$ to $ZnTBPc^{\bullet+}$ may also indicate the effect of electron delocalization within the nanostructure.

References and Notes

(1) (a) Hill, J. P.; Jin, W.; Kosaka, A.; Fukushima, T.; Ichihara, H.; Shimomura, T.; Ito, K.; Hashizume, T.; Ishii, N.; Aida, T. *Science* **2004**, *304*, 1481. (b) Loi, M. A.; Da Como, E.; Dinelli, F.; Murgia, M.; Zamboni, R.; Biscarini, F.; Muccini, M. *Nat. Mater.* **2005**, *4*, 81. (c) Jonkheijm, P.; van der Schoot, P.; Schenning, A. P. H. J.; Meijer, E. W. *Science* **2006**, *313*, 80. (d) Yamamoto, Y.; Fukushima, T.; Suna, Y.; Ishii, N.; Saeki, A.; Seki, S.; Tagawa, S.; Taniguchi, M.; Kawai, T.; Aida, T. *Science* **2006**, *314*, 1761. (e) Zhao, Y. S.; Fu, H.; Peng, A.; Ma, Y.; Xiao, D.; Yao, J. *Adv. Mater.* **2008**, *20*, 2859.

(2) (a) Peumans, P.; Uchida, S.; Forrest, S. R. *Nature* **2003**, *425*, 158. (b) Sugiyasu, K.; Fujita, N.; Shinkai, S. *Angew. Chem., Int. Ed.* **2004**, *43*, 1229. (c) Karapire, C.; Zafer, C.; Icli, S. *Synth. Met.* **2004**, *145*, 51. (d) Yang, F.; Shtein, M.; Forrest, S. R. *Nat. Mater.* **2005**, *4*, 37. (e) Balakrishnan, K.; Datar, A.; Oitker, R.; Chen, H.; Zuo, J.; Zang, L. *J. Am. Chem. Soc.* **2005**, *127*, 10496. (f) Liu, Y.; Wang, K.-R.; Guo, D.-S.; Jiang, B.-P. *Adv. Funct. Mater.* **2009**, *19*, 2230. (g) Huang, Y.; Quan, B.; Wei, Z.; Liu, G.; Sun, L. *J. Phys. Chem. C* **2009**, *113*, 3929. (h) Karak, S.; Ray, S. K.; Dhar, A. *Appl. Phys. Lett.* **2010**, *97*, 043306. (i) Che, Y.; Yang, X.; Liu, G.; Yu, C.; Ji, H.; Zuo, J.; Zhao, J.; Zang, L. *J. Am. Chem. Soc.* **2010**, *132*, 5743. (j) Wang, Q. H.; Hersam, M. C. *Nano Lett.* **2011**, *11*, 589.

(3) Balakrishnan, K.; Datar, A.; Naddo, T.; Huang, J.; Oitker, R.; Yen, M.; Zhao, J.; Zang, L. *J. Am. Chem. Soc.* **2006**, *128*, 7390.

(4) (a) Kazmaier, P. M.; Hoffmann, R. *J. Am. Chem. Soc.* **1994**, *116*, 9684. (b) Correa, D. S.; Oliviera, S. L.; Misoguti, L.; Zilio, S. C.; Aroca, R. F.; Constantino, C. J. L.; Mendonça, C. R. *J. Phys. Chem. A* **2006**, *110*, 6433.

(5) Zang, L.; Che, Y.; Moore, J. S. *Acc. Chem. Res.* **2008**, *41*, 1596.

(6) (a) Crispin, X.; Cornil, J.; Friedlein, R.; Okudaira, K. K.; Lemaur, V.; Crispin, A.; Kestemont, G.; Lehmann, M.; Fahlman, M.; Lazzaroni, R.; Geerts, Y.; Wendin, G.; Ueno, N.; Bredas, J.-L.; Salaneck, W. R. *J. Am. Chem. Soc.* **2004**, *126*, 11889. (b) Grimsdale, A. C.; Müllen, K. *Angew. Chem., Int. Ed.* **2005**, *44*, 5592. (c) Hoeben, F. J. M.; Jonkheim, P.; Meijer, E. W.; Schenning, A. P. H. J. *Chem. Rev.* **2005**, *105*, 1491. (d) Che, Y.; Datar, A.; Yang, X.; Naddo, T.; Zhao, J.; Zang, L. *J. Am. Chem. Soc.* **2007**, *129*, 6354.

(7) (a) Kavarnos, G. J.; Turro, N. J. *Chem. Rev.* **1986**, *86*, 401. (b) Weller, A. *Z. Phys. Chem.* **1982**, *133*, 93.

(8) (a) Gouloumis, A.; de la Escosure, A.; Vazquez, P.; Torres, T.; Kahnt, A.; Guldi, D. M.; Neugebauer, H.; Winder, C.; Drees, M.; Sariciftci, N. S. *Org. Lett.* **2006**, *8*, 5187. (b) Quintiliani, M.; Kahnt, A.; Wölfle, T.; Hieringer, W.; Vazquez, P.; Görling, A.; Guldi, D. M.; Torres, T. *Chem.–Eur. J.* **2008**, *14*, 3765. (c) Vivo, P.; Ojala, M.; Chukharev, V.; Efimov, A.; Lemmetyinen, H. *J. Photochem. Photobiol. A* **2009**, *203*, 125. (d) Cao, J.; Sun, J.-Z.; Hong, J.; Yang, X.-G.; Chen, H.-Z.; Wang, M. *Appl. Phys. Lett.* **2003**, *83*, 1896. (e) Kira, A.; Umeyama, T.; Matano, Y.; Yoshida, K.; Isoda, S.; Isosomppi, M.; Tkachenko, N. V.; Lemmetyinen, H.; Imahori, H. *Langmuir* **2006**, *22*, 5497.

(9) (a) Jimenez, A. J.; Spänig, F.; Rodriguez-Morgade, S.; Ohkubo, K.; Fukuzumi, S.; Guldi, D. M.; Torres, T. *Org. Lett.* **2007**, *9*, 2481. (b) Cespedes-Guirao, F. J.; Ohkubo, K.; Fukuzumi, S.; Sastre-Santos, A.; Fernandez-Lazaro, F. *J. Org. Chem.* **2009**, *74*, 5871. (c) Chen, Y.; Lin, Y.; El-Khouly, M. E.; Zhuang, X.; Araki, Y.; Ito, O.; Zhang, W. *J. Phys. Chem. C* **2007**, *111*, 16096. (d) Fukuzumi, S.; Ohkubo, K.; Ortiz, J.; Gutierrez, A. M.; Fernandez-Lazaro, F.; Sastre-Santos, A. *J. Phys. Chem. A* **2008**, *112*, 10744.

(10) Kitazume, K.; Chen, Y.; Itou, M.; Araki, Y.; Uchida, S.; Ito, O. *J. Porphyrins Phthalocyanines* **2006**, *10*, 1190.

(11) Gaspard, S.; Maillard, P. *Tetrahedron* **1987**, *43*, 1083.

(12) El-Khouly, M. E.; Choi, D. H.; Fukuzumi, S. *J. Photochem. Photobiol. A* **2011**, *218*, 17.

(13) (a) Hehre, W. J.; Radom, L.; Schleyer, P. V. R.; Pople, J. A. *Ab Initio Molecular Orbital Theory*; Wiley: New York, 1986. (b) Frisch, M. J.; Trucks, G. W.; Schlegel, H. B.; Scuseria, G. E.; Robb, M. A.; Cheeseman, J. R.; Montgomery, J. A.; Vreven, J., T.; Kudin, K. N.; Burant, J. C.; Millam, J. M.; Iyengar, S. S.; Tomasi, J.; Barone, V.; Mennucci, B.; Cossi, M.; Scalmani, G.; Rega, N.; Petersson, G. A.; Nakatsuji,

H.; Hada, M.; Ehara, M.; Toyota, K.; Fukuda, R.; Hasegawa, J.; Ishida, M.; Nakajima, T.; Honda, Y.; Kitao, O.; Nakai, H.; Klene, M.; Li, X.; Knox, J. E.; Hratchian, H. P.; Cross, J. B.; Adamo, C.; Jaramillo, J.; Gomperts, R.; Stratmann, R. E.; Yazyev, O.; Austin, A. J.; Cammi, R.; Pomelli, C.; Ochterski, J. W.; Ayala, P. Y.; Morokuma, K.; Voth, G. A.; Salvador, P.; Dannenberg, J. J.; Zakrzewski, V. G.; Dapprich, S.; Daniels, A. D.; Strain, M. C.; Farkas, O.; Malick, D. K.; Rabuck, A. D.; Raghavachari, K.; Foresman, J. B.; Ortiz, J. V.; Cui, Q.; Baboul, A. G.; Clifford, S.; Cioslowski, J.; Stefanov, B. B.; Liu, G.; Liashenko, A.; Piskorz, P.; Komaromi, I.; Martin, R. L.; Fox, D. J.; Keith, T.; Al-Laham, M. A.; Peng, C. Y.; Nanayakkara, A.; Challacombe, M.; Gill, P. M. W.; Johnson, B.; Chen, W.; Wong, M. W.; Gonzalez, C.; Pople, J. A. *Gaussian 03, Revision C.02*, Gaussian, Inc.: Wallingford CT, 2004.

(14) Yang, X.; Xu, X.; Ji, H.-F. *J. Phys. Chem. B* **2008**, *112*, 7196.

(15) Langhals, H. *Helv. Chim. Acta* **2005**, *88*, 1309.

(16) To increase the solubility of hydrazine in PhCN, it was first dissolved in a small amount of deaerated dimethylformamide (DMF).

(17) Chen, S.-G.; Branz, H. M.; Eaton, S. S.; Taylor, C.; Cormier, R. A.; Gregg, B. A. *J. Phys. Chem. B* **2004**, *108*, 17329.

(18) (a) Nojiri, T.; Alam, M. A.; Konami, H.; Watanabe, A.; Ito, O. *J. Phys. Chem. A* **1997**, *101*, 7943. (b) El-Khouly, M. E.; Islam, S. D.-M.; Fujitsuka, M.; Ito, O. *J. Porphyrins Phthalocyanines* **2000**, *4*, 713. (c) El-Khouly, M. E.; Fujitska, M.; Ito, O. *J. Porphyrins Phthalocyanines* **2000**, *4*, 591. (d) Takai, A.; Gros, C. P.; Barbe, J-M.; Guilard, R.; Fukuzumi, S. *Chem.–Eur. J.* **2009**, *15*, 3110. (e) Nakanishi, T.; Ohkubo, K.; Kojima, T.; Fukuzumi, S. *J. Am. Chem. Soc.* **2009**, *131*, 577. (f) Murakami, M.; Ohkubo, K.; Fukuzumi, S. *Chem.–Eur. J.* **2010**, *16*, 7820. (g) El-Khouly, M. E.; Jaggi, M.; Schmid, B.; Blum, C.; Liu, S.-X.; Decurtins, S.; Ohkubo, K.; Fukuzumi, S. *J. Phys. Chem. C* **2011**, *115*, 8325.

(19) (a) Danilov, E. O.; Rachford, A. A.; Goeb, S.; Castellano, F. N. *J. Phys. Chem. A* **2009**, *113*, 5763. (b) Supur, M.; El-Khouly, M. E.; Seok, J. H.; Kim, J. H.; Kay, K-Y.; Fukuzumi, S. *J. Phys. Chem. C* **2010**, *114*, 10969.

(20) Rehm, D.; Weller, A. *Isr. J. Chem.* **1970**, *8*, 259.

(21) (a) Harriman, A.; Porter, G.; Richoux, M.-C. *J. Chem. Soc., Faraday Trans.* **1971**, *55*, 4131. (b) Vincett, P. S.; Voight, E. M.; Rjeckhoff, K. E. *J. Chem. Phys.* **1971**, *55*, 4130. (c) Herkstroeter, W. G.; Merkel, P. B. *J. Photochem.* **1981**, *16*, 331. (d) D'Souza, F.; Maligaspe, E.; Ohkubo, K.; Zandler, M. E.; Subbaiyan, N. K.; Fukuzumi, S. *J. Am. Chem. Soc.* **2009**, *131*, 8787.

(22) Arnold, B. R.; Farid, S.; Goodman, J. L.; Gould, I. R. *J. Am. Chem. Soc.* **1996**, *118*, 5482.

(23) Marcus, R. A. *Annu. Rev. Phys. Chem.* **1964**, *15*, 155.

(24) Murov, S. I.; Carmichael, I.; Hug, G. L. *Handbook of Photochemistry*; Marcel Dekker: New York, 2nd ed., 1993.

(25) (a) Fukuzumi, S.; Koumitsu, S.; Hironaka, K.; Tanaka, T. *J. Am. Chem. Soc.* **1987**, *109*, 305. (b) Fukuzumi, S.; Ohkubo, K.; Suenobu, T.; Kato, K.; Fujitsuka, M.; Ito, O. *J. Am. Chem. Soc.* **2001**, *123*, 8459. (c) Murakami, M.; Ohkubo, K.; Mandal, P.; Ganguly, T.; Fukuzumi, S. *J. Phys. Chem. A* **2008**, *112*, 635.

(26) The chemical reduction of BPDI is achieved by using a strong reductant, tetrakis(dimethylamino)ethylene (TDAE)[27] in deaerated PhCN. Steady-state absorption spectrum of $(LPDI)_n^{\bullet-}$ was not observable due to broad NIR absorption of LPDI covering the reduction products.

(27) Fujitsuka, M.; Luo, C.; Ito, O. *J. Phys. Chem. B* **1999**, *103*, 445.

(28) van der Boom, T.; Hayes, R. T.; Zhao, Y.; Bushard, P. J.; Weiss, E. A.; Wasielewski, M. R. *J. Am. Chem. Soc.* **2002**, *124*, 9582.

(29) The absorption spectrum of $ZnTBPc^{\bullet+}$ in PhCN is obtained by the chemical oxidation with tris(4-bromophenyl)aminium hexachloroantimonate, as a strong oxidant.

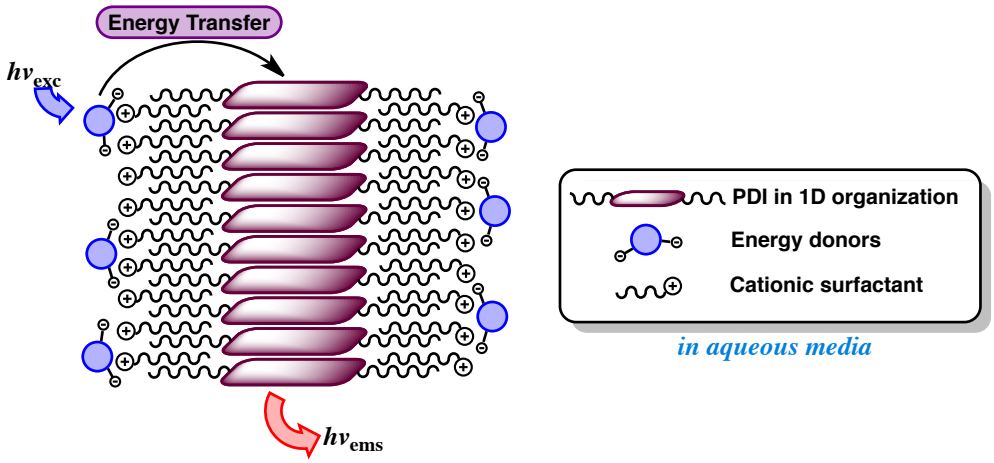
(30) Nyokong, T.; Gasyna, Z.; Stillman, M. *Inorg. Chem.* **1987**, *26*, 548.

(31) The ε value for $ZnTBPc^{\bullet+}$ at 840 nm is determined to be 6300 M^{-1} cm^{-1} in PhCN (Figure 12).

(32) The ε value for $BPDI^{\bullet-}$ at 720 nm was determined to be 76000 M^{-1} cm^{-1} in PhCN (Figure 12).

Chapter 3

Excitation Energy Transfer form Non-Aggregated Molecules to Perylenediimide Nanoribbons via Ionic Interactions in Water



Abstract: Two energy donor-acceptor self-assembly systems have been constructed by using π-π, lipophilic, and ionic interactions in water. π-Stacked *N*,*N*'-ditridecylperylenediimide (PDI), which forms nanoribbons, has been dispersed in water in the presence of myristyltrimethylammonium bromide (MTAB) through lipophilic interactions of tridecyl groups of PDIs with long tails of MTAB molecules. Cationic heads of MTAB molecules, anchored on the bulk of side-chains of nanoribbons, attract water-soluble zinc tetra(4-sulfonatophenyl)porphyrin tetrapotassium salt ($ZnTPPSK_4$) and lucifer yellow CH dipotassium salt (LY). By this design, efficient photosensitization of non-aggregated energy donors, $ZnTPPSK_4$ and LY, has been achieved while retaining the one-dimensional order at nanoscale, resulting in the efficient excitation energy transfer to PDI nanoribbons in each system.

Introduction

One-dimensional self-assemblies formed by π-π interactions, as organic materials, can provide morphology control at nanoscale and permit the charge or exciton delocalization along the long axis, which are important to improve the device efficiency.[1-5] Such self-assembled systems, involving both energy/electron donor and acceptor, should be efficiently sensitized by light in order to realize notable photoinduced applications. Besides the photoinduced electron-transfer (PET) process involved in these applications,[6-8] the excitation energy transfer in one dimension has been investigated extensively,[9-11] including its linear optical properties.[12-14] Self-organizations of aromatic structures via π-orbital overlap, however, usually afford lower emission quantum yields compared to those of their monomers.[12,15] Therefore, efficient photosensitization of donor or acceptor, which ultimately leads to an electron- or energy-transfer process, is severely obstructed by the π-stacks of donor-acceptor systems. Due to this obstruction, light-induced applications of one-dimensional structures are mostly limited to inorganic nanowires and carbon nanotubes,[16-20] except for only a few examples.[21-23] Moreover, π-stacked assemblies with increased photosensitization efficiency can also be alternatives to carbon nanotubes, in which charge delocalization mostly suffers because of the covalent attachment of donor or acceptor groups.[24-27]

In this study, we introduce a new design for π-stacked self-assemblies, which enables the efficient photosensitization of non-aggregated molecules while preserving the one-dimensional order at nanoscale. This design is realized in two energy donor-acceptor self-assembly systems, which are entirely constructed by using non-covalent interactions. The molecular components of these systems are *N,N'*-ditridecylperylenediimide (PDI), myristyltrimethylammonium bromide (MTAB), zinc tetra(4-sulfonatophenyl)porphyrin tetrapotassium salt ($ZnTPPSK_4$), and lucifer yellow CH dipotassium salt (LY), as their molecular structures are shown in Figure 1.

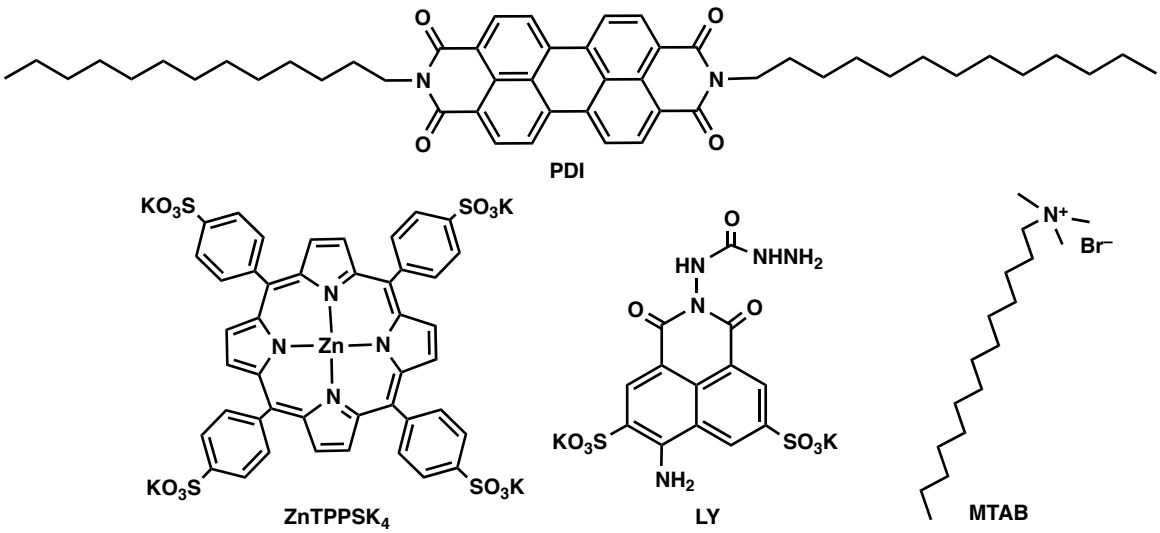


Figure 1. Molecular structures of the components used in this study.

In these systems, PDIs with linear alkyl chains, stacking cofacially and allowing the exciton migration,[28-30] form the main body of the nanostructure (nanoribbon) as in many examples.[1,30-34] The bulk of linear side-chains of PDI stacks provide a base for the long hydrophobic tail of cationic surfactant, MTAB, to be attached along the long axes of the nanoribbons through lipophilic interactions[34] in water. Hydrophilic heads distinctly increase the dispersion of the extremely hydrophobic nanoribbons and these positively charged nanostructures eventually host the photosensitizer energy donors, $ZnTPPSK_4$ and LY, bearing water-soluble, negatively charged sulphonic groups. Formation of the supramolecular systems by weak interactions is illustrated in Figure 2. By this way, excitation energy transfer from efficiently photosensitized donor groups to cofacially stacked PDIs has been achieved for the first time.

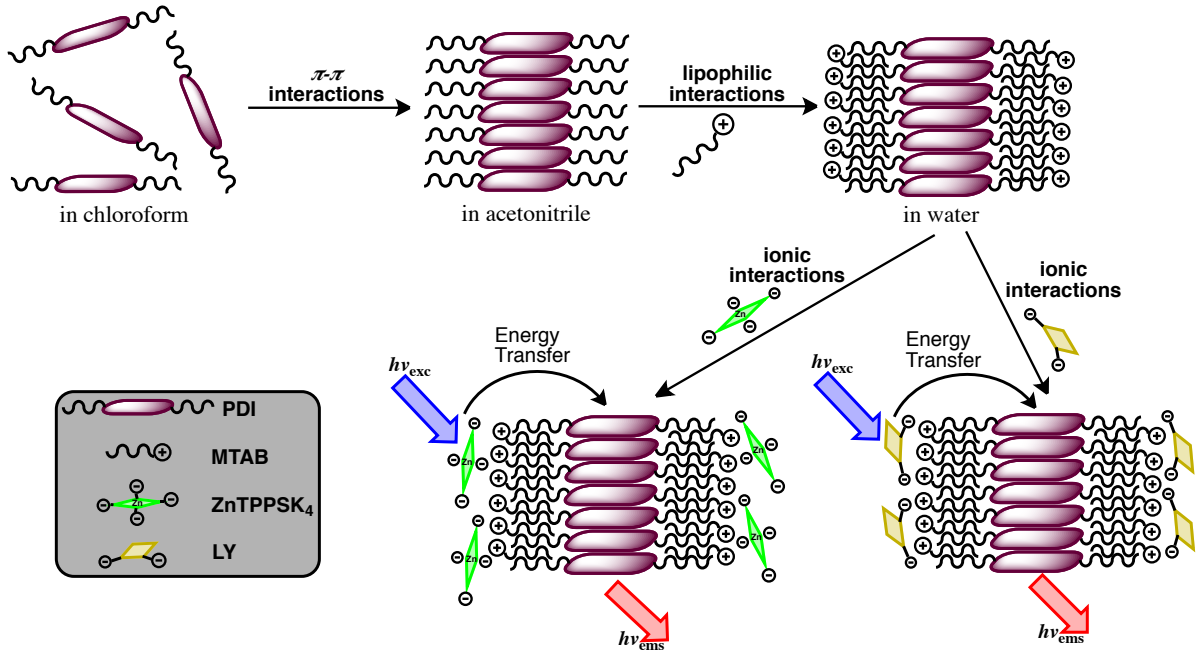


Figure 2. Representative illustration of the construction of self-assembly donor-acceptor systems and photophysical processes taking place in water with a legend showing the names of the components.

Experimental Section

Materials. *N,N'*-ditridecylperylenediimide (PDI), lucifer yellow CH dipotassium salt (LY), and myristyltrimethylammonium bromide (MTAB) were purchased from commercial sources and used as received. Fabrication of PDI nanoribbons was achieved through solution-based self-assembling.[1,16] The one-dimensional growth of the molecular assembly was processed by slow crystallization at the interface between chloroform in which PDI is dissolved appreciably and acetonitrile (ACN), in which PDI has very limited solubility. Polarity difference in the solvents provides separate phases for an extended period. Larger amount of polar solvent, i.e., ACN, is transferred atop a concentrated chloroform solution. Red crystals formed at the

interface within minutes, followed by slow diffusion into upper phase of polar solvent. The crystals, transferred by pipetting, were cast into a glass bottle to dry. PDI nanoribbons were, then, obtained from the dispersion of dried aggregates in water containing MTAB by using sonification for only a few seconds. Zinc tetra(4-sulfonatophenyl)porphyrin tetra potassium salt ($ZnTPPSK_4$) was prepared according to the literature.[35] Purification of water (18.2 MΩ cm) was performed with a Milli-Q system (Millipore; Direct-Q 3 UV).

Instruments. Steady-state absorption measurements were recorded on a Hewlett Packard 8453 diode array spectrophotometer. Fluorescence measurements were carried out on a Shimadzu spectrofluorophotometer (RF-5300PC). Measurements of emission quantum yields were carried out on a Hamamatsu C9920-0X(PMA-12) U6039-05 fluorescence spectrofluorometer with an integrating sphere adapted to a right angle configuration at room temperature. Transmission electron microscopy (TEM) images were collected on a Hitachi model H-800 transmission emission microscope operating at an accelerating voltage of 200 kV. TEM samples were prepared by depositing a drop of dispersion on carbon-coated copper grids (250 mesh). Scanning electron microscopy (SEM) images of nanoribbons were taken on a JEOL FE-SEM JSM-6701F instrument operating at 5kV. Femtosecond transient absorption spectroscopy experiments were conducted using an ultrafast source: Integra-C (Quantronix Corp.), an optical parametric amplifier: TOPAS (Light Conversion Ltd.) and a commercially available optical detection system: Helios provided by Ultrafast Systems LLC. The source for the pump and probe pulses were derived from the fundamental output of Integra-C (780 nm, 2 mJ/pulse and fwhm = 130 fs) at a repetition rate of 1 kHz. 75% of the fundamental output of the laser was introduced into TOPAS which has optical frequency mixers resulting in tuneable range from 285 nm to 1660 nm, while the rest of the output was used for white light generation. Typically, 2500 excitation pulses were averaged for 5 seconds to obtain the transient spectrum at a set delay time. Kinetic traces at appropriate wavelengths were assembled from the time-resolved spectral data. All measurements were conducted at 298 K. The transient spectra were recorded using fresh solutions in each laser excitation. Solutions were deoxygenated by nitrogen purging for 15 min prior to the measurements.

Results and Discussion

Characterization of PDI Nanoribbons Dispersed in Water containing MTAB. Nanoribbons show identical absorption bands, indicating the same aggregation behaviour in ACN and water containing MTAB (Figure 3).[36] Dispersion of PDI nanoribbons in water has been drastically improved by lipophilic interactions of MTAB molecules with long alkyl side-chains as indicated by increased absorbance compared to that in ACN, in which PDI aggregates immediately precipitate to the bottom of the cell (Figure 3, Inset). PDI nanoribbons have an emission band with a maximum at 632 nm when an excitation is given at 530 nm in water containing 0.10 M MTAB (Figure 3). Interestingly, the absolute fluorescence quantum

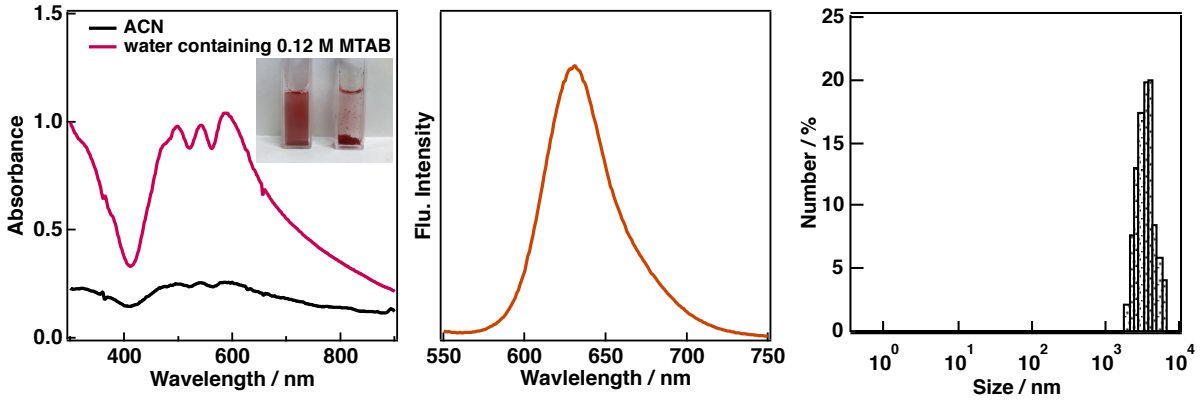


Figure 3. (i) Absorption of PDI nanoribbons in ACN and in water containing MTAB. (ii) Emission and (iii) size distribution of PDI nanoribbons in water containing MTAB. The inset photograph shows the dispersion difference of the same amount of PDI nanoribbons in water containing MTAB (left) and in ACN (right).

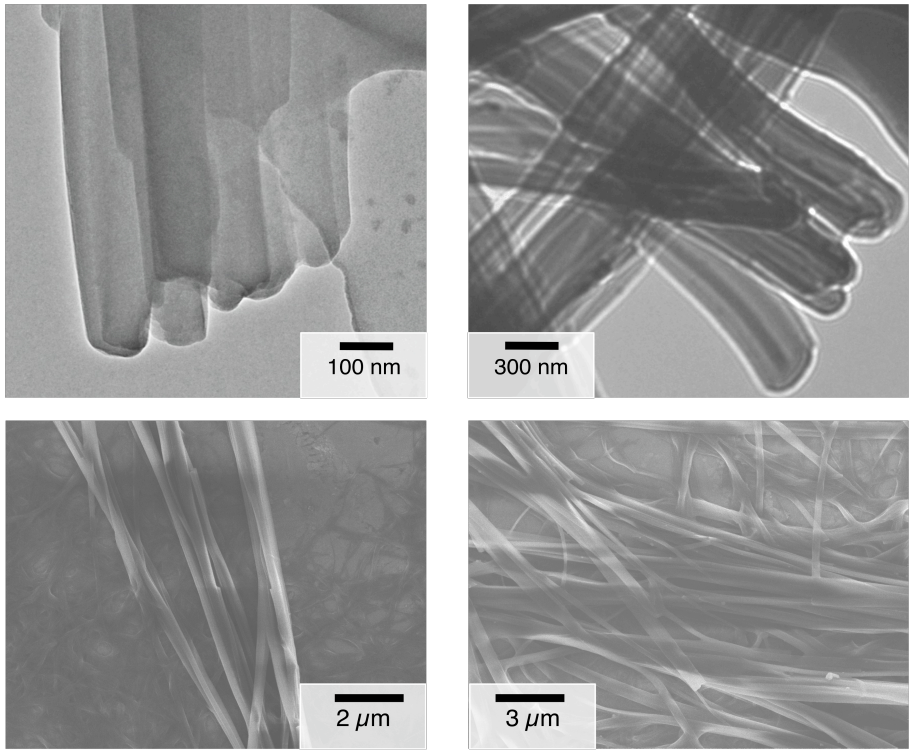


Figure 4. TEM (upper panel) and SEM images (lower panel) of nanoribbons obtained from the dispersion in water containing 0.12 M MTAB.

yield (Φ_f) of PDI nanoribbons is found to be 0.094 in water containing MTAB, whereas the Φ_f value was only 0.015 in ACN, suggesting the impact of good dispersion.

The size distribution of PDI aggregates was examined by dynamic light scattering (DLS) measurements. The DLS diagram of PDI aggregates reveals a size distribution between ca. 2000 and 6000 nm, giving a mean size of 3050 nm (Figure 3). Dimensions at micrometre scale are most likely to result from the long lengths of the one-dimensional nanostructures as observed earlier.[36]

One-dimensional patterns were clearly seen by using the transmission electron microscopy (TEM). Samples used for TEM were obtained from the dispersed aggregates in water containing MTAB (Figure 4). SEM images give more information about the length of the nanoribbons, which reasonably matches with mean size of nanoribbons obtained by DLS measurements (Figure 4). The average width of nanoribbons appears to be a few hundreds of nanometres, while the average length remains in the micrometre range. Previously, it was calculated that 100 of PDI molecules fit laterally to 250 nm of width of PDI nanoribbons.[36] The centre-to-centre distance between slightly tilted cofacial stacks of PDI planes has been estimated to be 0.46 nm,[32] which implies that ca. 6500 PDI molecules can be arranged in a length of 3050 nm. Thus, one layer of PDI nanoribbon contains approximately 6.5×10^5 PDI molecules in order.

Spectral Characterization of $ZnTPPSK_4$/PDI Nanoribbons and LY/PDI Nanoribbons Systems in Water containing MTAB. $ZnTPPSK_4$ has a Soret band at 422 nm in water.[37] The interaction of $ZnTPPSK_4$ with MTAB has been identified by a red shift of the Soret band to 426 nm. In the presence of PDI aggregates, the maximum shifts to 427 nm, suggesting that $ZnTPPSK_4$ has an interaction with MTAB molecules anchored to the linear chains of nanoribbons (Figure 5). The ionic interaction between LY and the MTAB molecules attached to the lipophilic side-surface of PDI nanoribbons causes a clear red shift of maximum of LY from 430 nm to 439 nm (Figure 5). Normally, absorption band of LY has a maximum at 428 nm in pure water.[38] It should be noted that in both cases, PDI aggregates have negligible absorption in the region where $ZnTPPSK_4$ and LY absorb light strongly, enabling selective photoexcitation at 427 and 439 nm, respectively (Figure 6). MTAB molecules do not cause any fluorescence quenching of donor molecules.[39] Intense absorption bands of donor molecules also indicates that they are not aggregated on the side-chains of the nanoribbons.

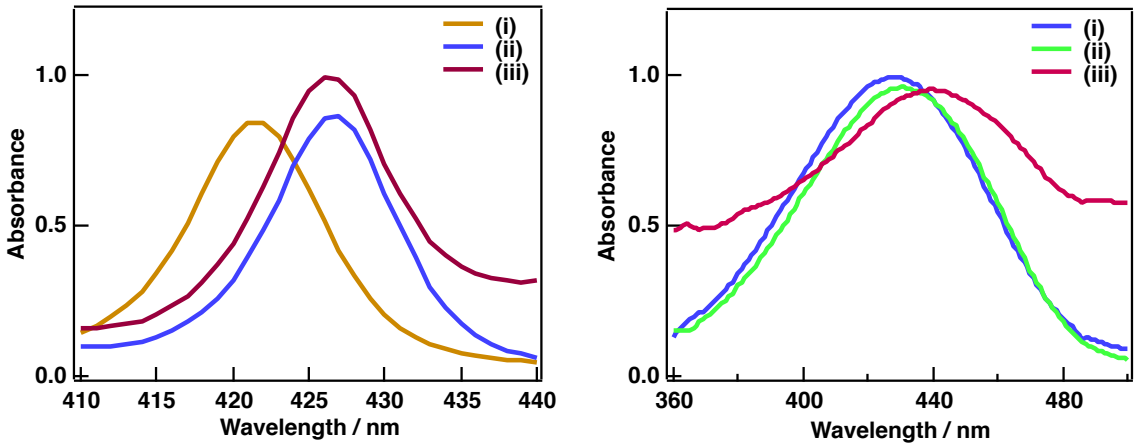


Figure 5. Absorption spectra of 2.1 μM $ZnTPPSK_4$ (left) and 70 μM LY (right) (i) in water, (ii) in water containing 0.10 M MTAB, and (iii) in water containing 0.10 M MTAB in the presence of PDI nanoribbons.

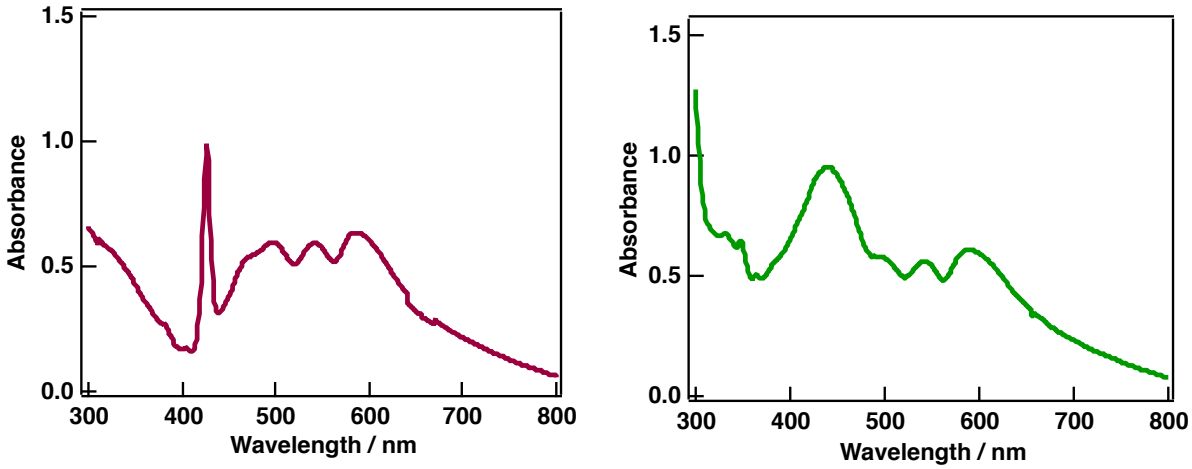


Figure 6. Absorption spectrum of $ZnTPPSK_4$ (left) and LY (right) in the presence of PDI nanoribbons in water containing 0.10 M MTAB.

In order to determine the average numbers of energy donors electrostatically interacting with the PDI nanoribbons, the solutions of $ZnTPPSK_4$ and LY, treated with PDI aggregates in 0.10 M MTAB, were centrifuged for 15 min and the absorption spectra of supernatants have been compared to those of untreated solutions of corresponding energy donors with the same concentration (Figure 7). 6% and 15% of absorbance of $ZnTPPSK_4$ and LY, respectively, have been reduced after the centrifugation, showing the amount of energy donors absorbed by the PDI aggregates in water containing MTAB. Assuming that PDIs form identical nanoribbon layers having a width of 250 nm and a length of 3 μm, averaged according to TEM images and DLS measurements, average numbers of $ZnTPPSK_4$ and LY molecules hosted by one layer of PDIs are estimated to be 140 and 2000, respectively.[40] Higher average number of LY molecules absorbed by nanoribbons might result from its smaller size rather than that of $ZnTPPSK_4$ and its relatively long tail, which probably enhances the fixation to the lipophilic bulk.

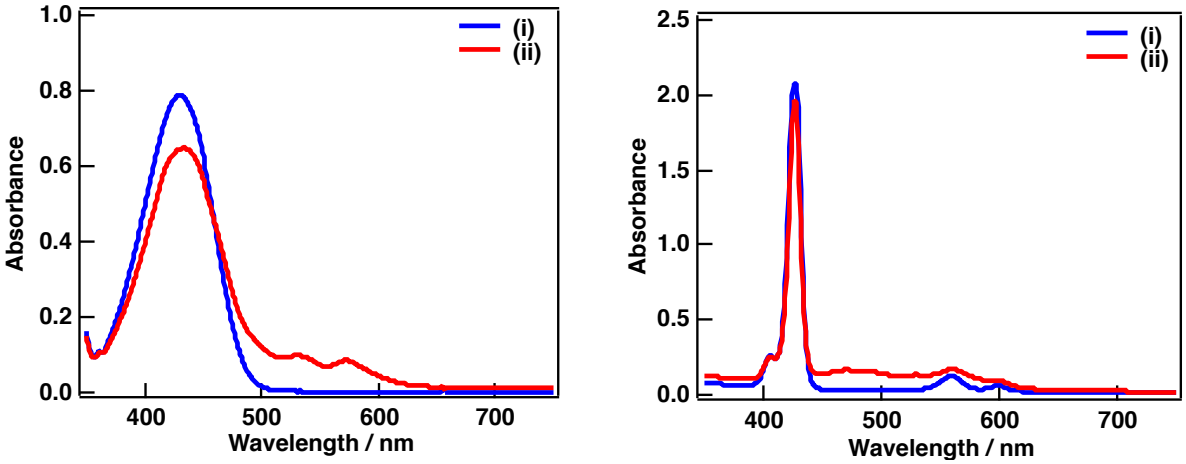


Figure 7. Absorption spectra of 7.5 μM $ZnTPPSK_4$ (left) and and 60 μM LY (right) before (i) and after (ii) the centrifugation to remove the PDI aggregates from their solution.

Energy-Transfer Processes of ZnTPPSK$_4$/PDI Nanoribbons and LY/PDI Nanoribbons Systems in Water containing MTAB. The singlet excited state energy transfer from ZnTPPSK$_4$ and from LY to nanoribbons has been detected by fluorescence spectroscopy. As shown in Figure 8, by the addition of PDI nanoribbons at indicated concentrations, the fluorescence emission of ZnTPPSK$_4$ with a maximum at 604 nm decreases gradually, while another emission band appears at 638 nm, which is assigned to the emission of PDI nanoribbons (Figure 3). On the other hand, the emission of LY at 526 nm is also

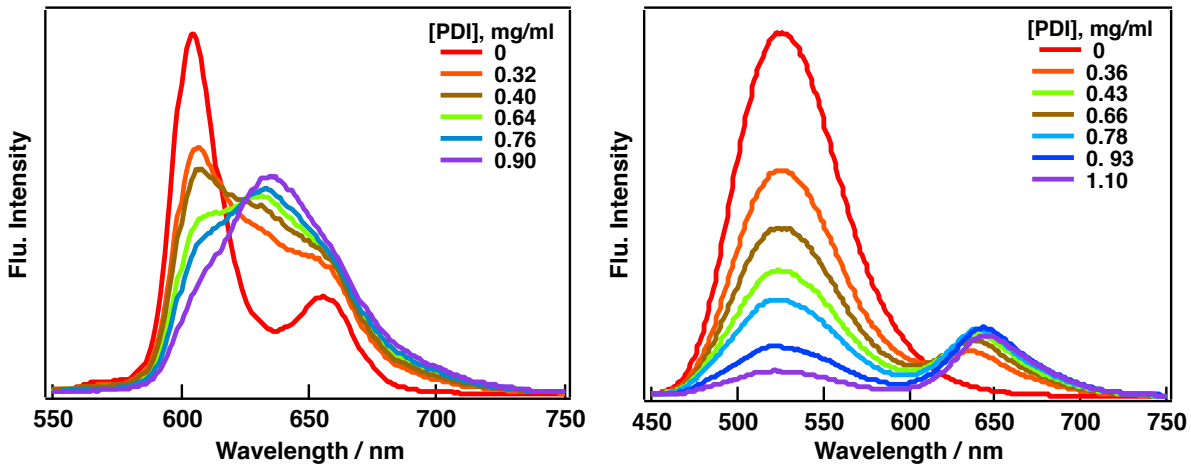


Figure 8. Emission spectra obtained by the titration of ZnTPPSK$_4$ (left) and LY (right) with PDI aggregates in water containing 0.10 M MTAB (λ_{exc} = 427 and 439 nm, respectively).

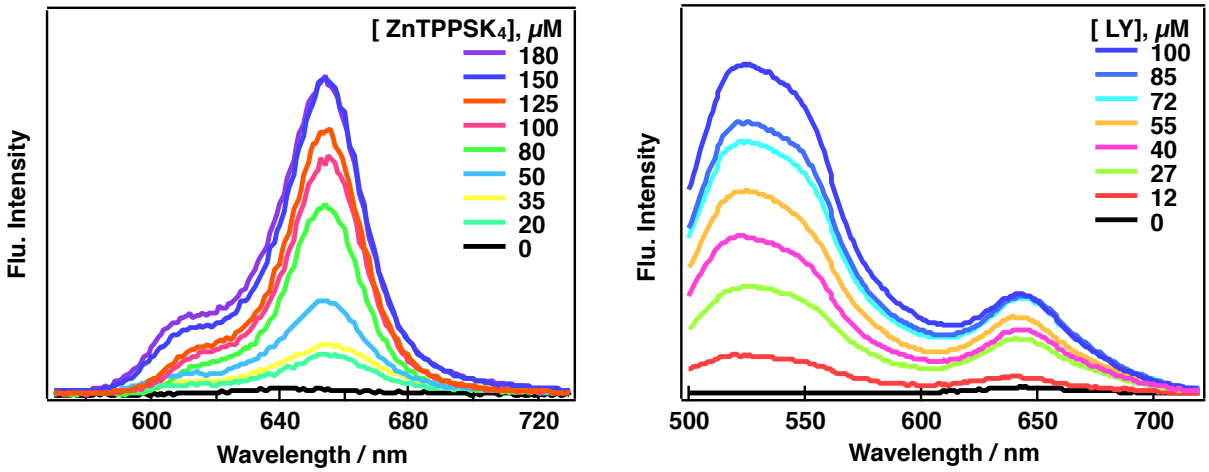


Figure 9. Emission spectra obtained by the titration of PDI aggregates with ZnTPPSK$_4$ (left) and LY (right) in water containing 0.10 M MTAB (λ_{exc} = 427 and 439 nm, respectively).

quenched by the addition of PDI resulting in the emission of PDI nanoribbons at 645 nm. Total quenching of emission of donors was not attained probably due to the presence of unbound donor molecules to the nanoribbons (Figure 9). In both cases, gradual red shift of emission of PDI is evident while its concentration is increasing. However, once the fixed amount of PDI aggregates are titrated with energy donors, no shift of fluorescence emission has observed

(Figure 9). Thus, it can be concluded that the growing length size of hydrophobic nanoribbons through the increased concentration causes this red shift. Because the concentration of PDI aggregates in the latter titrations is higher, the emission maxima were at located at slightly longer wavelength (653 nm) than those in the former case. The difference in the size distribution at different concentrations may also be the reason for obtaining slightly separated maxima in each case. In addition, the emission of unbound donor molecules is more noticeable at these titrations.

Excitation energy-transfer phenomena in these systems have been confirmed by the femtosecond transient absorption spectroscopy. The transient absorption traits of singlet excited states of $ZnTPPSK_4$ are similar to those of zinc porphyrin, which were examined extensively in previous studies.[41–46] The lifetime of the singlet excited state of $ZnTPPSK_4$ (τ_S) was determined to be 2.3 ns from the decay at 500 nm (Figure 10). In the transient absorption

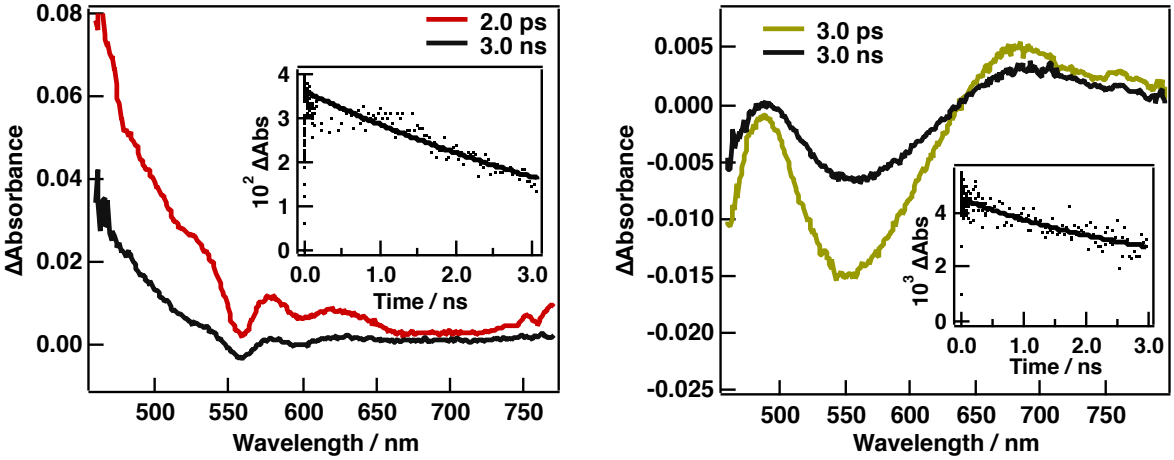


Figure 10. Femtosecond transient absorption spectra of $ZnTPPSK_4$ (left) and LY (right) in water (λ_{exc} = 390 nm). Insets: Time profiles at 500 and 680 nm, respectively.

spectra of LY, obtained by femtosecond laser pulses, the negative absorption stands out with a minimum at around 550 nm, which is the mirror image of the steady-state absorption of the charge transfer band and the stimulated emission. In the near-IR region, relatively broad positive absorption appears at 680 nm, which can be assigned to the absorption of the singlet excited state of LY. The incomplete decay at 680 nm gives a τ_S value for LY as 3.3 ns in water (Figure 10). By the addition of PDI nanoribbons, the transient features of the singlet excited states of the energy donors have been replaced by excited states of the nanoribbons. As shown in Figure 11, these new patterns are quite different than those of PDI monomer in chloroform, suggesting a distinct excited states dynamics.[47] In both self-assembly systems, the transient spectra of PDI nanoribbons are virtually the same. Two sharp peaks are observed at 525 and 565 nm, as positive absorption, while the negative absorption appears at 500, 545, and around 600 nm, reaching the end of spectral window, which is the mirror image of the ground state absorption with 5 nm of red shift (Figure 3). The deactivation of the singlet-excited states of

energy donors could not be detected probably because very fast energy transfer occurs below the picosecond time regime ($k_{EnT} > 10^{12}$ s^{-1}).

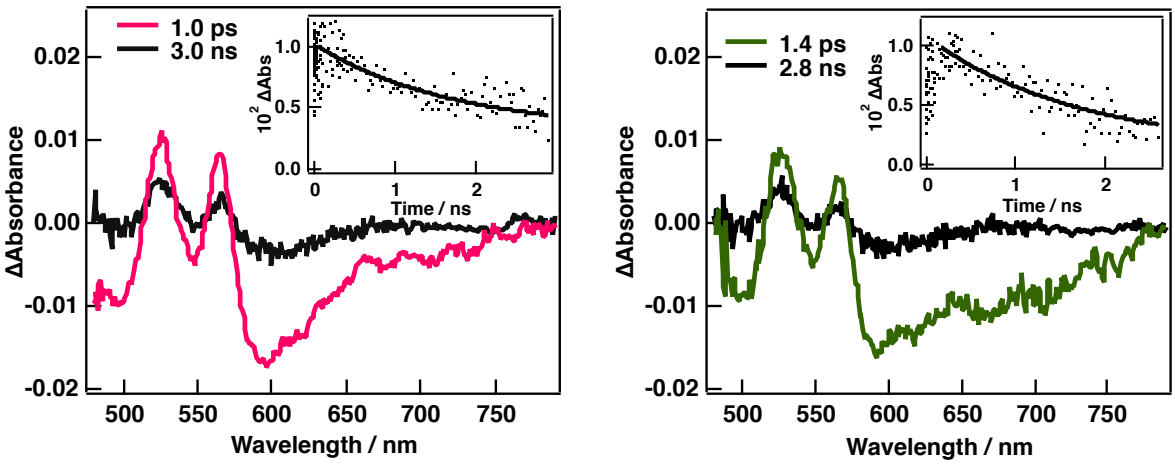


Figure 11. Femtosecond transient absorption spectra of $ZnTPPSK_4$ (4.5 μM)/PDI nanoribbons (1.2 mg/ml) (left) and LY (70 μM)/PDI nanoribbons (1.0 mg/ml) self-assembly systems in water containing 0.10 M MTAB at indicated time delays (λ_{exc} = 390 nm). Insets: Time profiles at 525 nm.

The decay kinetics of excited states of PDI nanoribbons is followed by the time profiles at 525 nm, which give the lifetimes of excited states of 1.6 and 1.5 ns for nanoribbons in $ZnTPPSK_4$/PDI nanoribbons and LY/PDI nanoribbons self-assembly systems (Figure 11), respectively. Slightly different τ_S values may be ascribed to the size distribution of the nanoribbons due to small concentration difference. The τ_S value of monomer PDI was estimated to be 4.5 ns.[3,47] In addition, there was no transient spectral trait assigned for the photoinduced electron-transfer products (i.e., radical ion pair). The absence of PET can be explained by the long distance between the energy donors located on the side-surface periphery and the PDI aromatic cores buried in the nanoribbons longer than approximately 10 Å.[48] While the long distance between the donor and the acceptor established by the linear alkyl chains of PDIs and the long tails of MTAB anchored on these chains seriously inhibits the PET mechanism, it favors the resonance interactions yielding excitation energy transfer. Efficient energy-transfer processes at long distances have been observed in previous examples.[49–51] Although the water provides very polar environment, which boosts the PET processes, local non-polar media formed by long saturated alkyl chains may have an effect on this inhibition. Adjusting the distance between donor and acceptor components may result in a PET process between $ZnTPPSK_4$ and PDI nanoribbons, which seems thermodynamically feasible.

Conclusion

To sum up, excitation energy transfer from non-aggregated $ZnTPPSK_4$ and LY to PDI nanoribbons has been efficiently achieved by the ionic interactions in aqueous media. The

design introduced in this study allows efficient photosensitization of single molecules attached to π-stacked nanostructures by weak interactions.

References and Notes

(1) Zang, L.; Che, Y.; Moore, J. S. *Acc. Chem. Res.* **2008**, *41*, 1596.

(2) Kim, F. S.; Ren, G.; Jenekhe, S. A. *Chem. Mater.* **2011**, *23*, 682.

(3) Würthner, F. *Chem. Commun.* **2004**, 1564.

(4) Wasielewski, M. R. *Acc. Chem. Res.* **2009**, *42*, 1910.

(5) Zhao, Y. S.; Fu, H.; Peng, A.; Ma, Y.; Xiao, D.; Yao, J. *Adv. Mater.* **2008**, *20*, 2859.

(6) Sinks, L. E.; Rybtchinski, B.; Iimura, M.; Jones, B. A.; Goshe, A. J.; Zuo, X.; Tiede, D. M.; Li, X.; Wasielewski, M. R. *Chem. Mater.* **2005**, *17*, 6295.

(7) Würthner, F.; Chen, Z.; Hoeben, F. J. M.; Osswald, P.; You, C.-C.; Jonkheijm, P.; Herrikhuyzen, J. v.; Schenning, A. P. H. J.; van der Schoot, P. P. A. M.; Meijer, E. W.; Beckers, E. H. A.; Meskers, S. C. J.; Janssen, R. A. *J. Am. Chem. Soc.* **2004**, *126*, 10611.

(8) Karak, S.; Ray, S. K.; Dhar, A. *Appl. Phys. Lett.* **2010**, *97*, 043306.

(9) Dudek, S. P.; Pouderoijen, M.; Abbel, R.; Schenning, A. P. H. J.; Meijer, E. W. *J. Am. Chem. Soc.* **2005**, *127*, 11763.

(10) Zhang, J.; Hoeben, F. J.; Pouderoijen, M. J.; Schenning, A. P. H. J.; Meijer, E. W.; De Schryver, F. C.; De Feyter, S. *Chem.–Eur. J.* **2006**, *12*, 9046.

(11) Hoeben, F. J. M.; Jonkheijm, P.; Meijer, E. W.; Schenning, A. P. H. J. *Chem. Rev.*, **2005**, *105*, 1491.

(12) Che, Y.; Yang, X.; Balakrishnan, K.; Zuo, J.; Zang, L. *Chem. Mater.* **2009**, *21*, 2930.

(13) Dakar, A.; Balakrishnan, K.; Yang, X.; Zuo, X.; Huang, J.; Oitker, R.; Yen, M.; Zhao, J.; Tiede, D. M.; Zang, L. *J. Phys. Chem. B* **2006**, *110*, 12327.

(14) Cui, Q. H.; Zhao, Y. S.; Yao, J. *J. Mater. Chem.* **2012**, *22*, 4136.

(15) Würthner, F.; Chen, Z.; Dehm, V.; Stepanenko, V. *Chem. Commun.* **2006**, 1188.

(16) Che, Y.; Yang, X.; Liu, G.; Yu, C.; Ji, H.; Zuo, J.; Zhao, J.; Zang, L. *J. Am. Chem. Soc.* **2010**, *132*, 5743.

(17) Wang, Z. L.; Gao, R. P.; Pan, W.; Dai, Z. R. *Adv. Eng. Mater.* **2001**, *3*, 657.

(18) Hochbaum, A. I.; Yang, P. *Chem. Rev.* **2010**, *110*, 527.

(19) Ohtani, M.; Fukuzumi, S. *Chem. Commun.* **2009**, 4997.

(20) Zhou, W.; Liu, H.; Boughton, R. I.; Du, G.; Lin, J.; Wang, J.; Liu, D. *J. Mater. Chem*. **2010**, *20*, 5993.

(21) Zhang, W.; Jin, W.; Fukushima, T.; Saeki, A.; Seki, S.; Aida, T. *Science* **2011**, *334*, 340.

(22) Yamamoto, Y.; Fukushima, T.; Suna, Y.; Ishii, N.; Saeki, A.; Seki, S.; Tagawa, S.; Taniguchi, M.; Kawai, T.; Aida, T. *Science* **2006**, *314*, 1761.

(23) Schmidt-Mende, L.; Fechtenkötter, A.; Müllen, K.; Moons, E.; Friend, R. H.; MacKenzie, J. D. *Science* **2001**, *293*, 1119.

(24) Guldi, D. M.; Rahman, G. M. A.; Sgobba, V.; Ehli, C. *Chem. Soc. Rev.* **2006**, *35*, 471.

(25) Guldi, D. M.; Rahman, G. M. A.; Zerbetto, F.; Prato, M. *Acc. Chem. Res.* **2005**, *38*, 871.

(26) D'Souza, F.; Sandanayaka, A. S. D.; Ito, O. *J. Phys. Chem. Lett.* **2010**, *1*, 2586.

(27) Chitta, R.; D'Souza, F. *J. Mater. Chem.* **2008**, *18*, 1440.

(28) Beljonne, D.; Hennebicq, E.; Daniel, C.; Herz, L. M.; Silva, C.; Scholes, G. D.; Hoeben, F. J. M.; Jonkheim, P.; Schenning, A. P. H. J.; Meskers, S. C. J.; Phillips, R. T.; Friend, R. H.; Meijer, E. W. *J. Phys. Chem. B* **2005**, *109*, 10594.

(29) Marciniak, H.; Li, X.-Q.; Würthner, F.; Lochbrunner, S. *J. Phys. Chem. A* **2011**, *115*, 648.

(30) Daniel, C.; Makereel, F.; Herz, L. M.; Hoeben, F. J. M.; Jonkheijm, P.; Schenning, A. P. H. J.; Meijer, E. W.; Silva, C. *J. Chem. Phys.* **2008**, *129*, 104701.

(31) Huang, Y.; Quan, B.; Wei, Z.; Liu, G.; Sun, L. *J. Phys. Chem. C* **2009**, *113*, 3929.

(32) Che, Y.; Yang, X.; Liu, G.; Yu, C.; Ji, H.; Zuo, J.; Zhao, J.; Zang, L. *J. Am. Chem. Soc.* **2010**, *132*, 5743.

(33) Yagai, S.; Monma, Y.; Kawauchi, N.; Karatsu, T.; Kitamura, A. *Org. Lett.* **2007**, *9*, 1137.

(34) Che, Y.; Huang, H.; Xu, M.; Zhang, C.; Bunes, B. R.; Yang, X.; Zang, L. *J. Am. Chem. Soc.* **2011**, *133*, 1087.

(35) Jiménez, H. R.; Julve, M.; Faus, J. *J. Chem. Soc. Dalton Trans*. **1991**, 1945.

(36) Spectral characterization of *N*,*N'*-ditridecylperylenediimide nanostructures used in this study has been discussed in comparison with a non-aggregated form of PDI in a previous report in the previous chapter. Also see: Supur, M.; Yamada, Y.; El-Khouly, M. E.; Honda, T.; Fukuzumi, S. *J. Phys. Chem. C* **2011**, *115*, 15040.

(37) Cheung, S. K.; Dixon, F. L.; Fleischer, E. B.; Jeter, D. Y.; Krishnamurty, M. *Bioinorg. Chem.* **1973**, *2*, 281.

(38) Stewart, W. W. *J. Am. Chem. Soc.* **1981**, *103*, 7615.

(39) Absolute fluorescence quantum yield (Φ_f) of $ZnTPPSK_4$ in pure water and water containing 0.1 M MTAB is 0.016. Φ_f of LY in water is 0.241, while it attains 0.406 in the presence of 0.1 M MTAB in water. F_f of LY has been reported to change intensely depending on the solvent conditions, see: Panda, D.; Mishra, P. P.; Khatua, S.; Koner, A. L.; Sunoj, R. B.; Datta, A. *J. Phys. Chem. A* **2006**, *110*, 5585.

(40) The total amount of PDI used for the treatment of energy donors was 3 mg in each case, which afforded 3.7×10^{12} nanoribbon layers (3000 × 250 nm).

(41) Damrauer, N. H.; Hodgkiss, J. M.; Rosenthal, J.; Nocera, D. G. *J. Phys. Chem. B* **2004**, *108*, 6315.

(42) El-Khouly, M. E.; Ryu, J. B.; Kay, K.-Y.; Ito, O.; Fukuzumi, S. *J. Phys. Chem. C* **2009**, *113*, 15444.

(43) El-Khouly, M. E.; Han, K.-J.; Kay, K.-Y.; Fukuzumi, S. *ChemPhysChem* **2010**, *11*, 1726.

(44) El-Khouly, M. E.; Ju, D. K.; Kay, K.-Y.; D'Souza, F.; Fukuzumi, S. *Chem.–Eur. J.* **2010**, *16*, 6193.

(45) Kodis, G.; Liddell, P. A.; de la Garza, L.; Moore, A. L.; Moore, T. A.; Gust, D. *J. Mater. Chem.* **2002**, *12*, 2100.

(46) Kuciauskas, D.; Lin, S.; Seely, G. R.; Moore, A. L.; Moore, T. A.; Gust, D.; Drovetskaya, T.; Reed, C. A.; Boyd, P. D. W. *J. Phys. Chem.* **1996**, *100*, 15926.

(47) Supur, M.; El-Khouly, M. E.; Seok, J. H.; Kim, J. H.; Kay, K.-Y.; Fukuzumi, S. *J. Phys. Chem. C* **2010**, *114*, 10969.

(48) Kavarnos, G. J.; Turro, N. J. *Chem. Rev.* **1986**, *86*, 401.

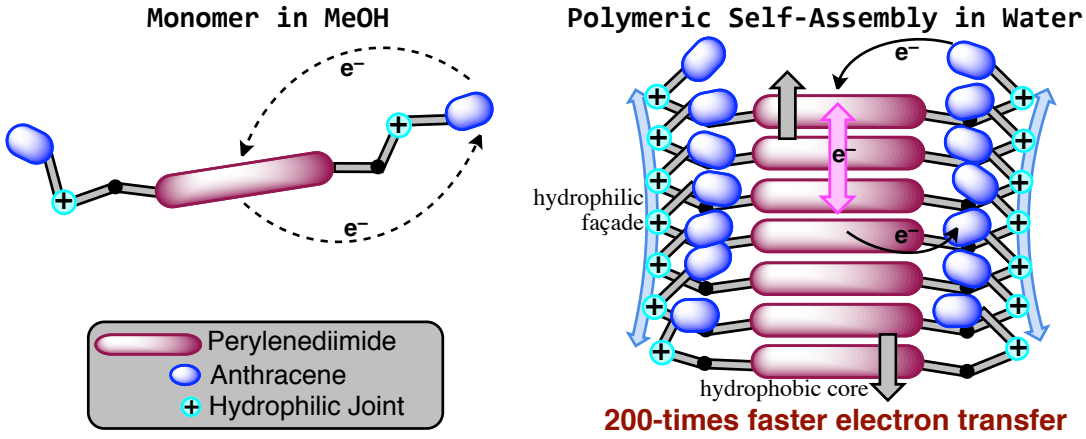
(49) Coskun, A.; Akkaya, E. U. *J. Am. Chem. Soc.* **2006**, *128*, 14474.

(50) Ziessel, R.; Alamiry, M. A. H.; Elliott, K. J.; Harriman, A. *Angew. Chem., Int. Ed.* **2009**, *48*, 2772.

(51) Guliyev, R.; Coskun, A.; Akkaya, E. U. *J. Am. Chem. Soc.* **2009**, *131*, 9007.

Chapter 4

Enhancement of Photodriven Charge Separation by Conformational and Intermolecular Adaptations of an Anthracene-Perylenediimide-Anthracene Triad to an Aqueous Environment



Abstract: Photoinduced electron-transfer dynamics of an electron donor-acceptor-donor triad, consisting of anthracenes and perylenediimide (An_2PDI) were investigated in different media by using time-resolved laser spectroscopic techniques. The aromatic components are attached by flexible linkers containing hydrophilic quaternary ammonium joints in the triad. In MeOH, in which An_2PDI dissolves completely, no electron-transfer products were observed in the transient absorption measurements after the excitation of anthracenes and PDI because of the rapid back electron transfer. The charge-separation rate of the triad in MeOH was estimated as 1.2×10^{10} s^{-1} from the quenching of the singlet-excited state of PDI. In contrast, the formation of electron-transfer products was evident in water and the electron-transfer rate was 200-times faster than the rate in MeOH in the course of the excitations of the selected components of An_2PDI (2.5×10^{12} s^{-1}). It is concluded from the time-resolved data that the conformational disposition of the hydrophilic joints due to hydrophilic–lipophilic interactions and the facile π-stacking of hydrophobic PDI cores in water result in the contraction and the relative rigidity of the electron-transfer distance, and the intermolecular stabilization of electron-transfer species within the polymeric self-assemblies of An_2PDI, enabling an efficient photodriven electron-transfer process to occur.

Introduction

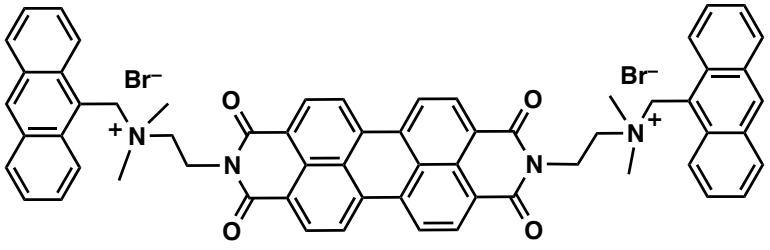
Local environments established by supramolecular organizations of protein subunits around the functional sites of photosystem II, such as light harvesting complexes, photosynthetic reaction center, and oxygen evolving complex, precisely control biophysical events and biochemical reactions (i.e., excitation energy transfer, charge separation, and water splitting) via weak interactions among the cofactors, amino acid residues, and lipid molecules.[1-5] Among these biological phenomena, charge separation realized at a high efficiency close to 100% quantum yield, a crucial way to convert solar energy into a chemical potential has been extensively studied in various photosynthetic reaction center models.[6-14] Although mimicking the natural stepwise electron-transfer mechanism in every aspect does not seem realistic for the current photovoltaic device fabrication due to synthetic and energetic considerations,[15-17] applications of non-covalent supramolecular arrangements of the natural lattice in the texture of the active layers of the organic photovoltaic cells can considerably improve the device efficiency.

Indeed, intermolecular order of π-conjugated molecular systems at nanoscale is proposed to control the morphology, which has a pivotal effect on the properties of electronic devices.[18-20] In this context, self-assemblies of perylenediimide (PDI) dyes have been investigated for various purposes.[21,22] PDI, capable of electron transport via its columnar π-stacks at nanoscale,[23] has been long considered as an effective electron acceptor material for organic photovoltaics.[24] The efficiencies of organic solar cells of PDIs with highly π-conjugated donors, however, leave much to be improved.[25] Strong electronic coupling at heterojunctions of PDIs and π-donors in the bulk, favoring the fast charge recombination, has been held responsible for the current efficiency values.[25,26]

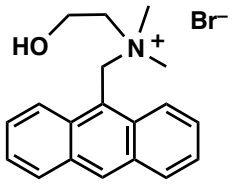
Previously, we have examined the photodynamics of the PDI nanoribbons in the presence of energy donors (zinc porphyrin with sulfonic groups and lucifer yellow CH dye) in two self-assembly models in aqueous media.[27] Ionic and π-π interactions were employed for the self-assembly of PDI stacks with the donor moieties in the presence of cationic surfactant. Although the photoinduced electron transfer from zinc porphyrin to PDI nanoribbons was feasible, no electron-transfer product was observed due to long distance, exceeding ca. 10 Å.

In this study, we examined the photoinduced electron-transfer dynamics of a triad, which consists of a PDI unit and two anthracenes (An_2PDI) in methanol (MeOH) and in water. As shown in Figure 1, triad and reference PDI bear hydrophilic components. Reference PDI undergoes π-stacking [$(TAIPDI)_n$] in water, resulting in one-dimensional nanostructures[28] without any other additional processes as described in the previous chapters. Moreover, the water facilitates the electron-transfer processes due to high polarity.[29] As to reference PDI, an aqueous medium contributes to self-assembly of triad yielding polymeric supramolecular structures. Hydrophobic components of the triad are attached by relatively long and loose alkyl linkers, carrying quaternary ammonium salts (Figure 1). Photoinduced charge separation in

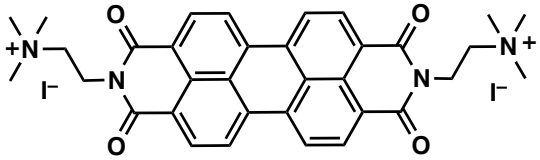
similar donor-PDI-donor[30,31] and donor-PDI[32,33] arrays was severed by uncontrollable geometric variations of long and flexible linkers in organic solvents. Such variations between PDI and some donor groups in the solution were remarkably limited by using sol-gel matrices immobilizing the molecules individually for more efficient electron transfer reactions.[34] In this triad, aromatic PDIs form strong π-stacks, allowing the electron migration via the intermolecular π-electron delocalization, while the positions of cationic sites are arranged by reasonable folding of linkers due to the hydrophilic–lipophilic interactions, resulting in a moderately rigid and proper distance for efficient charge separation in water.



An_2PDI



AnOH



PDI

Figure 1. Molecular structures of An_2PDI and the reference compounds.

Experimental Section

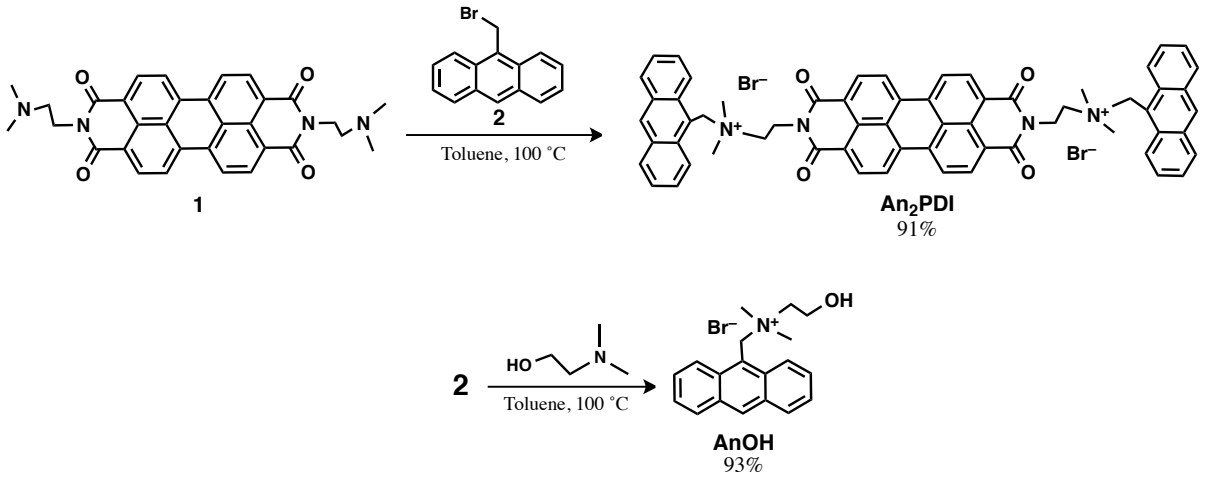
Synthesis. An_2PDI and the reference AnOH were prepared according to Scheme 1. Reference PDI was synthesized according to reported procedures.[35] Purification of water (18.2 MΩ cm) was performed with a Milli-Q system (Millipore, Direct-Q 3 UV).

Synthesis of An_2PDI. *N*,*N'*-di(ethylenedimethylamine)perylenediimide[35-38] (250 mg, 0.47 mmol, 1 equiv) and 9-bromomethylanthracene[39] (1.27 g, 4.7 mmol, 10 equiv) were added to 40 ml of toluene and heated under stirring to 100˚C overnight. After the mixture was cooled to room temperature, the precipitate was filtered and washed with benzene and THF, repeatedly. After drying, the solid was dissolved in high amount of water and filtered. Water was removed to yield the target compound as claret red solid (455 mg, 91%). ^{1}H NMR (DMSO) δ (ppm): 9.02 (d, 4H), 8.94 (s, 2H), 8.73 (d, 4 H), 8.66 (d, 2H), 8.23 (d, 4H), 7.73 (t, 4H), 7.62 (t, 4H), 5.79 (s, 4H), 4.64 (t, 4H), 4.15 (t, 4H), 3.06 (s, 12 H). IR (KBr) ν (cm^{-1}): 3050, 3021, 2360, 2341, 1691, 1650, 1592, 1578, 1479, 1440, 1402, 1365, 1340, 1252, 1157, 1045, 810, 747.

Synthesis of AnOH. 2-(dimetylamino)ethanol (3.3 g, 37 mmol, 10 equiv) was added to 9-bromomethylanthracene[39] (1.0 g, 3.7 mmol, 1 equiv) dissolved in toluene (40 ml) and heated

under stirring to 100˚C for 3 hours. The crude was filtered and washed with benzene and hexane, repeatedly. The obtained residue was dissolved in water and filtered. Water was removed to give the product as light yellow powder (1.24 g, 93%). ^{1}H NMR (D_2O) δ (ppm): 8.09 (s, 1H), 7.84 (d, 2H), 7.72 (d, 2H), 7.44 (t, 2H), 7.33 (t, 2H), 4.95 (s, 2H), 3.90 (t, 2H), 3.43 (t, 2H), 2.58 (s, 6H). IR (KBr) ν (cm^{-1}): 3327, 3052, 2024, 2915, 2360, 2340, 1627, 1525, 1468, 1260, 1085, 916, 808, 726.

Scheme 1. Synthesis of An_2PDI and Reference AnOH.



Instruments. Steady-state absorption measurements were recorded on a Hewlett Packard 8453 diode array spectrophotometer. Fluorescence measurements were carried out on a Shimadzu spectrofluorophotometer (RF-5300PC).

Fluorescence excitation spectra were obtained by a Hitachi model F-2500 fluorescence spectrophotometer at room temperature. Steady-state excitation anisotropy was assessed by changing the fluorescence detection polarization either parallel or perpendicular to the polarization of the excitation light. The excitation anisotropy spectra were calculated according to eq 1,

$$r = (E_{VV} - GE_{VH}) / (E_{VV} + 2GE_{VH}) \quad (1)$$

where E_{VV} (or E_{VH}) is the fluorescence excitation spectrum when the excitation light detected is the vertically (or horizontally) polarized portion of the fluorescence, denoting that the first and second subscripts represent excitation and detection polarization, respectively. The factor G is defined by E_{HV}/E_{HH}, which is equal to the ratio of the sensitivities of the detection system for vertically and horizontally polarized light.

Electrochemical measurements were performed on an ALS630B or ALS730D electrochemical analyzer in deaerated water containing 0.10 M Na_2SO_4 and in nitrobenzene containing 0.10 M $TBAPF_6$ as a supporting electrolyte. A conventional three-electrode cell was

used with a platinum working electrode (surface area of 0.3 mm^2) and a platinum wire as the counter electrode. The Pt working electrode was routinely polished with ALS polishing alumina suspension (0.05 μm) and rinsed with water and acetone before use. The measured potentials were recorded with respect to a saturated calomel electrode (SCE). All electrochemical measurements were carried out under an atmospheric pressure of N_2.

A time-correlated single-photon-counting (TCSPC) system was used for measurements of spontaneous fluorescence decay. As an excitation light source, we used a mode-locked Ti:sapphire laser (MaiTai BB, Spectra Physics) which provides ultrashort pulse (80 fs at full width half maximum, fwhm) with high repetition rate (80 MHz). This high repetition rate slows down to 1M ~ 800 kHz by using homemade pulse-picker. The pulse-picked output pulse was frequency-doubled by a 1 mm thickness of a BBO crystal (EKSMA). The fluorescence was collected by a microchannel plate photomultiplier (MCP-PMT, R3809U-51, Hamamatsu) with a thermoelectric cooler (C4878, Hamamatsu) connected to a TCSPC board (SPC-130, Becker & Hickel GmbH). The overall instrumental response function was about 25 ps (fwhm).

Femtosecond transient absorption spectroscopy experiments were conducted using an ultrafast source: Integra-C (Quantronix Corp.), an optical parametric amplifier: TOPAS (Light Conversion Ltd.) and a commercially available optical detection system: Helios provided by Ultrafast Systems LLC. The source for the pump and probe pulses was derived from the fundamental output of Integra-C (780 nm, 2 mJ per pulse and fwhm = 130 fs) at a repetition rate of 1 kHz. 75% of the fundamental output of the laser was introduced into TOPAS, which has optical frequency mixers resulting in a tunable range from 285 nm to 1660 nm, while the rest of the output was used for white light generation. Typically, 2500 excitation pulses were averaged for 5 seconds to obtain the transient spectrum at a set delay time. Kinetic traces at appropriate wavelengths were assembled from the time-resolved spectral data (see also Supporting Information). All measurements were conducted at 298 K.

The other instrumental setup that used for femtosecond transient absorption measurements: The femtosecond time-resolved transient absorption (TA) spectrometer consisted of Palitra (optical parametric amplifier (OPA), Quantronix) pumped by a Ti:sapphire regenerative amplifier system (Integra-C, Quantronix) operating at 1 kHz repetition rate and an optical detection system. The generated visible pulses by OPA had a pulse width of ~ 100 fs and an average power of 1-30 mW in the range 460-800 nm which were used as pump pulses. White light continuum (WLC) probe pulses were generated using a sapphire window (3 mm of thickness) by focusing of small portion of the fundamental 800 nm pulses which was picked off by a quartz plate before entering to the OPA. The time delay between pump and probe beams were carefully controlled by making the pump beam travel along a variable optical delay (ILS250, Newport). Intensities of the spectrally dispersed WLC probe pulses are monitored by miniature spectrograph (USB2000+, OceanOptics). To obtain the time-resolved transient absorption difference signal (ΔA) at a specific time, the pump pulses were chopped at 25 Hz and absorption spectra intensities were saved alternately with or without pump pulse.

Typically, 6000 pulses excite samples to obtain the TA spectra at a particular delay time. The polarization angle between pump and probe beam was set at the magic angle (54.7°) using a Glan-laser polarizer with a half-wave retarder in order to prevent polarization-dependent signals. Cross-correlation fwhm in pump-probe experiments was less than 200 fs and chirp of WLC probe pulses was measured to be 800 fs in the 400-800 nm region. To minimize chirp, all reflection optics in probe beam path and 2 mm path length of quartz cell were used. After fluorescence and TA experiments, we carefully checked absorption spectra of all compounds to avoid artifact from degradation and photooxidation of samples.

For nanosecond transient absorption measurements, deaerated solutions of the compounds were excited with a Panther optical parametric oscillator (OPO) equipped with a Nd:YAG laser (Continuum, SLII-10, fwhm = 4-6 ns) with a power of 10-15 mJ per pulse. The photochemical reactions were monitored by continuous exposure to a Xe lamp (150 W) as a probe light and a detector (SpectraPro 300i). The transient spectra were recorded using fresh solutions in each laser excitation. Solutions were deoxygenated by N_2 purging for about 15 min prior to the transient spectral measurements.

Results and Discussion

Synthesis. Preparation of An_2PDI and the reference AnOH was carried out as shown in Scheme 1. Quaternization of trialkylamino substituents of PDIs with alkyl halides was achieved with high yields in many studies.[35-38] An_2PDI was obtained from precursor **1**[35] by the addition of precursor **2**[39] in toluene. Precursor **2** was also quaternized in the presence of 2-(dimetylamino)ethanol to give water-soluble AnOH reference compound in a high yield under the same conditions as the former bis-quaternization reaction. While the precursors were hydrophobic, the products were hydrophilic due to the presence of ammonium salts. This difference was quite useful for the purification of the products (see the experimental experimental section).

Steady-State Spectral Features of An_2PDI in MeOH and Water. Reference PDI[28] and An_2PDI show similar absorption spectra in the visible region, showing that An_2PDI dissolves thoroughly in MeOH, while it forms polymeric self-assemblies in water (Figure 2). Comparing with those of PDI reference, a small red shift from 501 to 503 nm in water reflects some disturbance from regular stacking behavior of PDIs due to the presence of anthracene moieties in the triad.[40] In MeOH, on the other hand, no significant spectral shift in the absorption of PDI unit due to aggregation was observed even at very high concentrations (Figure 3). Reference AnOH has peaks at 355, 372, and 392 nm in MeOH and in water. Anthracene moieties of the triad show only 1 nm red shift in all peaks in MeOH whereas significant red shifts to 364, 376, and 395 nm are noted in an aqueous medium. This may be reasoned from the partial stacking of anthracenes on the periphery of tight PDI stacks.

Photoinduced events of An_2PDI triad have been probed by using fluorescence spectroscopy. After the triad is excited at 355 nm, 95% of the fluorescence emission of anthracenes [($^1An^*)_2PDI$] is quenched in MeOH while a weak emission originating from PDI moiety ($An_2{}^1PDI^*$) appears at 545 nm due to an inefficient energy transfer process from

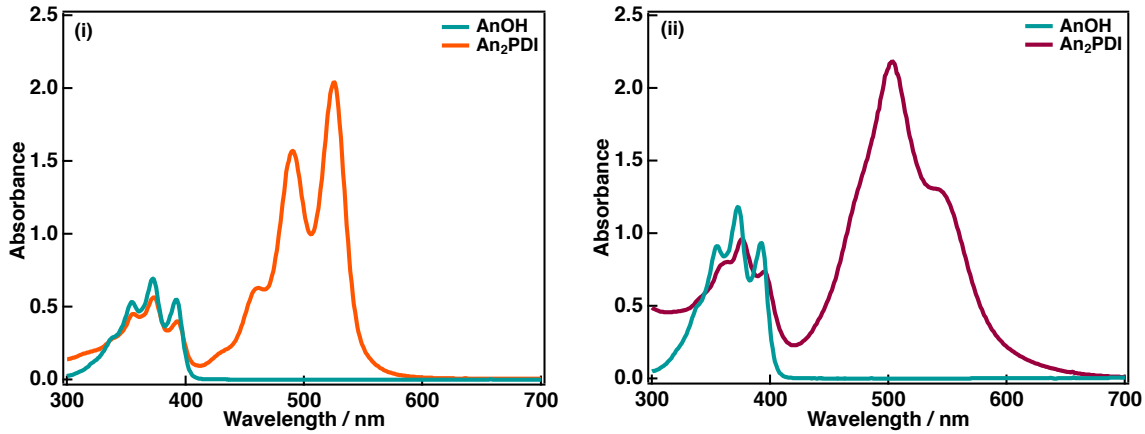


Figure 2. Steady-state absorption spectra of An_2PDI and AnOH (i) in MeOH and (ii) in water.

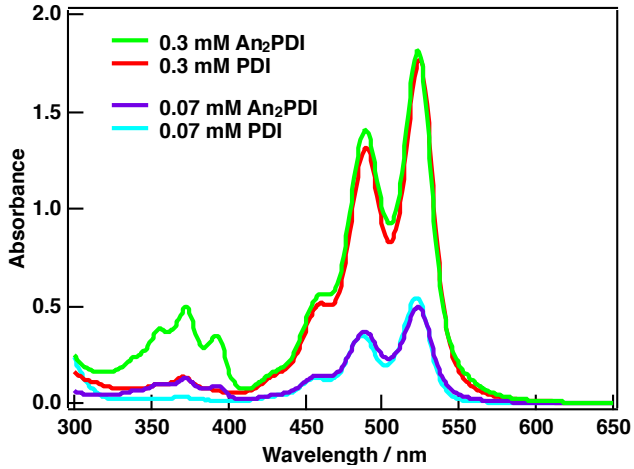


Figure 3. Steady-state absorption spectra of An_2PDI and PDI in MeOH at indicated concentrations. 2 mm-thick cells were used to obtain the spectra.

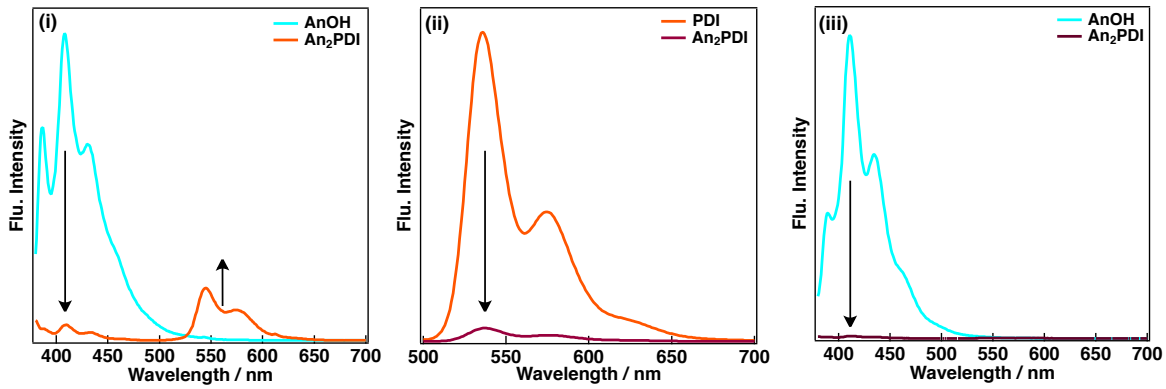


Figure 4. Steady-state emission spectra of An_2PDI, PDI, and AnOH: (i) excitation at 355 nm in MeOH, (ii) excitation at 490 nm in MeOH, and (iii) excitation at 355 nm in water.

anthracene to PDI (Figure 4). Besides this process, photoinduced electron transfer from anthracene to PDI is responsible for the marked quenching. In the case of excitation given at 490 nm in MeOH, fluorescence emission of PDI ($An_2{}^1PDI^*$) is also predominantly ceased. Energy transfer from PDI to anthracene is thermodynamically prohibited; therefore, such quenching is most likely to result from photodriven electron-transfer. In both cases, aggregation does not involve the emission quenching in MeOH as evidenced by the absorption spectra.

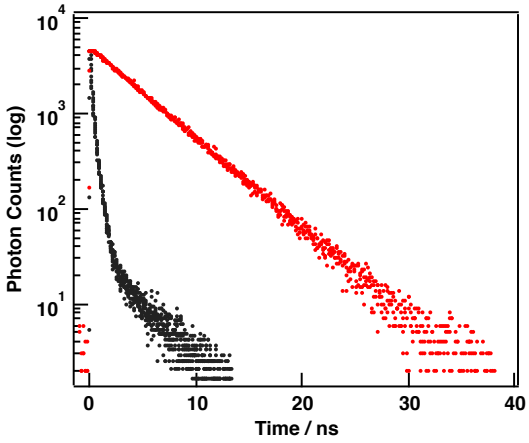


Figure 5. Fluorescence decay profile of PDI (red) and An_2PDI (black) in MeOH (λ_{exc} = 390 nm).

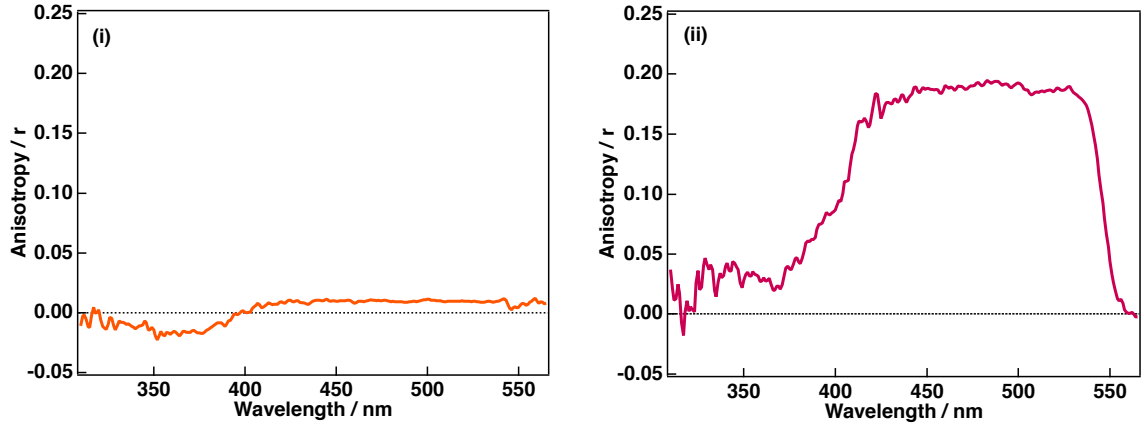


Figure 6. Steady-state fluorescence excitation anisotropy spectra of An_2PDI (i) in MeOH and (ii) in water.

Quenching in MeOH was also examined by fluorescence lifetime measurements. The fluorescence lifetime of the PDI reference is estimated to be 4.5 ns (Figure 5). Laser excitation at 390 nm afforded the fluorescence lifetime of the triad as 150 ps. In water, the quenching of the $({}^1An^*)_2PDI$ was more evident when it was excited at 355 nm because of a potential electron-transfer mechanism (Figure 4). Partial aggregation of the anthracene moieties around the PDI stacks is less likely to associate with such a distinct quenching. Stacking of An_2PDI molecules in water was confirmed by the fluorescence excitation anisotropy measurements.

Compared to that of the monomer triad in MeOH, anisotropy was markedly increased in water probably due to intermolecular order of the triads in a definite dimension (Figure 6).

Energetics of Photoinduced Electron Transfer in An_2PDI in Organic and in Aqueous Media. The free energy values for photoinduced charge separation (ΔG_{CS}) in An_2PDI triad in MeOH and in water have been calculated according to eq 2,[41]

$$\Delta G_{CS} = e(E_{ox} - E_{red}) - \Delta E_S + \Delta G_s \qquad (2)$$

where E_{ox} is the first one-electron oxidation potential of anthracenes, E_{red} is the first one-electron reduction potential of PDI, ΔE_S is the lowest singlet-excited state energy of anthracene or PDI, and ΔG_s is the static Coulomb energy.[42] Oxidation and reduction potentials were determined in organic and aqueous media containing 0.10 M $TBAPF_6$ and 0.10 M Na_2SO_4, respectively, by using differential pulse voltammetry (Figure 7) and the determined values are compiled in Table 1.

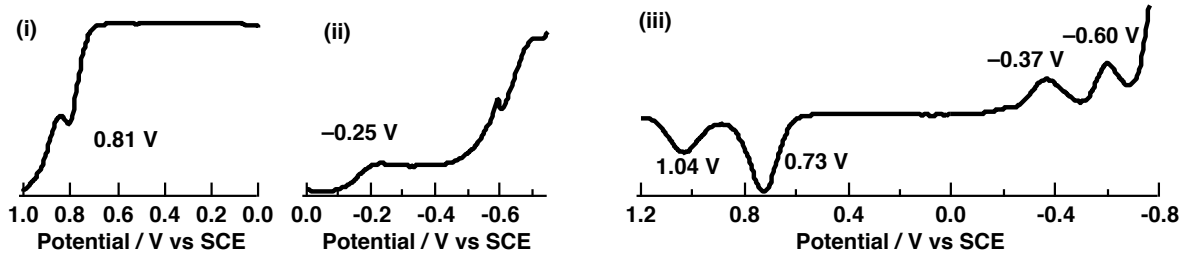


Figure 7. Differential pulse voltammogram of AnOH (i) and PDI (ii) in deaerated water containing 0.10 M Na_2SO_4 and An_2PDI (iii) in deaerated nitrobenzene containing 0.10 M $TBAPF_6$ (sweep rate: 0.1 mV/s).

Table 1. One-electron oxidation (E_{ox}) and reduction (E_{red}) potentials (V vs SCE) and free energy changes of the charge-separation ($-\Delta G_{CS}$ / eV) and charge-recombination ($-\Delta G_{CR}$ / eV) processes of the An_2PDI triad in organic and aqueous media.

solvent	E_{ox}	E_{red}	$-\Delta G_{CS}$ via ^{1}An*	$-\Delta G_{CS}$ via ^{1}PDI*	$-\Delta G_{CR}$
organic[a]	0.73	–0.37	2.12	1.29	1.05
water	0.81[b]	–0.25	2.13	1.27	1.05

[a] Because An_2PDI precipitates in the presence of supporting electrolyte in MeOH (ε = 33.6), nitrobenzene, having similar dielectric constant (ε = 35.7), was used as solvent.

[b] Because of the precipitation of the triad molecules in the presence of a supporting electrolyte in water, AnOH was used as reference to obtain the one-electron oxidation potential.

Proposed electron transfer from anthracenes to PDI can be driven by the singlet-excited states of the both components of the triad in both solvents. Depending on the ΔE_S values,

estimated from absorption and fluorescence emission of anthracene and PDI,[43] corresponding ΔG_{CS} and ΔG_{CR} values are collected in Table 1. Triplet-excited state energies of anthracene (1.77 eV)[44] and PDI (1.20 eV)[45] are sufficiently above the energy level of the charge-separated states in both media.

Excited-State Dynamics of Reference PDI in MeOH and in Water. The effect of π-stacking in water on the excited-state dynamics of reference PDI has been examined in comparison with those of its monomer in MeOH by using femtosecond transient absorption spectroscopy. As shown in Figure 8, the transient spectra of monomeric PDI in MeOH display

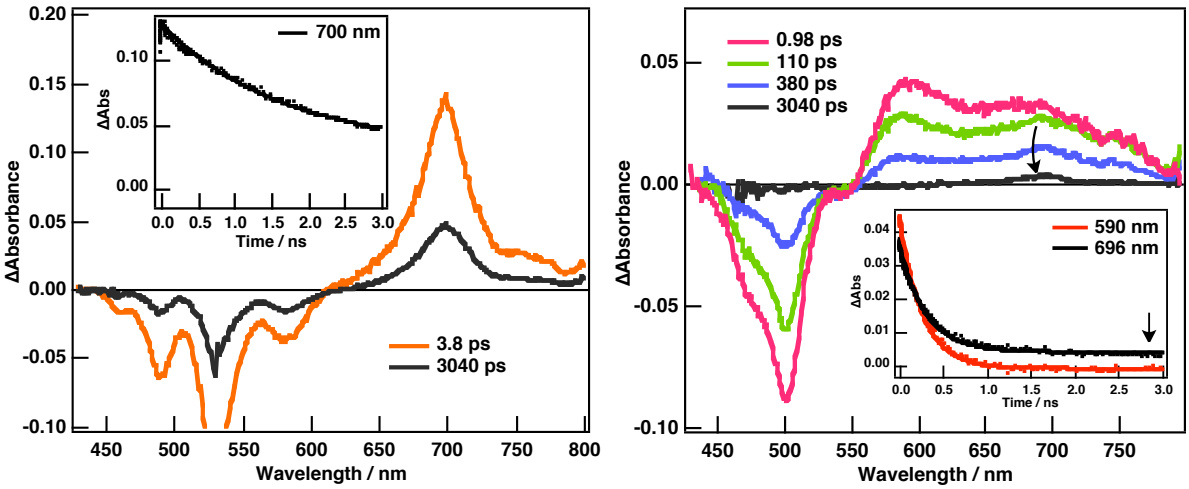


Figure 8. Femtosecond transient absorption spectra of 0.05 mM TAIPDI in MeOH (left) and in water (right) at indicated time delays (λ_{exc} = 390 nm). Insets: Time profiles at corresponding wavelengths.

mirror-imaged bleaching from 440 to 600 nm, which corresponds to ground state absorption and stimulated emission. The positive transient absorption centered at 700 nm is the attribute of singlet-excited states of PDI molecules. The lifetime of singlet-excited state was determined from time-resolved fluorescence measurements as 4.5 ns (Figure 5). All transient features and lifetime value are in agreement with the previously reported data.[46] On the other hand, PDI stacks (0.05 mM) in water reveal intense bleaching at 501 nm with a negative shoulder at 470 nm (Figure 8). Small negative absorption is also recognized at around 540 nm. These traits correspond to ground state absorption of PDI in water. Stimulated emission was not observed due to quenching. Besides, transient maxima at 590 nm and another absorption band centered at 696 nm emerge as broad positive features reaching to the end of spectral window. These traits are assigned to the singlet-excited states of $(PDI)_n$. As the time elapses, the peak at 590 nm decays faster than that at 696 nm and small positive signal at around 700 nm remains persistent. The decay profile at 590 nm affords a lifetime of 263 ps (3.8×10^9 s^{-1}), coinciding with that of bleaching at 501 nm (270 ps). 88% of the absorption band at 696 nm decays with a lifetime of 303 ps (3.3×10^9 s^{-1}) and 12% survives within the time course of the femtosecond

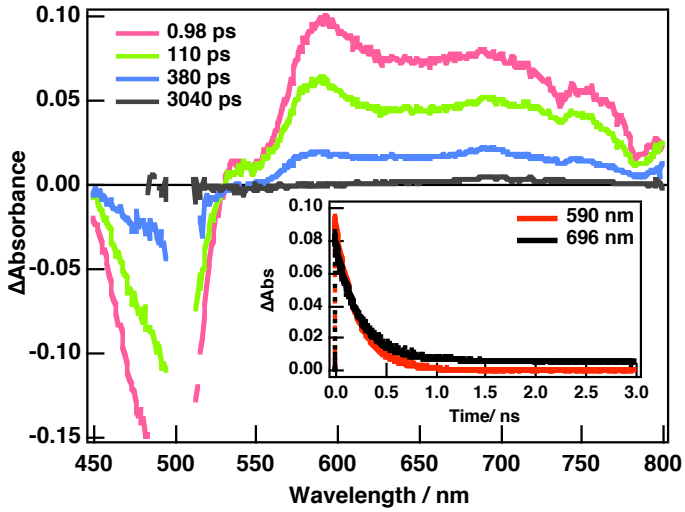


Figure 9. Femtosecond transient absorption spectra of 0.13 mM TAIPDI in water at indicated time delays (λ_{exc} = 390 nm). Inset: Time profiles at corresponding wavelengths.

measurements. At higher concentration (0.13 mM), the decays at 590 and 696 nm give a lifetimes of 220 ps (4.5×10^9 s^{-1}) and 235 ps (4.3×10^9 s^{-1}), respectively, shorter than former lifetime values (Figure 9). This time, 96% of the decay is completed at around 700 nm.

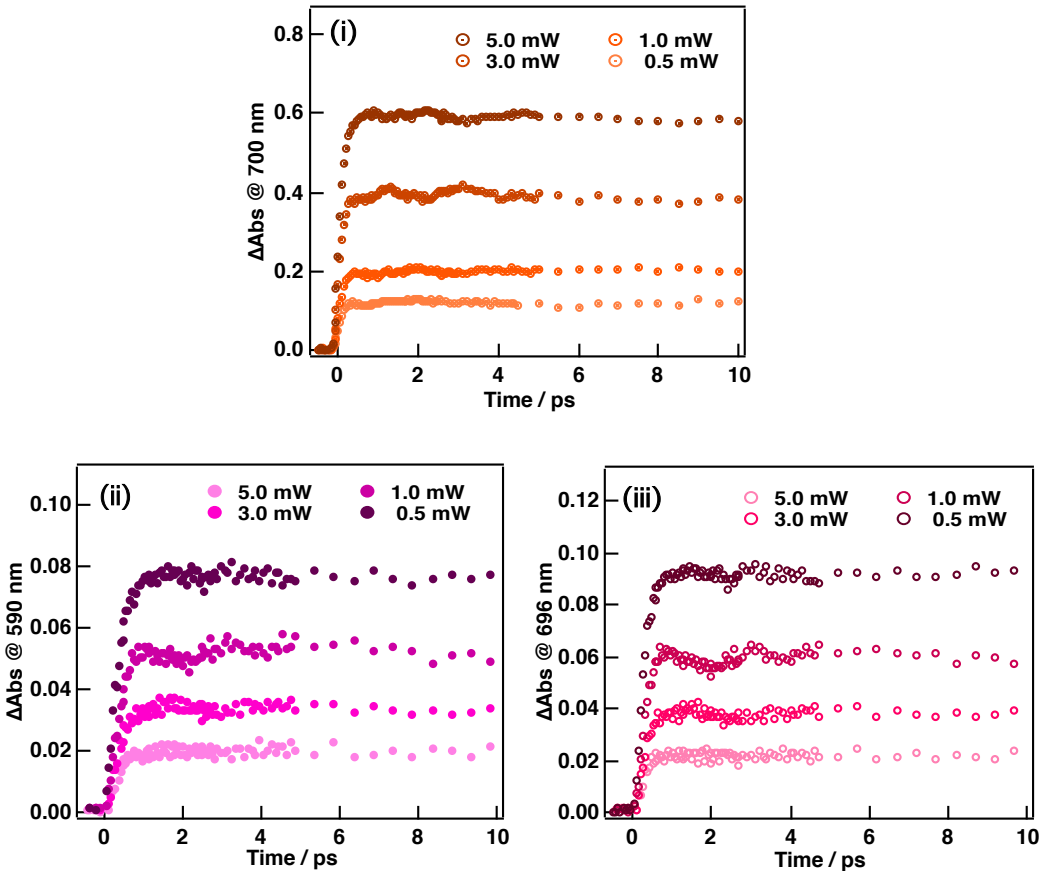


Figure 10. Time profiles of femtosecond transient absorption spectra of PDI reference at indicated wavelengths in MeOH (i), and in water (ii) and (iii), showing the excitation power dependence at the initial time domain.

Femtosecond transient absorption spectra of aggregates of reference PDI at early time delays have been also scrutinized in water in comparison with those of in MeOH. The formation of the excited states of PDI stacks are quite fast and exciton-exciton annihilation is not observed since the reference PDI, excited by femtosecond laser pulses in water, does not show excitation power dependence on the transient absorption decay profiles (Figure 10).[47]

The fluorescence lifetime measurements of reference PDI in water afford a lifetime of 5.0 ns, which is probably the trace of this remaining portion (Figure 11). The long-lived transient trait at around 700 nm seems like inheritance from unstacked TAIPDI present in water. In conclusion, the singlet-excited state lifetimes of PDI in water are concentration dependent. Although the lifetime values are shorter compared to their monomeric form, they seem still usable for supramolecular photoinduced processes.

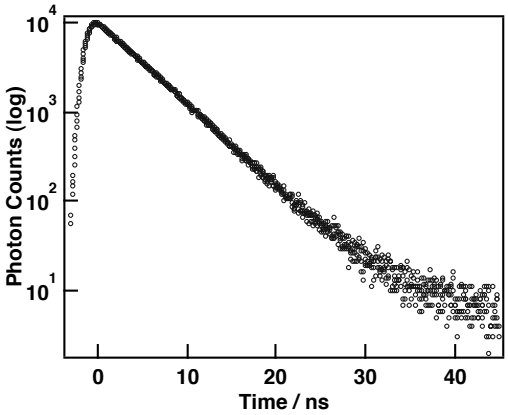


Figure 11. Fluorescence decay profile of reference PDI in water (λ_{exc} = 488 nm).

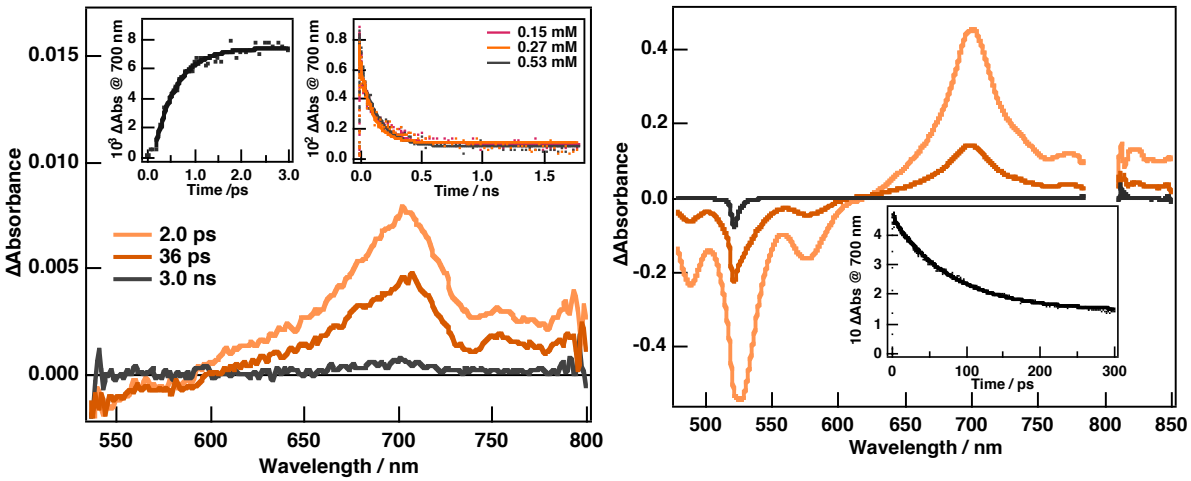


Figure 12. Femtosecond transient absorption spectra of An_2PDI in MeOH at indicated time delays. λ_{exc} = 390 (left) and 520 nm (right). Insets: Time profiles at 700 nm obtained at various concentrations.

Photoinduced Electron-Transfer Dynamics of An_2PDI in MeOH. The photoinduced processes taking place in the triad have been monitored by using femtosecond and nanosecond

transient absorption spectroscopy. In Figure 12, the femtosecond absorption transient spectra of An_2PDI show excited state absorption peak at 700 nm with bleaching around 550 nm after a laser excitation at 390 nm. These transient spectra match quite well with those of the singlet-excited states of PDI, indicating an energy transfer from anthracene to PDI.[46,48] From the rise in absorbance at 700 nm the rate of energy transfer is estimated as 2.1×10^{12} s^{-1} (Figure 12, inset). Similarly, excitation of An_2PDI at 520 nm also results in the spectral features of the singlet-excited state of the PDI reference (Figure 12). The decay profiles of absorbance at 700 nm, however, reveal that the lifetime of the singlet-excited state of PDI moiety (τ_S) is remarkably reduced in both cases (Figure 12, insets). The τ_S values were determined to be 110 ps and 81 ps after the excitations from 390 and 520 nm, respectively.

There was no transient signal to be assigned to electron-transfer products (i.e., the radical ion pair) probably because of rapid back electron transfer judging from the ΔG_{CR} value, which may be at the Marcus top region.[49,50] In addition, small concentrations of the radical anion and cation at the steady state with rapid back electron transfer may be hidden under the intense transient absorption of $An_2{}^1PDI^*$.[51-53] In such a case, the rate of charge separation can be estimated from the quenching of the singlet-excited states of PDI by using eq 3,[34,54]

$$k_{CS} = (1/\tau_q) - k_S \qquad (3)$$

where τ_q is the lifetime of the quenched singlet excite state due to photoinduced electron transfer and k_S is the rate constant of the singlet-excited state without any quenching. Thus, the k_{CS} values are calculated as 8.9×10^9 s^{-1} (113 ps) and 1.2×10^{10} s^{-1} (83 ps) after the excitations of anthracenes and PDI in the triad, respectively. Energy transfer apparently has an effect on different k_{CS} values.

An_2PDI did not reveal any transient spectra in the nanosecond transient absorption measurements after the excitation of anthracene and PDI to assign for charge

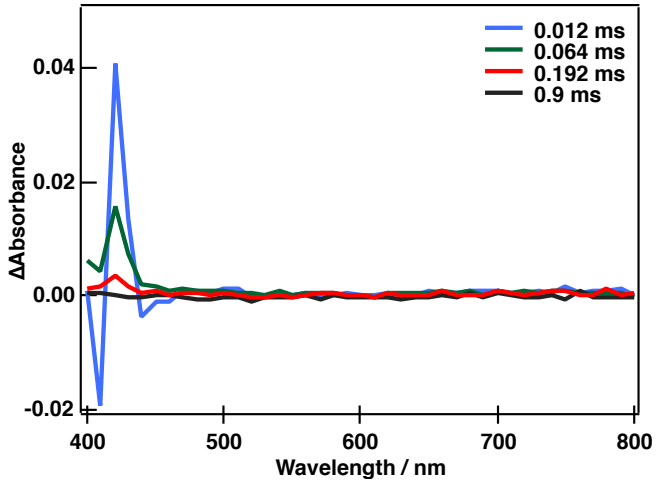


Figure 13. Nanosecond transient absorption spectra of AnOH in MeOH at indicated time delays (λ_{exc} = 355 nm).

separation or triplet-excited states (Figure 13). Fast singlet-singlet energy transfer most probablyimpedes the population of the triplet states of anthracene. Intersystem crossing of PDI is extremely inefficient[46] and population of $An_2{}^3PDI^*$ via the charge recombination is energetically unfeasible because the energy level of the $An_2{}^3PDI^*$ is above that of the charge separated state (Table 1).

Photoinduced Electron-Transfer Dynamics of An_2PDI in Water. In contrast to the results in MeOH, the femtosecond transient spectra of An_2PDI triad in water displayed very fast formation of broad transient absorption around 730 and 980 nm after an excitation at 390 nm (Figure 14). Together with the shoulder appearing around 695 nm, which can be assigned

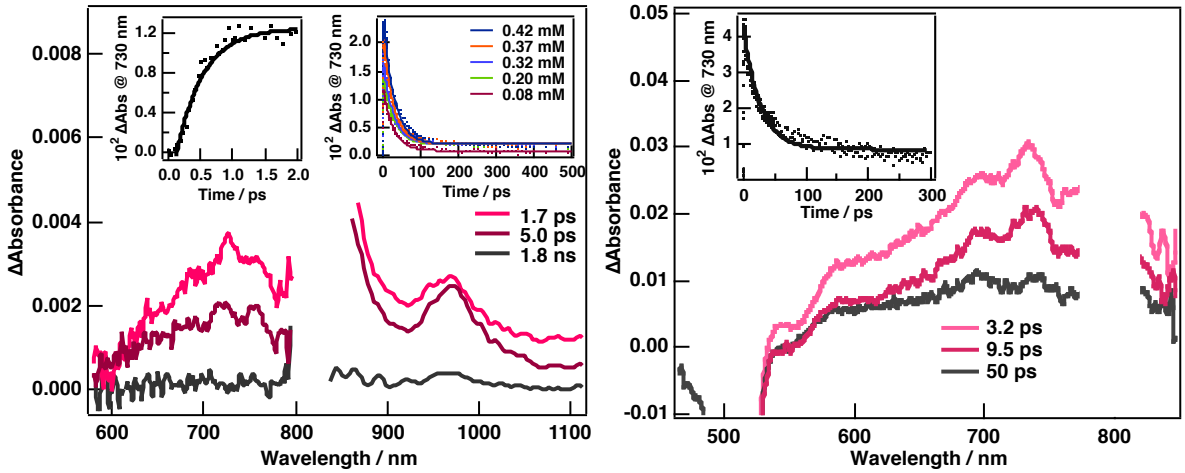


Figure 14. Femtosecond transient absorption spectra of An_2PDI in water at indicated time delays. λ_{exc} = 390 (left) and 520 nm (right). Insets: Time profiles at 700 nm obtained at various concentrations.

to the radical cation of anthracene,[53] these transient features agree well with those of the radical anion of $(PDI)_n$,[52] providing a solid proof of photoinduced electron transfer from anthracene to PDI stacks in water. It should be noted that the radical anion of monomer PDI has the absorption maxima at 716 and 960 nm. Formation of radical anion of $(PDI)_n$ [$(PDI)_n^{\bullet-}$] denotes the stabilization of the transferred electron realized within the stacks of PDI moieties. From the rise at 730 nm, the rate of charge separation (k_{CS}) is estimated to be 2.5×10^{12} s^{-1} (0.53 ps). The excitation of PDI moieties of the triad at 520 nm also results in the fast formation of the same transient patterns obtained in Figure 13 (2.6×10^{12} s^{-1}), which are also assigned to the charge separation (Figure 14).

Such fast charge separation processes were reported in the self-assembly systems, in which the donors with large π-extents were strongly coupled with the columnar PDI stacks via π-π interactions in aqueous media[55] and also in the covalently-attached donor-acceptor systems of PDI, in which the donors were closely positioned to the PDI by short and rigid linkers.[56] In the present case, there was no evidence for extensive π-π interactions between anthracenes and PDIs in the steady-state absorption spectrum (Figure 2). Then, it can be concluded that the

anthracene moieties and the PDI stacks are disposed in a sufficiently close manner as a result of a conformational arrangement in water, as described in Figure 15. π-Stacked PDIs construct

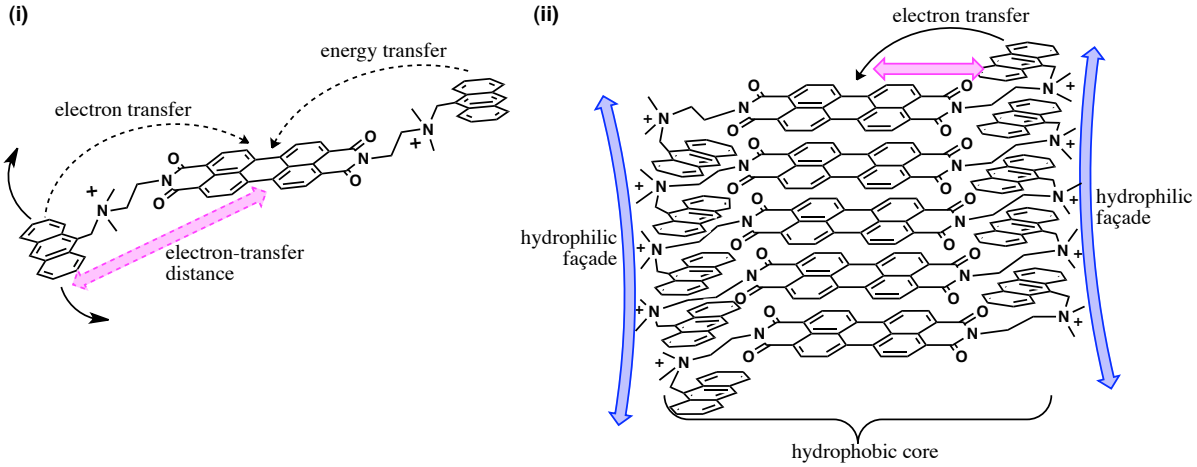


Figure 15. Comparison of the photoinduced processes of An_2PDI triad with electron-transfer distances in MeOH (i) and in water (ii) and illustration of its conformational arrangements and intermolecular stacking.

local hydrophobic domains together with the alkyl linkers, excluding the hydrophilic ammonium joints. These cationic parts remove from these hydrophobic assemblies to contact with the outer aqueous environment, thereby making the triad aggregates solubilized. Meanwhile, hydrophobic anthracene moieties are placed within the alkyl bulk around the aromatic PDI stacks. Such hydrophilic–lipophilic relocations prompt the folding of the flexible linkers to some extent. Inserted anthracenes are partially stacked within the alkyl bulk as understood from the red shift in the absorption spectrum (Figure 2). Thus, the stacking and the folding establish a moderately rigid and short electron-transfer distance in favor of fast charge separation in the assemblies of the triads in water while the electron-transfer process suffers from geometric variations of the long linkers and the competing energy transfer process in MeOH.

Lifetime of charge-separated state (τ_{CS}) in water is evaluated as 3.3×10^{10} s^{-1} (30 ps) from the time profiles at 730 nm (Figure 14, insets). Although the radical anion is stabilized by the PDI stacks as recognized from the formation of $(PDI)_n^{\bullet-}$ in the transient spectra, electron migration along the stacks does not seem extensive because of the short lifetime value. The same τ_{CS} values are observed at varying concentrations, implying that the transferred electron is delocalized on only a few PDIs. The τ_{CS} value of the triad is comparable to that of the molecular systems of PDI exhibiting no stacking in the solution.[56,57] In the present study, transferred electron and hole can easily recombine along the row of adjacent acceptor and donor groups, thereby impeding the extensive electron transport throughout the PDI stacks. Also, there was no sign for hole hopping among the anthracenes. An_2PDI triad did not display meaningful transient signal in the nanosecond transient measurements during the excitations of

both components to assign to formation of radical ion pair or triplet-excited states of the triad. Thus, long-range electron migration can be achieved by limiting the number of donors against the PDI stacks in a self-assembly system.

Conclusion

Photoinduced events of a newly synthesized An_2PDI triad in organic and in aqueous media have been investigated. Bearing both hydrophobic and hydrophilic sections, triad molecules can modify themselves to aqueous environment by conformational and intermolecular rearrangements, which greatly enhance the photoinduced charge separation. On the other hand, photoinduced electron transfer is not efficient against the geometric alterations, reasonably long electron-transfer distance, and competing energy transfer in MeOH, in which An_2PDI lacks such organizational behaviors.

References and Notes

(1) Minagawa, J.; Takahashi, Y. *Photosyn. Res.* **2004**, *84*, 241.

(2) Nelson, N.; Yocum, C. F. *Annu. Rev. Plant Biol.* **2006**, *57*, 521.

(3) Bricker, T. M.; Roose, J. L.; Fagerlund, R. D.; Frankel, L. K.; Eaton-Rye, J. J. *Biochim. Biophys. Acta* **2012**, *1817*, 121.

(4) Mizusawa, N.; Wada, H. *Biochim. Biophys. Acta* **2012**, *1817*, 194.

(5) Frankel, L. K.; Sallans, L.; Limbach, P. A.; Bricker, T. M. *PLoS ONE* **2013**, *8*, e58042. doi:10.1371/journal.pone.0058042

(6) Wasielewski, M. R. *Chem. Rev.* **1992**, *92*, 435.

(7) Gust, D.; Moore, T. A.; Moore, A. L. *Acc. Chem. Res.* **2001**, *34*, 40.

(8) Martín, N.; Sánchez, L.; Herranz, M. Á.; Illescas, B.; Guldi, D. M. *Acc. Chem. Res*. **2007**, *40*, 1015.

(9) Wasielewski, M. R. *Acc. Chem. Res*. **2009**, *42*, 1910.

(10) Fukuzumi, S.; Honda, H.; Ohkubo, K.; Kojima, T. *Dalton Trans*. **2009**, 3880.

(11) Bottari, G.; de la Torre, G.; Guldi, D. M.; Torres, T. *Chem. Rev*. **2010**, *110*, 6768.

(12) Fukuzumi, S.; Ohkubo, K. *J. Mater. Chem*. **2012**, *22*, 4575.

(13) D'Souza, F.; Ito, O. *Chem. Soc. Rev*. **2012**, *41*, 86.

(14) D'Souza, F.; Amin, A. N.; El-Khouly, M. E.; Subbaiyan, N. K.; Zandler, M. E.; Fukuzumi, S. *J. Am. Chem. Soc*. **2012**, *134*, 654–664.

(15) Fukuzumi, S. *Phys. Chem. Chem. Phys.* **2008**, *10*, 2283.

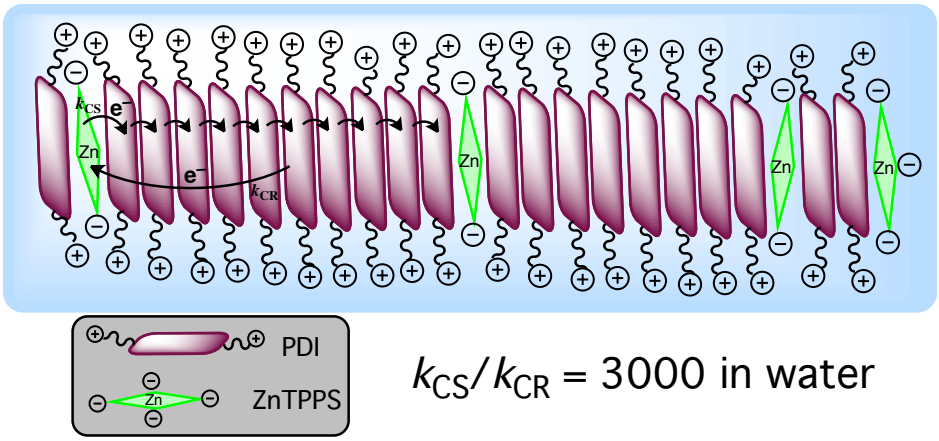
(16) Bakulin, A. A.; Rao, A.; Pavelyev, V. G.; van Loosdrecht, P. H. M.; Pshenichinikov, M. S.; Niedzialek, D.; Cornil, J.; Beljonne, D.; Friend, R. H. *Science* **2012**, *335*, 1340.

(17) Lightcap, I. V.; Kamat, P. V. *Acc. Chem. Res*. **2013**, *46*, in press DOI: 10.1021/ar300248f.
(18) Zhao, Y. S.; Fu, H.; Peng, A.; Ma, Y.; Xiao, D.; Yao, J. *Adv. Mater.* **2008**, *20*, 2859.
(19) Kim, F. S.; Ren, G.; Jenekhe, S. A. *Chem. Mater.* **2011**, *23*, 682.
(20) Wang, M.; Wudl, F. *J. Mater. Chem.* **2012**, *22*, 24297.
(21) Aida, T.; Meijer, E. W.; Stupp, S. I. *Science* **2012**, *335*, 813.
(22) Zang, L.; Che, Y.; Moore, J. S. *Acc. Chem. Res.* **2008**, *41*, 1596.
(23) Che, Y.; Datar, A.; Yang, X.; Naddo, T.; Zhao, J.; Zang, L. *J. Am. Chem. Soc.* **2007**, *129*, 6354.
(24) Schmidt-Mende, L.; Fechtenkötter, A.; Müllen, K.; Moons, E.; Friend, R. H.; MacKenzie, J. D. *Science* **2001**, *293*, 1119.
(25) Howard, I. A.; Laquai, F.; Keivanidis, P. E.; Friend, R. H.; Greenham, N. C. *J. Phys. Chem. C* **2009**, *113*, 21225.
(26) Pensack, R. D.; Guo, C.; Vakhshouri, K.; Gomez, E. D.; Asbury, J. B. *J. Phys. Chem. C* **2012**, *116*, 4824.
(27) Supur, M.; Yamada, Y.; Fukuzumi, S. *J. Mater. Chem.* **2012**, *22*, 12547.
(28) Huang, Y.; Quan, B.; Wei, Z.; Liu, G.; Sun, L. *J. Phys. Chem. C* **2009**, *113*, 3929.
(29) Kavarnos, G. J.; Turro, N. J. *Chem. Rev.* **1986**, *86*, 401.
(30) Zhang, R.; Wu, Y.; Wang, Z.; Xue, W.; Fu, H.; Yao, J. *J. Phys. Chem. C* **2009**, *113*, 2594.
(31) Ando, S.; Ramanan, C.; Facchetti, A.; Wasielewski, M. R.; Marks, T. J. *J. Mater. Chem.* **2011**, *21*, 19049.
(32) Körzdörfer, T.; Tretiak, S.; Kümmel, S. *J. Chem. Phys.* **2009**, *131*, 034310.
(33) El-Khouly, M. E.; Choi, D. H.; Fukuzumi, S. *J. Photochem. Photobiol. A* **2011**, *218*, 17.
(34) Karapire, C.; Zafer, C.; Icli, S. *Synth. Met.* **2004**, *145*, 51.
(35) Biedermann, F.; Elmalem, E.; Ghosh, I.; Nau, W. M.; Scherman, O. A. *Angew. Chem., Int. Ed.* **2012**, *51*, 7739.
(36) Deligeorgiev, T.; Zaneva, D.; Petkov, I.; Timcheva, Il.; Sabnis, R. *Dyes Pigments* **1994**, *24*, 75.
(37) Wang, B.; Yu, C. *Angew. Chem., Int. Ed.* **2010**, *49*, 1485.
(38) Reilly III, T. H.; Hains, A. W.; Chen, H.-Y.; Gregg, B. A. *Adv. Energy Mater.* **2012**, *2*, 455.
(39) Lan, P.; Berta, D.; Porco, Jr., J. A.; South, M. S.; Parlow, J. J. *J. Org. Chem.* **2003**, *68*, 9678.
(40) Molar extinction coefficient (ε) of maximum of An_2PDI (0.054 mM) at 503 nm is 3.7×10^4 M^{-1} cm^{-1} in water, which is the same value as PDI reference at 501 nm. See chapter 5.

(41) Weller, A. *Z. Phys. Chem.* **1982**, *133*, 93.
(42) Because electron-transfer products are assumed as solvent-separated ion pair, ΔG_s is calculated by using this correlation: ΔG_s (eV) = 0.56 (1/ε) + 0.003, where ε is the dielectric constant of the solvent. See: Arnold, B. R.; Farid, S.; Goodman, J. L.; Gould, I. R. *J. Am. Chem. Soc.* **1996**, *118*, 5482.
(43) Fukuzumi, S.; Amasaki, I.; Ohkubo, K.; Gros, C. P.; Guilard, R.; Barbe, J.-M. *RSC Adv.* **2012**, *2*, 3741.
(44) See chapter 6.
(45) Fukuzumi, S.; Ohkubo, K.; Ortiz, J.; Gutierrez, A. M.; Fernandez-Lazaro, F.; Sastre-Santos, A. *J. Phys. Chem. A* **2008**, *112*, 10744.
(46) (a) Danilov, E. O.; Rachford, A. A.; Goeb, S.; Castellano, F. N. *J. Phys. Chem. A* **2009**, *113*, 5763. (b) Würthner, F. *Chem. Commun.* **2004**, 1564.
(47) Lim, J. M.; Kim, P.; Yoon, M.-C.; Sung, J.; Dehm, V.; Chen, Z.; Würthner, F.; Kim, D. *Chem. Sci.* **2013**, *4*, 388-397.
(48) Reference AnOH did not display any transient trait in the same spectral window in the femtosecond transient absorption measurements.
(49) Marcus, R. A.; Sutin, N. *Biochim. Biophys. Acta* **1985**, *811*, 265.
(50) Kanematsu, M.; Naumov, P.; Kojima, T.; Fukuzumi, S. *Chem.–Eur. J.* **2011**, *17*, 12372.
(51) The PDI radical anion and the anthracene radical cation have absorption peaks at 716[52] and 695 nm,[53] respectively. Additionally, we could not observe the formation of PDI radical anion in the near-IR region in MeOH.
(52) Marcon, R. O.; Brochsztain, S. *J. Phys. Chem. A* **2009**, *113*, 1747.
(53) Shida, T. Electronic Absorption Spectra of Radical Ions, Elsevier, Amsterdam, 1988.
(54) Williams, R. M. *Turk. J. Chem.* **2009**, *33*, 727.
(55) See chapter 5 and 6.
(56) Supur, M.; El-Khouly, M. E.; Seok, J. H.; Kim, J. H.; Kay, K.-Y.; Fukuzumi, S. *J. Phys. Chem. C* **2010**, *114*, 10969-10977.
(57) Suzuki, S.; Kozaki, M.; Nozaki, K.; Okada, K. *J. Photochem. Photobiol. C* **2011**, *12*, 269.

Chapter 5

Photodriven Electron Transport within the Columnar Perylenediimide Nanostructures Self-Assembled with Sulfonated Porphyrins in Water



Abstract: Columnar stacks of *N,N'*-di(2-(trimethylammoniumiodide)ethylene) perylenediimide $(TAIPDI)_n$ can host *meso*-tetrakis(4-sulfonatophenyl)porphyrin zinc tetrapotassium salt ($ZnTPPSK_4$) molecules at different ratios through the ionic and π-π interactions prompted by an aqueous environment. Photoexcitation of this host-guest complex generates very fast charge separation (1.4×10^{12} s^{-1}). Charge recombination is markedly decelerated by a probable electron delocalization mechanism along the long range of tightly stacked TAIPDIs (4.6×10^{8} s^{-1}), giving an exceptional k_{CS}/k_{CR} ratio of 3000 as determined by using time-resolved transient absorption techniques.

Introduction

Charge separation is an essential process to convert solar energy into a chemical potential in the photosynthesis[1] and in the organic photovoltaic cells as well.[2] In the natural system, this process has been realized by utilizing a series of redox-active units meticulously aligned to transfer the electron to the next component until a distance to restrain the fast charge recombination is adequately reached. The charge separation distance between the primary electron donor, P680, and the electron-accepting plastoquinone Q_A ($P680^{\bullet+}Q_A^{\bullet-}$) in the photosynthetic reaction center of the cyanobacterial photosystem II is approximately 3.4 nm.[3] A number of photosynthetic reaction center mimicry have been so far developed,[4] extending the distances for charge separation up to 5.0 nm.[5] Assuming that such a distance is applicable for transporting the charge carriers (electron and hole) to the opposite electrodes in a solar cell, collecting the solar photons by a layer of this length will be insufficient because it is known that the active layers of current organic photovoltaic cells (bilayer or bulk heterojunction) require the thickness of at least 100 nm for efficient light harvesting if the organic materials, having high absorption coefficients (10^5 cm^{-1}), are used.[6,7] Taking the inevitable loss of the excitation energy at each step of electron transfer in natural and artificial systems into account,[4c] elongation of the charge separation distance by this strategy is not practical, because of the synthetic difficulties to fabricate multicomponent molecular arrays and additional light harvesting systems. Control of the molecular alignment of such complex systems at microscopic scale is another obstacle to deal with.

π-Conjugated polymers, on the other hand, have been extensively preferred for transporting the photogenerated charges throughout long distances within the active layer to obtain an electron flow.[8,9] Recently, Friend et al.[10] explained this long-range charge transport within the bulk heterojunction cells of such polymers through the presence of the charge delocalization. Delocalized states of π-electron systems were reported to enable the charges to override the Coulombic interactions and fast charge recombination, thereby enhancing the external quantum efficiencies. Extensive charge delocalization[11] and its effect on stabilizing the electron transfer products, i.e. radical cation and anion, against the charge recombination[12] have been investigated in dimer, oligomer, and polymer systems in solution.

In addition to π-delocalization, molecular orientation in one dimension at nanoscale is of importance to boost the device efficiency.[13] In this regard, the self-assemblies of perylenediimide (PDI) dyes, forming one-dimensional nanostructures, have drawn much attention.[14] An average length of PDI nanofibrils was reported to reach about 0.3 mm in a study,[15] exhibiting the effect of the strong π-π stacking in one dimension. Long axes of such molecular architectures of PDI exhibit electron hopping due to π-electron delocalization within the stacks when exposed to a reducing agent or n-dopant.[16] Electron migration in one dimension via π-delocalization can be accessed by light in the presence of photo-active electron donor.[17] There are only a few studies of one-dimensional self-assemblies of PDI,

examining the electron transport within the π-stacks.[18] Such self-assemblies were, however, mostly constructed in non-polar solvents.

In this study, the formation and the photo-initiated electron-transfer process of a self-assembly of *N*,*N'*-di(2-(trimethylammonium iodide)ethylene)perylenediimide (TAIPDI) and *meso*-tetrakis(4-sulfonatophenyl)porphyrin zinc tetrapotassium salt ($ZnTPPSK_4$) have been investigated in water, for the first time (Figure 1). An aqueous medium is of choice because it provokes the self-assembly of such highly extensive π-systems[19] without any other additional treatment, moreover, it facilitates the electron-transfer processes due to high polarity.[20] TAIPDI molecules undergo π-stacking [$(TAIPDI)_n$] in water, resulting in one-dimensional nanostructures.[21] Apart from solubilizing the TAIPDI stacks in water, cationic trimethylammonium heads also enhance the ionic interactions with water soluble $ZnTPPSK_4$, bearing anionic sulfonic groups. By this way, ionic interactions strongly support the hydrophobic interactions between the aromatic cores of TAIPDI and $ZnTPPSK_4$, thereby yielding robust and adjustable donor-acceptor self-assemblies, which seem suitable conduits for photodriven charge transport in an aqueous medium.

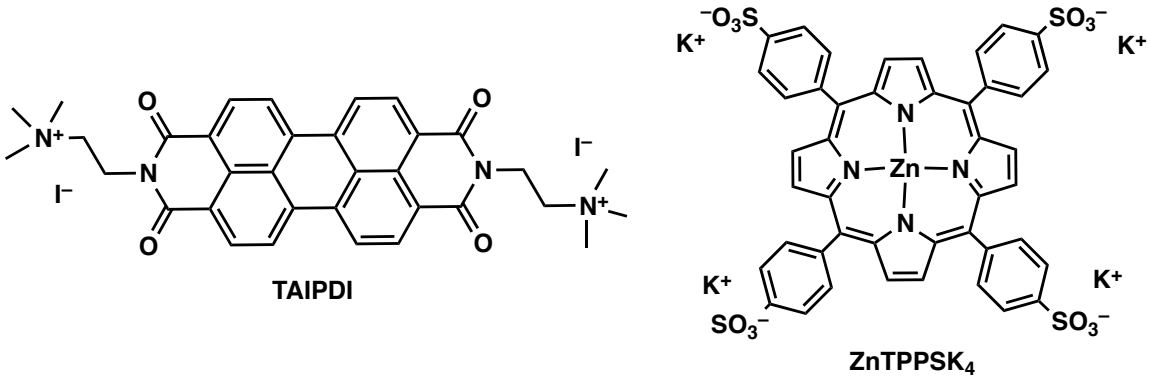


Figure 1. Molecular structures of the components used in this study.

Materials. *N*,*N'*-di(2-(trimethylammoniumiodide)ethylene)perylenediimide (TAIPDI) was synthesized according to reported procedures.[21,22] *Meso*-tetrakis(4-sulfonatophenyl)porphyrin zinc tetrapotassium salt ($ZnTPPSK_4$) was prepared from commercially available *meso*-tetrakis(4-sulfonatophenyl)porphyrin (TPPS).[23] Purification of water (18.2 MΩ cm) was performed with a Milli-Q system (Millipore, Direct-Q 3 UV).

Instruments. Steady-state absorption measurements were recorded on a Hewlett Packard 8453 diode array spectrophotometer. Fluorescence measurements were carried out on a Shimadzu spectrofluorophotometer (RF-5300PC). Measurements of emission quantum yields were carried out on a Hamamatsu C9920-0X(PMA-12) U6039-05 fluorescence spectrofluorometer with an integrating sphere adapted to a right angle configuration at room temperature. Dynamic light scattering (DLS) measurements were done by using a Zetasizer Nano S instrument (Malvern Instruments Ltd., Malvern, U.K.). The DLS instrument used in this work has a range between 0.6 and 6000 nm, therefore, any structures over this limit could

not be detected. Electrochemical measurements were performed on an ALS630B or ALS730D electrochemical analyzer in deaerated water containing 0.10 M Na_2SO_4 as supporting electrolyte. A conventional three-electrode cell was used with a platinum working electrode (surface area of 0.3 mm^2) and a platinum wire as the counter electrode. The Pt working electrode was routinely polished with ALS polishing alumina suspension (0.05 μm) and rinsed with water and acetone before use. The measured potentials were recorded with respect to a saturated calomel electrode (SCE). All electrochemical measurements were carried out under an atmospheric pressure of N_2. Scanning electron microscopy (SEM) images were taken on a JEOL FE-SEM JSM-6701F instrument operating at 5 kV. Femtosecond transient absorption spectroscopy experiments were conducted using an ultrafast source: Integra-C (Quantronix Corp.), an optical parametric amplifier: TOPAS (Light Conversion Ltd.) and a commercially available optical detection system: Helios provided by Ultrafast Systems LLC. The source for the pump and probe pulses was derived from the fundamental output of Integra-C (780 nm, 2 mJ per pulse and fwhm = 130 fs) at a repetition rate of 1 kHz. 75% of the fundamental output of the laser was introduced into TOPAS, which has optical frequency mixers resulting in a tunable range from 285 nm to 1660 nm, while the rest of the output was used for white light generation. Typically, 2500 excitation pulses were averaged for 5 seconds to obtain the transient spectrum at a set delay time. Kinetic traces at appropriate wavelengths were assembled from the time-resolved spectral data. All measurements were conducted at 298 K. For nanosecond transient absorption measurements, deaerated solutions of the compounds were excited with a Panther optical parametric oscillator (OPO) equipped with a Nd:YAG laser (Continuum, SLII-10, fwhm = 4-6 ns) with a power of 10-15 mJ per pulse. The photochemical reactions were monitored by continuous exposure to a Xe lamp (150 W) as a probe light and a detector (SpectraPro 300i). The transient spectra were recorded using fresh solutions in each laser excitation. Solutions were deoxygenated by N_2 purging for about 15 min prior to the all transient spectral measurements.

Results and Discussion

Characterization of TAIPDI in Solution and Solid State. TAIPDI dissolves in methanol (MeOH) as the representative 0-0, 0-1, 0-2, and 0-3 transitions of typical PDI are clearly observed at 522, 486, 457, and 429 nm, respectively (Figure 2). TAIPDI molecules, on the other hand, assembly into stacks in water via strong π-π interactions of hydrophobic aromatic cores. Solubilized by polar trimethylammonium heads in water, these π-stacks give absorption peaks at 537 and 501 nm with a shoulder around 470 nm. Due to high solubility of TAIPDI stacks in water, high absorption coefficients (ε = 37500 M^{-1} cm^{-1} for 0.02 mM at 501 nm) is observed, comparable to its monomer form (ε = 97200 M^{-1} cm^{-1} at 522 nm) in MeOH. In contrast, dispersed PDI aggregates usually have low absorption due to low solubility.[17,24] The 4-fold increase in concentration of TAIPDI causes 2 nm of red shift of the peak at 537 nm

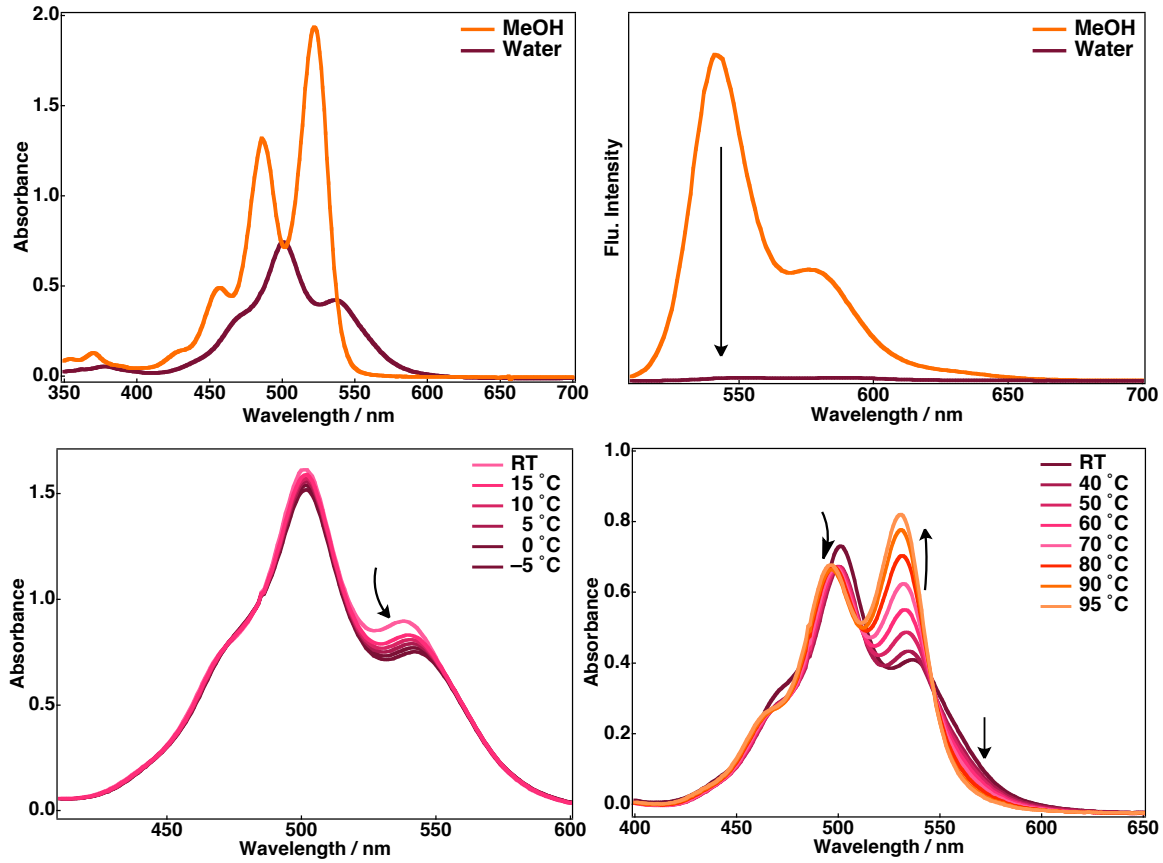


Figure 2. Upper panel: Steady-state absorption spectra of 0.02 mM TAIPDI (left) and emission spectra of 0.08 mM TAIPDI (right) in water and MeOH (λ_{exc} = 500 nm). Lower panel: Steady-state absorption spectra of TAIPDI upon cooling (left) and heating (right) in water.

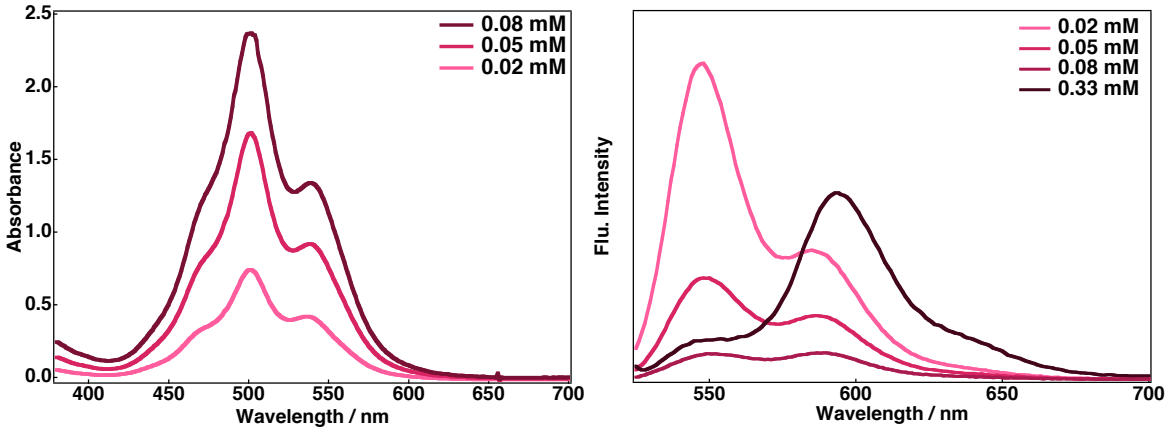


Figure 3. Steady-state absorption spectra (left) of TAIPDI and its emission spectra (right) at indicated concentrations in water (λ_{exc} = 520 nm). The emission at 0.33 mM has been magnified for clarification.

as shown in Figure 3. Temperature dependence of aggregation in water has also been tested (Figure 2). Cooling does not cause any shift at 501 nm; however, a meaningful red shift is

observed at 537 nm to 543 nm, which means the energy separation between two absorption peaks becomes greater. Thus, it can be concluded that high concentration or low temperature result in closer cofacial order of TAIPDI chromophores as the exciton coupling grows stronger.[25] The increase in the temperature causes apparent decomposition of aggregation as the vibrational transitions at 531 (0-0), 496 (0-1), and 465 nm (0-2) have been restored. Nonetheless, the lower ratio of 0-0 transition to 0-1 transition (1.21) in water at 95˚C than that in MeOH at room temperature (1.48) indicates that π-stacking is still present even at such a high temperature, emphasizing the effect of an aqueous environment on aromatic π-π interactions.[22]

Vibrationally resolved emission of TAIPDI in MeOH appears at 540 and 577 nm with high quantum efficiency. On the other hand, the fluorescence emission is drastically ceased by π-π electronic coupling in water (Figure 2 and Table 1).[26] Fluorescence quenching becomes notable as the concentration increases. Weak emission of TAIPDI stacks (0.02 mM) in water is detected at 548 and 585 nm, which are red shifted compared to that in MeOH. Emission spectrum of 0.33 mM of TAIPDI gives a maximum at 595 nm with a less intense peak at 549 nm, which in fact shows a reflection of its absorption spectrum in water (Figure 3). This mirror-imaged emission results from face-to-face arrangement of the TAIPDI molecules, whose transition dipoles are parallel.[27] Aggregation yields can be approximated from the emission quenching at different concentrations (Table 1).[28]

Table 1. Absolute fluorescence quantum yields (Φ_f) and aggregation yields of TAIPDI at different concentrations in water.

concentration	Φ_f	aggregation yield
0.02 mM[a]	0.059	0.92
0.05 mM	0.028	0.96
0.08 mM	0.014	0.98
0.15 mM	0.008	0.99

[a] Φ_f of 0.02 mM TAIPDI is 0.70 in MeOH.

The radical anion of TAIPDI stacks [$(TAIPDI)_n^{\bullet-}$], generated by using water soluble hydrazine as a strong electron donor, gives absorption at 730, 817, and 985 nm in water (Figure 4).[29] Compared to radical anion of monomer PDIs, the absorption spectra of $(TAIPDI)_n^{\bullet-}$ are broader and red shifted due to probable electron delocalization within the π-stacks of TAIPDI.[29,30] Such broadening has also been observed in the oligomeric self-assemblies of PDI.[31] $(TAIPDI)_n^{\bullet-}$ is quite stable in deaerated water for a few weeks. The size distribution of TAIPDI aggregates in water was examined by dynamic light scattering (DLS) measurements. The DLS diagram of TAIPDI aggregates reveals a size distribution ranging from 105 to 460 nm, with a mean size of 188 nm (Figure 5).[32]

The effect of π-stacking in water on the excited-state dynamics of TAIPDI was examined in comparison with those of its monomer in MeOH by using femtosecond transient absorption spectroscopy in chapter 4 (vide supra).

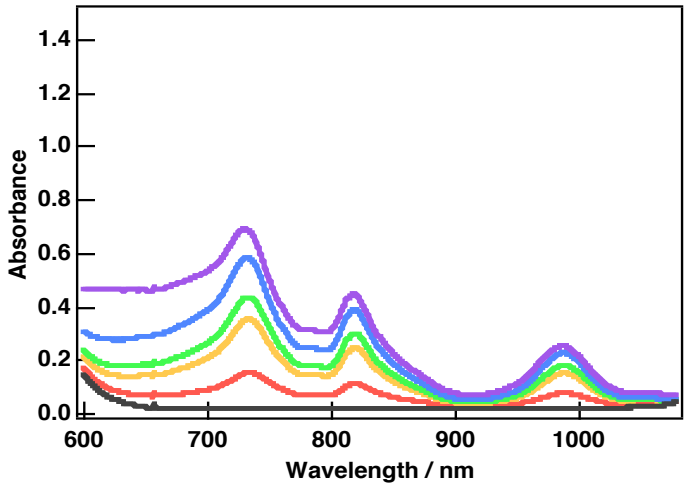


Figure 4. The absorption spectra of radical anion of TAIPDI stacks [$(TAIPDI)_n^{\bullet-}$], generated by using hydrazine in water.

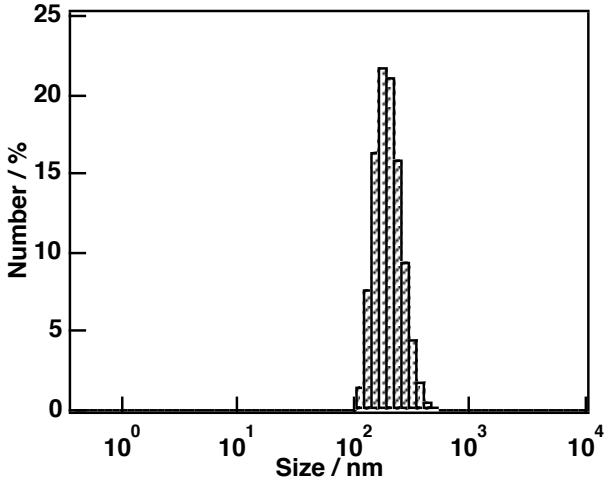


Figure 5. Size distribution diagram of TAIPDI (0.15 mM) in water at room temperature.

The stacking behavior of TAIPDI in the solid form has been displayed by using scanning electron microscopy (SEM). Extensive π-stacking results in a one-dimensional morphology, as shown in SEM images (Figure 6).[33] The columnar structures are about 100-150 nm in width and the average length is in micrometer scale ranging from 1 to 10 μm. Nanostructures of TAIPDI seem brittle, thereby decreasing the average length. Aspect ratio of these structures (length/width) is over 40. PDIs, having linear side-chains, generally tend to reveal one-dimensional morphologies in aggregation.[34] Linear ethylene chains of TAIPDI may have a controlling effect on this columnar stacking. Compared to other nanostructures of PDIs, bearing longer side-chains,[17] those of TAIPDI have narrower average width probably due to the electrostatic repulsion of positively-charged trimethylammonium heads or the short linkers.

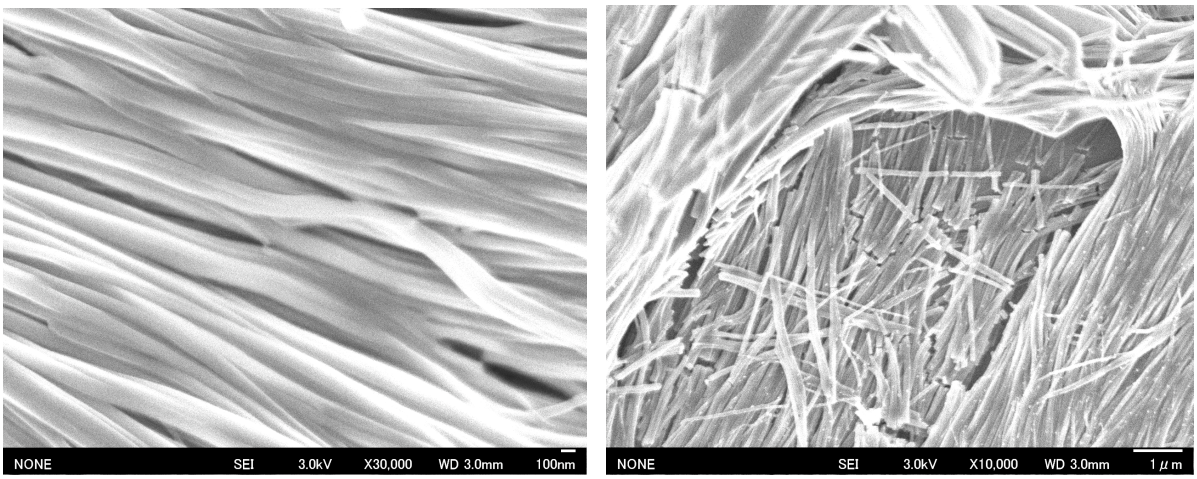


Figure 6. SEM images of nanostructures of TAIPDI obtained from its aqueous solution.

Formation of Self-assemblies of (TAIPDI)$_n$ and ZnTPPSK$_4$ in Water. Assembly formation between the TAIPDI stacks and water soluble ZnTPPSK$_4$ has been examined by steady-state absorption and emission spectroscopy and confirmed by DLS measurements. Upon addition of ZnTPPSK$_4$, the absorption features of (TAIPDI)$_n$ decline gradually while a red shift from 501 nm to 515 nm takes place (Figure 7). A new absorption band in regard to

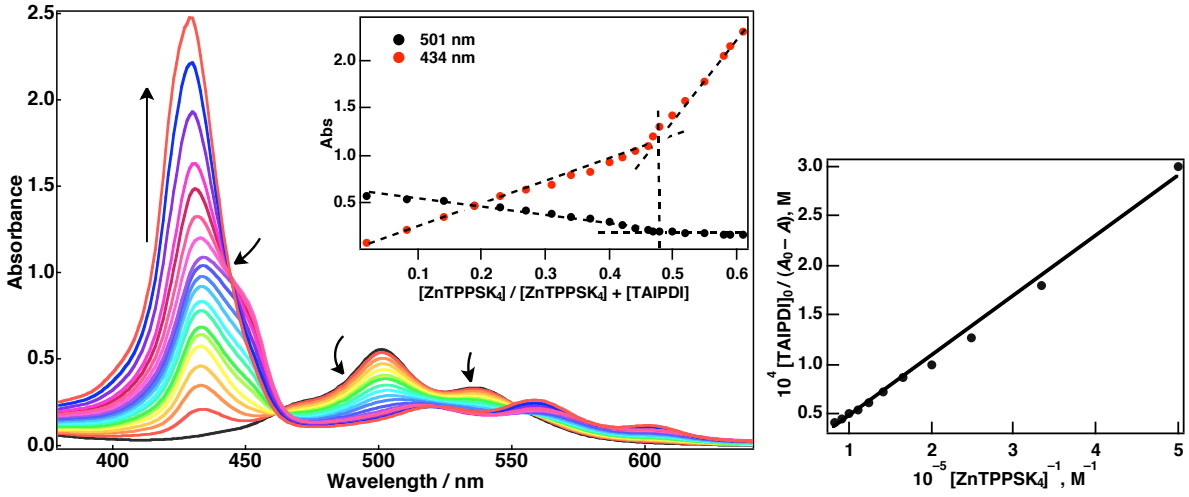


Figure 7. Absorption spectral changes during the titration of TAIPDI with ZnTPPSK$_4$ in water. Inset: Plots of absorbance vs ([ZnTPPSK$_4$] / [ZnTPPSK$_4$] + [TAIPDI]) showing the stoichiometry of the complex at indicated wavelengths (left). Linear plot of $[TAIPDI]_0 / (A–A_0)$ vs $[ZnTPPSK_4]^{-1}$ at 501 nm to evaluate the binding constant (right).

ZnTPPSK$_4$ evolves at 434 nm with a shoulder at around 450 nm. Additionally, the small rise at 559 and 601 nm is noticeable. ZnTPPSK$_4$ normally gives sharp Soret peak at 422 nm with the Q-bands at 556 and 595 nm in water.[24] As studied previously, ionic interactions cause only a few nm of red shift of the Soret of ZnTPPSK$_4$ without any decrease or broadening.[24] Thus, markedly different characteristics of new absorption spectra of the TAIPDI–ZnTPPSK$_4$

complex compared to those of its components indicate that the self-assembly has been established not only by ionic interactions but also by strong π-π interactions between the aromatic cores of TAIPDI and $ZnTPPSK_4$. To determine the stoichiometry of the complex, absorbance change at 434 and 501 nm versus the molar ratio of added $ZnTPPSK_4$ to the total concentration has been followed. Both plots of these wavelengths revealed breaks coinciding at ca. 0.47, indicating a 1:1 stoichiometry between TAIPDI and $ZnTPPSK_4$ (Scheme 1). It is worth to note that the ratio given does not mean that TAIPDI and $ZnTPPSK_4$ form individual 1:1 complexes in the water. This notion describes the number of the components present within the polymeric π-stacks assembled via ionic and π-π interactions.

Scheme 1

$$\text{TAIPDI} + \text{ZnTPPSK}_4 \underset{}{\overset{K_0}{\rightleftharpoons}} \text{TAIPDI–ZnTPPSK}_4$$

From the slope of the linear plot in Figure 7, the formation constant (K_0) of TAIPDI–$ZnTPPSK_4$ was determined to be 1.0×10^5 M^{-1}.[35,36] After the 1:1 ratio exceeded by the addition of $ZnTPPSK_4$, new isosbestic point emerges at 444 nm while the shoulder around 450 nm disappears and the absorption band at 434 nm rises with a blue shift to 429 nm probably due to penetration of more $ZnTPPSK_4$ molecules into TAIPDI stacks with a new stoichiometry.

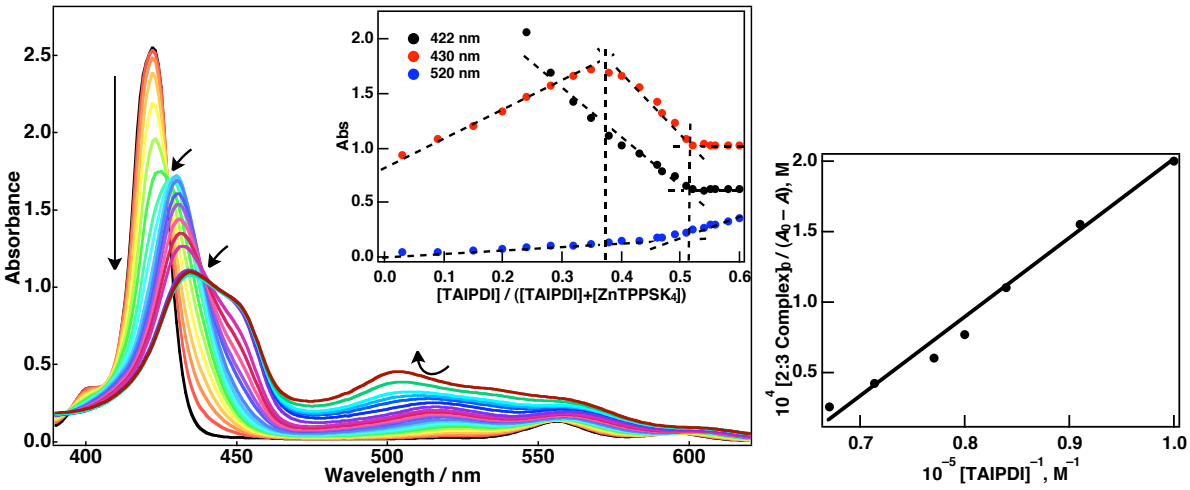


Figure 8. Absorption spectral changes during the titration of $ZnTPPSK_4$ with TAIPDI in water. Inset: Plots of absorbance vs ([TAIPDI] / [TAIPDI] + [$ZnTPPSK_4$]) showing the stoichiometry of the complex at indicated wavelengths (left). Plot of $[2:3\ Complex]_0 / (A–A_0)$ vs $[TAIPDI]^{-1}$ at 430 nm to evaluate the binding constant (right).

$ZnTPPSK_4$ has been titrated with TAIPDI as well. During the titration, the Soret of $ZnTPPSK_4$ at 422 nm decreases regularly, replacing with another peak at 430 nm, as isosbestic point appears at 428 nm (Figure 8). While the absorbance at 430 nm reaches its climax, the molar ratio of TAIPDI to the total concentration marks a value around 0.4 (Figure 8, inset),

implying a ratio of 2:3 between TAIPDI and $ZnTPPSK_4$ molecules within the stacks (Scheme 2). At this ratio, absorption characteristics of the complex seem almost identical to those of the

Scheme 2

$$TAIPDI_2 + 3ZnTPPSK_4 \overset{K_1}{\rightleftharpoons} TAIPDI_2\text{–}(ZnTPPSK_4)_3$$

$$TAIPDI_2\text{–}(ZnTPPSK_4)_3 + TAIPDI \overset{K_2}{\rightleftharpoons} TAIPDI_3\text{–}(ZnTPPSK_4)_3$$

or

$$TAIPDI_2\text{–}(ZnTPPSK_4)_3 + TAIPDI \overset{K_2}{\rightleftharpoons} (TAIPDI\text{–}ZnTPPSK_4)_3$$

complex formed by the addition of excess $ZnTPPSK_4$ in the former titration of $(TAIPDI)_n$ (Figure 7). This ratio may indicate the saturated state of TAIPDI stacks with $ZnTPPSK_4$ molecules. As the titration continues, the second isosbestic point appears at 444 nm, as observed in the former titration. Accordingly, the maximum at 430 nm reduces with a slight red shift to 434 nm, while a broad shoulder ascends around 450 nm. The Q-bands of $ZnTPPSK_4$ also reveal bathochromic shift. On the other hand, TAIPDI absorbs broadly at around 516 nm. Absorbance plots at 422, 430, and 520 nm properly give breaks at ~0.5 in the inset of Figure 8. All the absorption features at this ratio are the same as those of 1:1 assembly in Figure 7 (Scheme 2). The decrease at 430 nm yields a linear plot according to Scheme 2. From the slope of this linear correlation (Figure 8), the formation constant (K_2) of TAIPDI–$ZnTPPSK_4$ was determined to be 6.4×10^4 M^{-1}, which is quite close to K_0.[37] Further addition of TAIPDI does not change the absorption traits of the complex except for the rise at around 500 nm, resulting from free TAIPDI stacks.[38]

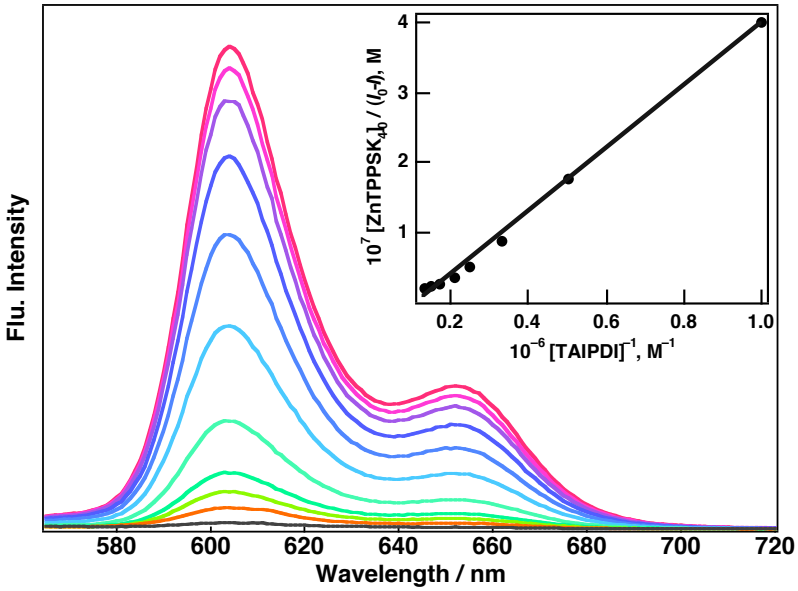


Figure 9. Emission spectral changes during the titration of $ZnTPPSK_4$ with TAIPDI in water. Inset: Plot of $[ZnTPPSK_4]_0 / (I–I_0)$ vs $[TAIPDI]^{-1}$ at 604 nm to evaluate the binding constant.

Titration of $ZnTPPSK_4$ with TAIPDI stacks also leads to fluorescence quenching, most probably due to intramolecular photoinduced electron transfer. $ZnTPPSK_4$ fluoresces with a maximum at 604 nm. Gradual decrease of this emission by the addition of TAIPDI is observed as the TAIPDI–$ZnTPPSK_4$ complex is eventually constructed with a formation constant (1.1×10^6 M^{-1}),[35,36] comparable to the K_0 (Figure 9).

DLS measurements display an average size distribution of 1085 nm for TAIPDI–$ZnTPPSK_4$ complex (Figure 10), which is significantly higher than that of TAIPDI itself. Strong π-π interactions together with the ionic interactions may cause growing size of the self-assemblies in water. To conclude, strong non-covalent interactions between TAIPDI and $ZnTPPSK_4$ represent versatile complex motifs as understood from the titrations.

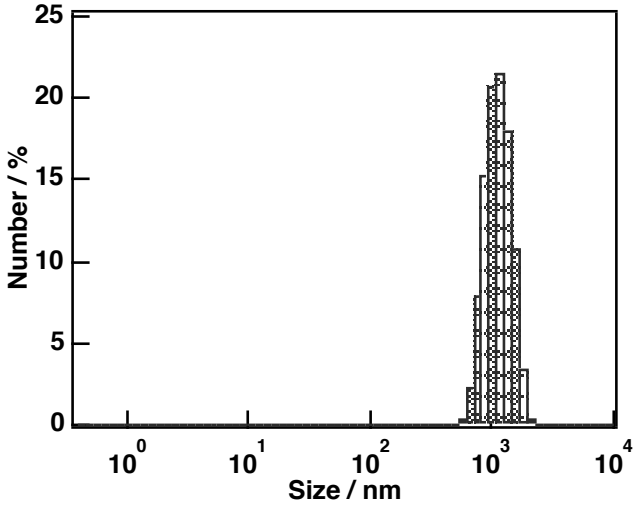


Figure 10. Size distribution diagram of TAIPDI–$ZnTPPSK_4$ (0.10 mM) in water at room temperature.

Photoinduced Electron Transfer Dynamics. The free energy values for supramolecular photoinduced charge separation (ΔG_{CS}) between TAIPDI and $ZnTPPSK_4$ in water have been calculated according to the eq 1:[39]

$$\Delta G_{CS} = e(E_{ox} - E_{red}) - \Delta E_S + \Delta G_s \quad (1)$$

where E_{ox} is the first one-electron oxidation potential of $ZnTPPSK_4$, E_{red} is the first one-electron reduction potential of TAIPDI, ΔE_S is the lowest excited state energy of $ZnTPPSK_4$ or TAIPDI stacks and ΔG_s is the static Coulomb energy in water.[40] E_{ox} for $ZnTPPSK_4$ and E_{red} for TAIPDI have been determined as 0.58 and –0.25 V[41] vs SCE in water containing 0.10 M Na_2SO_4, respectively, by using cyclic and differential pulse voltammetry (Figure 11). If the $ZnTPPSK_4$ is considered as a photosensitizer with a ΔE_S value of 2.07 eV estimated from its absorption and fluorescence emission, then, the driving force for charge separation is estimated to be 1.24 eV. Despite the π-stacking, driving force for charge separation via the

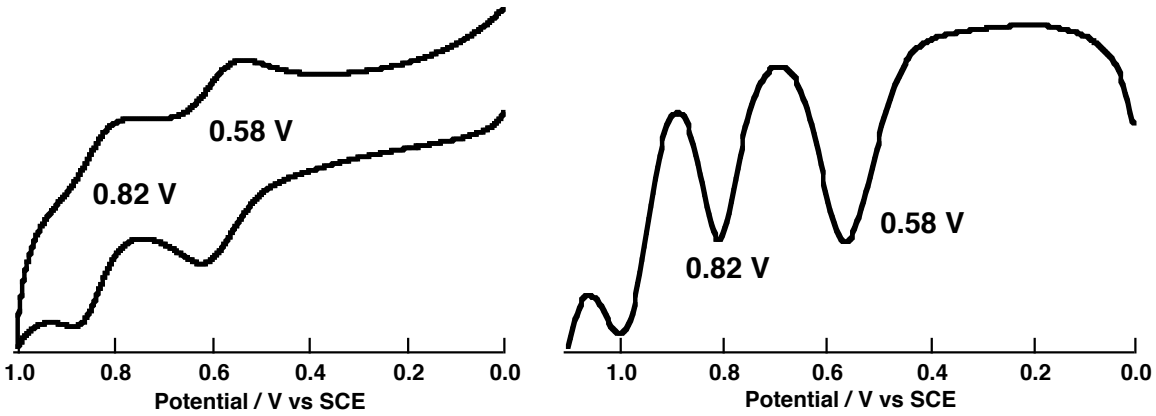


Figure 11. Cyclic and differential voltammograms of $ZnTPPSK_4$ in deaerated water containing 0.10 M Na_2SO_4 (sweep rate: 0.1 mV/s).

excited states of $(TAIPDI)_n$, having sufficient lifetimes for close interactions, is not out of the question (vide supra). Moreover, one-dimensional morphology facilitates the exciton migration, which can eventually produce charge separation.[24,42] Excitation of $(TAIPDI)_n$ can generate a driving force for charge separation of 1.49 eV as determined from the absorption and weak emission spectra at different concentrations (2.32 eV). Water, as an extremely polar ambience, has an important role for highly exothermic driving forces.

The photoinduced processes taking place within the TAIPDI–$ZnTPPSK_4$ self-assembly have been monitored by using femtosecond and nanosecond transient spectroscopy. A careful balance between obtaining the highest absorption at the excitation wavelength and permitting the maximum electron delocalization within the π-stacks of TAIPDI required mixing 1 equiv of $ZnTPPSK_4$ with 17 equiv of TAIPDI.

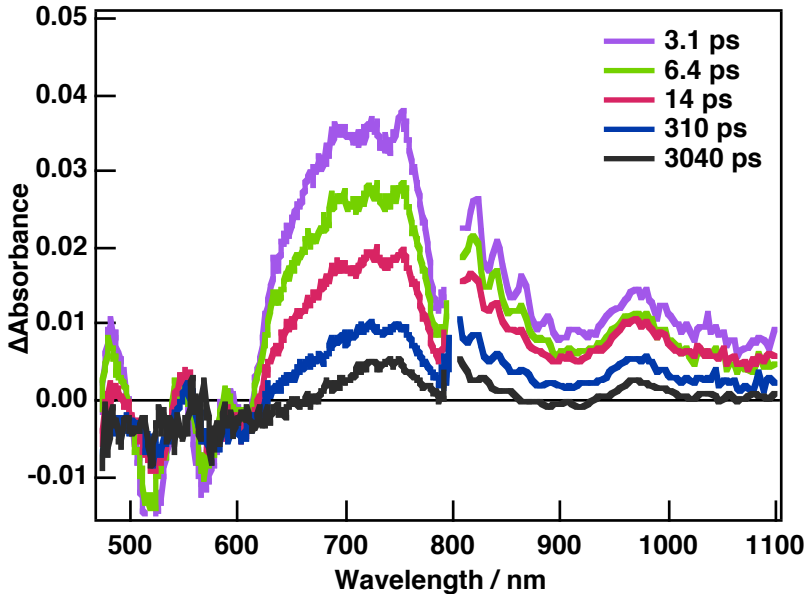


Figure 12. Femtosecond transient absorption spectra of TAIPDI–$ZnTPPSK_4$ in deaerated water at indicated time delays (λ_{exc} = 390 nm).

In Figure 12, the femtosecond spectra of TAIPDI–ZnTPPSK$_4$ in water display a very rapid formation of broad transient absorption around 730 nm and 980 nm. Different than those of singlet-excited states of TAIPDI (chapter 4, vide supra) and ZnTPPSK$_4$[24] (chapter 3, vide supra) in water, these patterns quite match the radical anion of (TAIPDI)$_n$ (Figure 4),[29] evidence of photoinduced electron transfer from ZnTPPSK$_4$ to (TAIPDI)$_n$. Radical cation of ZnTPPSK$_4$ at 670 nm may have a contribution to the broadening around 700 nm.[43] From the rise at 730 and 980 nm, the rate of charge separation (k_{CS}) is estimated to be 1.4×10^{12} s^{-1} (0.74 ps). Very fast charge separation results from the tight stacking of the donor and acceptor components in the columnar arrays. The time profiles of absorbance at 730 and 980 nm give two-component decay as shown in Figure 13. The first component decays with a rate of

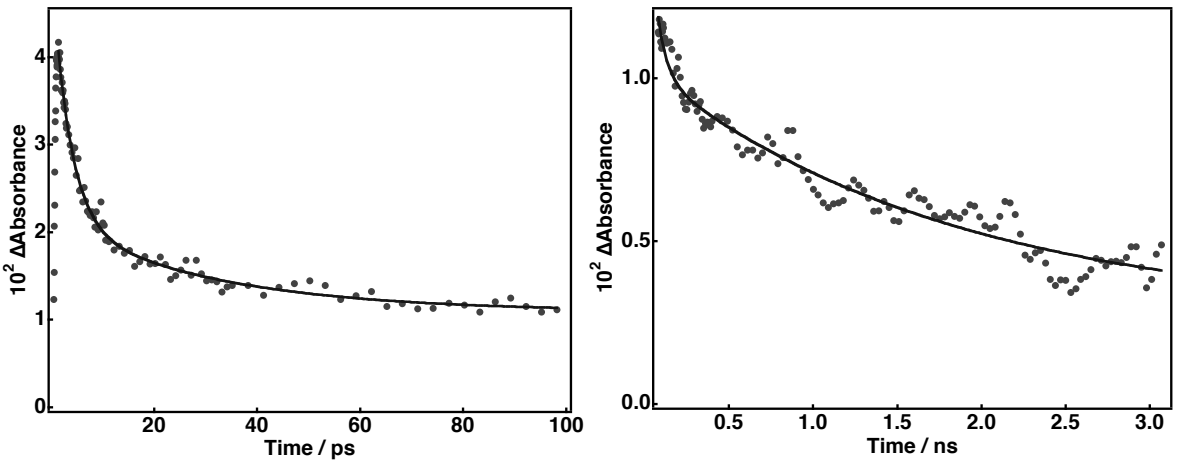


Figure 13. Decay time profiles of the transient absorbance at 730 nm at 0-100 ps (left) and 100-3000 ps (right) in water.

2.0×10^{11} s^{-1} (k_{CR1}), yielding a lifetime for first charge recombination as 5 ps (τ_{CS1}) at 730 nm. The second component declines so slowly that it remains incomplete as observed in all transient traits of (TAIPDI)$_n^{\bullet-}$ in Figure 12. The first-order plot fitted to this slow decay affords a rate constant for second charge recombination as 4.6×10^8 s^{-1} (k_{CR2}), corresponding to 2.2 ns (τ_{CS2}). Such a long-lived charge-separated state is most likely the outcome of the electron transport along the one-dimensional π-stacks of TAIPDI after the photoinduced charge injection occurs. The fast charge recombination correlated with k_{CR1} can be due to the tight stacking. As it facilitates the very fast charge separation, it also causes fast charge recombination due to enhanced electronic communication between the donor and acceptor moieties.[44] Another reason for the first decay component can be the random distribution of the ZnTPPSK$_4$ within the TAIPDI stacks as represented in Figure 14. As a result of this random disposition, there may exist extended domains of TAIPDIs (illustrated as domain 1 in Figure 14) permitting wide-ranging π-electron delocalization, while some domains (illustrated as domain 2 in Figure 14), severed by many ZnTPPSK$_4$ molecules, limit this process favoring the

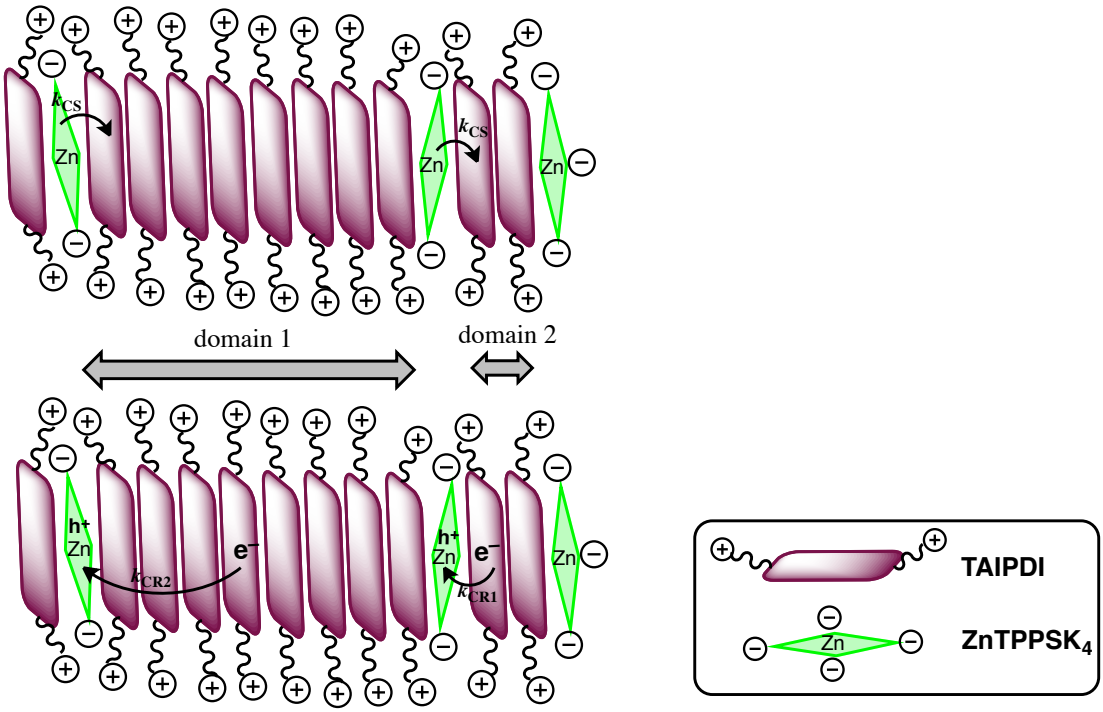


Figure 14. Representative illustration of the charge separation and charge recombination between the stacks of TAIPDI and randomly distributed $ZnTPPSK_4$.

fast recombination. Lastly, stacking defects among the TAIPDI molecules can severely hinder the charge hopping.[45] Despite these drawbacks, almost 3000-times elongated lifetime of the charge-separated state has been ultimately achieved by long range electron migration through the hydrophobic π-stacks triggered by an aqueous environment. This is the highest k_{CS}/k_{CR} ratio dated for such columnar systems to the best of our knowledge. Nanosecond transient spectra of the TAIPDI–$ZnTPPSK_4$ did not give any signal, indicating that the charge recombination completed before 100 ns.[46] Absence of the transient signal also proves that charge-separated state decays directly to the ground state without producing triplet state of $ZnTPPSK_4$[11g] or TAIPDI,[47] which is already energetically unfeasible. Furthermore, absence of the triplet-excited states of $ZnTPPSK_4$ indicates that $^1ZnTPPSK_4^*$ is efficiently used for charge injection to the TAIPDI stacks.

Conclusion

Columnar TAIPDI stacks at nanoscale have been thoroughly characterized in water and solid state. Excited-state dynamics of $(TAIPDI)_n$ have been explained by a comparison with those of unstacked TAIPDI. The one-dimensional stacks of TAIPDI can host $ZnTPPSK_4$ molecules at various ratios due to strong π-π and ionic interactions in an aqueous medium. Following the photoinduced charge injection from $ZnTPPSK_4$, electron transport owing to probable π-delocalization mechanism along the electron deficient TAIPDI stacks has been observed. This phenomenon facilitates the long-range charge separation with a high k_{CS}/k_{CR}

ratio, which is a fundamental parameter for organic photovoltaic applications targeting high efficiencies.

References and Notes

(1) (a) Marcus, R. A.; Sutin, N. *Biochim. Biophys. Acta* **1985**, *811*, 265. (b) Moser, C. C.; Keske, J. M.; Warncke, K.; Farid, R. S.; Dutton, P. L. *Nature* **1992**, *335*, 796.

(2) Sariciftci, N. S.; Smilowitz, L.; Heeger, A. J.; Wudl, F. *Science* **1992**, *258*, 1474.

(3) This distance includes all the electron-transfer components in the photosynthetic reaction center, see: Loll, B.; Kern, J.; Saenger, W.; Zouni, A.; Biesiadka, J. *Nature* **2005**, *438*, 1040.

(4) (a) Wasielewski, M. R. *Chem. Rev.* **1992**, *92*, 435. (b) Gust, D.; Moore, T. A.; Moore, A. L. *Acc. Chem. Res.* **2001**, 34, 40. (c) Fukuzumi, S. *Phys. Chem. Chem. Phys.* **2008**, *10*, 2283. (d) Fukuzumi, S.; Ohkubo, K. *J. Mater. Chem*. **2012**, *22*, 4575.

(5) (a) Imahori, H.; Guldi, D. M.; Tamaki, K.; Yoshida, Y.; Luo, C.; Sakata, Y.; Fukuzumi, S. *J. Am. Chem. Soc.* **2001**, *123*, 6617. (b) Imahori, H.; Sekiguchi, Y.; Kashiwagi, Y.; Sato, T.; Araki, Y.; Ito, O.; Yamada, H.; Fukuzumi, S. *Chem.–Eur. J.* **2004**, *10*, 3184. (c) Guldi, D. M.; Imahori, H.; Tamaki, K.; Kashiwagi, Y.; Yamada, H.; Sakata, Y.; Fukuzumi, S. *J. Phys. Chem. A* **2004**, *108*, 541.

(6) (a) Pivrikas, A.; Neugebauer, H.; Sariciftci, N. S. *Solar Energy* **2011**, *85*, 1226. (b) Günes, S.; Neugebauer, H.; Sariciftci, N. S. *Chem. Rev*. **2007**, *107*, 1324.

(7) Efficient light funneling in photosynthesis is achieved by an excitation energy-transfer mechanism from specialized light harvesting antenna complexes to the photosynthetic reaction center. Blankenship, R.E. *Molecular Mechanisms of Photosynthesis*; Blackwell Science: Oxford, 2002.

(8) (a) Brabec, C. J.; Sariciftci, N. S.; Hummelen, J. C. *Adv. Funct. Mater.* **2001**, *11*, 15. (b) Coropceanu, V.; Cornil, J.; Filho, D. A. d. S.; Olivier, Y.; Silbey, R.; Bredas, J.-L. *Chem. Rev.* **2007**, *107*, 926.

(9) Instead of polymers, small-molecular-weight organic materials, having extensive π-systems, have also been suggested, see: Peumans, P.; Uchida, S.; Forrest, S. R. *Nature* **2003**, *425*, 158.

(10) Bakulin, A. A.; Rao, A.; Pavelyev, V. G.; van Loosdrecht, P. H. M.; Pshenichinikov, M. S.; Niedzialek, D.; Cornil, J.; Beljonne, D.; Friend, R. H. *Science* **2012**, *335*, 1340.

(11) (a) Bonvoisin, J.; Launay, J.-P.; Van der Auweraer, M.; De Schryver, F. C. *J. Phys. Chem.* **1994**, *98*, 5052. (b) Bonvoisin, J.; Launay, J.-P.; Verbouwe, W.; Van der Auweraer, M.; De Schryver, F. C. *J. Phys. Chem.* **1996**, 100, 17079. (c) Nelsen, S. F.; Tran, H. Q.; Nagy, M. A.; *J. Am. Chem. Soc.* **1998**, *120*, 298. (d) Kochi, J. K.;

Rathore, R.; Le Magueres, P. *J. Org. Chem.* **2000**, *65*, 6826. (e) Le Magueres, P.; Lindeman, S. V.; Kochi, J. K. *J. Chem. Soc. Perkin Trans. 2* **2001**, 1180. (f) Onodera, H.; Araki Y.; Fujitsuka, M.; Onodera, S.; Ito, O.; Bai, F.; Zheng, M.; Yang, J.-L. *J. Phys. Chem. A* **2001**, *105*, 7341. (g) Takai, A.; Gros, C. P.; Barbe, J.-M.; Guilard, R.; Fukuzumi, S. *Chem.–Eur. J.* **2009**, *15*, 3110. (h) Takai, A.; Gros, C. P.; Barbe, J.-M.; Fukuzumi, S. *Chem.–Eur. J.* **2011**, *17*, 3420.

(12) (a) Tanaka, M.; Ohkubo, K.; Gros, C. P.; Guilard, R.; Fukuzumi, S. *J. Am. Chem. Soc.* **2006**, *128*, 14625. (b) Chen, Y.; El-Khouly, M. E.; Zhuang, X.-D.; He, N.; Araki, Y.; Lin, Y.; Ito, O. *Chem.–Eur. J.* **2007**, *13*, 1709. (c) El-Khouly, M. E.; Chen, Y.; Zhuang, X.; Fukuzumi, S. *J. Am. Chem. Soc.* **2009**, *131*, 6370. (d) Fukuzumi, S.; Hanazaki, R.; Kotani, H.; Ohkubo, K. *J. Am. Chem. Soc.* **2010**, *132*, 11002. (e) Takai, A.; Chkounda, M.; Eggenspiller, A.; Gros, C. P.; Lachkar, M.; Barbe, J.-M.; Fukuzumi, S. *J. Am. Chem. Soc.* **2010**, *132*, 4477.

(13) (a) Grimsdale, A. C.; Müllen, K. *Angew. Chem., Int. Ed.* **2005**, *44*, 5592. (b) Weickert, J.; Dunbar, R. B.; Hesse, H. C.; Wiedemann, W.; Schmidt-Mende, L. *Adv. Mater.* **2011**, *23*, 1810.

(14) (a) Hoeben, F. J. M.; Jonkheijm, P.; Meijer, E. W.; Schenning, A. P. H. J. *Chem. Rev.* **2005**, *105*, 1491. (b) Zang, L.; Che, Y.; Moore, J. S. *Acc. Chem. Res.* **2008**, *41*, 1596.

(15) Che, Y.; Datar, A.; Balakrishnan, K.; Zang, L. *J. Am. Chem. Soc.* **2007**, *129*, 7234.

(16) (a) Che, Y.; Datar, A.; Yang, X.; Naddo, T.; Zhao, J.; Zang, L. *J. Am. Chem. Soc.* **2007**, *129*, 6354. (b) Chen, S.-G.; Branz, H. M.; Eaton, S. S.; Taylor, P. C.; Cormier, R. A.; Gregg, B. A. *J. Phys. Chem. B* **2004**, *108*, 17329.

(17) Supur, M.; Yamada, Y.; El-Khouly, M. E.; Honda, T.; Fukuzumi, S. *J. Phys. Chem. C* **2011**, *115*, 15040.

(18) (a) Würthner, F.; Chen, Z.; Hoeben, F. J. M.; Osswald, P.; You, C.-C.; Jonkheijm, P.; Herrikhuyzen, J. v.; Schenning, A. P. H. J.; van der Schoot, P. P. A. M.; Meijer, E. W.; Beckers, E. H. A.; Meskers, S. C. J.; Janssen, R. A. *J. Am. Chem. Soc.* **2004**, *126*, 10611. (b) Sinks, L. E.; Rybtchinski, B.; Iimura, M.; Jones, B. A.; Goshe, A. J.; Zuo, X.; Tiede, D. M.; Li, X.; Wasielewski, M. R. *Chem. Mater.* **2005**, *17*, 6295.

(19) Related reviews: (a) Toksoz, S.; Acar, H.; Guler, M. O. *Soft Matter* **2010**, *6*, 5839. (b) Görl, D.; Zhang, X.; Würthner, F. *Angew. Chem., Int. Ed.* **2012**, *51*, 6328.

(20) Kavarnos, G. J.; Turro, N. J. *Chem. Rev.* **1986**, *86*, 401.

(21) Huang, Y.; Quan, B.; Wei, Z.; Liu, G.; Sun, L. *J. Phys. Chem. C* **2009**, *113*, 3929.

(22) (a) Wang, B.; Yu, C. *Angew. Chem., Int. Ed.* **2010**, *49*, 1485. (b) Biedermann, F.; Elmalem, E.; Ghosh, I.; Nau, W. M.; Scherman, O. A. *Angew. Chem., Int. Ed.* **2012**, *51*, 7739.

(23) Jimenez, H. R.; Julve, M.; Faus, J. *J. Chem. Soc. Dalton Trans.* **1991**, 1945.

(24) Supur, M.; Yamada, Y.; Fukuzumi, S. *J. Mater. Chem.* **2012**, *22*, 12547.

(25) Giaimo, J. M.; Lockard, J. V.; Sinks, L. E.; Scott, A. M.; Wilson, T. M.; Wasielewski, M. R. *J. Phys. Chem. A* **2008**, *112*, 2322.

(26) According to exciton coupling model, coupling of π-orbital electrons of identical chromophores in cofacial order results in two new exciton states: higher exciton state, to which the transition from ground state is allowed and lower exciton state, to which the transition from ground state is forbidden.[25]

(27) This emission band seems quite different from broad, featureless excimer-like emission, which arises from partial overlap of π-systems as reported earlier for a dimer system.[25]

(28) Aggregation yields have been estimated from the ratio of absolute quantum yield of TAIPDI in water at indicated concentrations to that in MeOH ($\Phi_{\text{f-water}}/\Phi_{\text{f-MeOH}}$). 0.02 mM of TAIPDI was assumed to dissolve completely in MeOH. It should be noted that emission originating from TAIPDI stacks at concentrations higher than 0.08 mM can be involved in the quantum yield measurements. However, compared to that of monomer, this emission is very small to cause significant variation of the aggregation values stated in Table 1.

(29) Marcon, R. O.; Brochsztain, S. *J. Phys. Chem. A* **2009**, *113*, 1747.

(30) Shirman, E.; Ustinov, A.; Ben-Shitrit, N.; Weissman, H.; Iron, M. A.; Cohen, R.; Rybtchinski, B. *J. Phys. Chem. B* **2008**, *112*, 8855.

(31) van der Boom, T.; Hayes, R. T.; Zhao, Y.; Bushard, P. J.; Weiss, E. A.; Wasielewski, M. R. *J. Am. Chem. Soc.* **2002**, *124*, 958.

(32) Size distribution is not correlated with concentration.

(33) Nanostructures are obtained by drop casting of a concentrated TAIPDI aqueous solution (ca. 0.4 mM) onto silicon substrate.

(34) Balakrishnan, K.; Datar, A.; Naddo, T.; Huang, J.; Oitker, R.; Yen, M.; Zhao, J.; Zang, L. *J. Am. Chem. Soc.* **2006**, *128*, 7390.

(35) According to 1:1 ratio, the absorbance change is given by the equation: $[\text{TAIPDI}]_0/(A_0-A) = (\varepsilon_c-\varepsilon_p)^{-1} + (K_0[\text{ZnTPPSK}_4](\varepsilon_c-\varepsilon_p))^{-1}$, where A_0 and A are the absorbance of TAIPDI at 501 nm in the absence and presence of ZnTPPSK_4, and ε_c and ε_p are the molar absorption coefficients of TAIPDI at 501 nm in the absence and presence of ZnTPPSK_4, respectively. This equation predicts a linear correlation between $[\text{TAIPDI}]_0/(A-A_0)$ and $[\text{ZnTPPSK}_4]^{-1}$.[36]

(36) (a) Fukuzumi, S.; Kondo, Y.; Mochizuki, S.; Tanaka, T. *J. Chem. Soc., Perkin Trans. 2* **1989**, 1753.

(37) According to 1:1 ratio, the absorbance change is given by the equation: $[\text{2:3 Complex}]_0/(A_0-A) = (\varepsilon_c-\varepsilon_p)^{-1} + (K_2[\text{TAIPDI}](\varepsilon_c-\varepsilon_p))^{-1}$, where A_0 and A are the absorbance of 2:3 Complex at 430 nm in the absence and presence of TAIPDI, and ε_c and ε_p are the molar absorption coefficients of 2:3 Complex at 430 nm in the

absence and presence of TAIPDI, respectively. This equation predicts a linear correlation between [2:3 Complex]$_0$/(A–A_0) and [TAIPDI]$^{-1}$.[38]

(38) It is also likely that TAIPDI stacks have only ionic interactions with ZnTPPSK$_4$ molecules buried in the complex, giving no spectral change.

(39) Weller, A. *Z. Phys. Chem.* **1982**, *133*, 93.

(40) Because TAIPDI and ZnTPPSK$_4$ are closely packed in the π-stacks, the initial products of photoinduced electron transfer are assumed to be contact radical ion pair and ΔG_s was estimated by using the expression: ΔG_s = –0.56 eV (1/ε) + 0.003 eV, where ε is the dielectric constant of water at room temperature. See: Arnold, B. R.; Farid, S.; Goodman, J. L.; Gould, I. R. *J. Am. Chem. Soc.* **1996**, *118*, 5482.

(41) See chapter 4 for the DPV of TAIPDI.

(42) (a) Beljone, D.; Hennebicq, E.; Daniel, C.; Herz, L. M.; Silva, C.; Scholes, G. D.; Hoeben, F. J. M.; Jonkheijm, P.; Schenning, A. P. H. J.; Meskers, S. C. J.; et al. *J. Phys. Chem. B* **2005**, *109*, 10594. (b) Marciniak, H.; Li, X.-Q.; Würthner, F.; Lochbrunner, S. *J. Phys. Chem. A* **2011**, *115*, 648.

(43) Ohkubo, K.; Kawashima, Y.; Fukuzumi, S. *Chem. Commun.* **2012**, *48*, 4314.

(44) (a) Ohtani, M.; Fukuzumi, S. *Chem. Commun.* **2009**, 4997. (b) El-Khouly, M. E.; Jaggi, M.; Schmid, B.; Blum, C.; Liu, S.-X.; Decurtins, S.; Ohkubo, K.; Fukuzumi, S. *J. Phys. Chem. C* **2011**, *115*, 8325. (c) Grimm, B.; Santos, J.; Illescas, B.; Munoz, A.; Guldi, D. M.; Martin, N. *J. Am. Chem. Soc.* **2010**, *132*, 17387.

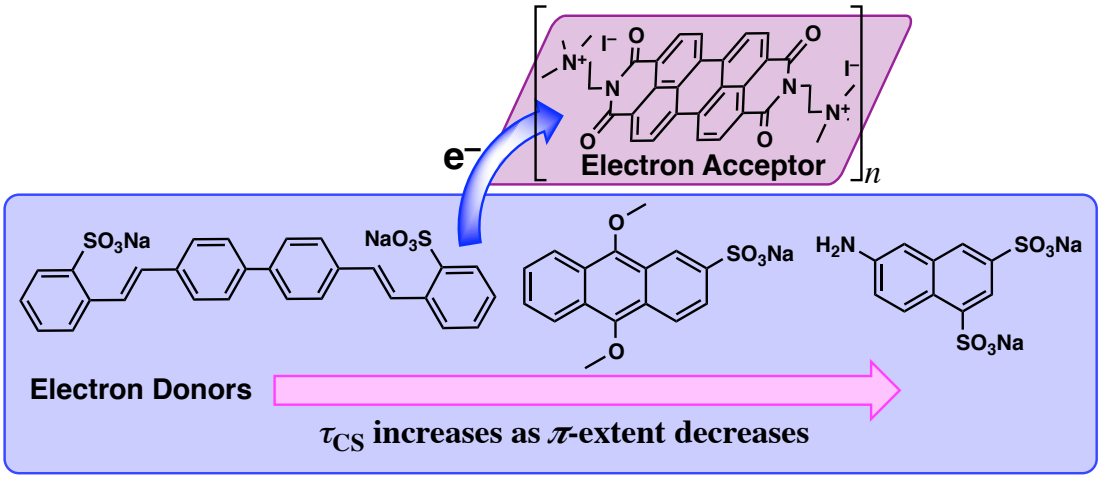
(45) Ide, J.; Mereau, R.; Ducasse, L.; Castet, F.; Olivier, Y.; Martinelli, N.; Cornil, J.; Beljonne, D. *J. Phys. Chem. B* **2011**, *115*, 5593.

(46) The time range between 3-100 ns is out of the range of our laser systems.

(47) Triplet-excited states of PDI have been discussed in detail in chapter 4.

Chapter 6

Tuning the Photodriven Electron Transport within the Columnar Perylenediimide Stacks by Changing the π-Extent of the Electron Donors



Abstract: Photodriven electron-transport properties of the self-assemblies of *N,N'*-di(2-(trimethylammoniumiodide)ethylene)perylenediimide stacks $(TAIPDI)_n$ with three electron donors, disodium 4,4'-bis(2-sulfonatostyryl)biphenyl (BSSBP, stilbene-420), sodium 9,10-dimethoxyanthracene-2-sulfonate (DANS) and disodium 6-amino-1,3-naphthalenedisulfonate (ANADS) have been studied in water. These electron donors vary in their π-extent to adjust the electronic coupling and the distance with the PDI stacks. Possessing the largest π-extent, BSSBP has strong π-π interactions as well as ionic interactions with $(TAIPDI)_n$. Instead of π-stacking with TAIPDI planes, DANS and ANADS, bearing relatively small π-extent, are embedded in the side chains of TAIPDIs via ionic interactions, resulting in distance increment with the aromatic TAIPDI cores. After excitation, the BSSBP–$(TAIPDI)_n$ system exhibits fast charge separation (0.70 ps) and relatively slow charge recombination (485 ps) due to intermolecular electron delocalization along the TAIPDI stacks. On the other hand, charge separation in DANS–$(TAIPDI)_n$ and ANADS–$(TAIPDI)_n$ occurs within 1.5 and 1.6 ns, respectively, calculated from the quenching of singlet excited states. The lifetimes of charge-separated states are determined to be 44 and 96 μs, at least 105 times slower than that of BSSBP–$(TAIPDI)_n$ due to remarkably improved electron transport throughout the $(TAIPDI)_n$.

Introduction

Self-organization of extensive π-systems at nanoscale provides a morphology control and long-range charge transport, both of which are of importance to enhance the efficiencies of photoinduced device applications, such as organic photovoltaic (OPV) cells.[1,2] Regarding to these aspects, the self-assemblies of perylenediimides (PDIs) at nanoscale have drawn much attention.[3,4] Self-assembly of electron deficient π-planes of PDIs in one dimension enhances the charge transport through the intermolecular π-electron delocalization following thermal or photoinduced electron transfer from an electron donor.[5-7] Nonetheless, efficiencies of organic solar cells of PDIs fabricated from a bulk heterojunction (BHJ) with a polymer donor are quite low when compared to those in which the fullerene derivatives are employed as electron acceptors. Two main reasons have been addressed for the low external quantum efficiencies of BHJ solar cells of PDIs:[8] (i) Fast charge recombination when the electronic communication between the donor and PDI is strong owing to π-π interactions and (ii) fast exciton quenching due to π-stacking of PDI molecules resulting in excimer-like (intermolecular) states[9] when charge transfer is reduced probably because of increased distance between polymer donor and PDI aggregates. In the former case, strong electronic communication of PDIs with the donor moieties also enhances the fast charge transfer but the charge transport among the PDI stacks is precluded.[10] In the latter case, because the stacking behaviour is preserved, the charge transport is relatively better.[8,11]

Disruption of the stacking behaviour of planar PDIs by the substitution of bulky groups from bay region[12] or by the joint of two twisted PDIs from imide positions[13] has been suggested in order to impede the fast charge recombination and exciton quenching. However, disturbance of aggregation sacrifices the extensive charge transport among the PDI stacks.

Overcoming the fast charge recombination may be achieved by adjusting the distance between the donor and acceptor, which should be long enough to avoid strong electronic coupling and to preserve columnar stacking of PDIs but sufficiently close so that the exciton can be utilized for charge separation before it is quenched or transferred.

Previously,[14] we studied the columnar stacks of *N,N'*-di(2-(trimethylammoniumiodide)ethylene) perylenediimide (TAIPDI), in which sulphonated porphyrins were intervening between the PDI stacks at various ratios through the strong π-π interactions assisted with ionic interactions in aqueous environment. Following the photoexcitation, the charge separation was quite fast due to strong electronic coupling between the PDI stacks and inserted porphyrins. However, the strong coupling also resulted in fast charge recombination, impairing the long-range photoinduced electron transport along the PDI stacks. We also showed that despite the quenching of singlet-excited states of monomer PDI, those of stacked PDIs have sufficient lifetimes for photoinduced processes with closely positioned donor or acceptor components.

In this study, we have examined the self-assemblies of TAIPDI stacks, $(TAIPDI)_n$, with three different electron donors, disodium 4,4'-bis(2-sulfonatostyryl)biphenyl (BSSBP, stilbene-420), sodium 9,10-dimethoxyanthracene-2-sulfonate (DANS) and disodium 6-amino-1,3-naphthalenedisulfonate (ANADS). These electron donors vary in their π-extent to adjust the electronic coupling and the distance with the PDI stacks (Figure 1). The photodriven electron-transport properties of these self-assembly systems have been investigated by using time-resolved transient techniques.

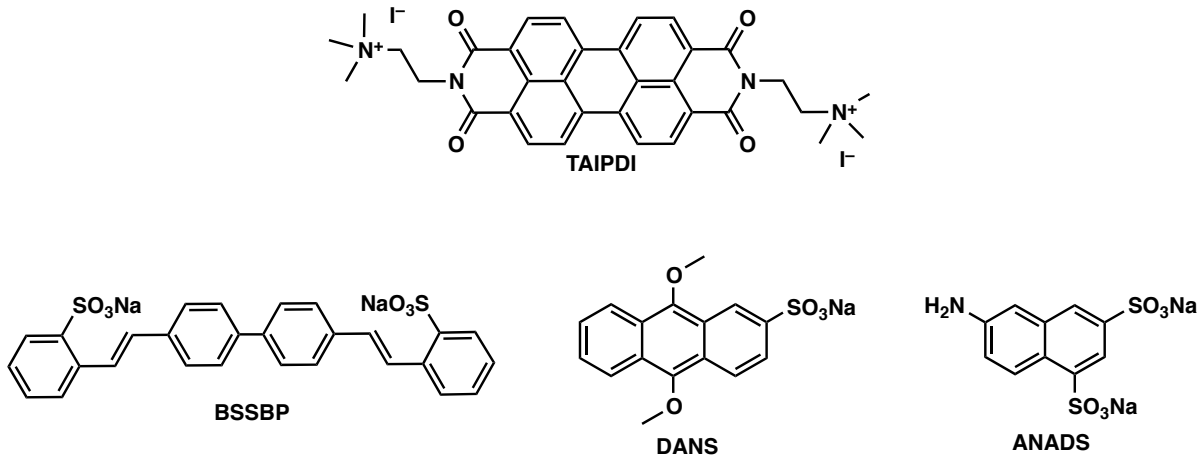


Figure 1. Molecular structures of the components used in this study.

Experimental Section

Materials. *N,N'*-Di(2-(trimethylammoniumiodide)ethylene)perylenediimide (TAIPDI) was synthesized according to reported procedures.[15,16] Electron donors, disodium 4,4'-bis(2-sulfonatostyryl)biphenyl (BSSBP), sodium 9,10-dimethoxyanthracene-2-sulfonate (DANS), and disodium 6-amino-1,3-naphthalenedisulfonate (ANADS) and napthalene-2-amine and 9,10-dimethylanthracene, used for the comparison of phosphorescence results, have been obtained from commercial sources (TCI) and used as received. Purification of water (18.2 MΩ cm) was performed with a Milli-Q system (Millipore, Direct-Q 3 UV).

Instruments. Steady-state absorption measurements were recorded on a Hewlett Packard 8453 diode array spectrophotometer. Fluorescence and phosphorescence measurements were carried out on a Shimadzu spectrofluorophotometer (RF-5300PC). Phosphorescence data were obtained from MeTHF/EtOH solutions in the presence of MeI (ca. 10%, v/v) at 77 K. Electrochemical measurements were performed on an ALS630B or ALS730D electrochemical analyzer in deaerated water containing 0.10 M Na_2SO_4 as supporting electrolyte. A conventional three-electrode cell was used with a platinum working electrode (surface area of 0.3 mm^2) and a platinum wire as the counter electrode. The Pt working electrode was routinely polished with ALS polishing alumina suspension (0.05 μm) and rinsed with water and acetone before use. The measured potentials were recorded with respect to a saturated calomel

electrode (SCE). All electrochemical measurements were carried out under an atmospheric pressure of nitrogen. Femtosecond transient absorption spectroscopy experiments were conducted using an ultrafast source: Integra-C (Quantronix Corp.), an optical parametric amplifier: TOPAS (Light Conversion Ltd.) and a commercially available optical detection system: Helios provided by Ultrafast Systems LLC. The source for the pump and probe pulses was derived from the fundamental output of Integra-C (780 nm, 2 mJ per pulse and fwhm = 130 fs) at a repetition rate of 1 kHz. 75% of the fundamental output of the laser was introduced into TOPAS, which has optical frequency mixers resulting in a tunable range from 285 nm to 1660 nm, while the rest of the output was used for white light generation. Typically, 2500 excitation pulses were averaged for 5 seconds to obtain the transient spectrum at a set delay time. Kinetic traces at appropriate wavelengths were assembled from the time-resolved spectral data. All measurements were conducted at 298 K. For nanosecond transient absorption measurements, deaerated solutions of the compounds were excited with a Panther optical parametric oscillator (OPO) equipped with a Nd:YAG laser (Continuum, SLII-10, fwhm = 4-6 ns) with a power of 10-15 mJ per pulse. The photochemical reactions were monitored by continuous exposure to a Xe lamp (150 W) as a probe light and a detector (SpectraPro 300i). The transient spectra were recorded using fresh solutions in each laser excitation. Solutions were deoxygenated by nitrogen purging for about 15 min prior to the transient spectral measurements.

Results and Discussion

Formation of Self-Assemblies of (TAIPDI)$_n$ and Electron Donors. BSSBP has an absorption maximum at 349 nm in water (Figure 2). By the addition of (TAIPDI)$_n$, the

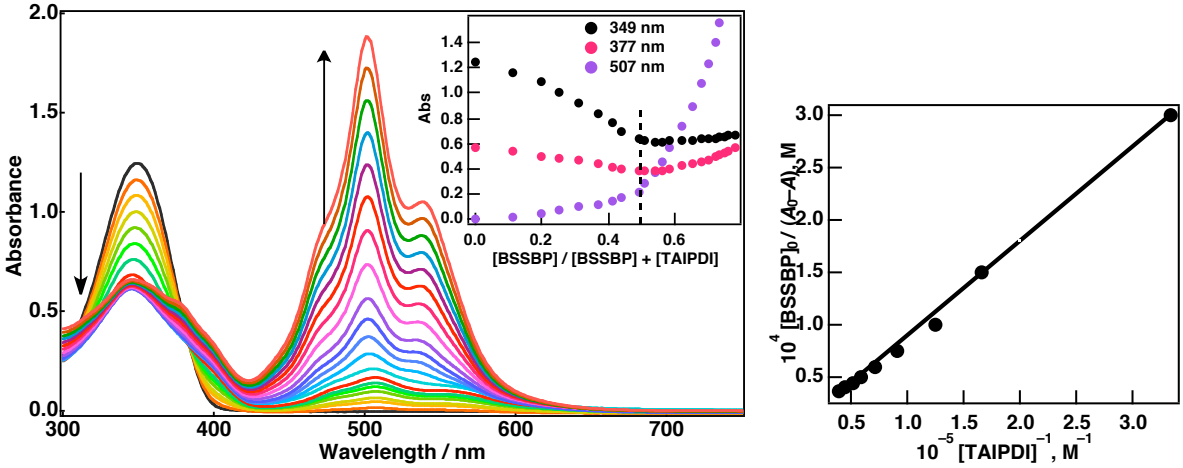


Figure 2. Absorption spectral changes during the titration of BSSBP with TAIPDI in water. Inset: Plots of absorbance vs. ([BSSBP] / [BSSBP] + [TAIPDI]) showing the stoichiometry of the complex at indicated wavelengths (left). Linear plot of $[BSSBP]_0 / (A - A_0)$ vs $[TAIPDI]^{-1}$ at 349 nm to evaluate a formation constant (right).

featureless absorption band of BSSBP starts to decrease with a small shift to 346 nm,[17] while the broad and red-shifted absorption of the TAIPDI stacks appears at 507 nm, which is seen at 501 nm in the absence of BSSBP.[14,18] Isosbestic points and drastic variations in absorption characteristics indicate an electronic interaction between the components dominantly through the π-π interactions. Decrease in absorbance at 349 nm continues until the 1:1 stoichiometry between TAIPDI and BSSBP is established as indicated by the plots of absorbance at 349, 377, 507 nm vs. the molar ratio of added TAIPDI to the total concentration (Figure 2, Inset). From the slope of the linear plot in Figure 2, the formation constant (K_1) is calculated to be 3.8×10^5 M^{-1}.[19,20] After the 1:1 ratio is surpassed upon the addition of further TAIPDI, a small shoulder appears at 377 nm, while the absorption at 349 nm arises moderately, indicating a new ratio along the row of the columnar TAIPDI stacks. The maximum of TAIPDI at 507 nm also shifts to 501 nm with increasing molar extinction coefficient. It should be noted that the ratio given does not represent the individual 1:1 complexes; instead, this expression describes the number of components present along the repeating columnar π-stacks.

Self-assembly of BSSBP with TAIPDI stacks also results in total quenching of BSSBP fluorescence emission at 437 nm due to intrasupramolecular electron transfer from BSSBP to $(TAIPDI)_n$ via strong π-π interactions. The decrease in this emission intensity with a red shift to 444 nm gives a formation constant as determined from a linear plot as 1.5×10^6 M^{-1} (Figure 3).[21] Self-assembly characteristics of TAIPDI with BSSBP resemble those with $ZnTPPSK_4$, which also has an extensive π-system.[14]

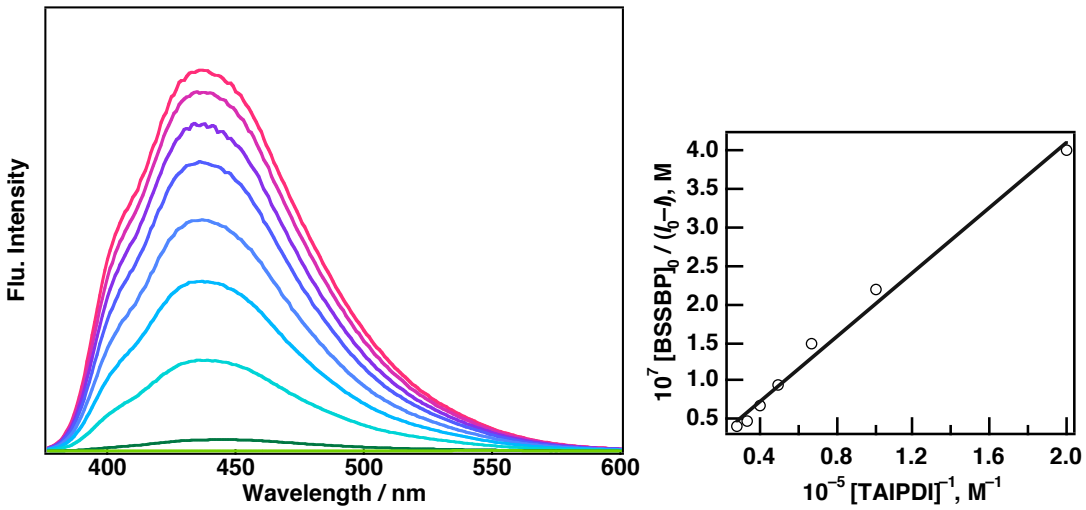


Figure 3. Emission spectral changes during the titration of BSSBP with TAIPDI in water. Inset: Linear plot of $[BSSBP]_0 / (I - I_0)$ vs $[TAIPDI]^{-1}$ at 437 nm to evaluate a formation constant.

DANS, on the other hand, gives absorption peaks at 403 and 382 nm with a shoulder at 370 nm in water (Figure 4).[22] Titration with TAIPDI causes indistinct decrease at 403 nm and

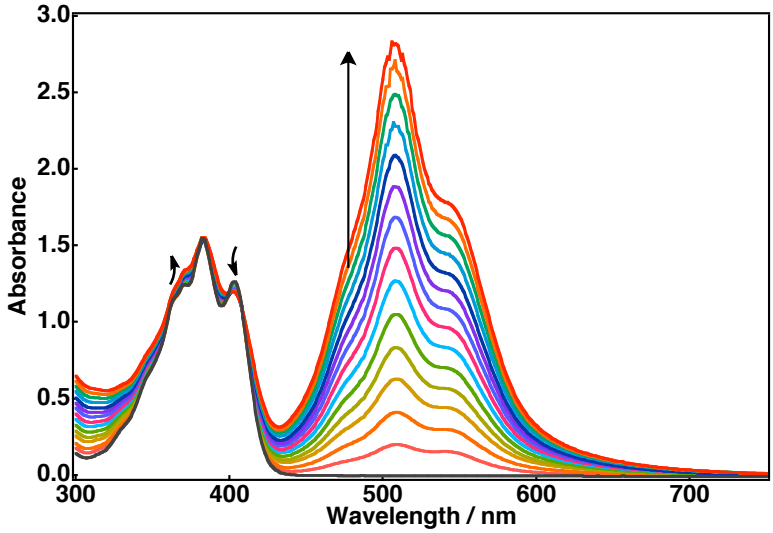


Figure 4. Absorption spectral changes during the titration of DANS with TAIPDI in water.

stacks first emerges at 510 nm, then, shifts to 508 nm. Molar extinction coefficient of TAIPDI is close to that in the absence of DANS. These absorption features reveal that π-π interactions between TAIPDI stacks and DANS are quite limited. On the contrary to slightly altered absorption features, the quenching of fluorescence of DANS is explicitly observed during the titration with TAIPDI stacks (Figure 5). Emission peak at 460 nm decreases with a shift to

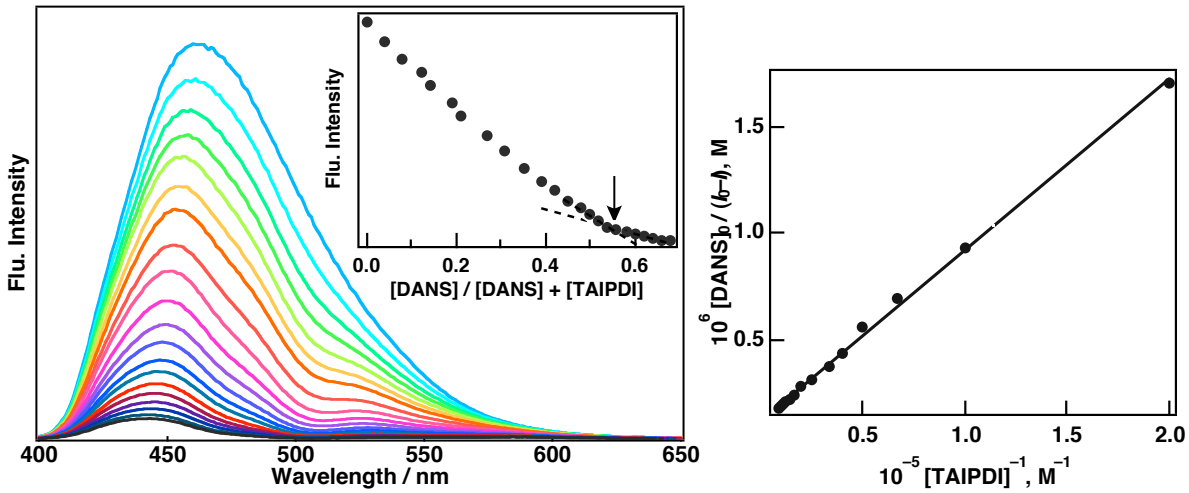


Figure 5. Emission spectral changes during the titration of DANS with TAIPDI in water. Inset: Plots of emission intensity vs ([DANS] / [DANS] + [TAIPDI]) showing the stoichiometry of the complex at 460 nm. (left) Linear plot of $[DANS]_0 / (I - I_0)$ vs $[TAIPDI]^{-1}$ at 460 nm to evaluate a formation constant (right).

422 nm by the addition of TAIPDI due to intrasupramolecular electron transfer via ionic interactions. Besides, featureless emission characteristics are altered vibrationally because DANS molecules are most probably positioned within the side chains of TAIPDIs while partially overlapping with TAIPDI aromatic core. Thus, the ionic interactions between TAIPDI

and DANS are more influential compared to π-π interactions due to modest π-extent of DANS. By this way, the distance between π-planes of TAIPDIs and DANS is extended to a degree. A plot of emission at 460 nm *vs*. the molar ratio of added TAIPDI to the total concentration revealed a break coinciding at 0.53, indicating a 1:1 ratio (Figure 5, Inset). The decrease in the emission intensity at 460 nm affords a linear plot, the slope of which gave the binding constant for DANS–TAIPDI (K_2) as 3.0×10^2 M^{-1} (Figure 5).[21] Compared to that of BSSBP–TAIPDI (K_1), this constant (K_2) is quite low due to reduced π-π interactions.

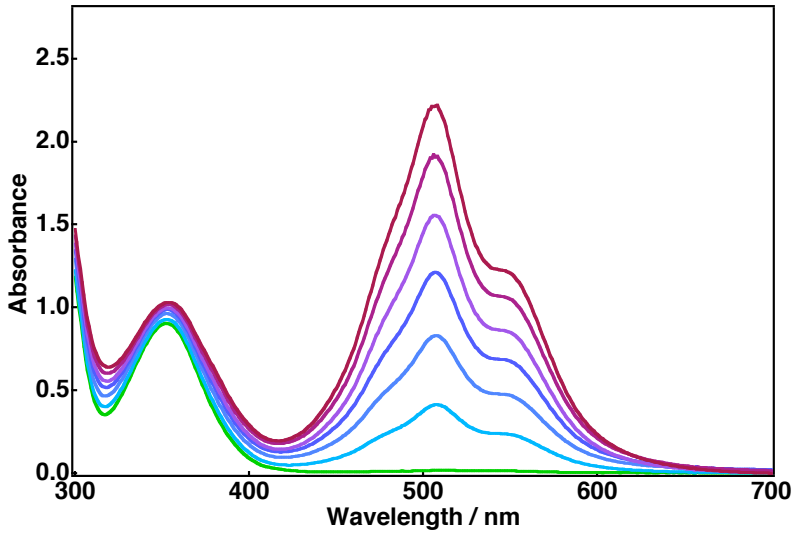


Figure 6. Absorption spectral changes during the titration of ANADS with TAIPDI in water.

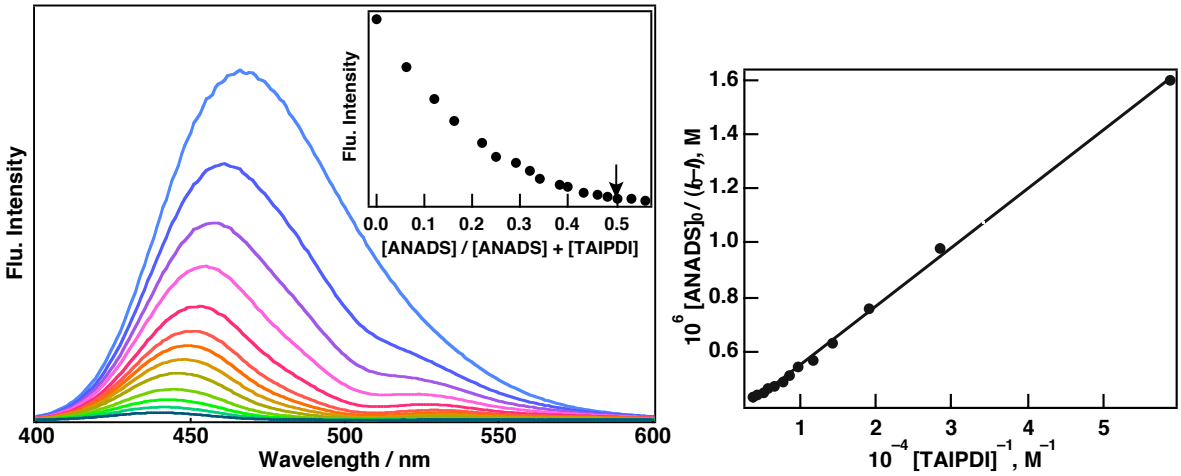


Figure 7. Emission spectral changes during the titration of DANS with TAIPDI in water. Inset: Plots of emission intensity vs ([ANADS] / [ANADS] + [TAIPDI]) showing the stoichiometry of the complex at 460 nm. (left) Linear plot of $[ANADS]_0 /(I - I_0)$ vs $[TAIPDI]^{-1}$ at 460 nm to evaluate a formation constant (right).

Lastly, ANADS, bearing small π-extent, has a charge-transition absorption band centred at 352 nm water (Figure 6). During the titration with TAIPDI, it gave no isosbestic point. Slight

shift from 352 to 354 nm is existent with a small rise in the absorbance due to probable ionic interactions with TAIPDI side chains.[23] $(TAIPDI)_n$ gives maximum at 506 nm. Thus, it can be concluded that there is no or negligible π-π interactions between ANADS and TAIPDI stacks. Similar to DANS, titration of ANADS with TAIPDI also leads to fluorescence quenching due to intrasupramolecular electron transfer via ionic interactions. ANADS gives a broad emission with a maximum at 466 nm. Another similarity is the blue shift of the emission to 441 nm while fluorescence quenching occurs. The emission is completely quenched when 1:1 ratio is reached upon the addition of TAIPDI (Figure 7, Inset). The decrease at 466 nm provides a linear correlation. From the slope of this linear plot, the binding constant for ANADS–TAIPDI (K_3) is determined to be 9.0×10^3 M^{-1} (Figure 7).[21]

Compared to that of DANS–TAIPDI, stronger binding of ANADS with TAIPDI can be explained by the presence of second anionic sulphonic group on the ANADS moiety. These anionic groups are strongly attracted by cationic heads of the side chains so that naphthalene cores barely communicate with the TAIPDI planes. ANADS moieties are most likely to be embedded in the side periphery of TAIPDI stacks. Hence, the distance between the stacked TAIPDI planes and the electron donors has been adjusted in accordance with the π-extents of the donor entities.

Energetics of Photoinduced Charge Separation. The driving forces for charge separation between $(TAIPDI)_n$ and electron donors in water have been calculated according to eq 1:[24]

$$\Delta G_{CS} = e(E_{ox} - E_{red}) - \Delta E_S + \Delta G_s \qquad (1)$$

where E_{ox} is the first one-electron oxidation potential of electron donors, E_{red} is the first one-electron reduction potential of $(TAIPDI)_n$, ΔE_S is the lowest singlet excited state energy of photosensitizer moiety in the complex, and ΔG_s is the static Coulomb energy in water.[25-27] The E_{ox} values of electron donors, obtained from water solutions containing 0.10 M Na_2SO_4 (Figure 8) are compiled in Table 1 together with corresponding ΔG_{CS} and ΔG_{CR} values. The E_{red} value of TAIPDI was already determined to be –0.25 V *vs* SCE in water containing 0.10 M Na_2SO_4.[14]

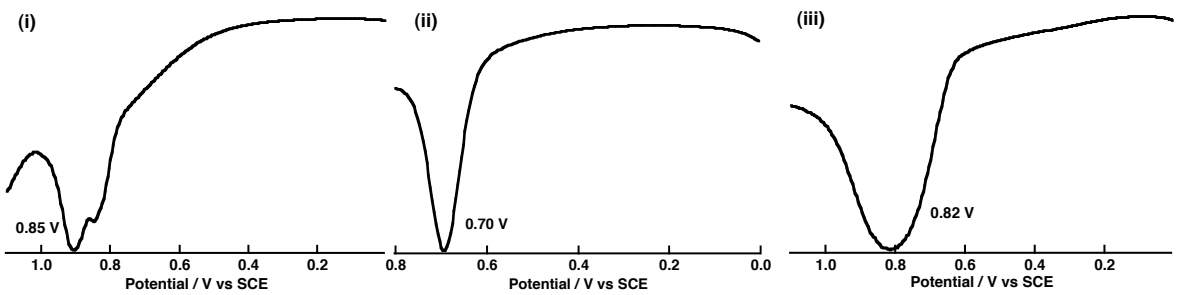


Figure 8. Differential pulse voltammogram of (i) BSSBP, (ii) DANS, and (iii) ANADS in deaerated water containing 0.10 M Na_2SO_4 (sweep rate: 0.1 mV/s).

Table 1. One-electron oxidation potentials (V vs SCE) and free energy changes of the charge separation ($-\Delta G_{CS}$) and charge recombination ($-\Delta G_{CR}$) of complexes of TAIPDI with donors

donor	E_{OX}	$-\Delta G_{CS}$	$-\Delta G_{CR}$
BSSBP	0.85	1.69	1.10
DANS	0.70	1.91	0.91
ANADS	0.82	1.79	1.03

Energy levels of triplet states have been calculated as 2.58, 1.75 and 2.43 eV for BSSBP, DANS and ANADS, respectively, based on phosphorescence measurements (Figure 9).[28] Triplet state energy of PDI was estimated to be 1.20 eV.[7,29] Thus, the triplet excited states of electron donors can undergo the charge separation.

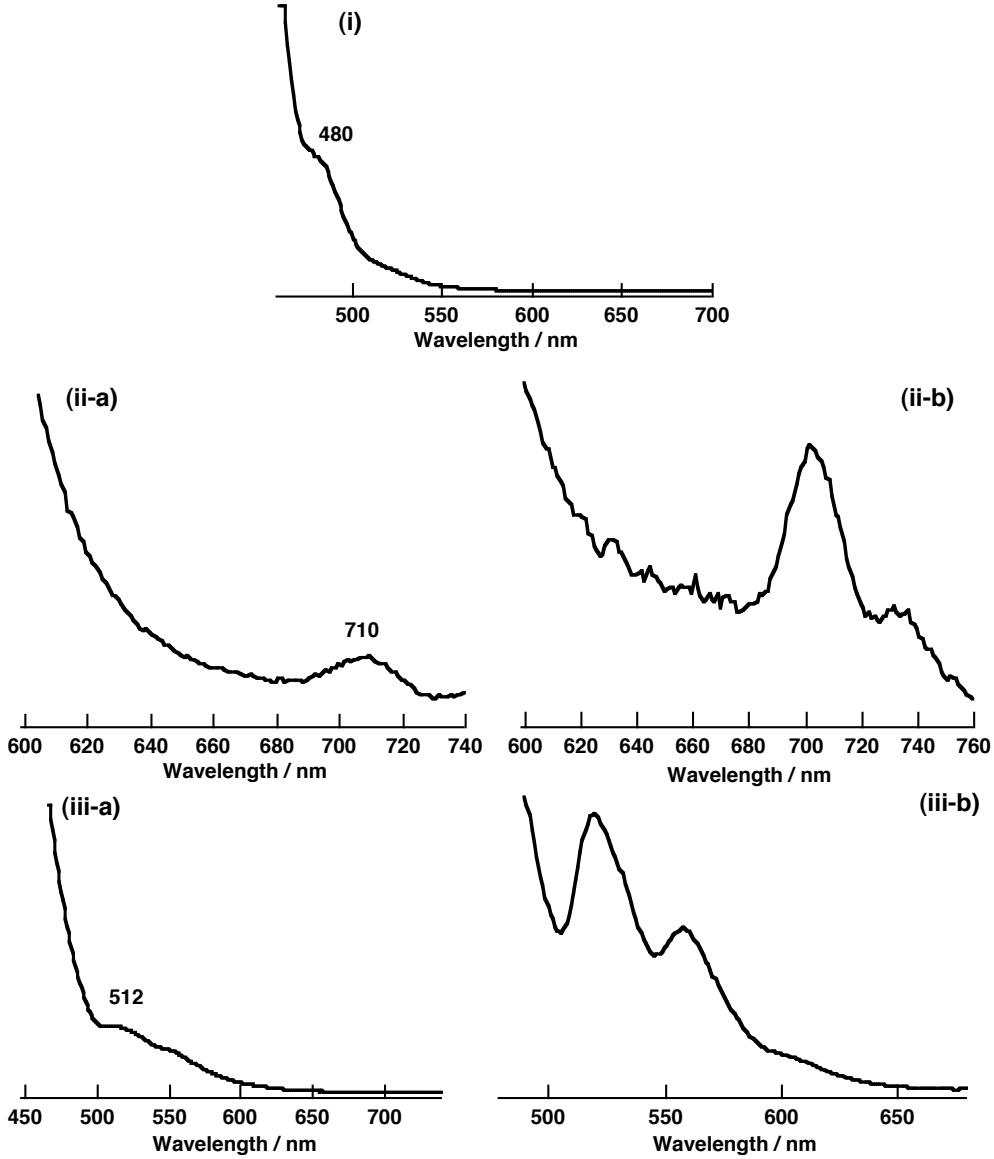


Figure 9. Phosphorescence spectra of (i) BSSBP in MeTHF/EtOH, (ii-a) DANS in MeTHF/EtOH, (ii-b) 9,10-dimethylanthracene in MeTHF, (iii-a) ANADS in MeTHF/EtOH, and (iii-b) naphthalene-2-amine in MeTHF containing MeI at 77 K.

Photoinduced electron-transfer processes taking place in the corresponding self-assembly systems have been observed by using femtosecond and nanosecond transient absorption measurements. To observe the extensive electron transport within the π-stacks of TAIPDI, the amounts of electron donors have been kept minimum while enough amounts of those are provided for the highest absorption at excitation wavelength as possible.

Photoinduced Charge Separation Dynamics of BSSBP–(TAIPDI)$_n$. Femtosecond transient measurements of BSSBP reveal the singlet excited states of BSSBP (^{1}BSSBP*), which give broad positive absorption, reaching a climax around 750 nm (Figure 10). The lifetime of ^{1}BSSBP* is determined as 0.8 ns in water. The femtosecond transient spectra of BSSBP–(TAIPDI)$_n$ in water display very fast formation of positive absorption with several maxima in the visible region, which are very different from those of ^{1}BSSBP* and ^{1}(TAIPDI)$_n$* (Figure 11).[14] These transient traits can be assigned to radical cation of BSSBP (BSSBP$^{\bullet+}$) and radical anion of (TAIPDI)$_n$ [(TAIPDI)$_n^{\bullet-}$], which are overlapping in the visible region.[30-33] Electron hopping in the TAIPDI stacks has also an effect on broadening of features of (TAIPDI)$_n^{\bullet-}$.[34] In the NIR region, broad transient around 970 nm distinctly originates from (TAIPDI)$_n^{\bullet-}$.[14,31] Thus, photoinduced electron transfer from BSSBP to TAIPDI stacks can be inferred from the transient spectral signatures of the radical ions of the electron donor and acceptor.

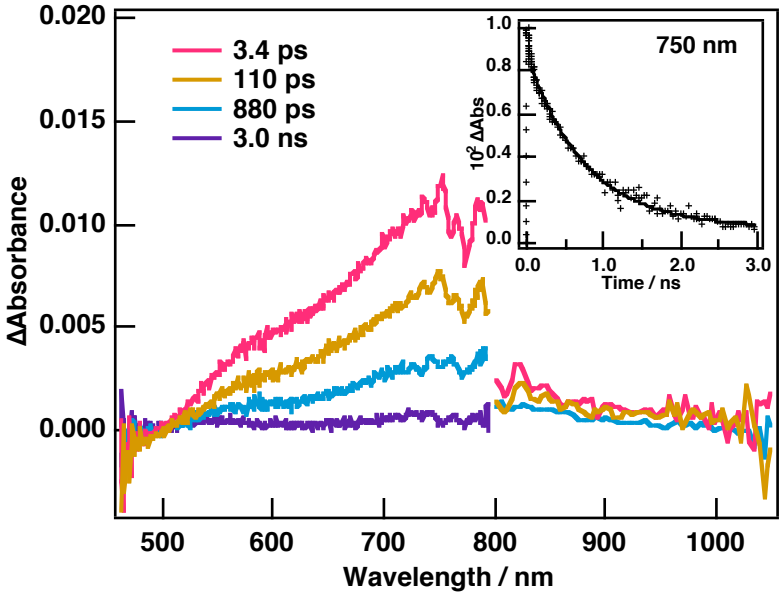


Figure 10. Femtosecond transient absorption spectra of BSSBP in water at indicated time delays. Inset: Time profile at 750 nm (λ_{exc} = 390 nm).

From the rise of absorbance at 730 and 970 nm, the rate of charge separation (k_{CS1}) is calculated as 1.4×10^{12} s^{-1} (0.70 ps). Very fast charge separation results from the strong π-π interactions between the donor and acceptor units within the columnar arrays. Similar to the ZnTPPSK$_4$–(TAIPDI)$_n$ case[14], the time profile at 730 nm gives two-component decay

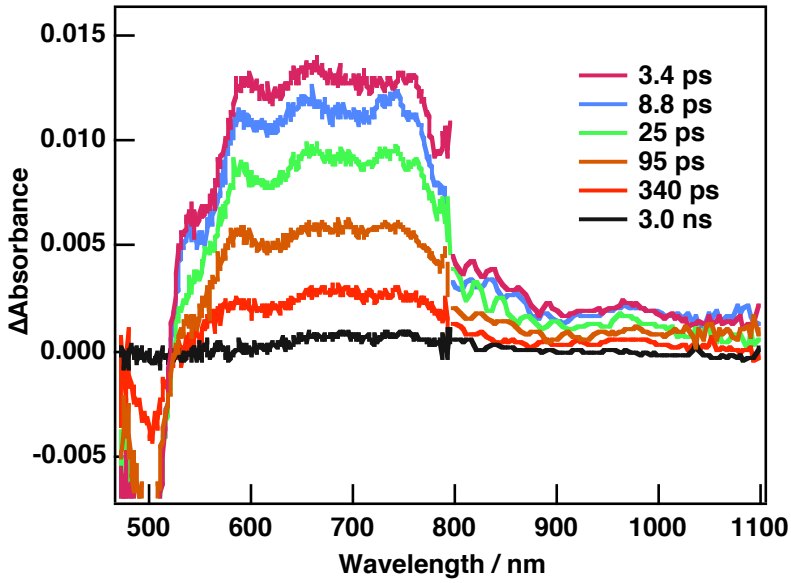


Figure 11. Femtosecond transient absorption spectra of BSSBP–(TAIPDI)$_n$ in water at indicated time delays (λ_{exc} = 390 nm).

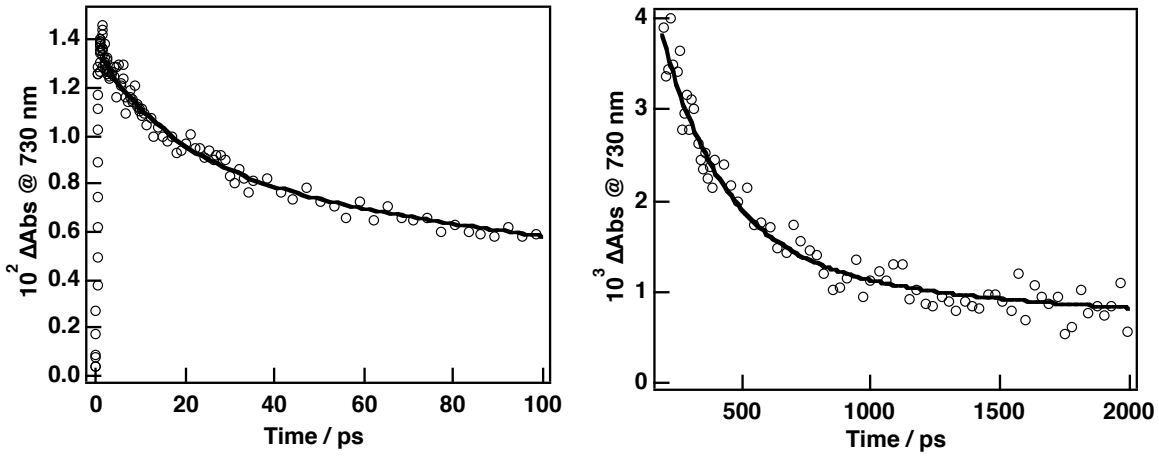


Figure 12. Time decay profiles of the transient absorbance at 730 nm at 0-100 (left) and 100-2000 ps (right).

As shown in Figure 12, the first component affords a decay rate constant of 5.8×10^{10} s^{-1} (τ_{CS1} = 17 ps) while the second component gives a slow decay with a rate constant of 2.1×10^{9} s^{-1} (τ_{CS2} = 485 ps), as a result of electron transport within the TAIPDI stacks, decelerating the charge recombination. The fast charge recombination, which is correlated with the first decay component, results from enhanced electronic coupling between the π-systems of the donor and acceptor[14,35] and the possible random distribution of the donor entities within the columnar arrays.[14] There was no transient signal in the nanosecond transient absorption spectra, suggesting that the charge recombination completes before 100 ns.[36]

Photoinduced Charge Separation Dynamics of DANS–(TAIPDI)$_n$ and ANADS–(TAIPDI)$_n$. Singlet excited states of DANS (^{1}DANS*) display broad peak at 550 nm and smaller absorption around 790 nm as monitored by femtosecond transient absorption

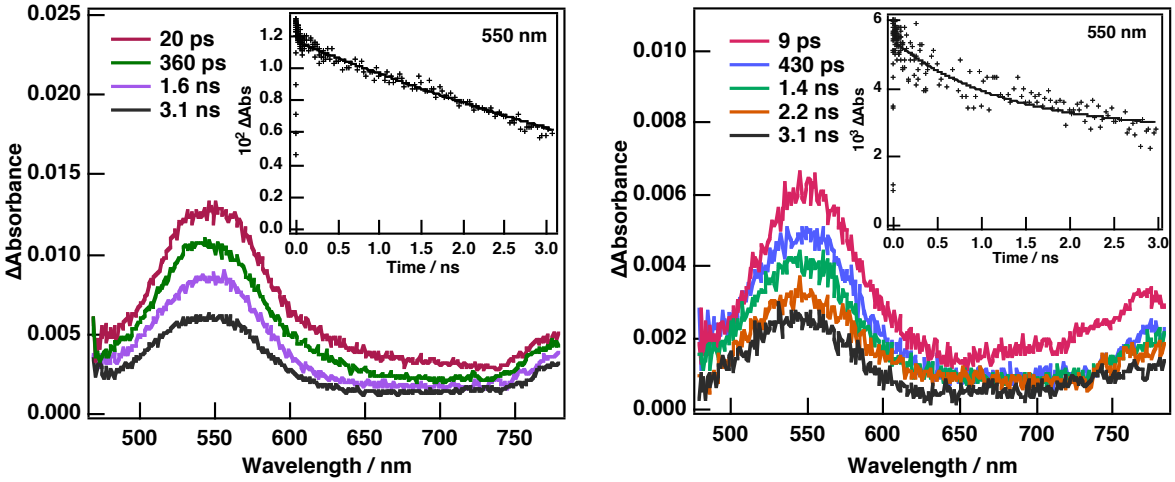


Figure 13. Femtosecond transient absorption spectra of DANS (left) and femtosecond transient absorption spectra of DANS–$(TAIPDI)_n$ in deaerated water at indicated time delays (right). Insets: Time profiles at 550 nm (λ_{exc} = 390 nm).

spectroscopy (Figure 13). The lifetime of ^{1}DANS* is determined from the decay at 550 nm as 6.0 ns (1.7×10^8 s^{-1}). As shown in Figure 13, the self-assembly of DANS with TAIPDI stacks exhibits almost identical femtosecond transient patterns to those of the singlet excited state of DANS except for the reduced lifetime to 1.2 ns ($k_q = 8.2 \times 10^8$ s^{-1}). On the other hand, the transient features of the self-assembly of ANADS with $(TAIPDI)_n$ are not significantly different from those of ^{1}ANADS* (Figure 14). Similarly, the lifetime of the ^{1}ANADS* (3.1 ns) is also decreased to 1.6 ns ($k_q = 6.1 \times 10^8$ s^{-1}). The shortened lifetimes of singlet excite states of

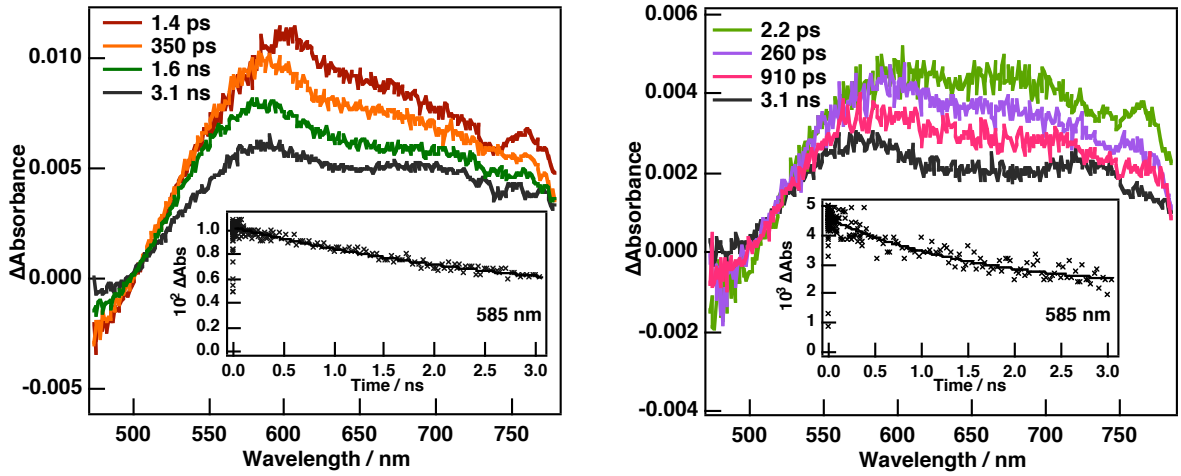


Figure 14. Femtosecond transient absorption spectra of ANADS (left) and femtosecond transient absorption spectra of ANADS–$(TAIPDI)_n$ in deaerated water at indicated time delays (right). Insets: Time profiles at 585 nm (λ_{exc} = 390 nm).

electron donors suggest the occurrence of photoinduced electron transfer to the TAIPDI stacks in both cases. The absence of transient traits of $^1(TAIPDI)_n$* or ^{1}TAIPDI* indicates that there

is no singlet-singlet energy transfer from electron donors. The rate of charge separation can be estimated from the quenching of the singlet excited state by using eq 2:[37]

$$k_{CS} = (1/\tau_q) - k_S \qquad (2)$$

where τ_q is the lifetime of the quenched singlet excite state due to electron transfer and k_S is the rate constant of the singlet excited state without any quenching. Then, k_{CS} for DANS–$(TAIPDI)_n$ is estimated as 6.7×10^8 s^{-1} (1.5 ns) while ANADS–$(TAIPDI)_n$ affords a charge separation rate constant of 6.1×10^8 s^{-1} (1.6 ns). Compared to that of BSSBP–$(TAIPDI)_n$, the charge-separation processes in these self-assemblies are quite slow because of increased distance between the donor and the acceptor.[38] Still, the access to the charge separation via the triplet states is feasible because energy levels of the charge-separated states of self-assemblies of DANS and ANADS are below those of triplet states of the electron donors.

To monitor the electron-transfer products, nanosecond transient absorption measurements have been performed for these self-assembly systems. The charge separation is evident in the nanosecond absorption spectra of DANS–$(TAIPDI)_n$ as the formation of radical cation of DANS ($DANS^{\bullet+}$) and radical anion of $(TAIPDI)_n$ is clearly observed (Figure 15). $DANS^{\bullet+}$

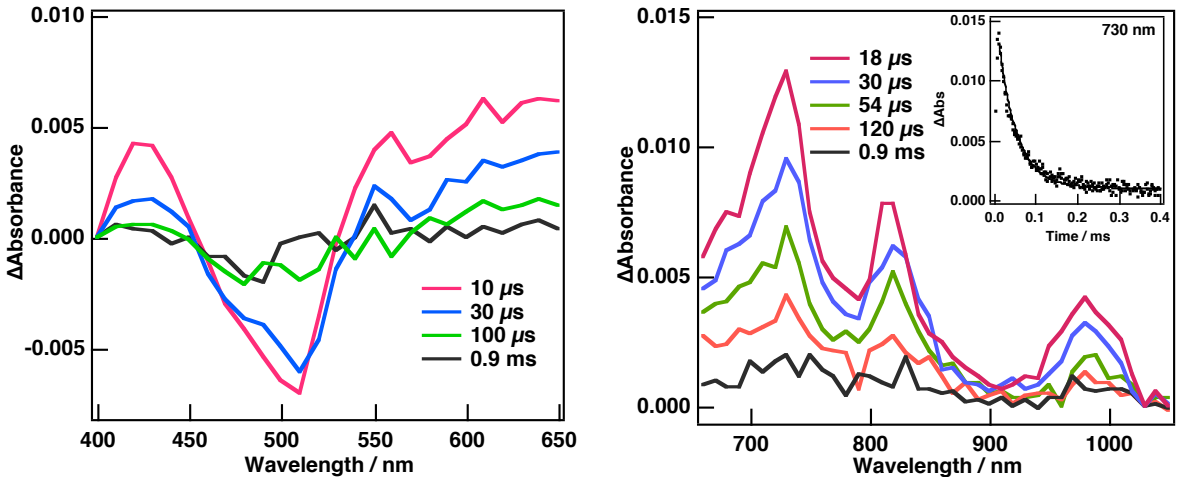


Figure 15. Nanosecond transient absorption spectra of DANS–$(TAIPDI)_n$ between 400 and 650 nm (left) and 650 and 1100 nm (right) in deaerated water at indicated time delays. Inset: Time profile at 730 nm (λ_{exc} = 355 nm).

appears at 420, 560 and 610 nm[32] while the typical peaks of $(TAIPDI)_n^{\bullet-}$ emerge at 730, 820, and 980 nm.[14,31] There was no signal to assign for the triplet excited states of DANS or TAIPDI, resulting from the triplet-triplet energy transfer.[39] The decay of electron-transfer species follows first-order kinetics. The rate constant for charge recombination is determined to be 2.3×10^4 s^{-1} from the decay at 730 nm, giving the lifetime of the charge-separated state as 44 μs (Figure 15, inset). When turning to ANADS–$(TAIPDI)_n$, the nanosecond transient spectra also exhibit the formation of $ANADS^{\bullet+}$ at around 400 and 540 nm[32] and $(TAIPDI)_n^{\bullet-}$ at

730, 810, and 980 nm as a result of the charge separation (Figure 16). The absence of transients due to the triplet-excited states suggests highly efficient photodriven charge-separation process. The decay rate of $(TAIPDI)_n^{\bullet-}$ at 730 nm was fitted to a first-order plot where the rate of charge recombination for ANADS–$(TAIPDI)_n$ was found to be 1.0×10^4 s^{-1} (τ_{CS} = 96 μs).

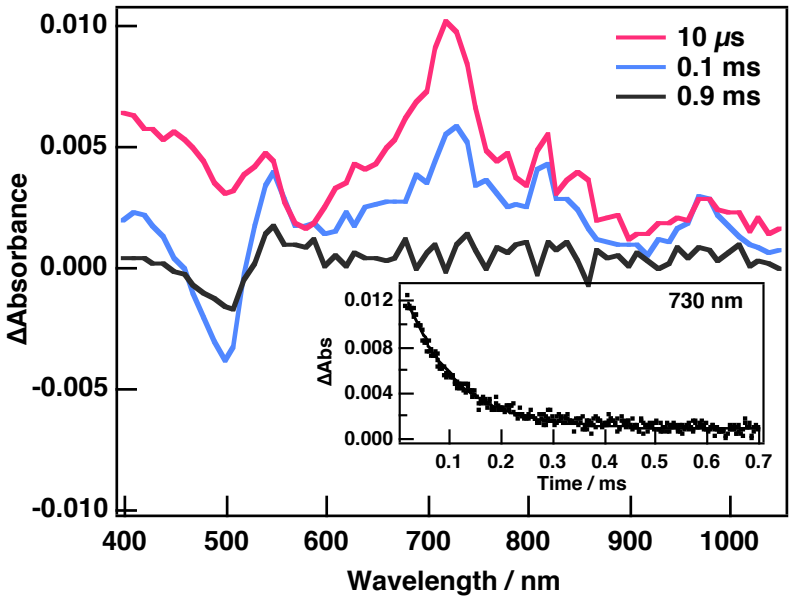


Figure 16. Nanosecond transient absorption spectra of ANADS–$(TAIPDI)_n$ in deaerated water at indicated time delays. Inset: Time profile at 730 nm (λ_{exc} = 355 nm).

Photoinduced processes observed in these systems are summarized in energy level diagrams (Figure 17). Compared to BSSBP–$(TAIPDI)_n$ case, exceedingly longer lifetime values for the charge-separated states in DANS–$(TAIPDI)_n$ and ANADS–$(TAIPDI)_n$ systems can be explained by the presence of improved charge transport in the TAIPDI stacks. The reduced electronic coupling also inhibits the fast exciton quenching of electron donors because of π-stacking with TAIPDIs. Increasing the distance has brought about slow charge separation. However, the higher k_{CS}/k_{CR} ratios of DANS–$(TAIPDI)_n$ and ANADS–$(TAIPDI)_n$ (29000 and 61000, respectively) than those of BSSBP–$(TAIPDI)_n$ and $ZnTPPSK_4$–$(TAIPDI)_n$ (667 and 3000,[14] respectively) sufficiently compensate this drawback. Because DANS and ANADS molecules are positioned at the side periphery of TAIPDI cores dominantly via ionic interactions with negligible π-π interactions, long-range electron transport in the $(TAIPDI)_n$ has not been interrupted. As might be expected, stacking defects still hinder the electron hopping along these stacks.[40] Utilizing the triplet states has an impact on the elongation of the electron transport due to spin restriction rules.[41] As a result, lifetimes of charge-separated states of DANS–$(TAIPDI)_n$ and ANADS–$(TAIPDI)_n$ are at least 10^5 times longer than that of tightly stacked BSSBP–$(TAIPDI)_n$ due to extensive electron transport without interruption of the penetrated electron-donor moieties.

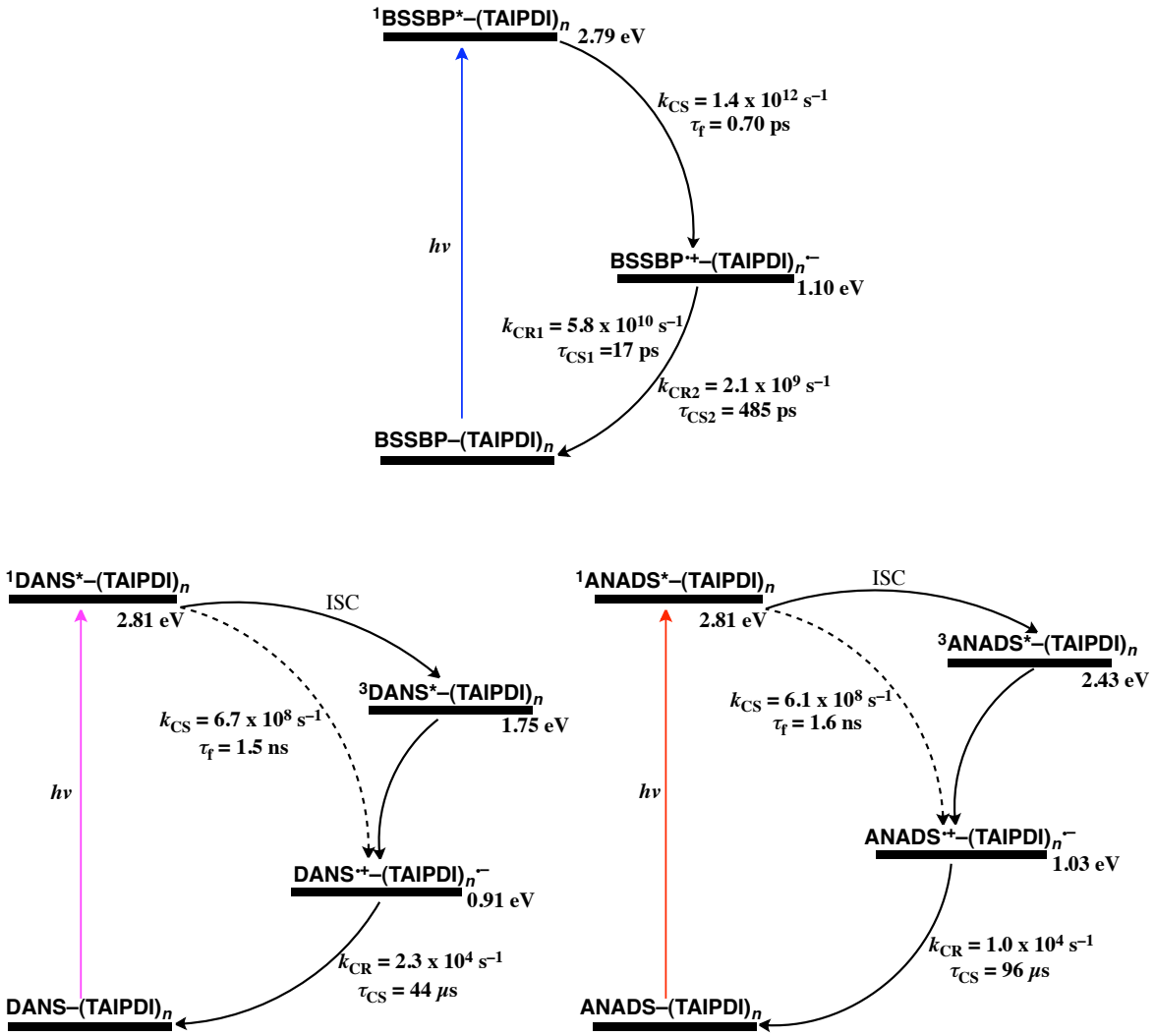


Figure 17. Energy level diagrams showing photoinduced events of corresponding self-assembly systems.

Conclusion

The columnar stacks of TAIPDI host BSSBP, DANS, and ANADS molecules at various ratios via intermolecular interactions. The π-π interactions mainly govern the self-assembly of $(TAIPDI)_n$ and BSSBP, having large π-extent, thereby favouring the electron coupling. On the other hand, DANS and ANADS, having relatively small π-extents, interact with the side chains of TAIPDI stacks via ionic interactions resulting in distance increment with TAIPDI π-planes. The enhanced distance improves the extensive electron transport along the TAIPDI stacks in DANS–$(TAIPDI)_n$ and ANADS–$(TAIPDI)_n$ after photoinduced electron transfer from electron donors.

References and Notes

(1) Aida, T.; Meijer, E. W.; Stupp, S. I. *Science* **2012**, *335*, 813.

(2) Wang, M.; Wudl, F. *J. Mater. Chem.* **2012**, *22*, 24297.
(3) Zang, L.; Che, Y.; Moore, J. S. *Acc. Chem. Res.* **2008**, *41*, 1596.
(4) Wasielewski, M. R. *Acc. Chem. Res*. **2009**, *42*, 1910.
(5) Chen, S.-G.; Branz, H. M.; Eaton, S. S.; Taylor, C.; Cormier, R. A.; Gregg, B. A. *J. Phys. Chem. B* **2004**, *108*, 17329.
(6) Che, Y.; Datar, A.; Yang, X.; Naddo, T.; Zhao, J.; Zang, L. *J. Am. Chem. Soc.* **2007**, *129*, 6354.
(7) Supur, M.; Yamada, Y.; El-Khouly, M. E.; Honda, T.; Fukuzumi, S. *J. Phys. Chem. C* **2011**, *115*, 15040.
(8) Howard, I. A.; Laquai, F.; Keivanidis, P. E.; Friend, R. H.; Greenham, N. C. *J. Phys. Chem. C* **2009**, *113*, 21225.
(9) Giaimo, J. M.; Lockard, J. V.; Sinks, L. E.; Scott, A. M.; Wilson, T. M.; Wasielewski, M. R. *J. Phys. Chem. A* **2008**, *112*, 2322.
(10) Pensack, R. D.; Guo, C.; Vakhshouri, K.; Gomez, E. D.; Asbury, J. B. *J. Phys. Chem. C* **2012**, *116*, 4824.
(11) Although the transportation of the photogenerated charges in the active layers of the BHJ solar cells has so far been achieved by using π-conjugated polymer donors, which are available for extensive charge delocalization along the polymer backbone, they hardly form one dimensional self-organizations at nanoscale without additional synthetic modifications. See: Bakulin, A. A.; Rao, A.; Pavelyev, V. G.; van Loosdrecht, P. H. M.; Pshenichinikov, M. S.; Niedzialek, D.; Cornil, J.; Beljonne, D.; Friend, R. H. *Science* **2012**, *335*, 1340.
(12) Ramanan, C.; Smeigh, A. L.; Anthony, J. E.; Marks, T. J.; Wasielewski, M. R. *J. Am. Chem. Soc.* **2012**, *134*, 386.
(13) Rajaram, S.; Shivanna, R.; Kandappa, S. K.; Narayan, K. S. *J. Phys. Chem. Lett.* **2012**, *3*, 2405.
(14) Supur, M.; Fukuzumi, S. *J. Phys. Chem. C* **2012**, *116*, 23274.
(15) (a) Biedermann, F.; Elmalem, E.; Ghosh, I.; Nau, W. M.; Scherman, O. A. *Angew. Chem., Int. Ed.* **2012**, *51*, 7739. (b) Wang, B.; Yu, C. *Angew. Chem., Int. Ed.* **2010**, *49*, 1485. (c) Reilly III, T. H.; Hains, A. W.; Chen, H.-Y.; Gregg, B. A. *Adv. Energy Mater.* **2012**, *2*, 455.
(16) Huang, Y.; Quan, B.; Wei, Z.; Liu, G.; Sun, L. *J. Phys. Chem. C* **2009**, *113*, 3929.
(17) Sharma, A. K.; Ahlawat, D. S.; Mohan, D.; Singh, R. D. *Spectrochim. Acta A*, **2009**, *71*, 1631.
(18) Besides the red shift, the extinction coefficient of TAIPDI (ε) at 501 nm is reduced to 11600 M^{-1} cm^{-1} when the 1:1 ratio is established. Normally, it has the ε value of 37 500 M^{-1} cm^{-1} at 501 nm.[14] After exceeding the 1:1 ratio, ε starts to converge to the normal value.
(19) Fukuzumi, S.; Amasaki, I.; Ohkubo, K.; Gros, C. P.; Guilard, R.; Barbe, J.-M. *RSC*

Adv. **2012**, *2*, 3741.

(20) According to the 1:1 ratio, the absorbance change is given by the equation $[BSSBP]_0 / (A - A_0) = (\varepsilon_c - \varepsilon_p)^{-1} + (K_1[TAIPDI](\varepsilon_c - \varepsilon_p))^{-1}$, where A_0 and A are the absorbance of BSSBP and ε_c and ε_p are the molar absorption coefficients of BSSBP at 349 nm in the absence and presence of TAIPDI, respectively. This equation predicts a linear correlation between $[BSSBP]_0 / (A - A_0)$ and $[TAIPDI]^{-1}$.[19]

(21) According to the 1:1 ratio, the emission change is given by the equation $[BSSBP]_0 / (I - I_0) = (\varepsilon_c - \varepsilon_p)^{-1} + (K_1[TAIPDI](\varepsilon_c - \varepsilon_p))^{-1}$, where I_0 and I are the emission intensity of BSSBP and ε_c and ε_p are the molar absorption coefficients of BSSBP at 437 nm in the absence and presence of TAIPDI, respectively. This equation predicts a linear correlation between $[BSSBP]_0 / (I - I_0)$ and $[TAIPDI]^{-1}$.[19]

(22) Itaya, T.; Kawabata, Y.; Ochiai, H.; Ueda, K.; Imamura, A. *Bull. Chem. Soc. Jpn.* **1994**, *67*, 1538.

(23) Supur, M.; Yamada, Y.; Fukuzumi, S. *J. Mater. Chem.* **2012**, *22*, 12547.

(24) Weller, A. *Z. Phys. Chem.* **1982**, *133*, 93.

(25) To calculate the ΔG_s, the two correlations have been used:[26] (i) ΔG_s (eV) = 0.56 $(1/\varepsilon)$ + 0.003 when electron-transfer products are contact ion pair and (ii) ΔG_s = 1.52 $(1/\varepsilon)$ – 0.064 when electron-transfer products are solvent-separated ion pair, where ε is the dielectric constant of the solvent. Because TAIPDI and BSSBP are closely positioned via π-π interactions, the initial products are assumed to be contact ion pair while those of TAIPDI[14] and the other electron donors (DANS and ANADS) are accepted as solvent separated ion pairs.[27]

(26) Arnold, B. R.; Farid, S.; Goodman, J. L.; Gould, I. R. *J. Am. Chem. Soc.* **1996**, *118*, 5482.

(27) Supur, M.; El-Khouly, M. E.; Seok, J. H.; Kay, K.-Y.; Fukuzumi, S. *J. Phys. Chem. A* **2011**, *115*, 14430.

(28) Because electron donors are not so soluble in MeTHF, the mixture of MeTHF and EtOH has been used. Phosphorescence emissions of DANS and ANADS have been compared to those of 9,10-dimethylanthracene and napthalen-2-amine obtained in MeTHF at 77 K.

(29) Fukuzumi, S.; Ohkubo, K.; Ortiz, J.; Gutierrez, A. M.; Fernandez-Lazaro, F.; Sastre-Santos, A. *J. Phys. Chem. A* **2008**, *112*, 10744-10752.

(30) $(TAIPDI)_n^{\bullet-}$ has a broad absorbtion centered at 730 nm.[31] Stilbene radical cation has also broad absorption around 760 nm with shoulder around 650 nm.[32,33] *Cis*- and *trans*-isomers of BSSBP may also cause the formation different maxima of radical cation.[32]

(31) Marcon, R. O.; Brochsztain, S. *J. Phys. Chem. A* **2009**, *113*, 1747.

(32) Shida, T. Electronic Absorption Spectra of Radical Ions, Elsevier, Amsterdam, 1988.

(33) El-Agamey, A.; Fukuzumi, S. *Chem.–Eur. J.* **2012**, *18*, 14660.
(34) van der Boom, T.; Hayes, R. T.; Zhao, Y.; Bushard, P. J.; Weiss, E. A.; Wasielewski, M. R. *J. Am. Chem. Soc.* **2002**, *124*, 9582.
(35) (a) Ohtani, M.; Fukuzumi, S. *Chem. Commun.* **2009**, 4997. (b) El-Khouly, M. E.; Jaggi, M.; Schmid, B.; Blum, C.; Liu, S.-X.; Decurtins, S.; Ohkubo, K.; Fukuzumi, S. *J. Phys. Chem. C* **2011**, *115*, 8325. (c) Grimm, B.; Santos, J.; Illescas, B.; Munoz, A.; Guldi, D. M.; Martin, N. *J. Am. Chem. Soc.* **2010**, *132*, 17387.
(36) The time range between 3 and 100 ns is out of the range of our laser system.
(37) (a) Williams, R. M. *Turk. J. Chem.* **2009**, *33*, 727. (b) Karapire, C.; Zafer, C.; Icli, S. *Synth. Met.* **2004**, *145*, 51. (c) Straight, S. D.; Kodis, G.; Terazono, Y.; Hambourger, M.; Moore, T. A.; Moore, A. L.; Gust, D. *Nat. Nanotechnol.* **2008**, *3*, 280.
(38) D'Souza, F.; Maligaspe, E.; Ohkubo, K.; Zandler, M. E.; Subbaiyan, N. K.; Fukuzumi, S. *J. Am. Chem. Soc.* **2009**, *131*, 8787.
(39) For the transient features of the triplet excited states of PDIs, see: Castellano, F. N. *Dalton Trans.*, **2012**, *41*, 8493 and references therein.
(40) Ide, J.; Mereau, R.; Ducasse, L.; Castet, F.; Olivier, Y.; Martinelli, N.; Cornil, J.; Beljonne, D. *J. Phys. Chem. B* **2011**, *115*, 5593.
(41) Suzuki, S.; Sugimura, R.; Kozaki, M.; Keyaki, K.; Nozaki, K.; Ikeda, N.; Akiyama, K.; Okada, K. *J. Am. Chem. Soc.* **2009**, *131*, 10374.

Concluding Remarks

In this thesis, the photoinduced electron-transfer processes (i.e.; charge separation, charge migration, and charge recombination) of the self-assembly systems of PDI nanostructures possessing one-dimensional organizations have been discussed. Fingerprints of the electron-transfer products of such systems have been monitored by using time-resolved transient absorption spectroscopy besides the other instruments, named in the experimental sections, used for the calculation of the photoinduced electron-transfer energetics and the characterization of the nanostructures and self-assembly systems of PDIs in each chapter. The main point of the thesis is the control of the directional charge migration (i.e., electron transport) along the columnar π-stacks of PDIs by the weak interactions with the electron donor moieties to obtain long-range electron transfer after a fast charge separation process takes place. As mentioned in the general introduction and in the corresponding chapters in detail, intermolecular weak interactions have also been utilized to control the entire electron-transfer processes in the protein environment of the photosynthetic reaction centers of the photosynthesis. Therefore, mimicking the well-ordered arrangement of the natural paradigm via these interactions is quite vital for practical purposes, such as material design for optoelectronics, in which the efficient electron transfer is of the essence. Throughout the related chapters, elongated lifetime values of charge separated states to nano and microsecond time regimes were considered to be the sign of extensive, long-range electron transfer within the columnar PDI stacks.

The thesis comprises the data for the electron-transfer events of monomer PDI for understanding and comparison with those of the PDI π-stacks, as detailed in the first chapter. Besides, this chapter includes the electron-accepting features of PDIs modified from their bay region with electron-donating and-withdrawing groups during the electron-transfer processes.

In the following chapter, a hybrid mixture system, consisting of nanobelt structures of a PDI with linear side chains and a soluble electron donor (ZnTBPc), has been characterized and the migration mechanism of the photoinduced-transferred electron within the nanobelts has been examined spectroscopically. Photodynamics of electron-transfer events of this hybrid system has been also compared to another mixture system of PDI, having soluble, non-directional components.

The chapter 3 manifests the importance of the electron-transfer distance between the one-dimensional PDI nanostructures and the electron donors in competing with energy-transfer process. For this purpose, the supramolecular self-assembly systems have been constructed by using weak interactions (i.e., π-π, lipophilic, and ionic interactions). Photoinduced electron transfer was absent in the self-assemblies described in this chapter due to the long distance between the donors located on the side-surface periphery and the PDI aromatic cores buried in

the nanoribbons although the water has been chosen as a very polar environment, which was expected to boost the electron-transfer reactions.

In chapter 4, photoinduced electron-transfer events of a newly synthesized An_2PDI triad have been clarified in organic and in aqueous media. Bearing both hydrophobic and hydrophilic sections, triad molecules can modify themselves to aqueous environment by conformational and intermolecular rearrangements, which greatly enhance the photoinduced charge separation. On the other hand, photoinduced electron transfer was not efficient against the geometric alterations, reasonably long electron-transfer distance, and competing energy transfer in MeOH, in which An_2PDI lacks such organizational behaviors.

In chapter 5, columnar nanostructures of a PDI derivative, which can be solubilized in an aqueous medium and can host π-electron donors, have been characterized and their electron-transfer features have been clarified. Excited-state dynamics of PDI aggregates have been explained by a comparison with those of unstacked PDI. Photoexcitation of host-guest complexes of PDI nanostructures generate very fast charge separation. Charge recombination is markedly decelerated by an electron migration mechanism along the long range of tightly stacked TAIPDIs, which eventually results in a k_{CS}/k_{CR} ratio of 3000 as determined by using time-resolved transient absorption techniques.

The last chapter demonstrates the photodriven electron-transport properties of the self-assemblies of the PDI stacks with three electron donors, which differ in their π-extent to adjust the electronic coupling and the distance with the PDI aggregates. The columnar stacks of PDI host these π-donor molecules at various ratios via intermolecular interactions. The strong electron coupling was favored by the extensive π-π interactions with the donor moiety having large π-extent. Due to these interactions, donor moieties penetrate into the PDI stacks, impeding the long-range electron transfer. On the other hand, the electron donors, having relatively small π-extents, mainly interact with side chains of the PDI stacks via ionic interactions resulting in distance increment with PDI π-planes, which improves the extensive electron transport along the PDI stacks without interruption, reaching k_{CS}/k_{CR} ratios up to 10^5.

As postulated in the above-mentioned chapters, weak interactions can control the mechanism of the electron transfer within the one-dimensional nanostructures of PDI. Morphological arrangements at nanometer scale established by such interactions in the active layers of the devices designed for solar energy conversion have a potential for improving the efficiency.

List of Publications

Publications Related to This Thesis:

(1) Efficient Electron Transfer Processes of the Covalently Linked Perylenediimide–Ferrocene Systems: Femtosecond and Nanosecond Transient Absorption Studies

Supur, M.; El-Khouly, M. E.; Seok, J. H.; Kim, J. H.; Kay, K.-Y.; Fukuzumi, S.

J. Phys. Chem. C **2010**, *114*, 10969.

(2) Electron Delocalization in One-Dimensional Perylenediimide Nanobelts via Photoinduced Electron Transfer

Supur, M.; Yamada, Y.; El-Khouly, M. E.; Honda, T.; Fukuzumi, S.

J. Phys. Chem. C **2011**, *115*, 15040.

(3) Excitation Energy Transfer from Non-Aggregated Molecules to Perylenediimide Nanoribbons via Ionic Interactions in Water

Supur, M.; Yamada, Y.; Fukuzumi, S.

J. Mater. Chem. **2012**, *22*, 12547.

(4) Enhancement of Photodriven Charge Separation by Conformational and Intermolecular Adaptations of an Anthracene–Perylenediimide–Anthracene Triad to an Aqueous Environment

Supur, M.; Sung, Y. M.; Kim, D.; Fukuzumi, S.

J. Phys. Chem. C **2013**, *117*, 12438.

(5) Photodriven Electron Transport within the Columnar Perylenediimide Nanostructures Self-Assembled with Sulfonated Porphyrins in Water

Supur, M.; Fukuzumi, S.

J. Phys. Chem. C **2012**, *116*, 23274.

(6) Tuning the Photodriven Electron Transport within the Columnar Perylenediimide Stacks by Changing the π-Extent of Electron Donors

Supur, M.; Fukuzumi, S.

Phys. Chem. Chem. Phys. **2013**, *15*, 2539.

Other Publications:

(1) A New Cyanofluorene–Triphenylamine Copolymer: Synthesis and Photoinduced Intramolecular Electron Transfer Processes

Lin, Y.; El-Khouly, M. E.; Chen, Y.; Supur, M.; Gu, L.; Li, Y.; Fukuzumi, S.

Chem.–Eur. J. **2009**, *15*, 10818.

(2) Photochemical Charge Separation in Closely Positioned Donor–Boron Dipyrrin–Fullerene Triads

Wijesinghe, C. A.; El-Khouly, M. E.; Subbaiyan, N. K.; Supur, M.; Zandler, M. E.; Ohkubo, K.; Fukuzumi, S.; D'Souza, F.

Chem.–Eur. J. **2011**, *17*, 3147.

(3) Syntheses, Electrochemistry, and Photodynamics of Ferrocene–Azadipyrromethane Donor–Acceptor Dyads and Triads

Amin, A. N.; El-Khouly, M. E.; Subbaiyan, N. K.; Zandler, M. E.; Supur, M.; Fukuzumi, S.; D'Souza, F.

J. Phys. Chem. A **2011**, *115*, 9810.

(4) Elongation of Lifetime of the Charge-Separated State of Ferrocene–Naphthalenediimide–[60]Fullerene Triad via Stepwise Electron Transfer

Supur, M.; El-Khouly, M. E.; Seok, J. H.; Kay, K.-Y.; Fukuzumi, S.

J. Phys. Chem. A **2011**, *115*, 14430.

(5) Charge Dynamics in a Donor–Acceptor Covalent Organic Framework with Periodically Ordered Bicontinuous Heterojunctions

Jin, S.; Ding, X.; Feng, X.; Supur, M.; Furukawa, K.; Takahashi, S.; Addicoat, M.; El-Khouly, M. E.; Nakamura, T.; Irle, S.; Fukuzumi, S.; Nagai, A.; Jiang, D.

Angew. Chem., Int. Ed. **2013**, *52*, 2017.

Acknowledgment

Many hands make light work…

I would like first to express my sincere thanks to Professor Shunichi Fukuzumi for his permanent enlightenment and lasting encouragement throughout doctoral course.

I convey my thanks to Dr. Mohamed E. El-Khouly for his guidance and fruitful discussions. I also extend my particular thanks to Dr. Yusuke Yamada, Dr. Kei Ohkubo, Dr. Tomoyoshi Suenobu, and Dr. Ali El-Agamey for their critical suggestions and invaluable contributions that I benefited a lot.

Thanks are also given to Professor Kwang-Yol Kay of Ajou University (Korea) and Professor Dongho Kim of Yonsei University (Korea) and their coworkers for their diligent collaboration.

I extend my cordial appreciation to present and former students, graduates, and postdoctoral associates of Fukuzumi Lab, who patiently and kindly expended their precious time for helping me during my research. I have benefited from their assistance very much. My thanks also go to the former and present secretaries of Fukuzumi Lab.

I acknowledge Ministry of Education, Culture, Sports, Science and Technology (MEXT), Japan for a scholarship throughout the master and doctoral courses.

Last but not least, I would like to express my profound gratitude to my whole family for their indispensable support during this study and my stay in Japan. This thesis is devoted to them.

Mustafa SUPUR

Department of Material and Life Science
Division of Advanced Science and Biotechnology
Graduate School of Engineering
Osaka University

Osaka, JAPAN
September, 2013